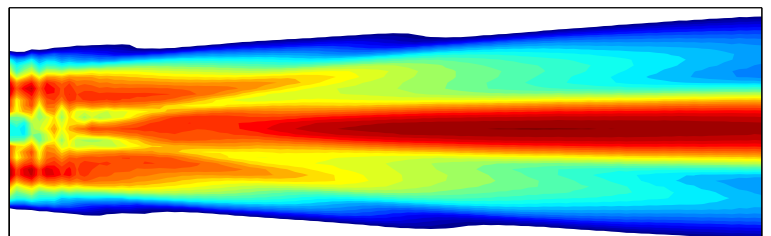
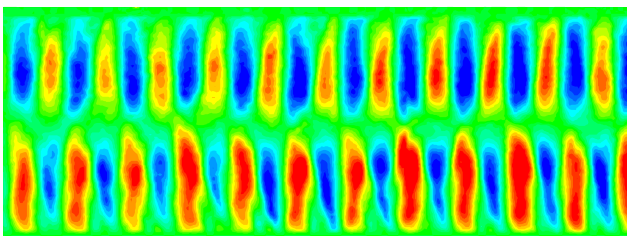


ISUD 8

Proceedings of the 8th International Symposium on Ultrasonic Doppler Methods for Fluid Mechanics and Fluid Engineering

19-21 September 2012, Dresden, Germany



HZDR

HELMHOLTZ
ZENTRUM DRESDEN
ROSSENDORF



Proceedings of the 8th International Symposium on Ultrasonic Doppler Methods for Fluid Mechanics and Fluid Engineering

19-21 September 2012, Dresden, Germany

Scientific Committee:

Dr. V. Bareš (Department of Sanitary and Ecological Engineering, CTU Prague, Czech Republic)

Dr. B. Birkhofer (Sika Services AG, Switzerland)

Dr. G. De Cesare (Laboratory of Hydraulic Constructions, Ecole Polytechnique Fédérale de Lausanne, Switzerland)

Dr. S. Eckert (Department Magnetohydrodynamics Helmholtz-Zentrum Dresden-Rossendorf, Germany)

Dr. S. Fischer (Ubertone, Strassbourg, France)

Dr. S.A.K. Jeelani (Food Process Engineering, Swiss Federal Institute of Technology Zurich, Switzerland)

Dr. H. Kikura (Research Laboratory for Nuclear Reactors, Tokyo Institute of Technology, Ohokayama, Japan)

Dr. M. Mori (Tokyo Electric Power Co., Inc., R&D Center, Yokohama, Japan)

Dr. C. Rennie (Department of Civil Engineering, University of Ottawa, Canada)

Prof. Dr. Y. Takeda (Hokkaido University, Sapporo, Japan)

Dr. Y. Tasaka (Division of Energy & Environmental Systems, School of Engineering, Hokkaido University, Sapporo, Japan)

Dr. J. Wiklund (SIK Gothenburg, Sweden)

Prof. Dr. E.J. Windhab, Chair (Food Process Engineering, Swiss Federal Institute of Technology Zurich, Switzerland)

Organizing Committee:

Dr. S. Eckert

S. Franke

D. Rübiger

Department Magnetohydrodynamics
Institute of Fluid Dynamics
Helmholtz-Zentrum Dresden-Rossendorf
Dresden, Germany

Copyright © 2012 by Helmholtz-Zentrum Dresden-Rossendorf

Proceedings of the 8th International Symposium on Ultrasonic Doppler Methods for Fluid Mechanics and Fluid Engineering

Editors:

**Dr. S. Eckert
S. Franke
D. Rübiger**

Published and distributed by:

**Department Magnetohydrodynamics
Institute of Fluid Dynamics
Helmholtz-Zentrum Dresden-Rossendorf
P.O. Box 510119
01314 Dresden, Germany**

<http://www.hzdr.de/isud8/>

Table of Contents

Keynote lecture: Future in Ultrasound Doppler Flow Measurements Y. Takeda	1
Optimisation of UVP measurements using new transducer technology and advanced signal processing techniques R. Kotzé, J. Wiklund, R. Haldenwang	3
Dual-plane Ultrasound Array Doppler Velocimeter for Flow Investigations in Liquid Metals R. Nauber, L. Büttner, M. Burger, M. Neumann, J. Czarske, S. Franke, S. Eckert ...	7
Two-dimensional flow mapping past a circular cylinder using a 7-channel UDV system O. Andreew, A. Thess	11
One- and two-dimensional UVP velocity sampling in a cuboidal basin subject to in- and outflow sequences M. Müller, G. De Cesare, A. Schleiss	15
Ultrasonic wave interaction with air-water boundary layer P. Schmitt, A. Pallares, Y. Tasaka, K. Sakurai, S. Fischer	19
Ultrasonic flow measurements and bubble detection in gas-stirred metallic melts T. Vogt, A. Andruszkiewicz, K. Eckert, S. Odenbach, S. Eckert, G. Gerbeth	23
Ultrasonic Doppler Flow Measurements applied to gas-lift pumping technique J. He, G. Bao, O. Huang, Z. Zhu, S. Gao	27
Flow patterns induced by a bubble screen in a sharply curved flume based on Acoustic Doppler Velocity Profiler measurements V. Dugué, K. Blanckaert, A.J. Schleiss	29
A very low velocity measurement using ultrasonic velocimetry T. Ihara, H. Kikura, Y. Takeda	33
Investigation of slurry flows in rectangular pressurized pipe flow by means of ultrasonic velocimetry V. Bareš, T. Pícek, J. Krupička, J. Brabec, V. Matoušek	37

Application of the Ultrasound Velocity Profiling + Pressure Difference (UVP+PD) method for cement based grouts	
M. Rahman, U. Håkansson, J. Wiklund	41
Development of rotational rheometers by introducing UVP	
T. Shiratori, I. Kumagai, Y. Tasaka, Y. Murai, Y. Takeda	45
Development of an industrial UVP+PD based rheometer - optimisation of UVP system and transducer technology	
J. Wiklund, R. Kotzé, R. Haldenwang, M. Stading	49
<i>Keynote lecture: Recent Developments in Ultrasound Imaging Velocimetry: toward Clinical Application</i>	
C. Poelma	53
Time dependent 2D flow structure measurements arising from melt stirring by means of various AC magnetic fields	
S. Franke, D. Rübiger, J. Czarske, G. Gerbeth, S. Eckert	59
Application of UDV for studying the flow and crystallization of liquid metal in the process of electromagnetic stirring	
I. Kolesnichenko, R. Khalilov, P. Oborin, A. Pavlinov	63
Flow measurements in a model of the Czochralski crystal growth process	
J. Pal, A. Cramer, G. Gerbeth	67
Flow measurements in a continuous casting model using a low temperature liquid metal	
K. Timmel, M. Röder, S. Eckert, G. Gerbeth	71
Random reversals of flow direction in Rayleigh-Bénard convection of liquid metal under a uniform magnetic field	
T. Yanagisawa, T. Miyagoshi, Y. Yamagishi, Y. Hamano, A. Sakuraba, Y. Tasaka, Y. Takeda	75
Inertial wave observations in liquid metal by means of ultrasound Doppler velocimetry	
D. Rübiger, T. Vogt, S. Franke, S. Eckert, G. Gerbeth, J. Czarske	79
Investigation of flow structure in electromagnetically driven liquid metal confined in an annulus by Ultrasound Doppler Velocimetry	
F. Samsami, A. Thess	83

A new fully digital UVP enabling quantitative in-line rheometry	
A. Debacker, B. Birkhofer, D. Lootens, R. Bourquin, S. Ricci, P. Tortoli	85
Characteristic velocity distribution of rectangular duct flow of a magnetic fluid under magnetic field	
M. Motozawa, T. Sekine, T. Sawada, Y. Kawaguchi	89
Heat and momentum transfer of a buoyant blob in low Prandtl number fluids	
K. Igaki, R. Abe, Y. Tasaka, I. Kumagai, Y. Murai	93
Applicability of ultrasonic pulsed Doppler for fast flow-metering	
S. Fischer, C. Rebattet, T. Lalande, D. Dufour, N. Bachellier	97
<i>Keynote lecture: Contactless Inductive Flow Tomography: A Liquid Metal Flow Measuring Technique Complementary to UDV</i>	
F. Stefani, G. Gerbeth, T. Gundrum, T. Wondrak	101
Effects of analysis algorithms and number of repetition pulses on velocity data by using ultrasonic Doppler method	
H. Murakawa, R. Sakagami, K. Sugimoto, N. Takenaka	105
Ultrasonic flow field measurement of a rotating flow with free surface	
Y. Tasaka, Y. Murai, M. Iima	109
Ultrasonic flow measurements in a downscaled water mockup of a large scale precession driven dynamo experiment	
T. Gundrum, F. Stefani, C. Ma, Y. Sun, A. Giesecke, T. Albrecht, G. Gerbeth	113
Experimental investigation of flow structure of a density current encountering a basal obstacle	
E. Khavasi, H. Jamshidnia, B. Firoozabadi, H. Afshin	117
UVP measurement of low speed natural convection in the internally heating rectangular cavity	
T. Kawaguchi	121
Improvement of acoustical characterization of suspended particles in wastewater	
P. Schmitt, A. Pallares, M.-N. Pons	125
Sound velocity measurements in fluids using echo signals from scattering particles	
M. Lenz, M. Bock, E. Kühnicke, J. Pal, A. Cramer	129

Uncertainty analysis of flowrate measurement using UVP	
N. Furuichi	133
Cavitation risk estimation at orifice spillway based on UVP and dynamic pressure measurements	
M. Pfister, R. Duarte, M. Müller, G. De Cesare	137
Peristaltic flow characterization of shear thinning fluid through elastic tube by UVP	
S. Nahar, S.A.K. Jeelani, Y. Takeda, E.J. Windhab	141
Fluid flow characterization of process equipment using ultrasonic pulsed Doppler technique	
K. Mohanarangam, K. Simic, A. Brent, P. Fawell	145

Author Index

Abe, R.	93	Kikura, H.	33
Afshin, H.	117	Kolesnichenko, I.	63
Albrecht, T.	113	Kotzé, R.	3, 49
Andreew, O.	11	Krupička, J.	37
Andruszkiewicz, A.	23	Kühnicke, E.	129
Bachelier, N.	97	Kumagai, I.	45, 93
Bao, G.	27	Lalande, T.	97
Bareš, V.	37	Lenz, M.	129
Birkhofer, B.	85	Lootens, D.	85
Blanckaert, K.	29	Ma, C.	113
Bock, M.	129	Matoušek, V.	37
Bourquin, R.	85	Miyagoshi, T.	75
Brabec, J.	37	Mohanarangam, K.	145
Brent, A.	145	Motozawa, M.	89
Burger, M.	7	Müller, M.	15, 137
Büttner, L.	7	Murai, Y.	45, 93, 109
Cramer, A.	67, 129	Murakawa, H.	105
Czarske, J.	7, 59, 79	Nahar, S.	141
De Cesare, G.	15, 137	Nauber, R.	7
Debacker, A.	85	Neumann, M.	7
Duarte, R.	137	Oborin, P.	63
Dufour, D.	97	Odenbach, S.	23
Dugué, V.	29	Pal, J.	67, 129
Eckert, K.	23	Pallares, A.	19, 125
Eckert, S.	7, 23, 59, 71, 79	Pavlinov, A.	63
Fawell, P.	145	Pfister, M.	137
Firoozabadi, B.	117	Picek, T.	37
Fischer, S.	19, 97	Poelma, C.	53
Franke, S.	7, 59, 79	Pons, M.-N.	125
Furuichi, N.	133	Räbiger, D.	59, 79
Gao, S.	27	Rahman, M.	41
Gerbeth, G.	23, 59, 67, 71, 79, 101, 113	Rebattet, C.	97
Giesecke, A.	113	Ricci, S.	85
Gundrum, T.	101, 113	Röder, M.	71
Håkansson, U.	41	Sakagami, R.	105
Haldenwang, R.	3, 49	Sakuraba, A.	75
Hamano, Y.	75	Sakurai, K.	19
He, J.	27	Samsami, F.	83
Huang, Q.	27	Sawada, T.	89
Igaki, K.	93	Schleiss, A.	15, 29
Ihara, T.	33	Schmitt, P.	19, 125
Iima, M.	109	Sekine, T.	89
Jamshidnia, H.	117	Shiratori, T.	45
Jeelani, S. A. K.	141	Simic, K.	145
Kawaguchi, T.	121	Stading, M.	49
Kawaguchi, Y.	89	Stefani, F.	101, 113
Khalilov, R.	63	Sugimoto, K.	105
Khavasi, E.	117	Sun, Y.	113

Takeda, Y.	1, 33, 45, 75, 141	Wiklund, J.	3, 41, 49
Takenaka, N.	105	Windhab, E. J.	141
Tasaka, Y.	19, 45, 75, 93, 109	Wondrak, T.	101
Thess, A.	11, 83	Yamagishi, Y.	75
Timmel, K.	71	Yanagisawa, T.	75
Tortoli, P.	85	Zhu, Z.	27
Vogt, A.	23, 79		

Future in Ultrasound Doppler Flow Measurements

Yasushi Takeda

Hokkaido University, Graduate School of Engineering, Prof. emeritus.

Research Laboratory for Nuclear Reactors, Tokyo Institute of Technology

N1-7, 2-12-1 Ookayama, Meguro-ku, Tokyo, 152-8550, Japan

Address: yft@eng.hokudai.ac.jp

Keywords: Book, Award, Very Slow Flow measurement, OpenUVP

1. NEWS FOR A COMMUNITY

1.1 A long waited **book** will appear in September 2012. The book is entitled "Ultrasonic Doppler Velocity Profiler for Fluid Flow" and published by Springer Verlag, ca. 350 pages with lots of figures and tables. This is a crystalized work of all community members and shall be used as a textbook for new users and as reference book for the current users.

1.2 **Condolence** - Mr. G.Gogniat passed away on 19. April 2012 in Vevey, Switzerland. He was a founder of Met-Flow S.A. and had been a strong promoter of the method and a supporter for the ISUD meetings. It is a great regret of us that he passed away. Continuing effort for promotion of the method and contribution to the fluid mechanic science will only be the way to show our gratitude to him.

1.3 The Fluid Engineering division of the JSME **awarded** me for recognition of the UVP method as a novel measurement method for fluid flow. This implies all the effort made by our community is recognized to have experienced a great deal of contribution to the science and technology of fluid mechanics. We shall be proud of this recognition and are encouraged for future work.

2. NEWS ON ACTIVITY

I presented in the earlier meeting a diagram which shows expansion of applied flow fields. Recent improvement of methodology and algorithms have been worked by some of our members as if it widens its application fields. A few examples will be introduced.

2.1 Low Velocity detection – For boundary layer measurement, it was needed to develop a new way of signal processing and an algorithm for a flow field where velocity is in the order of or less than 1mm/s. This was worked out by TIT group and presented in detail in the meeting. This may open up new application targets in various engineering fields.

2.2 Environmental flow – A device specially developed for environmental flow has been launched in the market by a company UBERTONE.

The device is robust in its use in natural environment such as rivers, channels and lakes, which is adequate for use out of the laboratory.

2.3 OpenUVP is a platform where all related topics and information is going to be shared, for instance, in the form of forum, software exchanging station, exchanging experiences etc.

3. NEW IDEAS for RESEARCH

When I overview a general trends of scientific and technological problems and their solutions, it is really an important task to obtain information on the flow field in spatio-temporal manner. Especially after the natural and man-made disaster by the Eastern Japan Earthquake 2011, its importance shall be re-recognized. Using a capability of obtaining spatio-temporal flow field in quantity, I see a huge variety of new applications in fluid flow measurement. These possible research topics will be opened for young researchers.

OPTIMISATION OF UVP MEASUREMENTS USING NEW TRANSDUCER TECHNOLOGY AND ADVANCED SIGNAL PROCESSING TECHNIQUES

Reinhardt Kotzé^a, Johan Wiklund^b and Rainer Haldenwang^a

^aFPRC - Flow Process Research Centre, Cape Peninsula University of Technology, PO Box 652-Cape Town, South Africa

^bSIK – The Swedish Institute for Food and Biotechnology, PO Box 5401-Gothenburg, Sweden

Studies have suggested that the accuracy of the measured velocity gradient close to pipe walls need to be improved. In order to increase the accuracy of velocity measurements close to wall interfaces a specially designed delay line transducer was acoustically characterised and evaluated. Velocity profiles measured using the delay line transducer, were initially distorted due to the effect of finite sample volume characteristics and propagation through the delay line material boundary layers. These negative effects were overcome by measuring physical properties of the ultrasonic beam and implementing a newly developed deconvolution procedure. The optimised UVP system was evaluated and compared to standard transducers and commercial software in a straight pipe (16 mm) for three different non-Newtonian fluids. The combination of the signal processing techniques and new transducer technology reduced previous problems and was found to be essential for accurate in-line process and quality monitoring within industrial applications.

Keywords: Ultrasonic Velocity Profiling, ultrasonic transducer, deconvolution, acoustic characterisation

1 INTRODUCTION

UVP is an ideal technique for flow behaviour measurements in a wide range of industrial applications since it is non-invasive, works with opaque fluid systems, inexpensive, and easy to implement relative to other velocity profile measurement methods [1-2]. The UVP technique has been evaluated in a wide range of model and industrial fluid suspensions, ranging from paper pulp, mineral suspensions, fat crystallisation, liquid metals and more, see e.g. [3-4]. However, there are still a few problems remaining with the current UVP instrumentation and methodology in order to achieve the robustness and accuracy required in industrial environments. These problems include, depending on the installation method, distortion caused by cavities situated in front of ultrasonic transducers, measurement volumes overlapping wall interfaces, refraction of the ultrasonic wave (Doppler angle changes), sound velocity variations as well as physical changes of the ultrasonic beam shape and intensity [5-6]. Such negative effects influence the effectiveness of using UVP within industrial applications such as in-line process monitoring, rheology (UVP+PD) and flow visualisation. The main objective of this research work was to optimise the UVP system for accurate complex flow measurements by evaluating a specially designed delay line transducer and implementing advanced signal processing techniques. Results were compared with that obtained using the existing standard UVP system as well as using the new delay line transducer combined with new software. These were also compared to theoretical velocity profiles obtained using tube viscometry data.

2 THEORY

2.1 Non-Newtonian flow

The equation for the Herschel-Bulkley model is as follows:

$$\tau = \tau_y + K(\dot{\gamma})^n, \quad (1)$$

where K , n and τ_y are three empirical curve-fitting parameters [7]. Eq. 1 can be integrated to give the radial velocity (v) profile [7]:

$$v = \left(\frac{n}{1+n} \right) \left(\frac{\Delta P}{2LK} \right)^{\frac{1}{n}} \left((R - R_{plug})^{1+\frac{1}{n}} - (r - R_{plug})^{1+\frac{1}{n}} \right). \quad (2)$$

It will be noted that the Herschel-Bulkley model can easily be modified to describe the power-law and Bingham plastic models [7]. Slatter and Lazarus [8] formulated a Reynolds number (Re_3) for non-Newtonian pipe flow and this number was used as an indication of the flow regimes during tests conducted in this work.

2.2 Deconvolution of velocity profiles

Velocity profiles are generally not known with sufficient accuracy as a result of the effect of the finite sample volume characteristics and propagation through solid boundaries or wall material layers [9]. Mathematically simplified, the measured Doppler profile (V_m) can be described as a one-dimensional convolution integral:

$$V_m = \int_0^r V_t(x) \cdot I(r-x) dx, \quad (3)$$

where V_t is the 'true' velocity profile and I the sample volume intensity distribution. Since, V_m and I are known, one can now apply a deconvolution

process in order to obtain the correct velocity profile (V_r). The basic deconvolution algorithm is shown, in block diagram form, in Fig. 1.

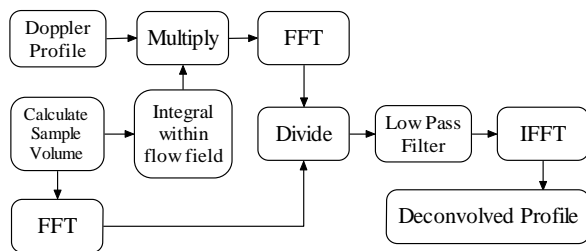


Figure 1: Deconvolution algorithm [9].

More information on deconvolution procedures and test setups for characterising sample volumes as well as UVP systems can be found in Jorgensen and Garbini [10] and Walker *et al.* [11].

3 MATERIALS AND METHODS

3.1 Materials

Carboxy Methyl Cellulose (CMC) was tested and is generally regarded as an ideal non-Newtonian power-law fluid for experimental work [5]. The CMC (Protea Chemicals, Bryanston, South Africa) solution used was 7% w/w. Bentonite powder (Protea Chemicals) was mixed with water to obtain different concentrations of bentonite:water suspensions. The concentration tested was 6.9% w/w. Dry kaolin powder (Protea Chemicals) was used to prepare a kaolin:water suspension of 17% v/v. Kaolin suspensions attenuate the ultrasonic energy significantly [5] and was thus used to test the limitations of the optimised UVP system.

3.2 Experimental flow loop UVP instrumentation

The experimental setup consisted of three pipes (9, 16 and 28 mm) which were connected to a 100 mm progressive cavity positive displacement pump with variable speed drive (maximum volumetric flow 11 l/s) to enable tests at different flow rates. Each line is also fitted with an electromagnetic flow meter (Krohne OptiFlux 4000, Gauteng, South Africa) to measure the flow rate. Pressure measurements were conducted over a set distance using high (130 kPa) and low (6 kPa) range differential pressure sensors (Danfoss, Cape Town, South Africa). In addition, the relative density and temperature of the slurries are measured with a mass-flow meter (MassFlo 6000, Danfoss-Siemens, Cape Town, South Africa). Procedure and method for obtaining accurate in-line experimental data as well as post data analysis is discussed in detail by Chhabra and Richardson [7]. A specially designed flow adapter for ultrasonic transducer installation [2-6] and housing was installed on the 16 mm pipe for flow measurements. Fig. 2 shows a schematic diagram of the pipe rig including the ultrasonic equipment fitted onto the 16 mm pipe.

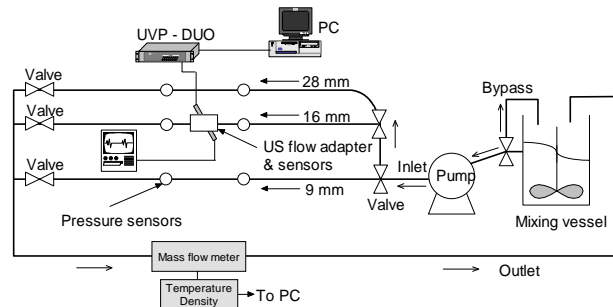


Figure 2: Schematic illustration of the pipe rig at FPRC.

In this work the latest UVP instrument (UVP-DUO-MX, Met-Flow SA, Lausanne, Switzerland) was used for velocity profile measurements. Doppler, Immersion type 4 MHz, 5 mm active element standard and delay line ultrasonic transducers were used. Fig. 3 shows a schematic diagram of the flow adapters with standard and delay line transducers. More information on the delay line transducers can be found in Kotzé *et al.* [5].

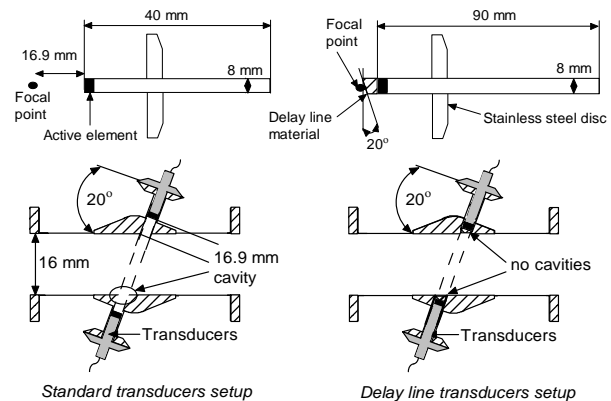


Figure 3: Standard and delay line transducers and installation setup [9].

3.4 Acoustic characterisation of transducers

For acoustic characterisation tests a high performance needle hydrophone (Precision Acoustics Ltd, 1 mm piezoelectric crystal) setup was used in combination with a high precision (± 0.03 mm) robotic arm (KUKA Robotics GmbH). Two ultrasonic transducers were tested: one delay line transducer and one standard transducer. The transducer was moved in a two-dimensional field from the centre of the needed hydrophone using the robotic arm. This enabled measurement of a range of acoustic intensities in increments of 0.1 mm in the Y direction and 1 mm in the X direction (see Fig. 4), which gave a complete acoustic map of the transducer. Tap water was used throughout all the tests and the temperature was continuously monitored using a temperature sensor submerged in the tank. A complete Graphical User Interface (GUI) was written in Matlab® to control the robot arm using a RS232 interface between the robot controller box and PC. An Agilent 100 MHz digital

oscilloscope (Model 54622A) with RS232 connectivity to a PC was used to record the data.

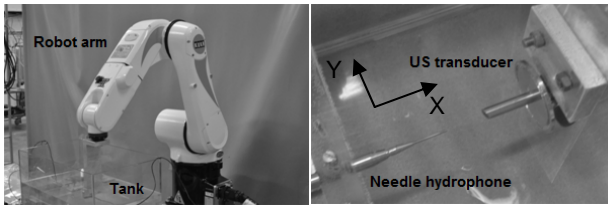


Figure 4: Acoustic characterisation using needle hydrophone and robot setup [5].

4 RESULTS AND DISCUSSION

4.1 Acoustic characterisation

Fig. 5 shows the complete acoustic map for the delay line transducer using the needle hydrophone setup. The results were interpolated in order to produce a more detailed representation of the acoustic field. The colour bar positioned at the right shows the intensity values in voltage (V). An excitation voltage of 150V was selected for these tests due to the design of the transducers.

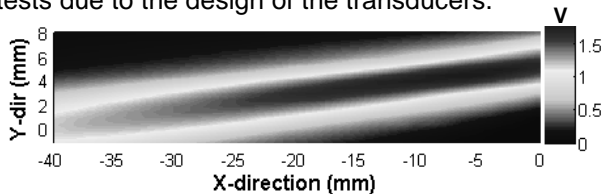


Figure 5: Acoustic map of delay line transducer.

Firstly it can be observed that the acoustic field of the transducer is fixed at an angle (with respect to the transducer). The angle with respect to the transducer was determined at 7.4 degrees. Also, notice that the focal point of the delay line transducer is situated just beyond the delay line material, which means no velocity measurements are taken within the near-field, where the acoustic pressure field is irregular. When results are compared to the standard transducer the standard transducer's signal intensities (see Fig. 6) are ± 1.5 times higher, showing that there is a loss of energy, possibly caused by the delay line material.

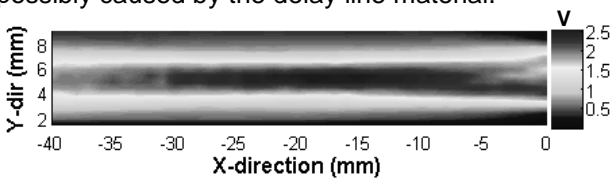


Figure 6: Acoustic map of standard transducer.

In this case the acoustic beam direction is parallel with respect to the transducer. The focal point of the standard transducer seems to be at around 10 mm from the surface.

4.3 Velocity profile measurements

Velocity profiles obtained using the delay line transducers are presented before and after

implementing the deconvolution procedure. Fig. 7 shows profiles measured in a 16 mm pipe using a standard and delay line transducer for CMC 7% w/w ($K = 1.43$, $n = 0.67$) at a bulk flow rate of 0.141 l/s ($Re_3 = 988$). Note the significant distortion of the measured velocity profile (crosses) due to averaging effects across the finite sample volume in the flowing liquid medium (see Sec. 2.2). A major improvement between the results obtained using the delay line transducer after deconvolution (circles) can be observed. A theoretical velocity profile (Eq. 2) was also plotted for comparison (using the tube viscometer data). The difference in magnitude between the profiles measured using the standard and delay line transducer was due to slight variations in flow during the measurements. Also, note from Fig. 5 that the Doppler angle had to be corrected due the angle refraction caused by the delay line material. The most important observation here is the increase in velocity at the pipe wall for the profile measured using the standard transducer (shown by diamonds). Here the effect of the cavity (Fig. 3) is more pronounced even for a power-law fluid where the velocity gradients are not high.

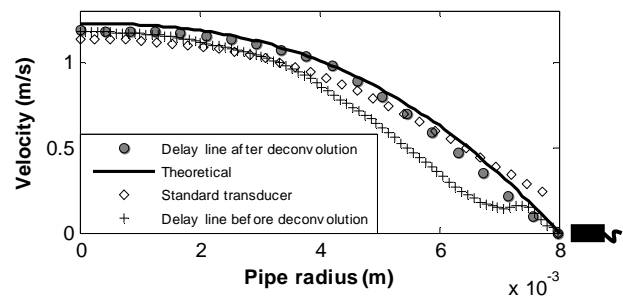


Figure 7: Comparison of profiles for CMC 7% w/w.

Fig. 8 shows a comparison of velocity profiles measured in bentonite 6.9% w/w ($K = 0.006$, $n = 1$, $\tau_y = 9$) at a flow rate of 0.4 l/s ($Re_3 = 1900$). In the case of measuring in fluids with a yield stress the cavity distorts profiles (diamonds) more significantly due to the high velocity gradients present close to the pipe walls. When comparing the profiles before and after deconvolution (crosses and circles), it can be seen that the deconvolution procedure improved the velocity data close to the wall significantly.

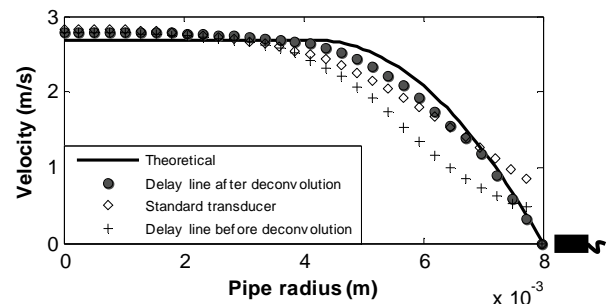


Figure 8: Comparison of profiles for bentonite 6.9% w/w.

The velocity profiles shown after implementing the deconvolution procedure also show better

agreement with the theoretical profiles. Velocity profiles measured in kaolin 17% v/v ($K = 0.54$, $n = 0.47$, $\tau_y = 16.77$) at a flow rate of 0.2 l/s ($Re_3 = 330$) are shown in Fig. 9. Due to the attenuating properties of the kaolin suspensions, it was not possible to measure velocity profiles using a standard transducer.

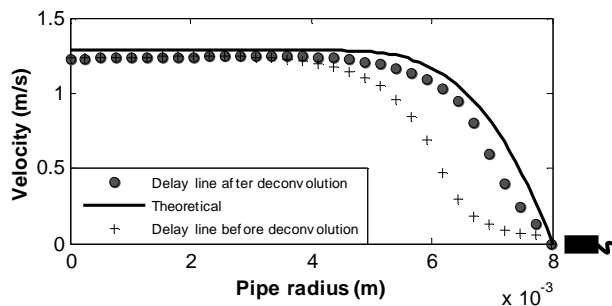


Figure 9: Comparison of profiles for kaolin 17% v/v.

According to the acoustic measurements of the different transducers (Sec. 4.1), the standard transducers generated more acoustic energy than when compared to the delay line transducer. However, due to the cavity between the standard transducer's surface and pipe wall (Sec. 3.2), which was filled with the test fluid, most of the energy was absorbed before the ultrasonic pulse can propagate across the pipe diameter, see Fig. 10. In this case the delay line transducer could measure profiles in this particular fluid as the only material (which also absorbs energy) between the wall interface and transducer surface is the actual delay line material and not the attenuating test fluid. As shown before, the deconvolution procedure improved the velocity data close to the wall significantly.

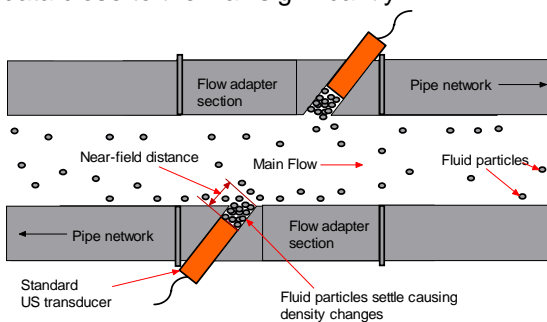


Figure 10: Fluid particles settling inside cavities with standard transducer installation setup [5].

5 CONCLUSIONS

A new type of ultrasonic transducer for velocity profile measurements in industrial applications was developed and tested. The new transducer technology was demonstrated to have superior accuracy and eliminated all existing problems with erroneous velocity data close to the wall. It has been shown how erroneous velocity data due to the finite size of the sample volume can be removed using a deconvolution procedure. Despite the improved accuracy, deconvolution has not been widely used

in the medical field. Also, to the authors' knowledge, it is believed that this concept has never been applied for measurements in the fluid engineering industry before. This may be a result of its complexity and because it has not been evaluated for different materials and under a full range of flow conditions. In conclusion, the UVP technique has been optimised by using new transducer technology and advanced signal processing techniques. The overall improvement will, for the first time, enable detailed flow behaviour measurements for industrial applications, especially for in-line rheometry and process monitoring. Furthermore, the improved methodology will enable more accurate verification of theoretical simulations for complex flow in different geometries.

ACKNOWLEDGEMENTS

The NRF of South Africa, CPUT and Vetenskapsrådet – The Swedish Research Council, Research Links, for funding. SIK is gratefully acknowledged for scientific collaboration.

REFERENCES

- [1] Takeda Y: Measurement of velocity profile of mercury flow by ultrasound Doppler shift method, Nucl. Technol. 79 (1987), 120-124.
- [2] Wiklund J, Shahram I, Stading M: Methodology for in-line rheology by ultrasound Doppler velocity profiling and pressure difference techniques, Chem. Eng. Sci. 62 (2007) 4159-4500.
- [3] Wiklund J, Stading M: Application of in-line ultrasound Doppler based UVP-PD method to concentrated model and industrial suspensions, Flow Meas. Instrum. 19 (2008) 171-179.
- [4] Kotzé R, Haldenwang R, Slatter P: Rheological characterization of highly concentrated mineral suspensions using an Ultrasonic Velocity Profiling with combined Pressure Difference method, Appl. Rheol. 18(6) (2008) 62114.
- [5] Kotzé R, Wiklund J, Haldenwang R: Optimisation of Pulsed Ultrasonic Velocimetry and Transducer Technology for Industrial Applications, Ultrasonics, (2012) (Accepted)
- [6] Kotzé R, Wiklund J, Haldenwang R, Fester V: Measurement and analysis of flow behaviour in complex geometries using the Ultrasonic Velocity Profiling (UVP) technique, Flow Meas. Instrum. 22 (2011) 110-119.
- [7] Chhabra RP, Richardson JF: Non-Newtonian Flow and Applied Rheology: Engineering Applications, Oxford, Great Britain: Butterworth-Heinemann (2008).
- [8] Slatter PT, Lazarus JH: Critical flow in slurry pipelines. British Hydromechanics Research Group, 12th Int. Conf. Slurry Handling & Pipeline Transport, (1993) 639-654.
- [9] Kotzé R, Haldenwang R: Development of an ultrasonic in-line rheometer: Evaluation, optimisation and verification, 15th Int. Conf. Transport & Sedimentation Solid Particles, 15 (2011) 49-61.
- [10] Jorgensen JE, Garbini JL: An Analytical Procedure of Calibration for the Pulsed Ultrasonic Doppler Flow meter, J. Fluid Eng. 96 (1974) 158-167.
- [11] Walker AR, Phillips DJ, Powers JE: Evaluating Doppler Devices Using a Moving String Test Target, J. Clin. Ultrasound, 10 (1982) 25-30.

Dual-plane Ultrasound Array Doppler Velocimeter for Flow Investigations in Liquid Metals

R. Nauber¹, L. Büttner¹, M. Burger¹, M. Neumann¹, J. Czarske¹, S. Franke², S. Eckert²

¹ Laboratory of Measurement and Testing Techniques, Faculty of Electrical Engineering and Information Technology, Technische Universität Dresden, 01062 Dresden, Germany

² Institute of Fluid Dynamics, Helmholtz-Zentrum Dresden-Rossendorf, P.O. Box 510119, 01314 Dresden, Germany

A dual-plane, dual-component ultrasound array Doppler velocimeter for investigating transient complex flow phenomena in liquid metals is presented. It utilizes four sensor arrays consisting of 25 single element transducers along a line of 67 mm. The system combines a spatial resolution of approx. 3 mm with a temporal resolution of up to 30 Hz using electronic beam traversing and time division multiplex. The modular realization of the measurement system allows flexible sensor configuration, e.g. four planes can be measured with one velocity component, two planes with two components or two lines with three components. Those capabilities are demonstrated by measurements in a magnetically stirred metal melt at room temperature.

Keywords: Ultrasound Doppler Velocimetry, Flow Field Measurements, Ultrasound Sensor Array, Liquid Metals, Magneto hydrodynamics, Rotating Magnetic Field

1 INTRODUCTION

Metal melts and the flows therein are of outstanding importance for a variety of technological processes, especially for steel production (continuous casting process) and crystal growth (Czochralsky method, etc.). In recent developments, the application of magnetic fields is investigated to influence the melt-flow in a defined way and to optimize the quality of the resulting product. Experimental flow investigations are indispensable to understand the interaction between the magnetic fields and the induced flows. It is common practice to conduct scaled model experiments in low melting alloys, for example gallium-indium-tin (GaInSn) [1]. Ultrasound pulse wave Doppler is an appropriate method for flow investigations [2,3], but commercial off-the-shelf devices often employ only a limited number of transducers and are hardly suitable for flow mapping of complex and unsteady flow phenomena.

We present an ultrasound array Doppler velocimeter (UADV) system for liquid metal flows at room temperature that uses four ultrasound (US) arrays and provides high temporal and spatial resolution suitable to investigate complex transient flows. The capabilities of the UADV system are demonstrated by two measurements in magnetically stirred GaInSn.

2 MEASUREMENT SYSTEM

2.1 Sensors

The measurement system utilizes US line arrays in order to obtain a one-component velocity measurement in a plane. An array consists of 25 single element piezo transducers (2.5 x 5 mm) with a total sensitive length of 67 mm (fig. 1). The active elements are driven pairwise to form a square transducer of approx. 5 x 5 mm. Those dimensions

are the result of a trade-off between element size and beam divergence and determine the lateral resolution to approx. 3 mm in GaInSn. This corresponds with the pitch of 2.7 mm that transducer pairs of the line array can be traversed electronically. The piezo-transducers are excited by a burst signal of eight sine periods at $f = 8$ MHz, which results in an axial resolution of about 1.4 mm in GaInSn [4].

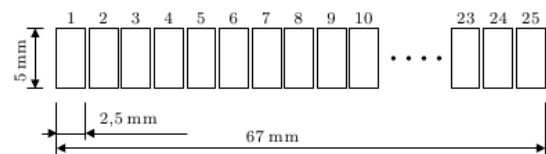


Figure 1: Linear ultrasound array with 25 transducer elements [5]

2.2 Time Division Multiplex

To obtain a high temporal resolution it is necessary to parallelize the measurement process along the line array. Therefore a time division multiplex (TDM) scheme is used to drive several transducer pairs simultaneously in order to measure multiple lines at once. It has been determined that a spatial distance of four inactive transducers and a temporal separation of one time step is sufficient to neglect cross-talk in GaInSn [4]. The outcome is an excitation pattern (fig. 2) that allows to scan a plane in $N_s = 6$ time steps with an overall frame rate up to 30 Hz [5].

In order to obtain two or more velocity components, multiple sensor arrays measure in overlapping planes and are driven mutually exclusive. This is achieved by interleaving the excitation patterns of the sensor arrays. To measure a two-component (2c) velocity field along two planes (2.5d) for instance, two arrays are arranged orthogonally per

plane and are electronically traversed in an alternating manner. Therefore twice the time is needed to completely capture a plane in a two-component configuration.

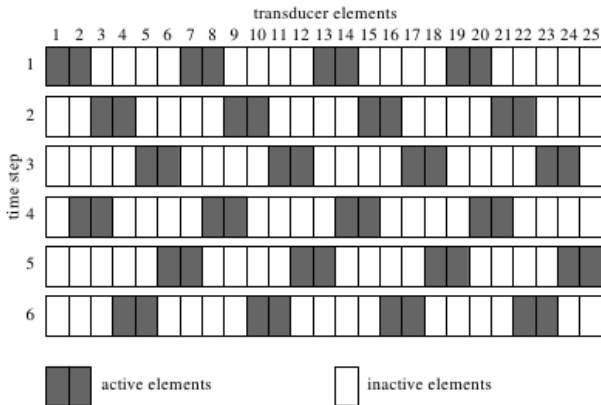


Figure 2: Time division multiplex scheme for a single array

2.3 Electrical Design

The UADV employs a modular design that consist of an arbitrary function generator (AFG), a power amplifier, an electronic switching matrix and an analog-digital converter (ADC) card for each sensor array. Each AFG generates a burst signal, which is amplified and routed to four transducer pairs in one line array. The received echoes are separated from the burst signals, amplified with variable gain and converted into digital signals. The echo amplification is determined by a voltage ramp that is chosen to compensate for increasing attenuation with increasing time of flight of US-pulses in fluids (time gain compensation, TGC).

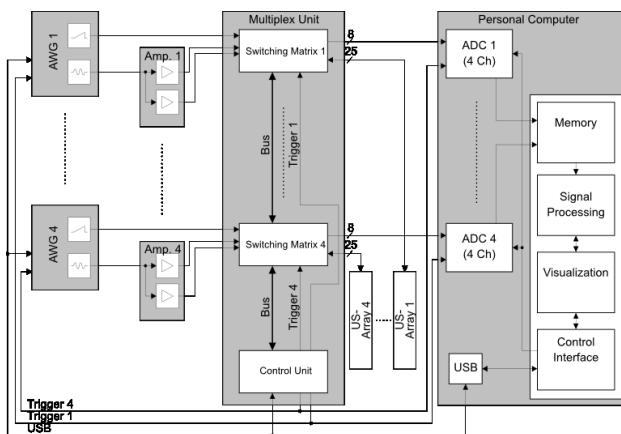


Figure 3: Block diagram of the UADV system

2.4 Signal Processing

The digitized echo signals are processed offline after acquisition by four ADC-cards to obtain the flow velocity profiles. The time-domain signal is processed through a finite impulse response (FIR) bandpass filter with 8 MHz center frequency and 0.3 MHz bandwidth. Subsequently the real-valued signal is complemented by a 90° phase shifted

imaginary part to form an analytic signal via the Hilbert transform. By sampling at specific time instances relative to the ultrasound burst emission a complex Doppler signal is derived. The mean frequency and directional information are subsequently estimated via an autocorrelation algorithm [6, 7]. The velocity of the fluid in the corresponding depth relative to the transducer is directly proportional to its Doppler frequency.

To obtain a spatial flow profile, the information of all line-arrays is combined according to their respective geometric positions and directions. A post-processing algorithm allows all orthogonal sensor configurations and provides the flexibility to measure for example multi-plane one (1c) and two-component (2c) velocity profiles as well as three velocity components (3c) along a line of three intersecting planes.

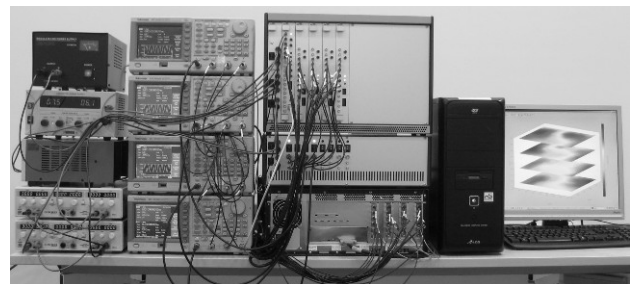


Figure 4: Deployment of the UADV system, from left to right: power supplies; arbitrary function generators (AFG); modular multiplex electronics, power amplifiers and signal acquisition; standard PC

3. Measurements in Liquid Metals

To demonstrate the capabilities of the UADV system, measurements are performed in magnetically stirred GaInSn. The metal melt is contained in a cubic vessel of 67x67x67 mm that has several mounting options for US line arrays. A US pulse repetition frequency of 538 Hz is used to obtain 30 profiles of 50 echoes each, which are temporally averaged subsequently.

In a dual-plane setup, four sensor arrays span two measurement planes to allow quasi-simultaneous capturing of two velocity components (2c). Arrays spanning the same plane are driven mutually exclusive, the crosstalk between two planes can be neglected ($\Delta z \geq 15$ mm). The resulting 2.5d-2c flow field is depicted in fig. 5.

Three velocity components (3c) can be measured by intersecting three orthogonal single-component planes. With four available sensor arrays, three-component measurements along two lines are possible. Fig. 6 shows the experimental setup and the obtained flow field.

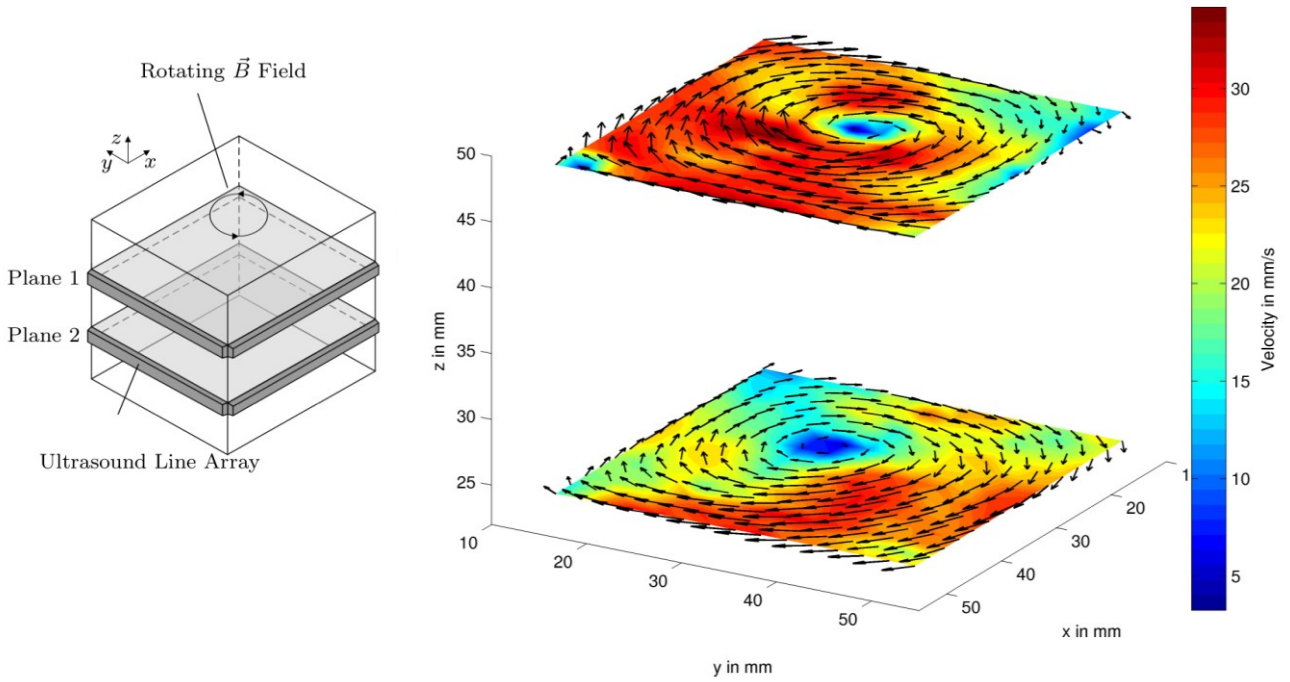


Figure 5: Dual-plane measurement (2.5d - 2c): Measurement setup and results for magnetically stirred GaInSn in a cubic vessel

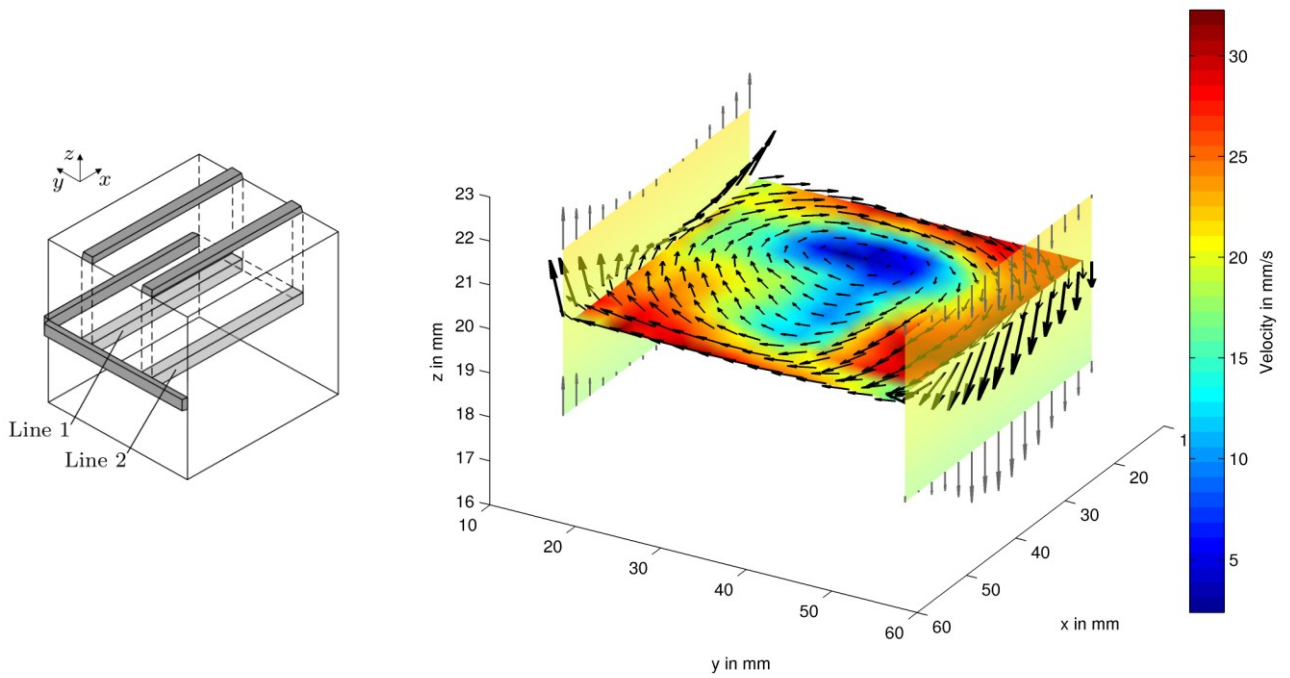


Figure 6: Dual-line measurement (1.5d - 3c): Measurement setup and results for magnetically stirred GaInSn in a cubic vessel; three-component vectors along two intersection lines are drawn bold

4 OUTLOOK

As the UADV system has proven usefully for complex flow mapping, a variety of applications arise. It is planned to apply the system to a scale-model of continuous steel casting in order to characterize the influence of magnetic fields to the melt flow [8]. Contactless mixing of metal melts by different means of magnetic fields [9] is studied as well, using the capabilities of the UADV system to simultaneously obtain primary and secondary flows. Further investigations of directed solidification process of silicon will be conducted in isothermal models that are especially relevant for the photovoltaic industry [10].

5 SUMMARY

We have presented a flexible UADV system to capture complex transient flows in liquid metals. Its modular design allows for multi-plane and multi-component flow mapping. A time division multiplex scheme ensures high temporal resolution (up to 30 Hz) while optimized ultrasound-beam characteristics determine a spatial resolution of approx. 3 mm. The system is demonstrated by a dual-plane (2.5d-2c) and a three-component (1.5d-3c) velocity measurement in a low melting liquid metal alloy.

The development of a capable UADV system poses great potential for the field of MHD and a profound understanding of the interaction between electromagnetic fields and conductive fluids.

ACKNOWLEDGEMENT

The authors like to thank the Deutsche Forschungsgemeinschaft (DFG) for financial support within the grant "SFB 609 - Electromagnetic Flow Control in Metallurgy, Crystal Growth and Electrochemistry".

REFERENCES

- [1] Eckert S, Gerbeth G, Rübiger D, Willers B, Zhang C: Experimental modeling using low melting point metallic melts: Relevance for metallurgical engineering, *Steel Res. Int.* 78 (2007), 419-425.
- [2] Eckert S, Cramer A, Gerbeth G: Velocity measurement techniques for liquid metal flows, in *Magnetohydrodynamics - Historical Evolution and Trends*, Molokov S, Moreau R, Moffatt HK (Eds.), Springer-Verlag, Dordrecht (2007), 275-294.
- [3] Takeda Y: Development of an ultrasound velocity Profile monitor, *Nucl. Eng. Design* 126 (1991), 277-284.
- [4] Franke S, Büttner L, Czarske J, Rübiger D, Eckert S: Ultrasound Doppler system for two-dimensional flow mapping in liquid metals. In: *Flow Measurement and Instrumentation* 21 (2010) 402-409.
- [5] Franke S, Lieske H, Fischer A, Büttner L, Czarske J, Rübiger D, Eckert S: 2d-2c Ultrasound a Doppler Array Velocimeter for Flow Investigations in Liquid Metals. In: *7th International Symposium on Ultrasonic Doppler*

Methods for Fluid Mechanics and Fluid Engineering, (2010), 89-92.

[6] Jensen JA: *Estimation of blood velocities using ultrasound*, Cambridge University Press, Cambridge (1996).

[7] Kasai C, Namekawa K, Koyano A, Omoto R: Real-time two-dimensional blood flow imaging using an autocorrelation technique, *IEEE Trans. Sonics. Ultrason.* 32 (1985), 458-464.

[8] Schwarze R, Maiwald A, Timmel K, Gerbeth G: Comparison of numerical and experimental flow data from a liquid-metal model of a continuous casting mold, *Proc. 6. International Conference on Electromagnetic Processing of Materials*, Dresden (2009).

[9] Frana K, Stiller J: A numerical study of flows driven by a rotating magnetic field in a square container, *Eur. J. Mech. B Fluid* 27 (2008), 491-500.

[10] Dadzis K, Ehrig J, Niemiets K, Pätzold O, Wunderwald U, Friedrich J: Model experiments and numerical simulations for directional solidification of multicrystalline silicon in a traveling magnetic field, *J. Cryst. Growth* 333, (2011), 7-15.

Two-dimensional flow mapping past a circular cylinder using a 7-channel UDV system

Oleg Andreew¹ and André Thess²

¹ Helmholtz-Zentrum Dresden-Rossendorf, Bautzner Landstraße 400, 01328 Dresden, Germany

² Institute of Thermodynamics and Fluid Mechanics, Ilmenau University of Technology, P.O. Box 100565, 98684 Ilmenau, Germany.

A multichannel ultrasonic velocity profile (UVP) method has been applied for investigation of unsteady flow behind a circular cylinder. Using velocity profiles obtained by the ultrasonic velocimeter and their numerical post processing, two-dimensional time dependent flow maps were efficiently produced. A system of seven transducers immersed directly into the working fluid was used in order to simplify alignment of measurement lines and avoid the undesirable refraction of the acoustic beam on the walls. The von Kármán vortex street behind a cylinder were reconstructed as a pattern of large scale vortical flow.

Keywords: Flow around a cylinder, 2D flow mapping, multichannel UDV system

1 INTRODUCTION

According to the functioning principles of pulsed Doppler ultrasound velocimetry, a single transducer provides the projection of velocity vector along the direction of emitted acoustic beam. Two velocity components can be extracted from the UDV data when a measuring point is observed under at least two different angles. For example the authors [1] used a single movable transducer immersed directly into the working fluid in order to obtain a time-averaged plane velocity distribution in a liquid metal flow. A polynomial decomposition can be used for recalculation of acquired raw data into the 2D field of velocity vectors.

The purpose of the present work is to apply simultaneously 7 transducers for monitoring of unsteady time-dependent flow past a circular cylinder. Here the von Kármán vortex street which is characterized by the relatively large flow structures and low frequencies is used as an appropriate test object for application of multichannel UDV measuring system.

2 EXPERIMENTAL SETUP

2.1 Water channel

The experimental setup is shown in Figure 1. A circular cylinder ($d=20$ mm in diameter) was dragged in a still water by a stepping linear motor with velocity varied in the range of $U_0=10-30$ mm/s. The corresponding value of Reynolds number $Re=U_0 d/\nu$ is $Re=200-600$. Here $\nu=10^{-6}$ m²/sec is kinematic viscosity of water. Length, width and depth of the vessel were 700 mm, 300 mm and 50 mm correspondingly. We used a vessel filled with the water at rest in order to insure a homogeneous incoming velocity profile.

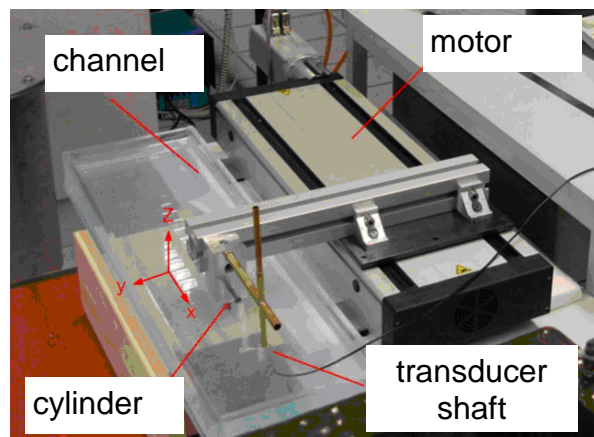


Figure 1: General view of experimental set up.

2.2 Measuring UDV system

We used a set of 7 transducers shown in Figure 2. The sound beams are adjusted in the horizontal plane situated on the half-depth of the vessel (25 mm). Angles of orientation of transducers with respect of the x direction are the following: $\alpha_1=\alpha_2=360^\circ-45^\circ$, $\alpha_3=360^\circ-30^\circ$, $\alpha_4=0^\circ$, $\alpha_5=30^\circ$, $\alpha_6=\alpha_7=45^\circ$. Diameters of transducers were 8 mm, operating frequency-8MHz. The transducers are acquired with the sampling rate of 50 ms by the multiplexer built in the DOP2000 system. The set of transducers was traveled at the distance of 150 mm behind the cylinder. For the flow mapping we recorded the data in the range between 15 and 135 mm along the ultrasound beam assuming that for every point the accuracy of the readings obtained from the different runs did not exceed 5% in relation to the bulk velocity. The estimated length of the "near field", where the acoustic field is nearly cylindrical, with a diameter slightly less than the diameter of emitter, is 47 mm. The half angle of the acoustic beam divergence for the "far field" is

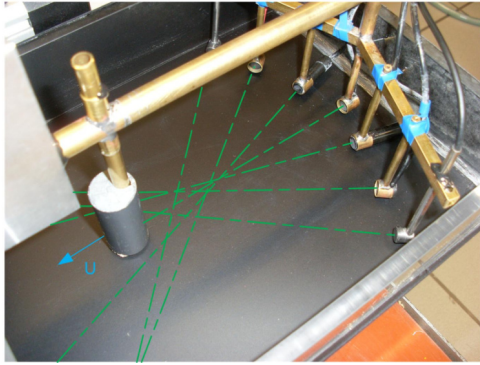
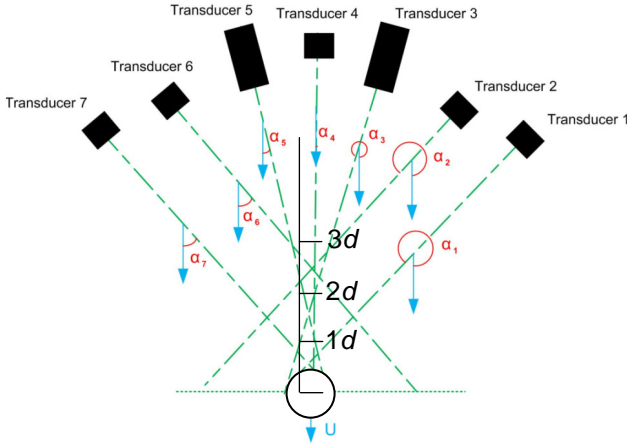


Figure 2: set of UDV transducers.

estimated to be $2.96^\circ \pm 0.02^\circ$. Thus, the beam diameter increases from 7-8 mm within the region of the “near field” to approximately 14-15 mm on the length of 120 mm from the surface of emitter. The spatial resolution of the method is defined by the mentioned diameters of the beam.

3 METHOD OF 2D FLOW MAPPING

3.1 Principles of UDV

The UVP method is based on a pulsed ultrasound echography. The principles of UVP are broadly described in relevant publications (see, for example, [2]). Using the UVP method, the velocity profiles are recorded along a measuring line as a projection U of the true velocity vector \vec{V} onto the measuring line as shown in Figure 3(a) and defined by equation (1)

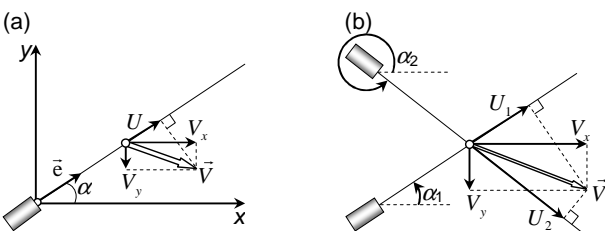


Figure 3: definition of velocity projection U measured by a UDV transducer.

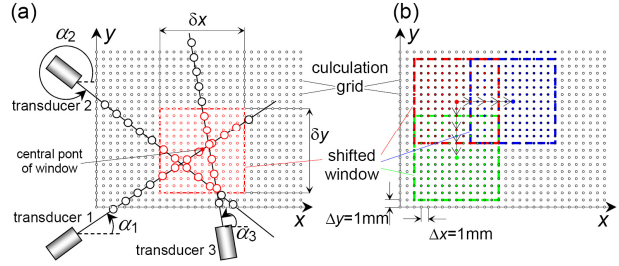


Figure 4: grid plane used for calculation of velocity components. (a) red color denotes the points of grid and UDV data used for polynomial decomposition within a current position of calculation window, (b) different position of the window and its central point.

$$U = \vec{V} \cdot \vec{e} = V_x \cos(\alpha) + V_y \sin(\alpha) \quad (1)$$

Here V_x , V_y and \vec{e} are respectively the streamwise and spanwise components of velocity and the unit vector that defines the direction of the measuring line (angle α) with respect to the x axis. The projection U and the angle α are the measured quantities. In order to calculate the true velocity vector, at least two measurement lines obtained under different angles $\alpha_1 \neq \alpha_2$ must be used so that two velocity components can be calculated at the crossing points of measurement lines according to the following system of two linear equations:

$$\begin{cases} U_1 = V_x \cos(\alpha_1) + V_y \sin(\alpha_1) \\ U_2 = V_x \cos(\alpha_2) + V_y \sin(\alpha_2) \end{cases}$$

This procedure is illustrated in Figure 3(b).

3.2 Two-D flow mapping

Practically it is not possible to identify precisely the position of the crossing points for the various sound beams. Moreover, the number of these points is not enough for a reliable flow mapping. For such a purpose we use all measurements points which lay within a small rectangular window as it illustrated in Figure 4(a). Here the red color identifies the points of a regular spatial grid used for velocity calculation and, also, the data from three transducers confined by the borders of the window.

For the flow mapping the stream- and spanwise velocity components, $V_x(x,y)$, $V_y(x,y)$ were approximated in the form of two-dimensional polynomial decomposition:

$$V_x(x,y) = \sum_{n=0}^4 \sum_{m=0}^4 u_{nm} \cdot P_{nm}(x,y), \quad V_y(x,y) = \sum_{n=0}^4 \sum_{m=0}^4 v_{nm} \cdot P_{nm}(x,y)$$

The polynomials $P_{nm}(x,y)$ are defined as follows:

$$P_{nm}(x, y) = (x^n \cdot y^m)_{n+m \leq 4} = \begin{pmatrix} 1 & x & x^2 & x^3 & x^4 \\ y & xy & x^2y & x^3y & 0 \\ y^2 & xy^2 & x^2y^2 & 0 & 0 \\ y^3 & xy^3 & 0 & 0 & 0 \\ y^4 & 0 & 0 & 0 & 0 \end{pmatrix}$$

The coefficients u_{nm} and v_{nm} were calculated by solving the following system of linear equations:

$$\begin{pmatrix} \cos(\alpha_1) \sum_0^4 \sum_0^4 x_1^n y_1^m + \sin(\alpha_1) \sum_0^4 \sum_0^4 x_1^n y_1^m \\ \cos(\alpha_2) \sum_0^4 \sum_0^4 x_2^n y_2^m + \sin(\alpha_2) \sum_0^4 \sum_0^4 x_2^n y_2^m \\ \dots \\ \cos(\alpha_k) \sum_0^4 \sum_0^4 x_k^n y_k^m + \sin(\alpha_k) \sum_0^4 \sum_0^4 x_k^n y_k^m \end{pmatrix} \begin{pmatrix} u_{00} \\ \dots \\ u_{44} \\ v_{00} \\ \dots \\ v_{44} \end{pmatrix} = \begin{pmatrix} U_1 \\ U_2 \\ \dots \\ U_k \end{pmatrix} \quad (2)$$

Here k is the number of the data points measured within a rectangular window, whose centre corresponds to a calculating point (see Fig. 4). A pair of velocity components $V_x(x, y)$, $V_y(x, y)$ was calculated and associated with this central point according to the obtained coefficients u_{nm} and v_{nm} . These calculating points constituted a regular grid generated in the mid-plane of the channel with a 1 mm step in the spanwise streamwise directions. The vector (U_1, U_2, \dots, U_k) is the projection of velocity vectors obtained by the velocimeter for the data point with coordinates $(x_1, y_1, x_2, y_2, \dots, x_k, y_k)$ observed by the transducer under the angles of $(\alpha_1, \alpha_2, \dots, \alpha_k)$ in respect to the x axis. The data are distributed irregularly in the plane of measurement. The system (2) was solved by the standard solver for the linear least-squares problems implemented into the MatLab [3]. The size of the window was chosen as 15×15 mm, the orders of polynomial decomposition were $N = 4$ in streamwise and spanwise directions. This choice was a compromise in the order to ensure a well-posed system (2) and better spatial resolution of the data treatment procedure. The lower polynomial orders smooth the result, the higher ones give spurious extremes in velocity distribution.

4 RESULTS AND DISCUSSION

In Figure 5 we plot three flow patterns reconstructed by the described method for the flow past a circular cylinder at Reynolds number $Re=500$. In Figure 5(d) we show visualization for the same flow made by the small gas bubbles generated due to electrolysis on a thin tungsten wire. The wire was fed by the pulse electrical current. Duration of pulses and pauses was 2 sec. The flow behind a cylinder is an appropriate test object for our purpose. The von Kármán street is presented by a sequence of the large scale vortices. Dimensions of such vortices is commensurable with the diameter of the cylinder in the moment of generation and then increase in downstream direction. Reconstructed images in

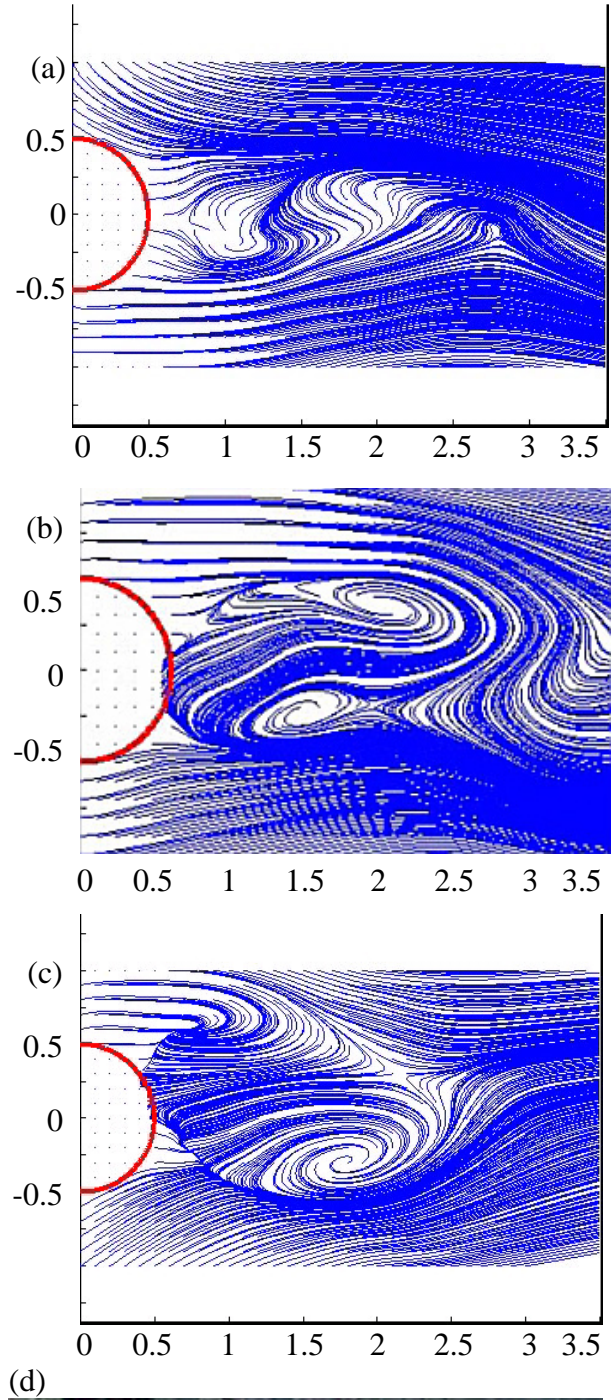


Figure 5: (a)-(c) snapshots of flow patterns reproduced according to the UDV data and (d) optical visualization of the flow behind the circular cylinder (von Kármán vortex street). $Re=500$

Figures 5(a-b) present streamlines. Here we show snapshots of video file sampled with the rate of 20 frames per second. In general we managed to reproduce the pair of vortices on the distance of 2.5 gauges directly past the cylinder. According to Figure 2, this is the region which contains the data supplied by all seven transducers. In the transverse to the main flow y -direction the region of reliable flow reconstruction is restricted to one gauge of the cylinder. In spite of that the original flow (visualized in Figure 5(d)) is presented by the well pronounced vortices of the Kármán street, the applied method was not able to reproduce such flow structures continuously. Only 35% of the obtained by calculation frames contained the well developed vortices. The examples of successful frames are illustrated by images (b) and (c) in Figure 5. Unfortunately, the UDV data do not reproduce development of the vortex street in downstream direction. The region situated on the distance of 3-4 diameters of the cylinder is 'observed' by transducers number 3, 4 and 5 (see Figure 2). This is the region of so-called 'near field' of the ultrasound beam, where the transducers ensure the most reliable data. In spite of that, the method of flow mapping does not reproduce here the flow field reliably. That is definitely result of lack of data.

CONCLUSIONS

The applied method of two-dimensional flow reconstruction is very exacting to plenitude of data. We managed to get the most reliable results in the flow regions where at least five transducers supplied the measurements under the different angles of observation. The time resolution was restricted approximately to 7 realistic frames per second at the acquisition rate of raw data 20 UDV profiles per second.

ACKNOWLEDGMENTS

This work was supported by the Deutsche Forschungsgemeinschaft under contract number TH497/27-1.

REFERENCES

- [1] Andreev, O., Kolesnikov, Yu., Thess, A. Application of the ultrasonic velocity profile method to the mapping of liquid metal flows under the influence of a non-uniform magnetic field, *Experiments in Fluids*, Volume 46, Number 1, January 2009, pp. 77-83(7)
- [2] Takeda Y; Kikura H (2002) Flow mapping of the mercury flow. *Exp Fluids* 32: 161-169
- [3] Coleman T; Li Y (1996) A Reflective Newton Method for Minimizing a Quadratic Function Subject to Bounds on Some of the Variables. *SIAM Journal on Optimization*, Vol. 6, Number 4: 1040-1058.

One- and two-dimensional UVP velocity sampling in a cuboidal basin subject to in- and outflow sequences

Michael Müller, Giovanni De Cesare and Anton Schleiss

Laboratory of Hydraulic Constructions (LCH), Ecole Polytechnique Fédérale de Lausanne (EPFL), CH-1015 Lausanne, Switzerland. E-mail: michael.mueller@epfl.ch

In the framework of an experimental study on the influence of in- and outflow sequences on flow patterns and suspended sediment behavior in reservoirs, flow fields and inflowing jet were sampled by Ultrasonic Velocity Profilers (UVP). The laboratory set-up consisted of two interconnected rectangular basins between which water was moved back and forth. A parametric study was performed on the magnitude and the frequency of in- and outflow cycles. Jet centerline velocities during inflow sequences were measured by UVP transducers with sampling frequencies of 0.5 and 1.0 MHz. Results were compared to jet behavior given in literature and used to calibrate a numerical model. Then, the main basin was equipped with seventeen 2 MHz UVP transducers to measure horizontal 2D velocity fields at several levels inside the test volume. Such, flow patterns during in- and outflow sequences were monitored, allowing the detection of three-dimensional flow behavior and the estimation of the mean kinetic energy in the test volume.

Keywords: In- and outflow sequences, reservoir, jet centerline velocity, 2D flow patterns

1 INTRODUCTION

Reservoir sedimentation impacts reliability, efficiency and safety of hydropower schemes. Beside traditional storage plants, also pumped-storage facilities are affected. Such schemes are composed of two reservoirs, between which the water is moved up and down for peak energy generation and grid regulation. The influence of cyclic bidirectional water exchange on flow patterns and suspended sediment behavior in lakes and reservoirs was investigated experimentally at the Laboratory of Hydraulic Constructions (LCH) of the Ecole Polytechnique Fédérale de Lausanne (EPFL).

Understanding of flow behavior in reservoirs submitted to in- and outflow cycles allows specific design of hydraulic structures such as intakes or sluice gates and helps describing entrainment and settling processes of suspended particles. Particle Image Velocimetry (PIV) and Ultrasonic Velocity Profiling (UVP) methods are commonly applied in experimental studies, i.e. to describe flow fields upstream of orifices and sluice gates [1], to study flow patterns in shallow reservoirs [2, 3] as well as to monitor 2D flow fields in front of an intake structure due to jet induced flow [4]. However, most of the studies concern the evolution of flow patterns due to a specific flow direction, while the effect of in- and outflow sequences with different magnitude and frequency has not been analyzed yet.

In preliminary clear water tests, one-dimensional UVP velocity sampling was carried out to calibrate a numerical model and to describe the jet behavior during inflow sequences. During the main testing phase with sediment laden water, two-dimensional

UVP flow mapping was performed to evaluate flow patterns due to in- and outflow sequences. This paper briefly describes the test rig and the instrumentation and presents some of the results of one- and two-dimensional velocity sampling by the mean of three different types of UVP transducers.

2 EXPERIMENTAL SET-UP

2.1 Laboratory facility

In- and outflow sequences were effectuated between two interconnected reservoirs, the so-called main basin (subscript *MB*) and the mixing tank (*MT*, Fig. 1). The connecting pipe system was equipped with a pump and a flow diverter allowing rapidly changing two flow directions:

- *IN*: jet entering the main basin (inflow)
- *OUT*: water withdrawn from the basin (outflow)

The intake/outlet is located at the front wall of the main basin and can be positioned at $z_i = 0.25, 0.5$ and 0.75 m above the reservoir bottom. The intake is followed by a cylindrical throat with an inner diameter of $D_i = 4.8$ cm, connected to a rigid PVC pipe of a length of $L = 1.5$ m ($\sim 30 D_i$).

2.2 Instrumentation

To describe jet characteristics for inflow sequences as well as flow fields in front of the intake for outflow sequences, the main basin was equipped with UVP transducers (MetFlow SA, Switzerland). The flow mapping system had been applied in former studies on turbidity currents and 2D flows in shallow reservoirs [3, 5]. Walnut shell powder and hydrogen bubbles were used as flow tracers [6].

For measuring the centerline velocity of the jet, two

MetFlow prototype transducers with sampling frequencies of $f = 0.5$ and 1.0 MHz were applied. These devices are especially well suited for non-intrusive long distance measurements in the jet axis. The sensors were fixed on a steel bar and placed in the jet axis between $s = 0.5$ to 1.7 m from the intake/outlet in the main basin.

Horizontal 2D velocity fields were measured at several levels in the main basin. Seventeen 2 MHz UVP transducers were aligned along the side wall of the test volume on an aluminum frame, guaranteeing non-intrusive measurement. Operating azimuth angles of 90° and 45° were applied, allowing flow velocity sampling at 28 grid points in one quadrant of the test volume (Fig. 1b), corresponding to an area of 1.0×2.0 m². The frame was moved vertically to perform measurements at $z = 0.25, 0.50$ and 0.75 m from the bottom.

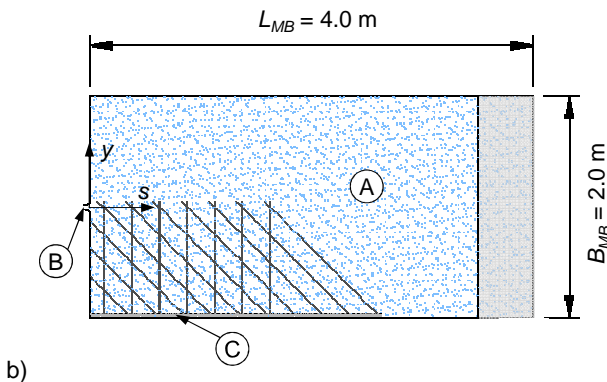
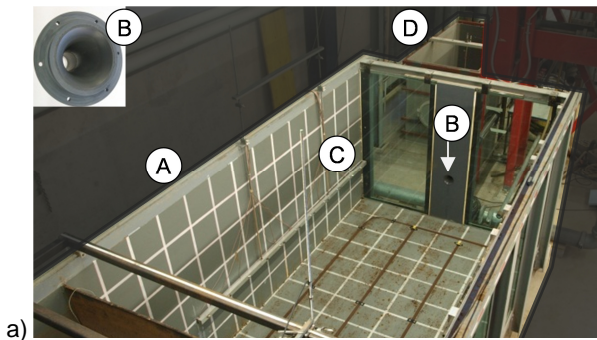


Figure 1: Picture of test facility (a) and schematic plan view of the main basin (b). A is the main basin; B, the intake/outlet; C, the UVP-frame with indicated 2D velocity sampling grid, and D, the mixing tank.

2.3 Parameter variation and procedure

To investigate the influence of in- and outflow sequences on the flow patterns and fine sediment behavior, parameters were varied as follows: five different cycle magnitudes (discharges) from $Q = 0.3$ to 1.1 l/s were applied, taking into account the volume of the main basin as well as real case pumped-storage cycles. The basic configuration considered in- and outflow sequences of the duration t_p to achieve steady state conditions in the

main basin (Fig. 2b). Then, four cycle frequencies Kt_p were studied, resulting in discharge curves corresponding to a square wave function. As illustrated in Fig. 2, five in- and outflow cycles were fixed for the experiments, resulting in test durations of 1 h 20 min to 13 h 36 min, as t_p depends on discharge. Three more parameters of minor concern for the presented results were the relative duration between in- and outflow sequences $t_{p,IN}/t_{p,OUT}$, the initial sediment concentration C_0 and the intake position z_i .

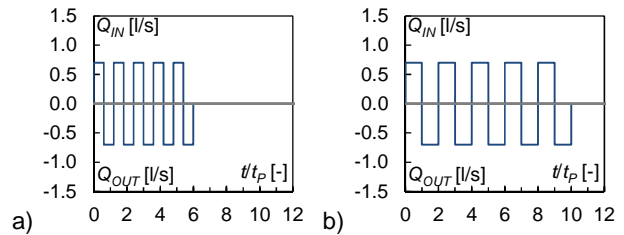


Figure 2: Configurations of tested in- and outflow cycles, example for $Q = 0.7$ l/s and $Kt_p = 0.6$ (a) and 1.0 (b).

The experiments were performed according to Froude similarity, respecting the same ratio between inertia and gravity forces in prototype and model conditions. Reynolds similarity was not an issue due to the turbulent conditions at the intake/outlet for every tested discharge.

After filling the main basin and the mixing tank, the two reservoirs were disconnected from the laboratory circuit. Thus, the total water volume remained constant over the test duration. Consequently, water level in the basins varied according to the operation mode, with maximum level variation in the main basin of $\Delta H_{MB} = 0.18$ m.

UVP measures were carried out once to three times a sequence, depending on the cycle duration t_p .

3 JET CENTERLINE VELOCITY

3.1 Submerged turbulent jet

Water ejected into the basin during inflow sequences forms a so-called submerged axisymmetric turbulent round jet. Such jets consist in an initial core, a transition zone and a fully developed jet region (Fig. 3).

The core flow is nearly free of shear and its velocity is equal to the nozzle exit velocity v_0 under uniform inflow conditions. It is surrounded by a mixing layer, forming a boundary between the core flow and the reservoir fluid. The imprint of the nozzle shape disappears when the turbulent eddies in the shear layer destroy the nozzle core flow and penetrate to the jet axis. The resulting eddy-dominated flow is called fully developed and starts at a distance of $s/D_j = 4.3$ to 10 from the nozzle.

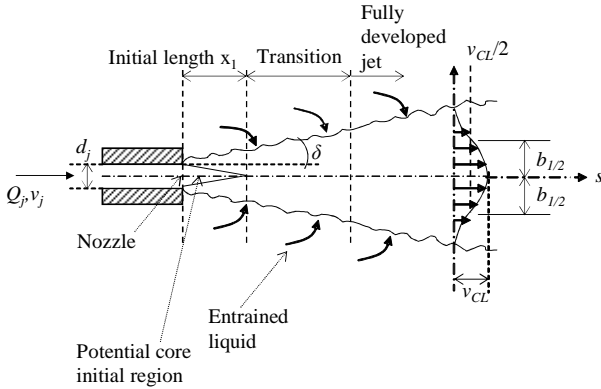


Figure 3: Jet flow behavior according to [7].

In the fully developed jet region, the centerline velocity v_{CL} continuously decreases with the distance s in jet direction. Centerline velocity can be defined as

$$v_{CL}(s) = C_1 \frac{v_0 \cdot D_j}{s} \quad (1)$$

where C_1 : a constant [-],
 v_0 : the jet velocity at the nozzle [m/s],
 D_j : the jet diameter at the nozzle [m], and
 s : the distance from the nozzle [m].

According to literature, values of the constant vary between $C_1 = 5.75$ and 7.32 [7-10].

3.2 Experimental results

Two low frequency UVP prototype transducers were tested to describe the jet behavior in the main basin during inflow sequences. Sampled centerline velocities were compared to values given in literature and should provide a calibration possibility to define the adequate turbulence model for numerical simulations. Velocities are commonly normalized by the approach flow velocity in the pipe $v_0 = Q_{IN}/A$, lengths are normalized by the jet diameter D_j .

With increasing sampling distance, the recordable velocity magnitude of the UVP decreases. When the ultrasonic beam emitted by the transducer exceeds the jet dimensions, ambient stagnant water will be taken into account for velocity averaging. Such, a transducer located far away from the jet nozzle will record reliable data until the point when the emitted ultrasonic beam exceeds the jet dimensions. From there, the probe starts underestimating the jet velocity. Therefore, the centerline velocity v_{CL} over a distance up to $s/D_j = 30$ was established by several measures, as illustrated in Fig. 4. Based on the different UVP measurements, an envelope curve could be established, as indicated in Fig. 4a.

The particular bell mouth shaped intake/outlet geometry leads to slightly different jet characteristics than investigated by other authors. The jet core is short and the centerline velocity is higher than the estimated inflow velocity v_0 , indicating a non-uniform velocity distribution at the nozzle. The distance up to

$s/D_j = 5$ is marked by a drop to approximately $v_{CL}/v_0 = 0.8$. Then, the decrease of centerline velocity follows the values given in literature with $C_1 = 6$ approximately, independent on discharge. The short and fast decrease of v_{CL} over a length of approximately $s/D_j = 5$ to 6 is common for all tested discharges.

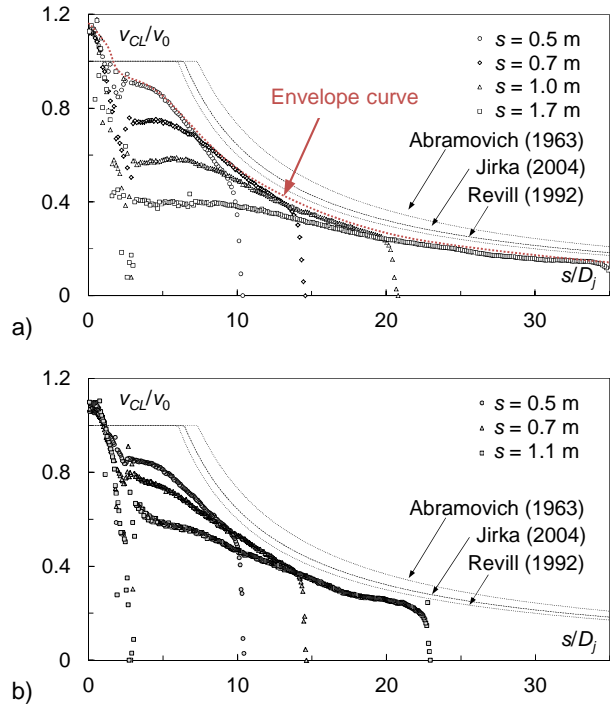


Figure 4: Dimensionless jet centerline velocity v_{CL}/v_0 as a function of dimensionless distance s/D_j from the nozzle. Comparison between experiments and values from literature. 0.5 MHz UVP sampling for $Q_{IN} = 0.7$ l/s (a) and 1.0 MHz UVP sampling for $Q_{IN} = 0.5$ l/s (b).

4 TWO DIMENSIONAL FLOW PATTERNS

Results from 2D flow mapping are represented for one quadrant of the main basin (Fig. 1b) and the case $z/B_{MB} = 0.25$. Based on the 28 UVP measuring points, linear interpolation allowed a finer grid to illustrate the flow patterns. Distances s and y are normalized by the main basin width B_{MB} , while velocities are normalized by the approach flow velocity in the pipe v_0 .

4.1 Flow patterns for variable cycle discharge

UVP flow maps show that during inflow sequences, the jet starts developing immediately after the start of the sequence and oscillates slightly along its axis. Small circulation cells are formed at the boundary between the jet and the surrounding water. This initial behavior is similar for all discharges. By the end of a sequence, a big recirculation cell is established which occupies the entire sampling section for high discharges. For lower discharges, the boundary of the recirculation cell establishes at approximately $s/B_{MB} = 0.4$ (Fig. 5a).

Flow patterns at $z/B_{MB} = 0.125$ and 0.375 during inflow sequences show the expansion of the jet as well as some unsteady behavior with an oscillating and sometimes deflected jet due to secondary flow phenomena. These sections also include the recirculation cells around the jet. For discharges $Q = 0.9$ and 1.1 l/s, backflow zones toward the intake/outlet are systematically observed at $z/B_{MB} = 0.125$ (Fig. 5c). This movement on the bottom layer of the basin might be interesting regarding suspended sediment behavior. For lower discharge, such conditions do not establish in the bottom layer (Fig. 5b).

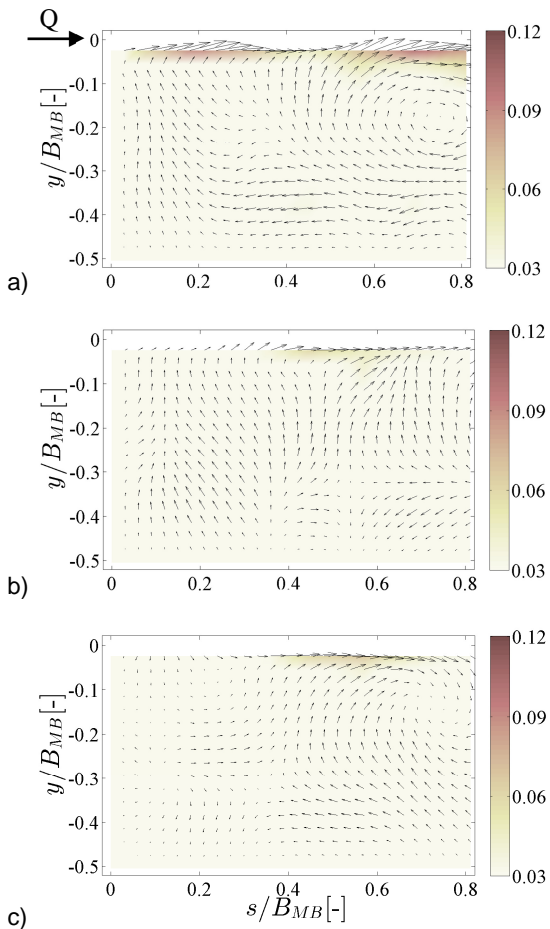


Figure 5: Sampled flow patterns for a jet entering at $s/B_{MB} = y/B_{MB} = 0$ and $z/B_{MB} = 0.25$, for $Kt_P = 0.8$ and $Q = 0.7$ (a & b) and 1.1 l/s (c). Dimensionless velocity v/v_0 at $z/B_{MB} = 0.25$ (a, at jet axis) and 0.125 (b & c, below jet axis).

The flow patterns at $z/B_{MB} = 0.25$ recorded shortly after the change in operation mode, i.e. at the beginning of an outflow sequence, show that the big recirculation cell persists in time before dissipating its energy. Independent on discharge, the velocities near the intake/outlet are mainly orientated toward the latter by the end of an outflow sequence, while the rear of the sampled section is quasi stagnant.

The 2D flow pattern at $z/B_{MB} = 0.125$ and 0.375 are very similar with fluctuating flow orientation, influenced by the precedent inflow sequence.

4.2 Flow patterns for variable cycle frequency

Cycle frequency influences the time available for flow patterns development. Thus, for $Kt_P = 0.6$ and 0.8 flow direction is reversed before flow patterns in the main basin reach steady state conditions. For $Kt_P = 1.2$, the flow patterns are supposed to be steady as observed for $Kt_P = 1.0$. Higher frequency of in- and outflow cycles leads to an amplification of movement in the main basin. The shorter outflow sequences do not allow entire dissipation of the recirculation cells. This leads to a slightly faster jet formation during the following inflow sequence.

5 CONCLUSIONS

One-dimensional velocity sampling with 0.5 and 1.0 MHz UVP transducers allowed adequate description of centerline velocity of the inflowing jet. Results were used later on to calibrate a numerical model of the experimental test rig.

The 2D UVP flow mapping allowed the analysis of horizontal flow fields at three levels in the main basin. Flow patterns at intake axis revealed the recirculation cells establishing for inflow sequences, while sampling in horizontal sections above and below the intake/outlet axis allowed the observation of some 3D behavior in the test volume.

6 BIBLIOGRAPHY

- [1] Shammaa Y et al: Flow upstream of Orifices and Sluice Gates, J Hydraulic Eng, 131(2), 127-133 (2005).
- [2] Shammaa Y et al: Flow field in a Rectangular Basin with a Line Inlet and a Circular Outlet, J Hydraulic Eng, 135(10), 857-864 (2009).
- [3] Kantoush SA et al: Flow field investigation in a rectangular shallow reservoir using UVP, LSPIV and numerical modeling, Flow Measurement and Instrumentation 19(3), 139-144 (2008).
- [4] Jenzer Althaus J: Sediment evacuation from reservoirs through intakes by jet induced flow, Communication N°45 du Laboratoire de constructions hydrauliques, Schleiss A (ed.), Ecole Polytechnique Fédérale de Lausanne, Switzerland (2011).
- [5] De Cesare G, Schleiss A: Turbidity current monitoring in a physical model flume using Ultrasonic Doppler Method, 2nd International Symposium on Ultrasonic Doppler Methods for Fluid Mechanics and Fluid Engineering, Villigen, Switzerland, 61-64 (1999).
- [6] Meile T et al: Improvement of Acoustic Doppler Velocimetry in steady and unsteady turbulent open-channel flows by means of seeding with hydrogen bubbles, Flow Measurement and Instrumentation 19(3), 215-221 (2008).
- [7] Blevins RD: Applied fluid dynamics handbook, Krieger Publishing Company, Malabar, Florida, US (1984).
- [8] Abramovich GN: The theory of turbulent jets, M.I.T. Press, Cambridge, Massachusetts, US (1963).
- [9] Revill BK: Jet mixing, in Mixing in the Process Industries, Harnby J, Edwards NF, Nienow AW (eds.), Butterworth-Heinemann, Oxford, UK (1992).
- [10] Jirka G: Integral Model for Turbulent Buoyant Jets in Unbounded Stratified Flows. Part I: Single Round Jet, Environmental Fluid Mechanics 4(1), 1-56 (2004).

Ultrasonic wave interaction with air-water boundary layer

Philippe SCHMITT¹, Anne PALLARES¹, Yuji TASAKA², Kousuke SAKURAI²,
Stéphane FISCHER³

¹Institut de Mécanique des Fluides et des Solides, Université de Strasbourg,

2, rue Boussingault, F-67000 Strasbourg, France

² Division of Energy & Environmental Systems, School of Engineering, Hokkaido University,
N13W8, Sapporo 060-0628, Japan

³Ubertone, SAS,

4, rue Boussingault, F-67000 Strasbourg, France

This paper presents a collaborative study of the Universities of Strasbourg and Hokkaido with the support of Ubertone. Its goal is to analyze and understand the ultrasound wave behavior at the water-air boundary. Measurements with an Ubertone UB-Flow profiler have been done for different water height and discharge configurations on a flume of 16 meter length and 0.6 meter wide. The instrument allows the possibility to work on the raw Doppler data. This facility was used to dissect the phenomena on the air-water interface and to get the interpretations.

Keywords: Acoustic, Doppler method, water height scattering

1 INTRODUCTION

There are several methods for the flow velocity profile evaluation. One of the commonly used is the pulsed ultrasound technique: the estimation of the flow velocity at different depths along a profile can be obtained by Doppler evaluation from the backscattered acoustic signal. The measured ultrasonic signal at each depth is the result of the reflection of the emitted beam by the moving scatterers in a volume defined by the ultrasonic beam geometry and the range-gated echo duration [1].

Getting accurate velocity or amplitude measurements through this technique might become difficult if the observed volume is close to a physical boundary. Indeed the amplitude of the generated parasitic echo might strongly disturb the measurement. This disturbance can be observed in configurations where the Doppler instrument is placed in the bed of an open channel flow, emitting the ultrasonic beam up, with a weak angle to the vertical. Often a significant decrease in the fluid velocity near the surface is observed although it doesn't reflect the flow's physics.

Many studies have been done on the ultrasonic detection of moving interfaces in gas-liquid two-phase flows [2], using variety of information's coming from the scattered intensity, Doppler shift or statistics about Doppler velocity spreading near the interface.

The aim of the present work focuses on analyzing and understanding the ultrasound wave behaviour at the water-air boundary, when the instrument has a weak angle with the vertical for both measurement of the velocity profile on the flow and the water height. In order to understand the different effects

on the fluid velocity and amplitude measurements near the surface, the study of the air-liquid moving interface is carried out on the complex raw Doppler data samples accessed for each volume. Arguments for the observed phenomena will be given as well as an interpretation of the possible information on the ultrasound beam after reflection on water height.

2 METHODS

2.1 Pulsed ultrasound principle

The measurements were performed with an UB-Flow profiler [3], which has three functionalities: it allows to record a flow velocity profile, the measurement of the backscattered signal amplitude and the determination of the water height. This instrument works on the pulsed principle and thereby allows precise knowledge of the position in the flow of a given data at a given time stamp [4].

The UB-Flow is a single immersed hydrodynamic device equipped with two transducers placed at the front. Measurements from this study were performed with the transducer centered on 1.5MHz with the first layout of the instrument (figure 1).

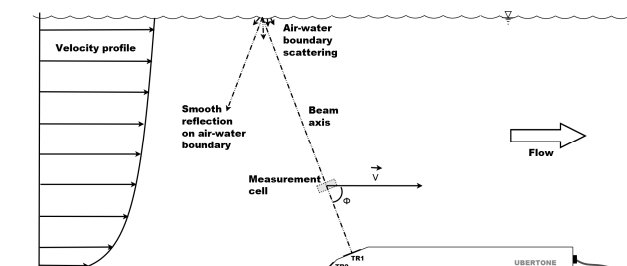


Figure 1: UB-Flow in a flume

A standard set-up for velocity profiling with this instrument is to place it on the bed of a flume. In this

case the 1.5MHz transducer presents an angle of 75° with the flow, and is used for both measurements of velocity profile and water height. Collected data near the air-water boundary can then present following behavior:

- spreading of backscattered amplitude over several cells
- substantial velocity decrease near the boundary layer

2.2 Background on air-water boundary layer

Ultrasound wave reflection on the water-air boundary layer exhibits a complex behavior depending on the size, the shape and the motion of the interface.

With a smooth, undisturbed air-water interface, the ultrasound waves reflect symmetrically to the plane perpendicular to the boundary layer. Thus, in our layout, with an angle of 15° with vertical, no signal from the interface returns to the transducer and the interface acts like a mirror for ultrasounds (figure 1).

When the air-water interface is in a disturbed state, motion and shape of the boundary layer as well as the surface wavelets allow the scattering of the ultrasonic waves in a large cone that can be received by the transducer (figure 1).

As our measurements were carried out with an ultrasonic beam showing a weak angle of 15° to the vertical, no detection is possible in the case of a smooth interface, but only in a turbulent situation, which is the case in a standard flow.

The air-water interface information can then be present in several measurement cells depending on the instrument configuration, and is mixed with backscattered signal coming from the suspended particles in motion within the flow. The main criterion is the position of the cells in relation to the ellipsis formed by intersection of ultrasound beam and air-water interface.

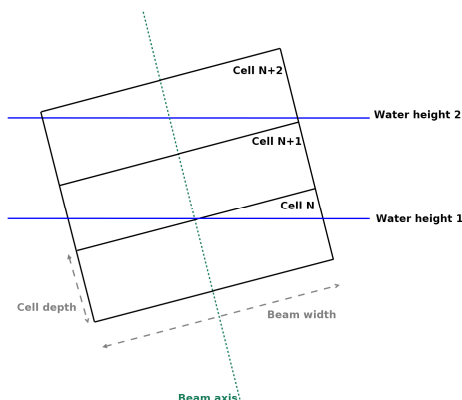


Figure 2: Ultrasound cells placement and different air-water interfaces

An example of measurement cells with different possible water heights is shown figure 2. The number of cells impacted by the air-water interface

depends on the beam width and depth, for a given transducer angle with the vertical.

3 MEASUREMENTS AND OBSERVATIONS

3.1 Open Channel setup

Measurements were done on the flume of the hydrologic platform of University of Strasbourg. This flume has a length of 16 m , a width of 60 cm and a maximum water height of 80 cm . Its slope is adjustable. The flow rate and height of water in the channel were controlled by a pump and were measured by an electromagnetic flow meter and a scale, respectively. The instruments were placed in the flow, in an area where the hydraulic regime is well established. Their measurement beams go from the canal bottom to the water surface (figure 3), therefore with an angle of 75° with the flow.



Figure 3: Two UB-Flow's placed in the flume

A typical configuration for the instrument is given in Tab. 1.

Table 1: Parameters of the instrument.

Variable	Symbol	Value
Carrier frequency	$f_0(\text{MHz})$	1.5
Cycles per pulse	N_{em}	4
Pulse Repetition frequency	$PRF(\text{Hz})$	500
Number of cells	N_{vol}	62
Cell depth	$d_{vol}(\text{mm})$	2.5

Measurements were done for different water heights growing from $\sim 30\text{ cm}$ to $\sim 45\text{ cm}$.

3.2 Profile scanning

Figure 4 shows a typical velocity and echo intensity record for a configuration with a water height of 44.5 cm . The main peak in the echo intensity profile corresponds to the air-water interface detected by the ultrasonic beam. However we can observe a second peak on the same curve synchronized with a fall in the velocity profile (around 43 cm). In order to

verify that it is not a multi-reflection of the ultrasonic waves from a previous burst, the PRF was changed, without effect on the shape and the position of this phenomenon.

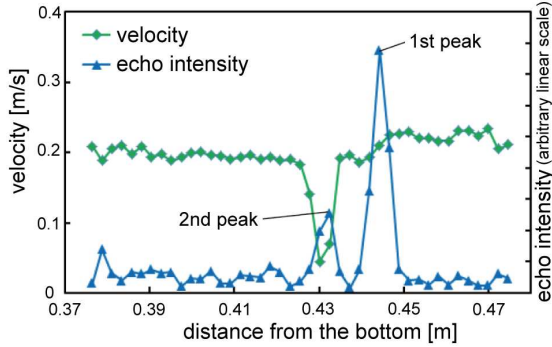


Figure 4: Detailed profiles of the velocity and the echo intensity with a free surface at 44.5cm

The hypothesis investigated is that this behavior is generated by the side lobes of the ultrasonic beam. These lobes send hugely less energy in the medium but if they meet large elements, like the air-water interface, the backscattered signal can be important. In order to understand this phenomenon, the raw data have been investigated. The UB-Flow allows the record of the complex envelope with in-phase and quadrature components of the Doppler signal for a selected cell. The Doppler signal in several cells was analyzed for the same established flow rate.

4 RESULTS AND DISCUSSION

4.1 Transducer radiating aperture

A cylindrical transducer produces an ultrasonic beam which is equivalent to a spherical wave in his farfield region and can be written [5] at range r and time t as follows:

$$P(r, \theta, t) = \Re \left(P_0 r_0 \frac{D(\theta)}{r} e^{-\alpha r} e^{i(kr - \omega t)} \right) \quad (1)$$

P_0 is the reference pressure, normally defined at $r_0 = 1m$, $D(\theta)$ is the transducer directivity function, θ is the angle between the position r and the axis of the transducer, α is the medium attenuation, k is the wavenumber for the sound in water and ω is the wave pulsation. The directivity function represents the angle reliance of the emitted pressure and is written as:

$$D(\theta) = \frac{2J_1(ka_t \sin \theta)}{ka_t \sin \theta} \quad (2)$$

J_1 is a Bessel function of the first kind and a_t is the radius of the transducer. Figure 5 represents the modulus of this function and shows clearly that there is a part of the ultrasound intensity that is emitted in a direction near to an angle of 15° with the axis of the transducer. As the transducer in this case has an angle of 75° with the flow, this part is therefore

emitted perpendicular to the air-water interface.

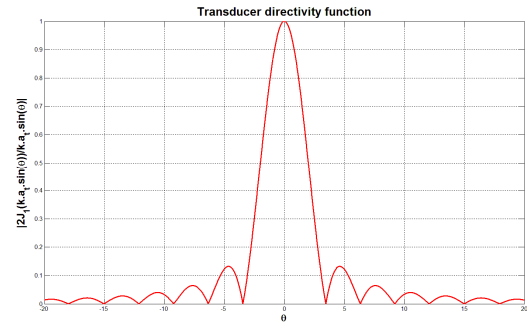


Figure 5: Modulus of the directivity function $D(\theta)$

4.2 Air-water interface

To analyze and fully understand the behavior of the intensity and the velocity profiles at the interface, measurements were carried out in this area. Figure 6 shows a schematic illustration of the measurement points for the signal investigation. The cell located on point A is fully in the flow. The cell located on C contains the information coming from the flow through the main lobe of the ultrasonic beam, but can also get air-water interface information on C' through the lobes at nearly 15° . The cell located on B contains the information coming directly from the air-water interface area through the main lobe.

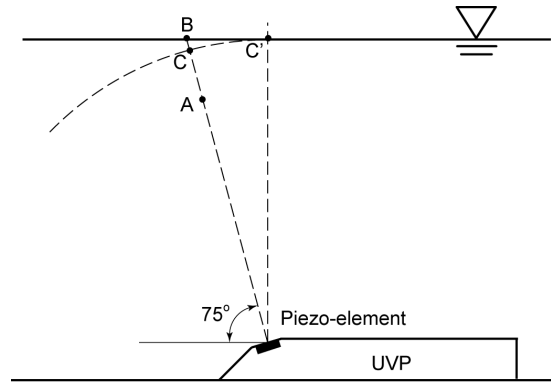


Figure 6: Schematic illustration of the investigated areas

Figure 7 shows the complex raw data and their corresponding Fourier spectra on cell A .

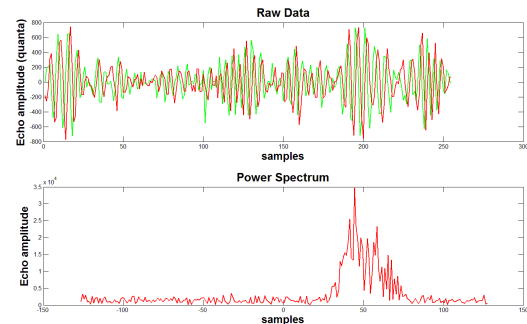


Figure 7: a) Complex raw Doppler data b) Associated Power Spectrum

The Doppler signal backscattered by the particles

moving with the flow can easily be observed on the raw data. The Fourier transform's gives a standard spectrum centered on a mean Doppler shift.

Figure 8 shows a typical result on the complex raw data and their corresponding Fourier spectra for the cell located at position *C*.

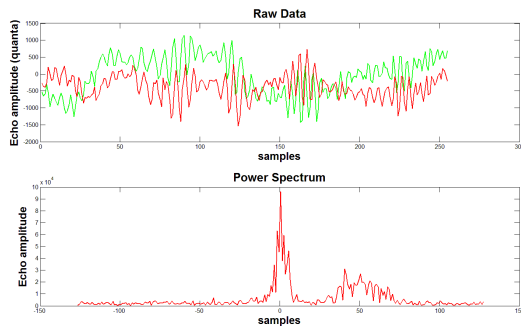


Figure 8: a) Complex raw Doppler data b) Associated Power Spectrum

The raw data show the presence of the signal coming from the moving particles, but superimposed with a kind of moving baseline. According to these fluctuations with different time scales, the power spectrum has two clear peaks: the peak at a higher frequency shows a similar Doppler frequency as that on cell *A*, and a peak at lower frequency, around zero. These results can be interpreted as the superposition of Doppler signal backscattered by particles in the main lobe of the ultrasonic beam and air-water interface reflecting waves coming from other lobes with a perpendicular incidence. In spite of the poor energy present in these lobes, the energy of the perpendicular reflection is close to the energy backscattered by particles in the main lobe.

Finally, figure 9 shows a typical result on the complex raw data and their corresponding Fourier spectra for the cell located at position *B*.

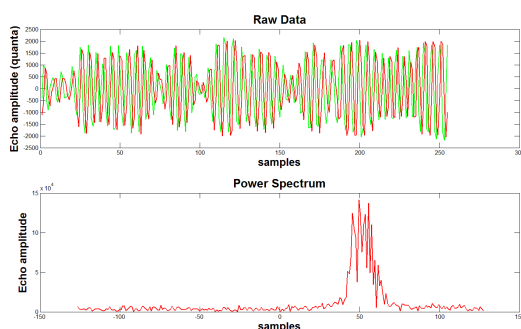


Figure 9: a) Complex raw Doppler data b) Associated Power Spectrum

Here, there is no presence of energy around zero in the power spectrum. Indeed, the symmetrical reflection of the main beam to the plane perpendicular to the boundary layer avoids a strong backscattering from the air-water interface. Nevertheless, the Doppler echo characterizing the particle motion in the flow is several times stronger

than in the cell *A*. An interpretation can be that the state of the air-water interface is enough turbulent so that the surface wavelets (which move at a velocity near to that of the particles) allow the scattering of the ultrasonic waves back to the transducer's direction.

Figure 10 shows the mean power spectrum for the three cases discussed before. It is clear that, compared to cell *A*, there is a phenomenon on the cell *C/C'* which is linked to the reflection of waves from secondary lobes on the air-water interface, but we can see that the Doppler frequency backscattered from particles is not biased, so frequency filtering could be applied here. Another phenomenon, explained before, occurs on cell *B* where the backscattered echo is stronger than in cell *A*.

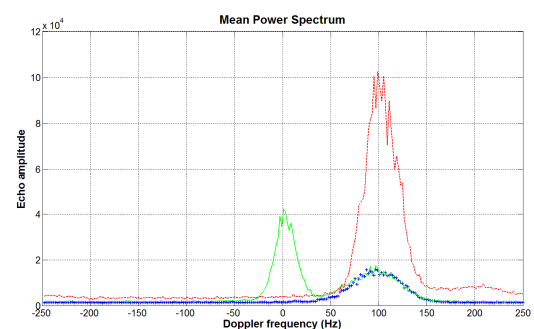


Figure 10: a) Blue cross line for cell *A* b) Red dashed line for cell *B* c) Green full line for cells *C/C'*

5 CONCLUSIONS

The present study focused on the examination of velocity and echo intensity near the air-water interface in an open channel flow. The observed phenomena (figure 4) can be explained by the echos coming from the secondary lobes of the ultrasonic beam and by the surface conditions of the flow.

It could be interesting to make further investigations in order to understand the weak increase of the Doppler shift in cell *B*, as well as the impact of the motion of the free surface.

REFERENCES

- [1] Yu A.C.H. et al.: Transit-time broadening in pulsed Doppler ultrasound: a generalized amplitude modulation model, *IEEE Transactions on Ultrasonics, Ferroelectrics, and Frequency Control*, 53-3(2006) 530- 541.
- [2] Murai Y. et al.: Ultrasonic detection of moving interfaces in gas-liquid two-phase flow, *Flow Measurement and Instrumentation* 21-3 (2010), 356-366.
- [3] Fischer S.: A new high resolution velocity and acoustic turbidity profiler for open channels, *ISUD7 Proceedings* (2010), 35-38.
- [4] Schmitt P. et al.: Instrumental development and characterization for loaded liquid flow measurement, *ISUD6 Proceedings* (2008), 151-154.
- [5] Thorne P.D., Hanes D.M.: A review of acoustic measurement of small-scale sediment processes, *Cont. Shelf Res.* 22 (2002), 603-632.

Ultrasonic flow measurements and bubble detection in gas-stirred metallic melts

T.Vogt¹, A. Andruszkiewicz², K. Eckert², S. Odenbach², S.Eckert¹, G. Gerbeth¹

¹Helmholtz-Zentrum Dresden-Rossendorf, 01314 Dresden, Germany

²Technische Universität Dresden, Germany

In this study we investigate the flow structure in a liquid metal cylinder while a bubble-driven recirculation flow is superposed with a rotating magnetic field (RMF). The flow structure and the bubble positions were measured by means of the ultrasound Doppler velocimetry (UDV) and the ultrasound transit-time technique (UTTT), respectively. The measurements revealed the potential of the RMF to control both the amplitude of the meridional flow and the bubble distribution and to provide an effective mixing in the entire fluid volume. Various periodic flow patterns were observed in a certain parameter range with respect to variations of the magnetic field strength and the gas flow rate.

Keywords: Bubble detection, Bubble flow, rotating magnetic field, mixing

1 INTRODUCTION

Bubble-driven flows are widely used in industrial technologies. In metallurgical applications gas bubbles are injected into a bulk liquid metal in order to force a motion, to homogenize the physical and chemical properties of the melt or to refine the melt [1,2]. Another way to drive a liquid metal into motion is the application of a rotating magnetic field (RMF) [3,4].

In this study we investigate the flow structure in a liquid metal cylinder while these two different driving mechanisms are used simultaneously. A schematic drawing of the experimental setup is shown in Fig. 1. A cylindrical vessel having an inner diameter of 90 mm and an aspect ratio $A = H_0 / (2 \cdot R_0) = 2$ was filled with the eutectic alloy GaInSn, which is liquid at room temperature. The cylinder was placed concentrically in the magnetic induction system PERM at the Helmholtz-Zentrum Dresden-Rossendorf (HZDR). The PERM stirrer was equipped with six coils, arranged as pole pairs in order to create a rotating magnetic field with a field strength up to 17 mT. The magnetic field frequency was fixed to $\omega = 2\pi 50$ Hz. Argon gas was injected with an adjustable flow rate in the middle of the cylinder bottom. The fluid velocities were measured using the ultrasound Doppler velocimetry (UDV). For that purpose we placed five ultrasound transducers at the bottom of the fluid container. The transducers were aligned vertically in order to record axial profiles of the vertical velocity between the bottom and the lid of the fluid cylinder at different radial and azimuthal positions. The detection of the gas bubbles in the liquid metal was realized by means of an ultrasound transit-time technique [5]. Two ultrasonic heads, each consisting of 10 ultrasonic transducers, were placed horizontally at different heights at the sidewall of the cylinder. An ultrasound defectoscope (USIP 40) together with the software UltraPROOF (both from GE Inspection Technologies) were used to calculate the bubble position from the transit time of the ultrasound signal from the transducer to the bubble and return. The time resolution of the measuring system is about 2.5 ns. Twenty ultrasound transducers were allocated along the vessel side wall to monitor the full vessel height while only 10 transducers could be multiplexed. For a particular measurement the respective 10 transducers were selected according to the best compromise with respect to a suitable

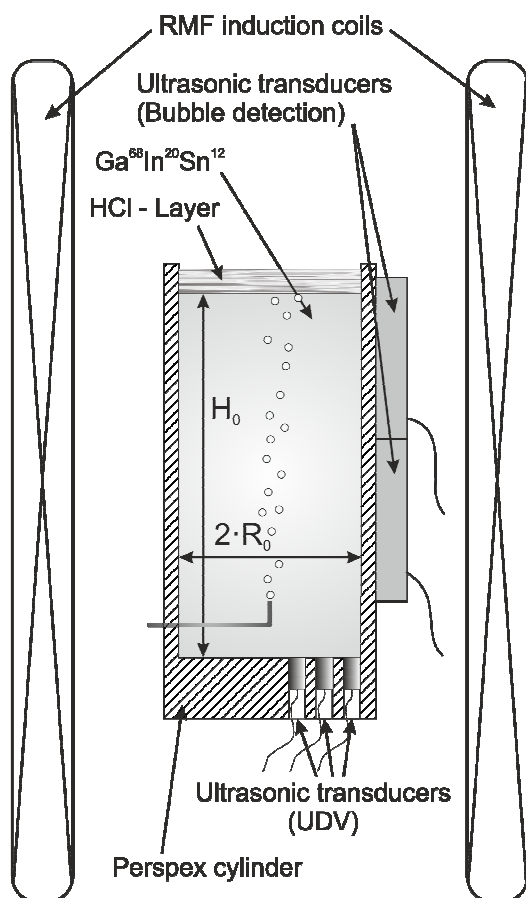


Figure 1: Schematic drawing of the experimental setup

detection of the bubble path variations.

2 RESULTS

Depending on the gas flow rate Q_G (sccm stands for standard cubic centimeters per minute) and the magnetic field strength (expressed by the magnetic Taylor-number) we observed five main flow regimes. The Taylor number is defined as follows

$$Ta = \frac{\sigma \omega B_0^2 R_0^4}{2\rho\nu^2} \quad (1)$$

where σ stands for the electrical conductivity, ρ is the density and ν is the kinematic viscosity of the fluid.

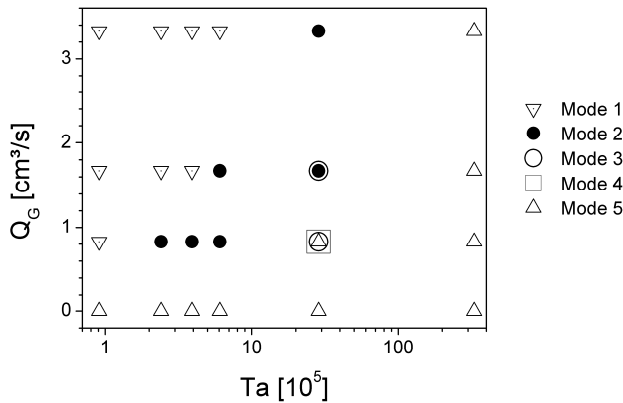


Figure 2: Map of the specific flow patterns at different parameter combinations

When the rising bubble plume is superposed with a low power RMF, the flow pattern in the cylinder consists of a recirculation zone in the upper half of the cylinder which is almost identical to the bubble plume without a magnetic field (in the following denoted with “mode 1”). In the opposite, if the bubble-driven flow is exposed to a very strong RMF, the resulting strong swirling motion forces the bubbles to the rotational axis of the vessel (mode 2). The resulting flow pattern consists of the well-known double vortex of the RMF-driven flow in the meridional plane of the vessel [6-7]. In between these two limiting parameter regimes we observed three new flow patterns (mode 3 – mode 5) showing a remarkably oscillating behavior of the velocity field. The parameter range where the different flow modes were observed is shown in Fig 2.

Mode 3 is a flow pattern characterized by very high fluid velocities in the entire flow volume. Fig. 3 shows an UDV measurement of this flow pattern. Here, the bubble plume is rising off-axis at approximately $r \approx 0.3 \cdot R_0$ and produces a large recirculation zone that occupies almost the entire fluid volume. Furthermore, this flow configuration rotates around the vessel axis in the same direction as the RMF. Fig. 4 shows the corresponding histogram of the spatial distribution of the bubbles

for ten transducers positioned at increasing distance

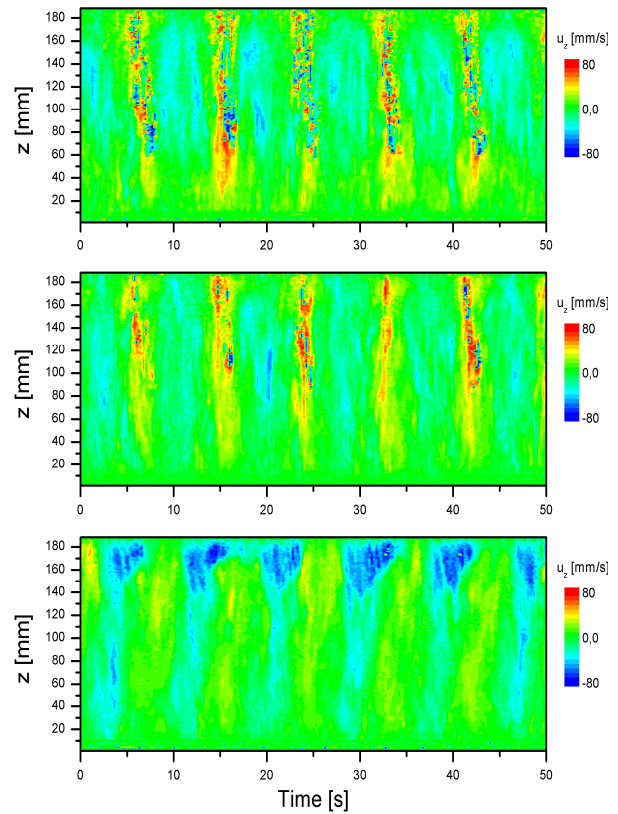


Figure 3: Periodic flow pattern (mode 3) resulting from the superposition of RMF ($B = 1$ mT) and rising gas bubbles ($Q_G = 100$ sccm); UDV measurements are recorded at $r/R_0=0.3$ (top), $r/R_0=0.6$ (middle) and $r/R_0=0.9$ (below)

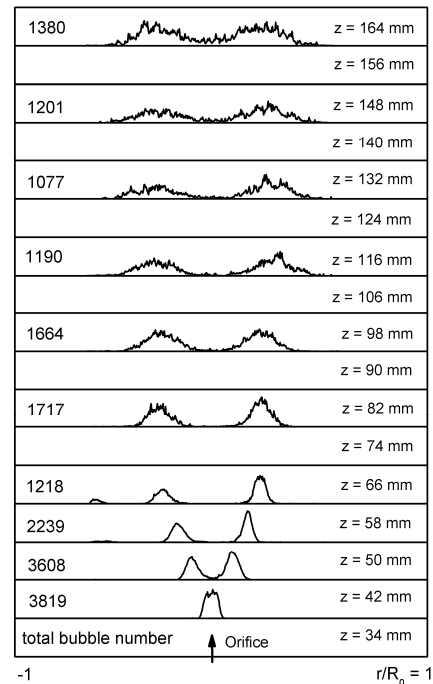


Figure 4: Bubble histogram corresponding to the measurements shown in Fig. 2. $Q_G = 100$ sccm; $B = 1$ mT ($Ta = 28,6 \cdot 10^5$); $\Delta T = 360$ s

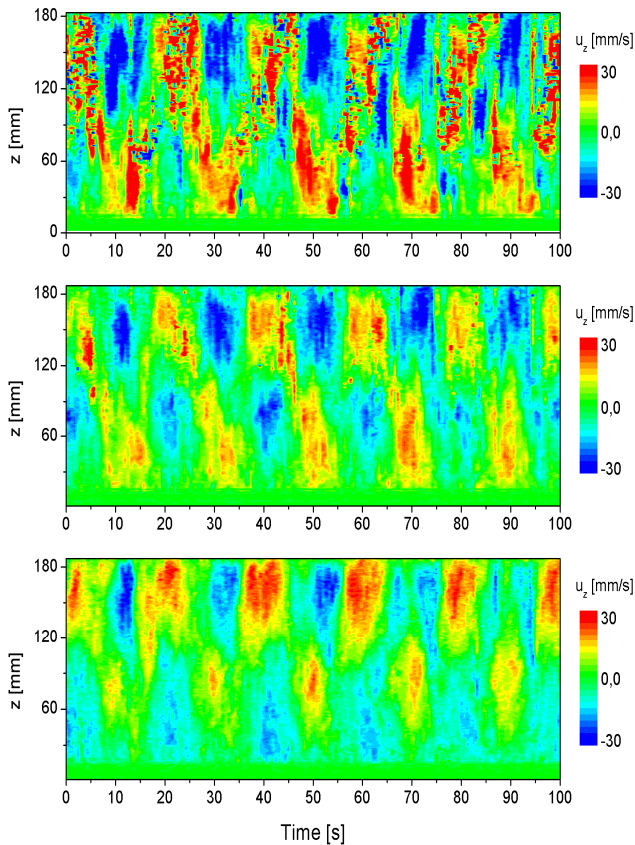


Figure 5: Periodic flow pattern (mode 4) resulting from the superposition of RMF ($B = 1$ mT) and rising gas bubbles ($Q_G = 100$ sccm); UDV measurements are recorded at $r/R_0=0.3$ (top), $r/R_0=0.6$ (middle) and $r/R_0=0.9$ (below)

from the orifice. The value on the left hand side in the histogram is the total number of bubbles detected by each transducer within the measuring interval of $\Delta T = 360$ s. This value decreases in z -direction due to the increase of the radial spreading of the gas bubble distribution during their rise. The key information of these bubble histograms is the spatially varying bubble distribution over the cross section of the vessel.

A further remarkable flow pattern that was observed in our experiments is shown in Fig. 5 - 6. This flow mode, which is denoted with mode 4, differs from mode 3 by the S-shaped bubble path. This S-shaped bubble path produces two recirculation zones. A schematic drawing of both, mode 3 and 4 is shown in Fig 7.

The last flow pattern - mode 5 - is very similar to the pure RMF induced swirling flow (mode 2). The only difference is a weak oscillation of the fluid flow in the center region of the vessel due to the rising gas bubbles.

3 CONCLUSION

In our experiments we studied the flow in a liquid metal cylinder which is driven by the superposition of a rising bubble plume and a rotating magnetic field. Both driving mechanisms are used separately

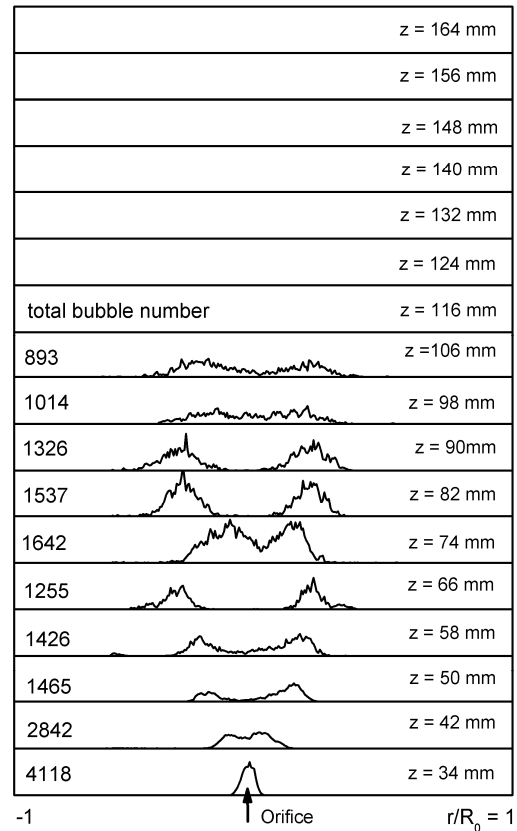


Figure 6: Bubble histogram corresponding to the measurement shown in Fig. 5. $Q_G = 100$ sccm; $B = 1$ mT ($Ta = 28,6 \cdot 10^5$); $\Delta T = 360$ s

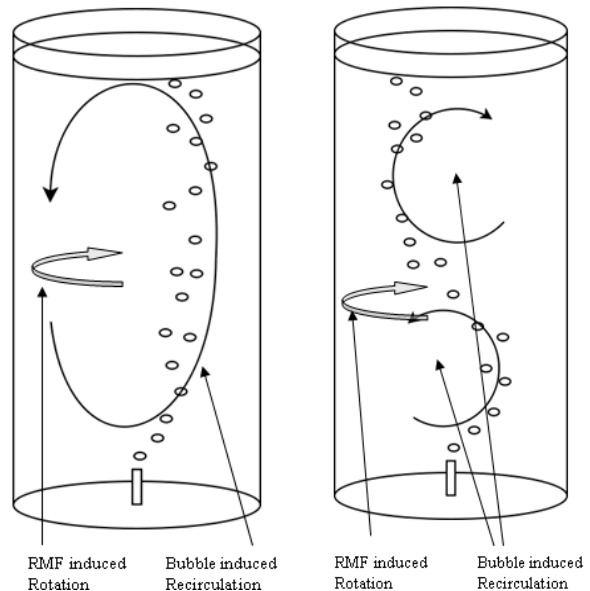


Figure 7: Schematic drawing of the periodic flow patterns mode 3 and mode 4

in metallurgical applications for purposes of melt stirring. Likewise, the resulting flow structure was studied in depth in many experiments and numerical simulations. In contrast, the flow structure resulting from the simultaneous usage of rising bubble plume and RMF is a rather low explored flow configuration.

We found out that the superposition of these two driving mechanisms within a distinct parameter range yield some striking new flow patterns of oscillating nature. These flow patterns are attributed with increasing fluid velocities in the whole fluid volume. In addition, the undesired dead water zones, which occur in pure bubble driven recirculation flows, can effectively be avoided. Therefore, this new flow configuration has a high potential to increase the efficiency of metallurgical applications where a high mixing rate is desired.

ACKNOWLEDGEMENT

The research is supported by the Deutsche Forschungsgemeinschaft (DFG) through the SFB 609 "Electromagnetic Flow Control in Metallurgy, Crystal Growth and Electrochemistry." This support is acknowledged gratefully by the authors

REFERENCES

- [1] Sahai and Guthrie. Hydrodynamics of gas stirred melts: Part I and II. Metallurgical and Materials Transactions B, 1982
- [2] Johansen et al. Fluid dynamics in bubble stirred ladles Part I and II. Metallurgical and Materials Transactions B, 1988
- [3] Davidson and Hunt. Swirling recirculating flow in a liquid-metal column generated by a rotating magnetic field. J. Fluid Mech. 1987
- [4] Eckert et al. Efficient Melt Stirring Using Pulse Sequences of a Rotating Magnetic Field: Part I. Flow Field in a Liquid Metal Column. Metallurgical and Materials Transactions B, 2008
- [5] Andruszkiewicz et al. Ultrasonic measurements of flow in two-phase liquid gas systems I – III. Chemical and Process Engineering, 2008
- [6] Rübiger et al. Measurements of an unsteady liquid metal flow during spin-up driven by a rotating magnetic field. Exp. Fluids. 2010
- [7] Vogt et al. On the formation of Taylor-Görtler vortices in RMF-driven spin-up flows. Exp Fluids, 2012

Ultrasonic Doppler Flow Measurements Applied to Gas-Lift Pumping Technique

Jian HE^{1,2}, Guogang BAO², Qunying HUANG^{1,2}, Zhiqiang ZHU², Sheng GAO², FDS Team

1 Institute of Nuclear Energy Safety Technology, Chinese Academy of Sciences, Hefei, Anhui, 230031, China

2 School of Nuclear Science and Technology, University of Science and Technology of China Hefei, Anhui, 230027, China

Corresponding author: jian.he@fds.org.cn

Abstract: The Lead bismuth eutectic (LBE) is considered as the candidate spallation target material and coolant for the Accelerator Driven sub-critical Systems (ADS) as well as coolant for fast neutron reactor. Series of liquid PbBi loops named KYLIN series has been designed and built or under construction by FDS Team to investigate the key issues of LBE. One of the main objectives of KYLIN-II facilities was to investigate and confirm the possibility of using the gas-lift pumping technique to obtain a steady flow of liquid metal on significant scale, and make know the exact velocity profile in the gas-lift test section. The Ultrasound Doppler Velocimetry (UDV) is a non-intrusive way to measure opaque fluids and has the ability to deliver complete velocity profiles online. For this reason, The UDV was applied to the experimental activities performed to characterize the gas enhanced circulation technique and analyze the fluid dynamic behavior of the system.

Taking into account that UDV technique was restricted by some problems, such as high temperature, acoustic coupling and the wetting condition, the verification of the UDV was carried out in the gas-lift facility. At first, the velocity profile of water flow with no air injection in a rotating device was investigated by experimental and numerical approaches. Then, the echo signals reflected from air-water bubbly flow in the gas-lift test section were measured and the flowing profile were estimated by statistical analysis and velocity profiling process of echo signals. Good results were achieved during these tests, which mean that the UDV is available for the velocity measurement, and the application of UDV method to the gas lifting in KYLIN loop will be achieved in future.

Key words: Liquid metal facilities; UDV; Velocity profile

Corresponding Author:

Author Name: Jian He

E-mail Address: jian.he@fds.org.cn

Organization: Institute of Nuclear Energy Safety Technology, Chinese Academy of Sciences
City, State, Country: P.O Box 1126, Hefei, Anhui, 230031, China

Telephone Number: +86-551-5592123

Fax Number: +86-551-5591397

Flow patterns induced by a bubble screen in a sharply curved flume based on Acoustic Doppler Velocity Profiler measurements

Violaine Dugué, Koen Blanckaert and Anton J. Schleiss

Laboratory of Hydraulic Constructions (LCH), Ecole Polytechnique Fédérale de Lausanne (EPFL), CH-1015 Lausanne, Switzerland.

Addresses: violaine.dugue@epfl.ch, koen.blanckaert@epfl.ch, anton.schleiss@epfl.ch

Koen Blanckaert

State Key, Laboratory of Urban and Regional Ecology, Research Center for Eco-Environmental Sciences, Chinese Academy of Sciences, Beijing, China.

Open-channel bends are characterized by a bed morphology where erosion occurs near the outer bank and a point bar develops at the inner bend. This morphology is induced by complex interactions between the streamwise flow, the curvature-induced secondary flow and the bed topography. Several techniques already exist to counteract the development of bend scour, which can endanger foundations of structures. However, existing techniques mostly imply substantial construction works in the river. Preliminary laboratory experiments have shown that a porous tube placed near the outer bank can generate a bubble screen that modifies the flow patterns and leads to a substantial reduction of the bend scour. A better understanding of the hydrodynamic mechanisms induced by the bubble screen and involved in the morphological development will allow determining the range of application of the bubble-screen technique. Experiments performed in a sharply curved open-channel bend under live-bed conditions show that the bubble screen is able to redistribute the velocity patterns in the bend. The bed morphology is then partially modified, specially at the bend exit. This paper illustrates Acoustic Doppler Velocity Profiler measurements of the bubble-induced secondary flow and its interaction with the channel base flow in the most influenced cross-section.

Keywords: ADVP, Bubble screen, Erosion, Scour, Morphodynamics, Open-channel bends

1 INTRODUCTION

Open-channel bends are characterized by strong interactions between the streamwise flow, the curvature-induced secondary flow and the bed morphology. This interplay leads to the development of a typical bar-pool bed topography [1]. Outer banks are vulnerable to scour whereas sediment deposition occurs at the inner bank and may reduce the navigable width.

Several techniques to counteract the development of the typical bar-pool bed morphology, such as bottom vanes [2] or a fixed outer bank layer [3] have already been studied and applied. However, most of them imply substantial construction works in rivers. Previous experiments performed in a sharply curved laboratory channel at LCH-EPFL have shown that a porous tube placed near the outer bank can generate a bubble screen strong enough to redistribute the velocity patterns on a fixed horizontal bed [4] and can even modify the bed morphology and avoid bend scour on a mobile bed under clear-water scour conditions [5].

Similar experiments have been performed in the same sharply curved flume under live-bed conditions with and without the bubble screen in order to give insights in the underlying flow mechanisms involved in both cases. Comparisons of the bed morphology are provided in order to determine the efficiency of the technique. Velocity

measurements performed with an Acoustic Doppler Velocity Profiler (ADVP) are provided in one cross-section where the morphological impact of the bubble screen was found to be the strongest.

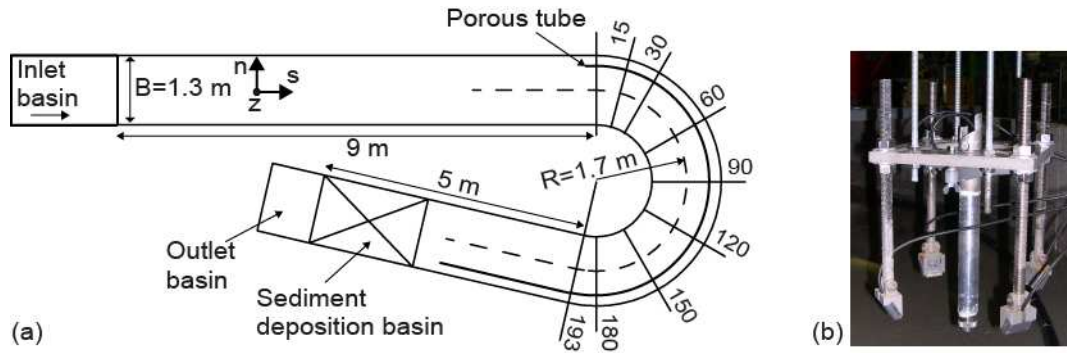
2 EXPERIMENTAL SET-UP

2.1 Experimental set-up

Experiments were performed in a sharply curved laboratory flume of constant width $B = 1.3$ m that consists of a 9 m long upstream straight reach, followed by a 193° bend with a constant centerline radius of curvature $R = 1.7$ m and finished by a 5 m long downstream straight reach (Figure 1a). The sediment used was uniform quartz sand with a mean diameter $d = 0.002$ m.

A curvilinear reference system (s, n, z) was adopted where s represents the streamwise direction, the transverse n -axis point in the outward direction and the vertical z -axis in the upward direction.

The bubble screen was generated by means of a porous tube placed at 0.2 m from the outer bank starting 0.2 m before the entry of the bend. It was connected at both ends to a pressurized air circuit in order to have a quasi-uniform bubble generation along the entire length of the porous tube. The air pressure was controlled by means of a manometer and the air discharge was measured with a rotameter.



	Q	q_s	Pa	H	U	R/B	R/H	B/H
Label	[l/s]	[kg/(m.s)]	[kPa]	[m]	[m/s]	[-]	[-]	[-]
LB_NB	75	0.025	-	0.14	0.41	1.31	12.1	9.2
LB_B	75	0.025	600	0.14	0.41	1.31	12.1	9.2

Figure 1: (a) Plan view of the curved channel with the porous tube. (b) Acoustic Doppler Velocity Profiler (ADVP). Experimental conditions (Q is the water discharge, q_s is the sediment discharge, Pa is the chosen air-pressure, H is the final flume-averaged flow depth, U is the flume-averaged velocity ($U = Q/BH$), In the labels, LB stands for live-bed, NB for no bubble screen, and B for bubble screen experiments)

2.2 Instrumentation

Flow characteristics were measured in several cross-sections around the bend by means of an Acoustic Doppler Velocity Profiler (Figure 1b). The ADVP, developed at EPFL, consists of a central emitter surrounded by 4 receivers and measures the quasi-instantaneous velocity vector along an entire profile. From these measurements, the mean velocity vector with its three components (v_s, v_n, v_z) can be obtained as well as the bed elevation. A detailed description of the working principle of the ADVP and its experimental accuracy can be found in literature [1, 6-8].

Due to constraints imposed by the size of the ADVP, velocity profiles were measured every 0.05 m only in the range $n = -0.45 \text{ m}$ to $n = 0.45 \text{ m}$ in the reference experiment and in the range $n = -0.45 \text{ m}$ to $n = 0.4 \text{ m}$ when using the bubble screen. Indeed, velocity measurements were not possible near the bubble screen because the bubbles interfered with the acoustic signal of the ADVP.

The bed morphology was measured with a laser distometer on a refined grid.

2.3 Experimental conditions

Main hydraulic and air parameters are summarized in Figure 1.

Two experiments have been performed under similar hydraulic and sediment conditions. The reference experiment LB_NB was performed without the porous tube and the bubble screen whereas the bubble screen LB_B experiment was performed with the porous tube and the bubble screen.

For both experiments, the bed was initially flat.

Experiments were then performed under live-bed conditions with constant sediment feeding at the entrance of the flume ($q_s = 0.025 \text{ kg/(m.s)}$) until morphological equilibrium was achieved.

3 RESULTS

3.1 Influence of the bubble screen on the bed morphology

Figure 2 illustrates the final bed morphology for the two experiments. The bed reference level for each experiment ($z = 0 \text{ m}$) coincides with the flume-averaged bed level.

The streamwise evolution of the transverse bed slope (Figure 2a) indicates two deep scour holes in the LB_NB experiments located in the cross-sections at 90° and 180° in the bend, as found in literature [1, 3]. The existence of these two scour holes is related to the sudden change of curvature at the entry and the exit of the bend.

In the LB_B experiment, the first scour hole is as deep as in the reference experiment. However, the second scour hole due to the disappearance of curvature is strongly reduced by the influence of the bubble screen.

The bubble screen influence is further illustrated in Figures 2b and c where the water surface and bed elevations in two cross-sections at 90° and 180° in the bend are represented. In the cross-section at 90° , only small differences in the bed morphology can be observed and are due to mesoscale bedforms migration.

However, in the cross-section at 180° , the bed has been substantially modified under the influence of

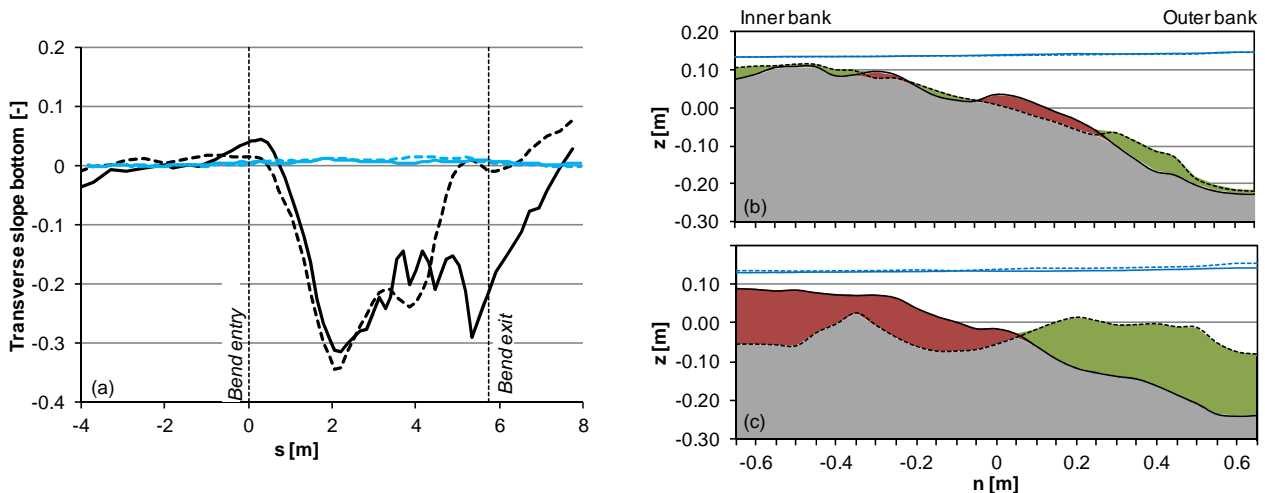


Figure 2: Morphological comparison of the reference (full line) and the bubble screen (dotted line) experiments (a) Streamwise evolution of the transverse bed slope around the flume and bed and water surface elevations in the cross-section at 90° (b) and at 180° (c) in the bend. Red and green areas represents respectively erosion and deposition in comparison with the reference morphology without the bubble screen.

the bubble screen. Deposition near the outer bank and erosion of the bar at the inner bank lead to a more regular profile in the cross-section.

3.2 Influence of the bubble screen on the flow field

In order to explain the strong morphological difference induced by the bubble screen in the cross-section at 180° in the bend, the flow field measured with ADVP is shown in Figure 3. The three velocity components, as well as water surface and bed elevations are reported for the two experiments.

In the reference LB_NB experiment (Figure 3a), a pronounced transverse slope can be observed with a deep scour hole near the outer bank. Maximum streamwise velocities are located near the water surface and in the outer part of the cross-section. A secondary flow with strong outwards velocities near the water surface and inwards velocities near the bed can also be observed. Small downward velocities are located in the middle of the cross-section but the core of maximal downwards velocities is supposed to be located very near the outer bank due to mass conservation in the secondary flow cell. Also the core of maximum streamwise velocities is supposed to be located near the outer bank outside the measuring grid.

In the bubble screen LB_B experiment (Figure 3b), the bed morphology is flatter with three small scour holes located near each bank and at $n = -0.05$ m. The scour hole at the outer bank is supposed to be due to the outer bubble-induced secondary flow located between the porous tube and the bank. The scour hole located at the middle of the cross-section is due to the inner bubble-induced secondary flow. Indeed, inwards velocities are observed near the

water surface between the position of the porous tube ($n = 0.45$ m) and the position of the scour hole ($n = -0.05$ m) which is also characterized by maximum downward velocities. Outwards velocities are located near the bed.

The core of maximum streamwise velocities is observed from $n = 0$ m to the outer bank with a maximum value of 0.6 m/s. Low streamwise velocities not sufficient to enhance sediment transport are observed in the inner part of the cross-section. As a result, the bed remains almost horizontal in this location.

These observations confirm that the bubble screen can generate a secondary flow that can modify the base flow distribution and consequently have an effect on the bed morphology under live-bed conditions.

5 CONCLUSION

This paper compared ADVP measurements of the flow obtained in the same cross-section of an open-channel bend in a reference experiment and in an experiment involving an air-bubble screen placed near the outer bank. Velocities measurements have shown that the bend natural flow can be fundamentally modified by the bubble-induced secondary flow. In the cross-section at 180° in the bend, the core of maximum downward velocities has been shifted from near the outer bank to the middle of the cross-section, resulting in a flatter bed profile and a reduction of the outer bank scour hole.

The capabilities of an Acoustic Doppler Velocity Profiler (ADVP) in the investigation of flow structures induced by a bubble screen in a curved open-channel flow are highlighted in the present paper.

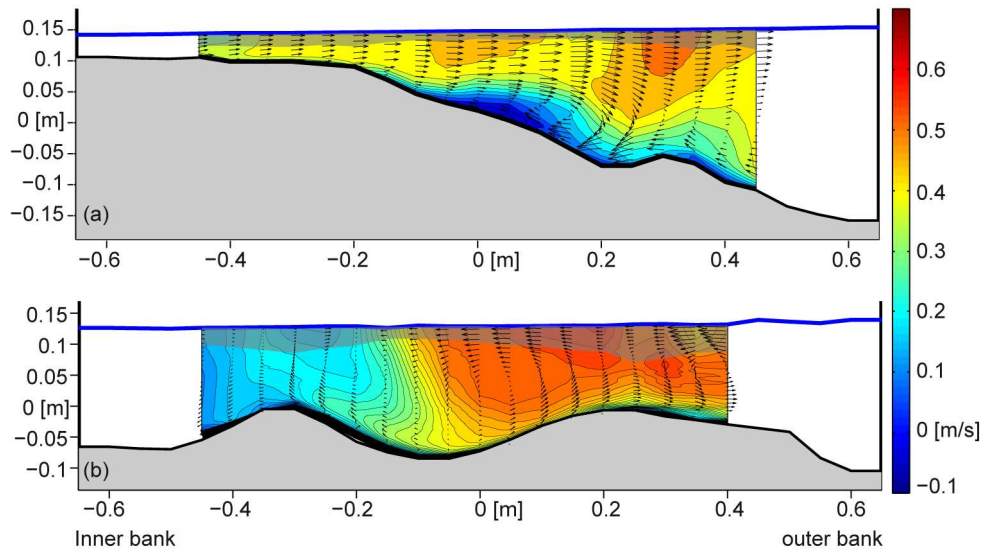


Figure 3: Downstream view of the mean streamwise flow velocities v_s (contours) and cross-sectional velocities v_n, v_z (vectors) in the cross-section at 180° in the bend for the reference LB_NB experiment (a) and for the bubble screen LB_B experiment (b). The bed elevation has been estimated from ADV measurements (thick black line) and from the laser distometer measurements (thin black line). The shaded area near the water surface indicates extrapolated values.

6 ACKNOWLEDGMENT

This research was financially supported by the Swiss National Science Foundation under grants 200021-125095. The second author was partially funded by the Chinese Academy of Sciences Visiting Professorship for Senior International Scientists, grant number 2011T2Z24, and by the Sino-Swiss Science and Technology Cooperation for the Institutional Partnership Project, grant number IP13_092911.

REFERENCES

- [1] Blanckaert, K.: Topographic steering flow recirculation, velocity distribution, and bed topography in sharp meander bends. *Water Resources Research*, 46, W09506, doi:10.1029/2009WR008303.
- [2] Odgaard, A. J., Spoljaric, A.: Sediment control by submerged vanes. *Journal of Hydraulic Engineering-ASCE*, 112 (1986) 1164-1181.
- [3] Roca, M. et al.: Reduction of bend scour by an outer bank footing: Footing design and bed topography. *Journal of Hydraulic Engineering-ASCE*, 133 (2007) 139-147.
- [4] Blanckaert, K. et al.: Redistribution of velocity and bed-shear stress in straight and curved open-channels by means of a bubble screen: Laboratory experiments. *Journal of Hydraulic Engineering-ASCE*, 134 (2008) 184-195.
- [5] Dugué, V. et al.: Reduction of bend scour with an air-bubble screen: Morphology and flow patterns. *International Journal of Sediment Research*, (in press) (2012).
- [6] Lemmin, U., Rolland, T.: Acoustic velocity profiler for laboratory and field studies. *Journal of Hydraulic Engineering-ASCE*, 123 (1997) 1089-1098.
- [7] Hurther, D., Lemmin, U.: A constant-beam-width-transducer for 3D acoustic Doppler profile measurements in open-channel flows. *Measurement Science and Technology*, 9 (1998) 1706-1714.

- [8] Blanckaert, K., Lemmin, U.: Means of noise reduction in acoustic turbulence measurements. *Journal of Hydraulic Research*, 44 (2006) 3-17.

A Very Low Velocity Measurement Using Ultrasonic Velocimetry

Tomonori Ihara, Hiroshige Kikura, Yasushi Takeda

Research Laboratory for Nuclear Reactors, Tokyo Institute of Technology, N1-7, 2-12-1 Ookayama,
Meguro-ku, Tokyo, 152-8550, Japan

Address: ihara@us.nr.titech.ac.jp

In order to measure a very low velocity using UVP, the conventional algorithm of signal processing could not be applied because of the lower velocity limitation. Recently, phase difference method was proposed to overcome this limitation. However, the characteristics of this method are not yet fully investigated, and we studied them in this paper. Firstly, a measurement system was constructed using digital signal processing technique. Secondly, measurement limitation of the system at a very low velocity was investigated using wall-reflected signals. Finally, real time profile measurement was demonstrated with the flow in a rotating cylinder, and measurement accuracy was also discussed.

Keywords: Very Slow Flow, Phase Difference Method, Accuracy Verification

1 INTRODUCTION

Isolation of High Level Radioactive Wastes (HLWs) from biosphere and its disposition in a deep geological repository is an urgent problem and vitrification technique of HLW has to be improved in the industrial scale. This vitrification melter is operated with internal Joule-heat generation, and the temperature of glass exceeds 1000°C. For understanding a thermal hydraulics behavior of the vitrification melter, experimental technique has to be invented. Several velocity measurement techniques such as PIV/PTV, LDA had been developed. However, because of high temperature and opaqueness, these techniques cannot be applied for glass melts. To overcome these difficulties, we focused ourselves on UVP technique[1]. Realization of such a technique has difficulties in two fold; high temperature and very low velocity. We already demonstrated ultrasonic measurement technique inside glass melts employing buffer-rod [2]. In this paper, we present a system developed to measure an extremely low velocity flow.

Many methods have been presented to calculate velocity from pulsed-echo signals, and most widely-used method is Doppler frequency determination technique. In this technique, FFT or Zero-crossing counter is often used to estimate Doppler-shift frequency from echo sequence (typically, a number of repetition pulses is over 100.). Recently, the phase difference method was proposed for a low velocity measurement [3-4]. This technique detects the phase of the ultrasonic carrier frequency directly from the echo signal, and determines its difference between two successive echo receptions. Then, velocity is calculated from the phase difference. Since this technique basically needs only two times of echo reception, it can provide a higher temporal resolution than conventional methods. However, the low limit of speed by this method is not fully investigated.

2 IMPLEMENTATION

In this section, velocity calculation procedures of conventional method and phase difference method are described. FFT based method [5] is employed as a conventional method, and compared with phase difference method in this work. All signal processing were performed digitally on LabVIEW.

2.1 FFT Based Doppler Method

Fig.1 shows a schematic block diagram of this FFT method. The procedure can be divided into 2 parts; quadrature demodulation and frequency analysis. In the diagram, digitized echo signal is expressed as d_{ij} where the subscript i denotes channel index, and j denotes repetition index. In order to distinguish the Doppler signal, echo signals of each channel are demodulated to in-phase and quadrature phase with reference signal, which has the same center frequency f_0 as the transmitted signal. After complex FFT is carried out for each phase, power spectra of forward direction and backward direction are obtained as P_f and P_b respectively. Finally, the Doppler-shift frequency f_{Di} and flow direction are determined by their peak value. Therefore, flow velocity V_i is calculated as Eq. (1).

$$V_i = \frac{f_{Di}}{2f_0} c \quad (1)$$

where c is sound speed in the fluid. Because a spectrum is calculated at discrete points, velocity values have limitations as follows:

$$V_{\max} = \frac{f_{PRF}}{4f_0} c \quad (2)$$

$$V_{\text{step}} = \frac{f_{PRF}}{N_j f_0} c \quad (3)$$

where f_{PRF} is a pulse repetition frequency, and N_j is a number of pulse emissions. Practically, the peak of

the spectra is calculated from three point Gaussian curve fitting to improve the velocity resolution. Nevertheless, this V_{step} could be equal to the lower velocity limitation.

Since this technique does not require high speed ADC, it has been widely used. However, there is a trade-off relationship between temporal and velocity resolutions depending on N_j . The temporal resolution ΔT can be expressed as Eq. (4).

$$\Delta T = \frac{N_j}{f_{PRF}} \quad (4)$$

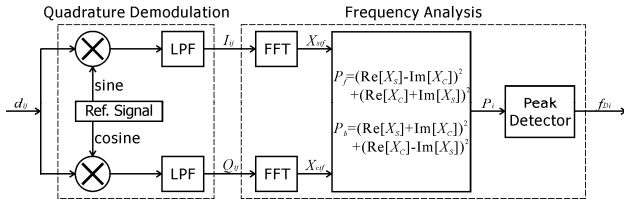


Figure 1: Schematic block diagram of FFT based Doppler method.

2.2 Phase Difference Method

Fig.2 shows a schematic block diagram of this method. The echo signal is sampled with ADC which has more than twice higher sampling rate than center frequency of the emission pulse to fulfill Nyquist theorem, and consequently each channel has many sampled values. In the diagram, the subscript k is added sampling index, and signal is expressed as d_{ijk} . In order to calculate the phase of the signal, complex FFT function X_{ijf} is computed where f is the frequency index. From conjugate complex product of two successive functions, phase difference $\Delta\theta$ is obtained. Therefore, flow velocity V_{ij} is calculated as Eq. (5).

$$V_{ij} = \frac{f_{PRF}}{4\pi f_0} c \cdot \Delta\theta_{ij} \quad (5)$$

For calculating the velocity, the number which indicates the center frequency f_0 is usually selected as frequency index f . If they are not equal, an estimated phase has a leakage induced error [6].

Since this technique can calculate velocity from two echoes, the temporal resolution of this method can be expressed as Eq. (6).

$$\Delta T = \frac{2}{f_{PRF}} \quad (6)$$

As for V_{max} , it is equal to Eq. (2) because the range of $\Delta\theta$ remains between $-\pi$ and π .

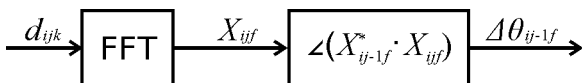


Figure 2: Schematic block diagram of phase difference method.

3 VERIFICATIONS OF LOW LIMIT OF MEASUREMENT SPEED

3.1 Configuration

To examine the low limit speed of phase difference method, a wall-reflected echo signal was used. Fig.3 shows a schematic illustration of the experimental setup. A PZT composite transducer, which has a center frequency of 2MHz and an element diameter of 20mm (2k20N, Japan Probe Co., Ltd), was immersed in a water of 30°C and fixed on the stage. Measurement axis is perpendicular to the wall. The stage moves toward the wall at a constant speed. Motion speeds are controlled by PC from 0.0012 to 5 mm/s. To discriminate the echoes from front-wall and back-wall, the reflector acrylic block has a thickness of 100mm. A pulser/receiver (JPR-10CN, Japan Probe Co. Ltd) was used to generate the ultrasonic tone burst pulse and to receive the echo signal. The signal is sampled by the digitizer (PXI-5105, National Instruments Inc.).

Tab.1 shows measurement configuration. Applied voltage and gain is chosen such that echo amplitude from the wall is almost equal to the full scale of digitizer input range. During the transducer motion at a constant speed, 7680 reputational waveforms are stored. Velocity calculations are performed off-line using the same signal data to evaluate the difference of signal processing method between FFT method and phase difference method. With FFT method, one velocity profile is calculated from 128 waveforms and hence 60 profiles are obtained. The mid-point of each channel is used to calculate FFT signal. As phase difference method needs two waveforms for calculation, 7679 profiles are obtained. Erroneous velocity information is also included in the profile, which is caused by multipath reflections between wall and transducer, or inside wall. To remove these errors, a velocity is extracted from those whose original signal amplitude is higher than 80% in full scale. Therefore, measured velocities are determined from ensemble average of these profiles.

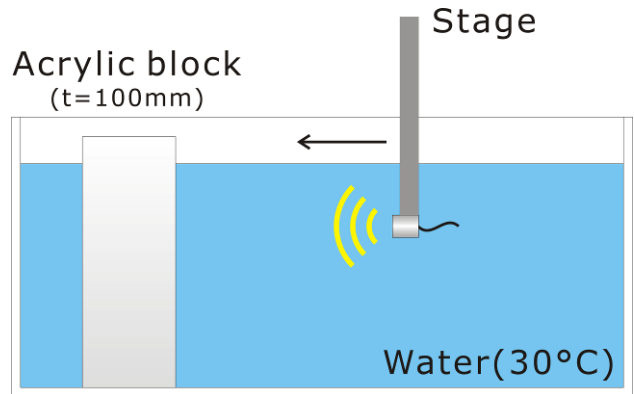


Figure 3: Schematic illustration of experimental setup

Table 1: Signal collection configuration

Pulser/Receiver	
Basic Frequency f_0	2MHz
Pulse Repetition Frequency f_{PRF}	100,500,1000Hz
Burst Cycle	8
Applied Voltage	50V
Gain	+40dB
Digitizer	
Sampling Speed	60MS/s
Number of Channels N_i	140chs
Number of Repetitions N_j	128
Number of Samples N_k	60/ch
Number of Stored Signals	7680
AD bit lengths	12bits
Vertical Input Range	1V

3.2 Results and Discussion

Figs. 4-6 show measured results of phase difference method and FFT method in different PRF. Vertical broken lines indicate the lower velocity limit of FFT method which is derived from Eq. (3). Equivalent phase difference is given at the top.

Measurement errors of FFT method remained under 10% when the motion speed is over half of their lower limits, and yet errors became bigger. From this result, we conclude that Gaussian interpolation improved velocity accuracy, but it was not sufficient to measure a sub mm/s velocity.

On the other hand, the error of phase difference method remains under 10% down to ca. 10^{-2} mm/s in Fig. 4. As shown in the other figures, it can be concluded that overall accuracy was within 10% when phase difference is over 10^{-3} rad. This might be an effective limit with this setup. As we used the 12bits digitizer, phase resolution can be considered as 1.5×10^{-3} rad., and it shows good agreement with the experiment. It indicates that one needs to use slower pulse repetition or a digitizer having higher resolution for improving the measurement accuracy.

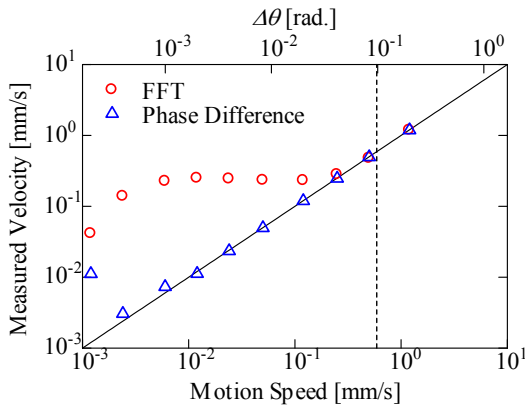


Figure 4: Measured velocity versus motion speed for FFT method and phase difference method ($f_{PRF}=100$ Hz)

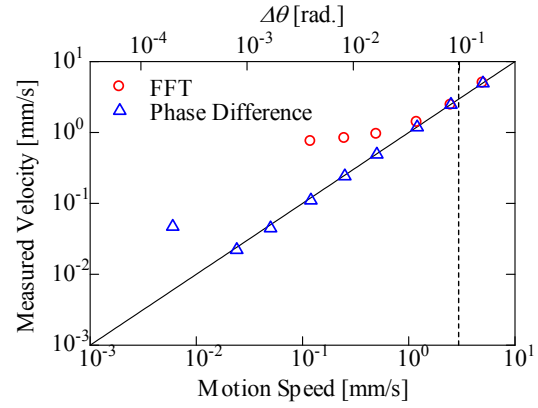


Figure 5: Measured velocity versus motion speed for FFT method and phase difference method ($f_{PRF}=500$ Hz)

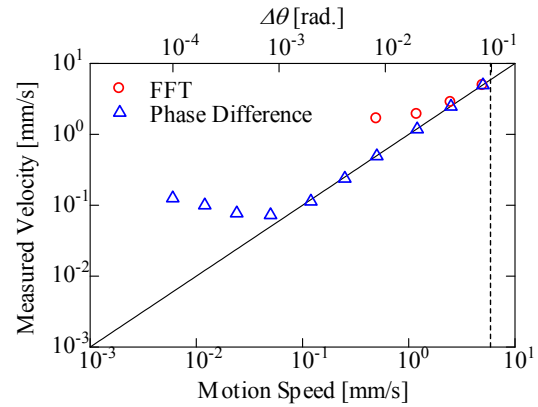


Figure 6: Measured velocity versus motion speed for FFT method and phase difference method ($f_{PRF}=1000$ Hz)

4 FLOW MEASUREMENTS INSIDE A ROTATING CYLINDER

4.1 Configuration

We constructed an UVP system employing phase difference method. In this section, flow measurement using tracer particle inside a rotating cylinder is demonstrated using phase difference method. Fig. 7 shows schematic of experimental set up. The acrylic rotating cylinder has an outer diameter of 160mm and a wall thickness of 3mm. The cylinder is set up in the water tank and its temperature is controlled to 30°C. Nylon 12 particle (WS-200P, Daicel-Evonik Ltd.; an average size is 80 μ m, and specific density is 1.02) is used as the tracer particle. To match the tracer and fluid density, 10wt% glycerol/water solution is filled inside the cylinder, and its sound speed was 1550 m/s. The stepping motor is mounted underneath the tank and drives the cylinder directly. Ultrasonic transducer of 4MHz basic frequency and 5mm element diameter is fixed at the position $L = 2.5$ mm in Fig. 7. The same pulser/receiver and the digitizer were employed as the previous chapter. Pulse repetition frequency (f_{PRF}) is fixed to 500Hz, applied voltage is 100V, and burst cycle is 4 times. Echo signals are sampled with 20MHz and number of samples N_k is

20 for each channel and total channel number N_i is 240. Vertical input range is 200mV. Other parameters are the same in Tab. 1.

Although the minimum temporal resolution of phase difference method can be described as Eq. (6), it is limited by bottlenecks such as data transfer (bandwidth) from digitizer to PC, computation speed. To realize real time measurement, several successive signals are processed to calculate a velocity profile and the next acquisition and transfer must wait for the previous calculation. So, signals between their processing will be discarded. In this experiment, we used 128 repetitional signals for each profile calculation (duration is 64 μ s) and total processing times between profiles were ca. 280 μ s. using core i5 M460 (2.53GHz) PC.

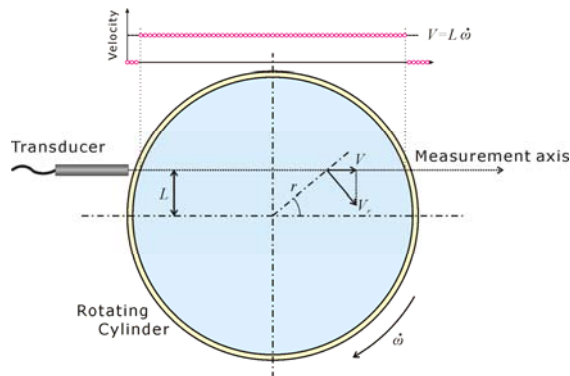


Figure 7: Schematic illustration of rotating cylinder, transducer position, and ideal measurement result for steady rigid-body flow.

4.2 Results and Discussion

Fig. 8 shows a color density plot of the measured results when the cylinder starts rotation by 30rpm. As shown in the plot, in the near-wall region fluid is accelerated by the shear stress by the container at $t=0$. Velocities become constant along the fluid region like Fig. 7 as the stress diffuses to the center. We could confirm that phase difference method can be applied to observe the transient behaviour quite well from this result.

Fig. 9 shows an averaged velocity profile between $t=200-300$ s. Although velocities of the far half seem to contain some error because signal is disturbed by multiple reflections inside the container, measurement errors of the front half were less than 5% from the theoretical value.

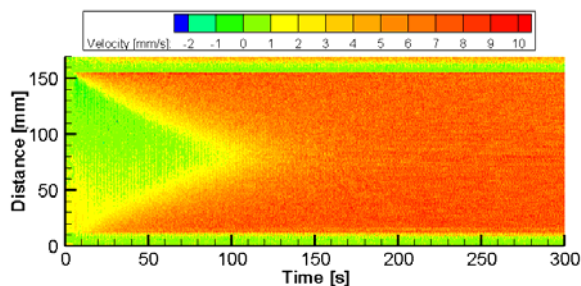


Figure 8: Measured flow map inside the spinning-up rotating cylinder.

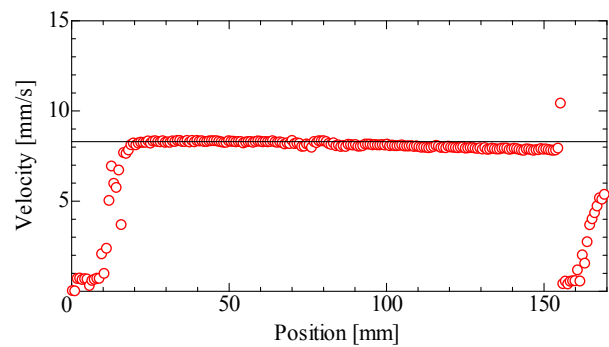


Figure 9: Averaged velocity profile after the flow is fully developed.

5 SUMMARY

The verification and application of phase difference method were demonstrated in this paper. The real time measurement system was also constructed employing pulser/receiver, high speed digitizer, and signal processing on LabVIEW.

Using a wall-reflected echo, we validated the measurement accuracy of the velocity values by the phase difference method down around 1 μ m/s. As a result, it was concluded that overall accuracy was within 10% when phase difference is over 10-3 rad., which is lower than conventional method by one order of magnitude.

A flow inside a rotating cylinder was also measured. It showed good performance of phase difference method for measuring the velocity profile using an echo signal from tracer particle. The flow measurement accuracy is also discussed, and its error was less than 5%.

Other measurement result will be also presented in the presentation.

REFERENCES

- [1] Takeda Y: Measurement of velocity profile of mercury flow by ultrasound Doppler shift method, Nucl. Technol. 79 (1987), 120-124.
- [2] Ihara T., Kikura H. et al.: Ultrasound characteristics in high-temperature fluid, Proc. 8th ASME-JSME Therm. Eng. Joint Conf. (2011-3), AJTEC2011-44243.
- [3] Kitaura H., Tadada Y., et al.: A new algorithm for low velocity measurement by UVP, Proc. 4th ISUD, (2004-9), 121-124.
- [4] Ihara T., Kikura H. et al.: The study of measurement for a very slow flow using phase difference method, IEICE Technical Report 112 (2012), 7-11 (in Japanese).
- [5] Aydin N. and Evans D.H.: Implementation of directional Doppler techniques using a digital signal processor, Med. Biol. Eng. Comput. 32 (1994), 157-164.
- [6] Dishan H.: Phase error in fast Fourier transform analysis, Mech. Sys. Sig. Proc. 9 (1995), 113-118.

Investigation of slurry flows in rectangular pressurized pipe flow by means of ultrasonic velocimetry

Vojtěch Bareš¹, Tomáš Pícek², Jan Krupička², Jan Brabec² and Václav Matoušek²

¹Department of Sanitary and Ecological Engineering, ²Department of Hydraulics and Hydrology, Czech Technical University in Prague, Thákurova 7, 166 29 Praha 6, Czech Republic

Ultrasonic velocimetry was used to study flow and turbulence characteristics in both clear water and slurry flows with different sediment transport regimes. The velocity and turbulence profiles were investigated in the vertical plane at the centreline of a rectangular channel. Reference measurements in clear water delivered the vertical distribution of velocity components and turbulence characteristics in rectangular cross section. Strong symmetrical secondary currents were observed and evaluated. Those flow structures affect the velocity and the Reynolds stress vertical distribution as presented. Experiments with solid particles provided the information about the influence of solids concentration on flow and turbulence properties at different transport regimes. An attenuation of the velocity fluctuation with increasing solids concentration was observed. A critical aspect of experiments seems to be an attenuation of ultrasonic signal by solid particles especially at higher concentration rates.

Keywords: Pressurized flow; Reynolds stress; slurry flow; ultrasonic velocimetry; velocity distribution

1 INTRODUCTION

Intense sediment transport at high bed shear is a phenomenon associated with flows in open mobile-bed channels and pressurized industrial slurry pipes. For instance, flood flows in steep mountain streams can carry sediments at high concentration over the upper plane bed. Lately, increasing research attention has been focused to high concentrated flows in natural channels [1-3] and laboratory conduits. The well-controlled laboratory flows have been subject to both mathematical [4-5] and physical modelling in either steep flumes [5-6] or pipe loops [7-8].

Investigation of slurry flows by means of velocity and turbulence measurements is mostly associated with acoustic methods while the applicability of the optical methods such as Laser Doppler anemometry or Particle Image Velocimetry is difficult or impossible [9]. Most of experiments with suspensions in pipe loops based on ultrasonic velocimetry were conducted with non-Newtonian systems [10-11].

The paper deals with a Newtonian system in turbulent flow regime with the uniform particle size phase of glass spheres and a wide range of solids concentrations.

2 METHODS

2.1 Experimental loop

Experiments were carried out on a closed pipeline circuit (Fig. 1) placed in the Water Engineering Laboratory of the Czech Technical University in Prague. Differential pressures were measured on sections 1, 2 and 3. Differential pressures in the upward pipe (section 1) and in the downward pipe (section 2) were measured in order to determine the

density of flowing mixture (and thereafter concentration of the solid phase in the mixture). The differential pressures measured in Section 3 were used for determination of the hydraulic gradient in the horizontal plexiglass pipe of a rectangular cross section (of length 6 m, inner width 50.8 mm, inner height 51.6 mm). The flowrate was measured using an electromagnetic flow meter Krohne Optiflux 5000 installed at the vertical pipe. The flow of the mixture was obtained by a centrifugal pump. The speed of pump was smoothly regulated by a frequency converter. The temperature of the mixture was measured to determine of its viscosity and density. Data from all differential pressure transmitters, flow meter and thermometer were collected by an electronic data acquisition system. Besides the electronically collected data, the thickness of sediment deposits in the horizontal transparent plexiglass section was measured manually.

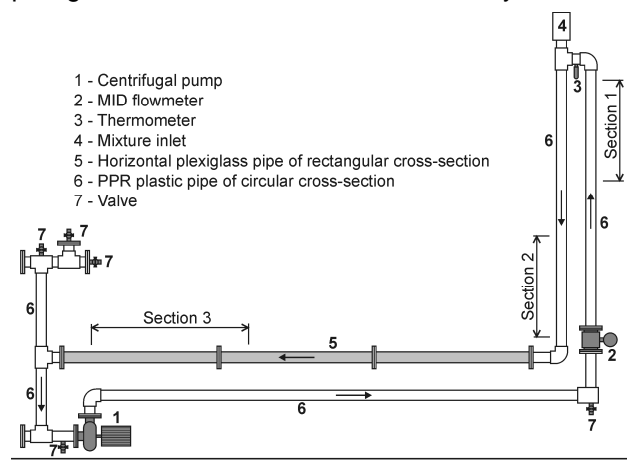


Figure 1: Scheme of experimental loop.

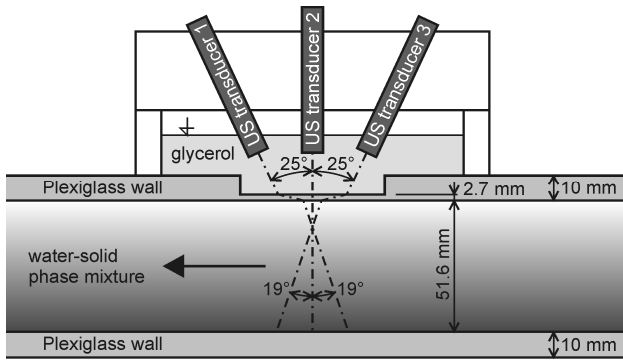


Figure 2: Arrangement of US transducers on the plexiglass pipe of rectangular cross section.

2.2 Velocity and turbulence measurements

Instantaneous velocity profiles were measured using Ultrasonic Velocity Profile (UVP) monitor (Met-Flow SA) in the vertical longitudinal plane passing through the centre in Section 3. US transducers of basic frequencies of 4 MHz, 2 MHz and 1 MHz were used in dependence on the mixture concentration and the velocity magnitude of the mixture. For higher concentrations of the solid phase lower basic frequencies were used. Sampling frequency was kept at constant level of 20 Hz ($\Delta t = 50$ ms) for all experiments and the full range of basic frequencies.

Three various positions of the probes were used (Fig. 2). Transducers angle to the main flow's normal (transducer 1 and 3) was 25° . However, the resulting active angle was estimated by 19° due to different acoustic impedance of glycerol and water. The velocity was decomposed under the same assumptions as in previous studies [12-13]. Thus, the point time-averaged quantities of the longitudinal and the vertical velocity and the Reynolds stress can be expressed as follows:

$$\bar{u} = \frac{\bar{V}_{R1} - \bar{V}_{R3}}{2 \sin \alpha} \quad (1)$$

$$\bar{v} = \frac{\bar{V}_{R1} + \bar{V}_{R3}}{2 \cos \alpha} \quad (2)$$

$$-\overline{u'v'} = -\frac{\overline{V'_{R1}} - \overline{V'_{R3}}}{2 \sin 2\alpha} \quad (3)$$

where V_R are radial components measured by individual transducers 1 – 3.

2.3 Flow conditions, sediment transport modes and solid phase characteristics

A wide range of flow conditions was simulated in the experimental track. An average velocity in the cross section varied from 0.2 to 3.5 m/s. Reynolds numbers Re in clear water flows were between 1.6×10^4 - 1.0×10^5 , Re in slurry flows was of a magnitude smaller. The volumetric concentration varied from 5 to 40%, which is given by volume of the solid phase and fluid in the experimental loop. Flow conditions and volumetric concentration naturally influence a delivered concentration which

was measured continuously during each experiment (range of $c_{vd} = 3 - 29\%$). Those data are consistent with the mode of slurry flows – upper plane bed (UPB), stratified flow (SF) and heterogeneous flow (HF). A stable plane bed with intense sediment transport upwards with a high concentration gradient is a typical characteristic of the UPB regime. The nature of SF flows is similar, however all particles are in motion. The time-averaged suspension concentration is considered to be quasi-constant in HF flow runs (Fig. 3).

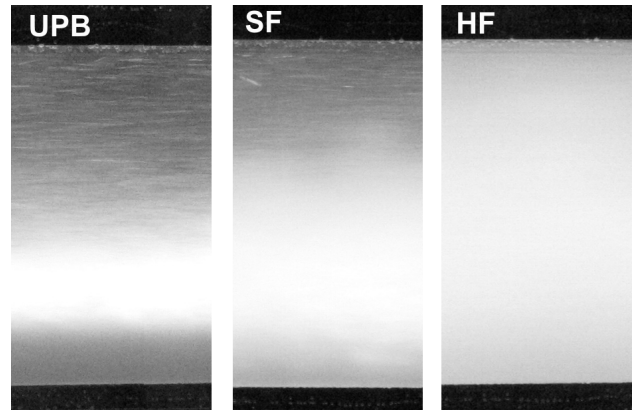


Figure 3: Visual comparison of studied transport regimes.

The tested granular fraction was an industrial ballotini (fraction B134, PRECIOSA) that is relatively narrow graded ($d_{15} = 0.16$ mm, $d_{50} = 0.18$ mm, $d_{85} = 0.24$ mm) and has the density similar to natural sands and gravels (2450 kg/m³). Our tests determined the sediment properties mentioned above and the settling velocity of the sediment, $w_s \approx 18$ mm/s. Hence, the ballotini particle Reynolds number was $Re_p \approx 3.2$.

3 RESULTS

3.1 Clear water flows

The reference measurements of clear water turbulent flows delivered the vertical distribution of velocity components and turbulence characteristics. All experiments were carried out in smooth flow regime with $Re = 1.6 \times 10^4 - 1.0 \times 10^5$. Time-averaged longitudinal velocity profiles for different flow conditions are presented in Fig. 4. A symmetrical distribution with maxima in the centre of the rectangular duct can be observed. Comparing the shape of the distribution with theoretical models significant differences can be seen (Fig. 5). That can be explained by symmetrical secondary currents with vertical components oriented from walls to the center of the pipe. Those findings correspond well with the findings of Knight and Patel [14] who described secondary currents in rectangular ducts.

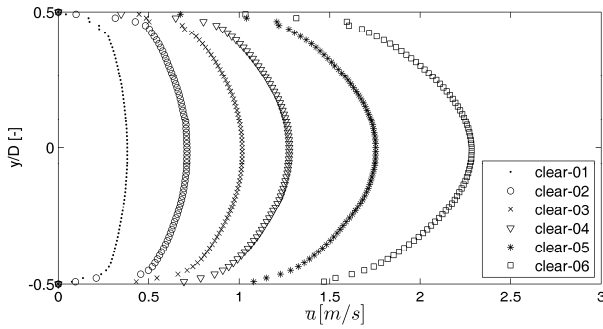


Figure 4: Vertical velocity distribution of time-averaged longitudinal components.

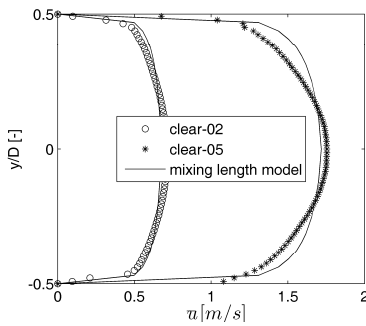


Figure 5: Comparison of measured and theoretical velocity distribution.

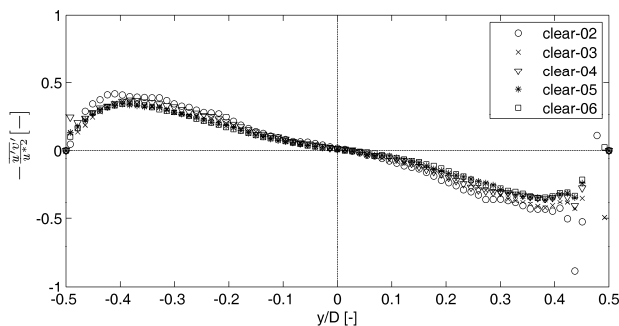


Figure 6: Normalized Reynolds stress distribution for $Re = 2.9 \times 10^4 - 1.0 \times 10^5$.

Theoretically, the normalized vertical distribution of Reynolds stress should be a linear function of flow depth with absolute maxima (± 1.0) near the pipe walls and zero values at the centerline. Fig. 6 presents measured data sets for different flow conditions. The wall boundary shear tends to be round 50% of the shear given by the energy grade line i_e and hydraulic radius as $u_*^2 = gRi_e$. Such difference can be hardly explained by secondary currents as the vertical velocity components are about 1% of the average cross section velocity. Knight and Patel [14] reported a maximal decrease of the Reynolds stress to be 10% compared to the averaged shear rate along the wetted perimeter of pipe cross section.

3.2 Slurry flows

We present only results obtained in SF and HF

transport modes as a concentration gradient above the plane bed in UPB mode is similar to SF transport mode. Typical normalized velocity and Reynolds stress distributions are presented in Fig. 7 (SF mode) and Fig. 8 (HF mode).

In SF mode the velocity distribution is affected by the varying concentration along the vertical. The maximal velocity is located in the upper part of the pipe with a lower concentration. The higher concentration of particles in the lower section results in a higher friction and velocity decrease. Higher concentration gradient results in a stronger asymmetry of the velocity profile.

Velocity data correspond well with the Reynolds stress distribution. The maximal velocity and zero Reynolds stress occurs at the same flow depth y/D . The maximal values of Reynolds stress are reported near by the top wall and the bed.

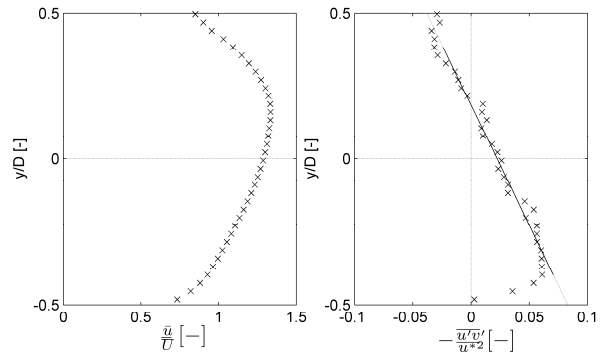


Figure 7: Normalized velocity (left) and Reynolds stress (right) distribution for SF mode with delivered concentration of 29% and $Re = 7.1 \times 10^3$.

When the concentration of the mixture becomes quasi-constant, the velocity distribution starts to be symmetrical. That is valid also for the Reynolds stress distribution with zero value in the centre of the rectangular duct (Fig. 8).

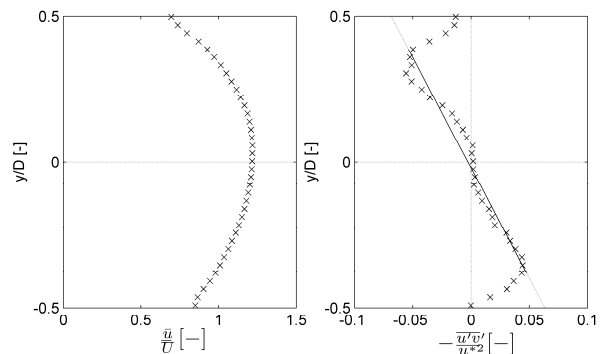


Figure 8: Normalized velocity (left) and Reynolds stress (right) distribution for HF transport mode with delivered concentration of 29% and $Re = 1.9 \times 10^4$.

In fact, the measured instantaneous velocity components in slurry flows represent the speed of solid particles (ballotini). Velocity fluctuation of the particles seems to be strongly attenuated even for small delivered concentration c_{vd} (Fig. 9).

Comparing the run with the lowest concentration ($c_{vd} = 3\%$) and the clear water (Fig. 6) shows that the decrease in normalized Reynolds stress is more than double. With increasing concentration further decrease of normalized Reynolds stress can be observed.

Presented data show slight difference between the Reynolds stress in bottom ($y/D = -0.5 - 0$) and upper region ($y/D = 0 - 0.5$), which can be caused by a concentration gradient. Similar to clear water flows the maximal values of normalized Reynolds stress were found to be very low compared to the calculated wall shear stress based on the energy grade line.

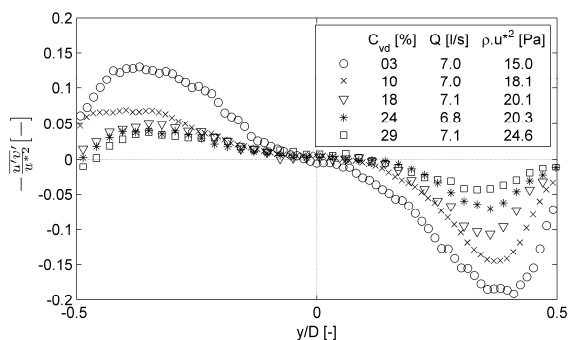


Figure 9: Normalized Reynolds stress distribution for HF mode with delivered concentrations from 3 to 29% and $Re = 1.9 \times 10^4$.

6 SUMMARY

The presented study introduces results of an ultrasonic velocimetry investigation on water/solid-water mixture flows in a rectangular pipe.

Reference measurements of clear water turbulent flows provided expected distributions of longitudinal and vertical velocity components. However, the level of normalized Reynolds stress seems to be significantly underestimated in comparison with theoretical considerations.

Investigation of slurry flows brings the information about the influence of the sediment transport regime on the velocity distribution in the pipe. Further, a strong attenuation of the velocity fluctuation under the presence of the suspended particles is reported.

ACKNOWLEDGMENTS

The research has been supported by the Czech Science Foundation through the grant project No. P105/12/1082 and by Faculty of Civil Engineering of Czech Technical University in Prague through the student grant project No. SGS10/238/OHK1/3T/11.

REFERENCES

[1] Frey H, Church M: How river beds move. *Science*, 325 (2009), 1509-1510
 [2] Chiari M, Friedl K, Rickenmann D: A one-dimensional bedload transport model for steep slopes. *J. Hydraul. Res.*, 48, 2 (2010), 152–160

[3] Rickenmann D, Koschni A: Sediment loads due to fluvial transport and debris flows during the 2005 flood events in Switzerland. *Hydrol. Process.* 24 (2010): 993-1007.

[4] Berzi D: Analytical solution of collisional sheet flows. *J. Hydraul. Eng.*, 137, 2 (2011), 1200-1207

[5] Capart H, Fraccarollo L: Transport layer structure in intense bed-load. *Geophys Res Lett*, 38 (2011), L20402, 6 p.

[6] Recking A, Frey P, Paquier A, Belleudy P, and Champagne JY: Bed-load transport flume experiments on steep slopes. *J. Hydraul. Eng.*, 134, 9 (2008), 1302-1310

[7] Matoušek V: Concentration profiles and solids transport above stationary deposit in enclosed conduit. *J. Hydraul. Eng.*, 135, 12 (2009), 1101-1106

[8] Matoušek V, KRUPÍČKA J: Friction coefficient for upper plane bed. *Proc. Second European IAHR Congress, Munich, Germany (2012)*

[9] Best JL, Kirkbride AD, Peakall J: Mean Flow and Turbulence Structure of Sediment-Laden Gravity Currents: New Insights using Ultrasonic Doppler Velocity Profiling. *Particulate Gravity Currents*, Ch. 12 (2009), Wiley.

[10] Wiklund J and Stading M: Application of in-line ultrasound Doppler-based UVP-PD rheometry method to concentrated model and industrial suspensions. *Flow Measurement and Instrumentation*, 19(3-4) (2008):171–179.

[11] Birkhofer B, Jeelani SAK, Ouriev B, Windhab EJ: In-Line Characterization and Rheometry of Concentrated Suspension Using Ultrasound. *Proceedings - 4th ISUD, Sapporo, Japan, (2004), 65-68. 24*

[12] Song T and Graf WH: Velocity and turbulence distribution in unsteady open-channel flows, *Journal of Hydraulic Engineering-Asce*, 122(3) (1996) 141-154.

[13] Bareš V: Spatial and temporal variation of turbulence characteristics in combined sewer flow, *Flow Measurements and Instrumentation* 19(3-4) (2008), 145-154.

[14] Knight DW, Patel HS. Boundary shear in smooth rectangular ducts. *Journal of Hydraulic Engineering-ASCE*, 111(1) (1985) 29-47.

Application of the Ultrasound Velocity Profiling + Pressure Difference (UVP+PD) method for cement based grouts

Mashuqur Rahman^a, Ulf Håkansson^{a,b} and Johan Wiklund^c

^aKTH – Royal Institute of Technology, SE -100 44, Stockholm, Sweden.

^bSkanska AB – SE -169 83 Solna, Sweden

^cSIK - The Swedish Institute for Food and Biotechnology, PO Box 5401, Göteborg, Sweden.

For grouting applications in underground construction, cement grouts with a water to cement ratio (w/c) typically 0.6 - 1.0 by weight, are used. Measurement of the rheological properties of the cement grouts and suspensions, consisting of a solid volume fraction up to 30 %, during field grouting operation directly in-line is of major interest from an industrial point of view. However, no such in-line monitoring device is available today. The present data recording system, to monitor and control the grouting operations in the field, are only performed by measuring the pressure and the grout volumetric flow in real time. Now for the first time, the ultrasound velocity profiling + pressure difference (UVP+PD) method has been applied directly in-line in field like conditions to determine its feasibility for cement based grouts. The experiments were performed with water to cement ratios 0.6 and 0.8 in a flow loop consisting of a standard grouting rig (UNIGROUT E22H) and LOGAC data recording system, to ensure field like conditions. The UVP+PD method was found successful to measure the rheological properties of micro fine cement suspensions during field like conditions. A further study in a laboratory based flow loop, consisting of a progressive cavity pump was also performed to measure the rheological properties during such conditions. The UVP+PD method was proven successful to obtain satisfactory and promising results and it was also found to be an effective tool for the determination of grout pump characteristics.

Keywords: Cement grouts, in-line rheometry, cement suspensions, UVP+PD method, grouting, cement rheology.

1 INTRODUCTION

Rock grouting is a common practice to increase the water tightness of rock fractures and strength stiffness of the rock mass in underground construction. Grouting practice is still based on rules of thumb and an in-line system for the measurement of cement grout properties, continuously during field operations, is still unavailable [1]. Difficulties associated with conventional rheometers have been pointed out by Håkansson [2] and in a recently proposed methodology it has been showed that the design and steering of a grouting operation necessitates an accurate and reliable determination of the rheological properties, as well as their change with time [3]. For the first time, the ultrasound velocity profiling + pressure difference (UVP+PD) method was applied directly in-line in field like conditions to determine the feasibility of this method for cement based grouts. The results from the feasibility study showed that it is possible to use the UVP+PD method for determining the rheological properties of cement grouts in field like conditions [4,5]. Subsequently it was found that the UVP+PD method could also be an efficient tool for grout pump characterization [6]. However, further development is required concerning the ultrasound transducers. A further study was performed using a laboratory based flow loop to determine the rheological properties of the grouts in a stable flowing condition. This paper presents an overview

of the works that has been performed using the UVP+PD method on cement based grout together with a future outlook.

2 MATERIALS AND METHODS

2.1 Materials

In this work, Cementsa IC 30 micro fine cement has been used to prepare the grout. Cementsa IC 30 has a particle size distribution where 95% of the cement particles are less than 30 microns and the setting time of the cement is approximately 100 minutes. The cement grout was prepared with water/cement ratio 0.6, 0.7 and 0.8 (by weight). A mixing time of 4 minutes was used for all batches. A commercial high performance binding time regulator, Cementsa SetControl II was used as additive and a dosage of 2% (by weight) was used. Cementsa SetControl II is used in the field to reduce the setting time of the prepared grout. In the experiments, SetControl II was used to keep the conditions the same as in the field. A total of 8 batches were made with w/c ratio 0.6, 0.8 and 5 batches with w/c ratio 0.7.

2.2 Experimental flow loop

Two sets of flow loops were used for the experimental works. One flow loop consisted of the conventional UNIGROUT E22H grouting rig from Atlas Copco, a commercial flow meter and pressure sensor LOGAC unit and the UVP+PD test section. The equipment's were connected using high

pressure grouting hoses and stainless steel pipe with an inner diameter of 22.5 mm. A standard grouting rig, UNIGROUT E22H from Atlas Copco, was used to perform the feasibility studies with conditions the same as in the field. A schematic illustration of the experimental flow loop is shown in Figure 1. The second flow loop was used to perform a follow up study in laboratory like conditions. The UNIGROUT E22H was replaced by a progressive cavity pump to obtain a stable flow rate of the grout. The LOGAC flow meter and pressure sensor was used as a reference instrument to compare the flow properties determined with the UVP. The flow was circulated through a storage tank, a progressive cavity single screw pump, UVP+PD test section, LOGAC flow meter and temperature sensors. A schematic illustration of the second flow loop is shown in Figure 2.

2.3 UNIGROUT E22H

The UNIGROUT E22H is a standard grouting rig commonly used for field applications. It consists of a grout mixer - Cemix 203H, a grout agitator - Cemag 402H, a grout pump - Pumpac, control unit and necessary hoses.

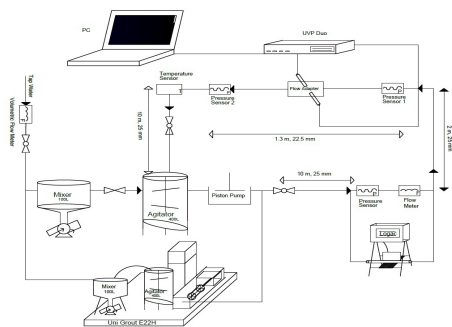


Figure 1 Schematic illustration of the flow loop used for field like conditions

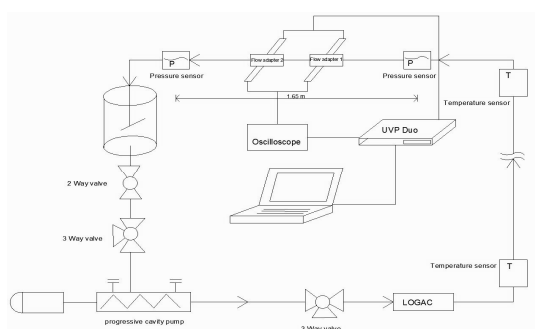


Figure 2 Schematic illustration of the flow loop used for laboratory experiments

2.4 LOGAC recording system

LOGAC 4000 is a recording system for storing and sampling data during a grouting operation. The parameters that can be logged are the volumetric flow, pressure, volume, time and real time. Data can be stored in every 1st, 5th and 10th second. It consists of an electromagnetic flow meter and a

pressure sensor. LOGAC was primarily used as a reference to compare the volumetric flow rate obtained using the ultrasound velocity profiling (UVP) technique.

2.5 Progressive cavity pump

A progressive cavity pump type MAE 50-2/BB.BBNT32 Pompe-Raccordea, known as single screw pump, was used in the laboratory based flow loop. Stable flow condition were achieved while using the progressive cavity pump. The objective of using the progressive cavity pump and the laboratory based flow loop was to obtain repetitive velocity profiles in stable flow condition. The pump can be operated at a flow rate range up to 10 l/min and with a pressure limit of maximum 1.2 MPa.

2.6 UVP+PD method and instrumentation

The LOGAC recording system is based on the capillary and pipe viscometry which is well described in the literature [7]. The capillary and pipe viscometry methodology can perform single point measurement for corresponding shear rate, thereby limiting its use to Newtonian fluids. In this work, the ultrasound velocity profiling (UVP) technique was used in combination with pressure difference (PD) measurements. The UVP+PD method is a multi-point method that has been reported to perform rheological property measurements under true dynamic industrial processing conditions [8]. The UVP+PD methodology and system has been developed by SIK – The Swedish Institute for Food and Biotechnology. Details about the system and applications for industrial and model fluids can be found in other literatures [9].

In this work, a test section comprising of a flow adapter cell consisting of a pair of custom made 4 MHz ultrasound transducers and a differential pressure sensor was used. The transducers featured a delay line, which made it possible to measure the velocity of the cement particles just in front of the transducers. The pressure sensors were installed to measure the pressure difference over a distance of 1.3 m for the field like set up and over a distance of 1.65 m for the laboratory based set up. A detail description of the test section can be found in [4]. The velocity profiles were measured using UVP-DUO-MX Monitor (Met-Flow SA, Switzerland), a pulser/receiver instrument. Velocity estimation was performed using both time domain and Fast Fourier Frequency (FFT) algorithms. A Matlab based software 'Rheoflow', developed by SIK, was used to control all hardware devices for data acquisition, signal-processing, visualization of the data and real time monitoring of the rheological properties.

3 RESULTS AND DISCUSSION

3.1 Velocity profile

The velocity profiles were measured for cement grouts with w/c 0.6 and 0.8 during the field like

conditions and with w/c 0.7 during the laboratory based conditions. For w/c 0.6 and 0.8, velocity profiles were captured over a time period of 1-3 hours. The velocity profiles were measured in ambient temperature 16^o-20^o C and over a flow rate range of 15-30L/min.

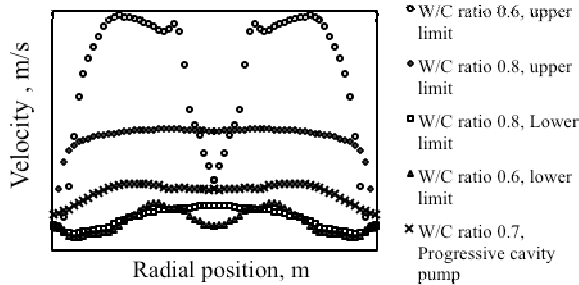


Figure 3 Velocity profiles measured by UVP

In Figure 3, the measured velocity profiles are shown as a function of the radial position, where position zero indicates the center of the pipe. Since the profile on both sides of the center of the pipe should ideally be identical, a mirrored image is shown to illustrate the full velocity profiles. For the field like conditions, a piston pump was used as an integral part of the UNIGROUT E22H and as a result, high fluctuations of the velocity profiles were observed. Only the maximum and minimum velocity profiles have been shown in Figure 3 to demonstrate the fluctuation of the velocity profiles. For the w/c 0.7 laboratory based experiments, a progressive cavity pump was used which yielded a very stable flow rate. Therefore, the average velocity profile has been shown. For w/c 0.6, 512 profiles were captured over 1 minute, 60 minutes after mixing and for w/c 0.8, 1024 profiles were captured over 3 minutes, 90 minutes after mixing. As can be seen, for w/c 0.6, the velocity profiles fluctuated from 1.6 m/s to 1 m/s and for w/c 0.8, the velocity profiles fluctuated from 0.8 m/s to 0.1 m/s. However, it should be noted that the pressure was higher for the w/c 0.6 measurements. Negative velocity was observed, which resembles the suction force occurring due to the cyclic pressure of the piston pump. Nevertheless, the visualization of the velocity profiles in real time is a significant application of the UVP in cement grouts since no other instrument used in the grouting industry are capable of providing this. For w/c 0.6, a lack of signal penetration is observed as the velocity profile was erroneous near the center of the pipe. This distortion was due to the strong attenuation of the ultrasound signal in a thick grout mix, such as w/c 0.6.

3.2 Comparison of the flow rate measured by the LOGAC and UVP

The UVP determines the volumetric flow rate by integration of the velocity profile. The LOGAC flow meter is capable of continuously measuring the volumetric flow rate. However, the measured flow

rate is the average over a certain period of time; hence the true fluctuation of the flow rate remains unknown.

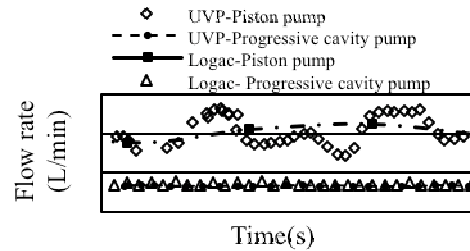


Figure 4 Comparison of the volumetric flow rate determined by the UVP and measured by the LOGAC

Figure 4 shows the comparison of the volumetric flow rate determined by the UVP and measured by the LOGAC. As can be seen, both of the methods yield results of the same order of magnitude. While using the UNIGROUT E22H, flow rate measurement was stored at LOGAC at every 10th seconds and for the progressive cavity pump, it was stored every second. From Figure 4, it is evident that during a field grouting operation the true fluctuation of the flow rate remains unknown. Moreover, negative velocity due to the cyclic pressure of the piston pump cannot be measured using the commercial coriolis flow meters and, in addition, they are not capable of measuring a flow rate when it is less than 1 l/min, which is common at the later stage of grouting. Since the stop criteria for grouting operation depends on the flow of grouts into the rock fractures, a more accurate measurement of the flow rate will lead to a improved decisions. In addition, UVP can be used as an efficient tool for grout pump characterization and optimization of the pulsation effect.

3.3 Rheological analysis

The rheological properties obtained off line, using a conventional rheometer and in-line, using the UVP+PD method, is shown in Table 1. The recorded data were fitted to the Herschel-Bulkley model since this model is capable of incorporating the yield stress and the shear thinning behavior. As can be seen, the flow index, n decreases and consistency index, K increases with decreasing w/c ratio, as expected. From Table 1, a higher yield stress for higher w/c ratio is observed, which however can be explained by the fact that the data was sampled after a longer period of time from mixing, which will have an influence on the rheological properties, due to the hydration of the cement.

Figure 5 and 6 show the corresponding shear stress vs. shear rate plot and the viscosity vs. shear rate plot, respectively. A higher shear stress is observed for the decreased w/c ratio, as expected. A time dependent behavior was observed for w/c 0.8 with an increased yield stress with time.

Table 1 Rheological parameters obtained by H-B model

W/C	Set up	Time min	H-B Parameter		H-B Yield stress, Pa	R ²
			n	k		
0.6	Off line	71	0.33	2.2	2.5	0.98
0.6	Field	68	0.25	2.01	2.4	0.96
0.7	Laboratory	52	0.62	0.45	3.6	0.98
0.8	Off line	30	0.52	0.37	1.3	0.99
0.8	Field	30	0.47	0.35	1.1	0.98
0.8	Laboratory	105	0.63	0.58	3.5	0.98

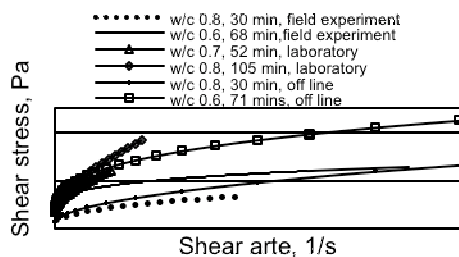


Figure 5 Shear stress vs. shear rate curve for different w/c ratio

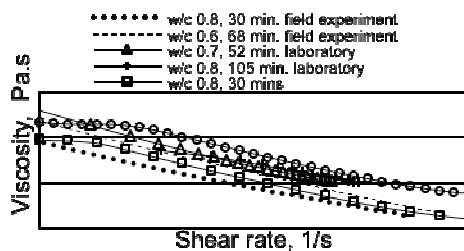


Figure 6 Viscosity vs. shear rate curve for different w/c ratio

From Table 1, it is observed that a higher flow index, n was achieved from the laboratory based set up. This can however be explained due to the short shear rate range. Since, the flow rate was lower (~6 l/min) for the progressive cavity pump compared to the field set up, a lower shear rate range was obtained. From Figure 6, a higher viscosity was observed for decreased w/c, which was expected.

A higher viscosity was observed for w/c 0.8, laboratory based set up, which can be explained by the longer time of performing data sampling after the mixing of the cement grouts. The off-line results showed the apparent viscosity as given by the slope from the origin to the individual data points. A Newtonian plateau was observed at low shear rates, which was expected. On the contrary, it should be noted that the in-line is showing the shear rate dependent viscosity as the slope of the each data point of the shear stress vs. shear rate curve, i.e. not starting from the origin.

4 CONCLUSION

The primary objective of this study was achieved since it was possible to measure the rheological properties of cement based grouts in field like conditions. It was demonstrated possible to obtain the velocity profiles up to the center of the pipe for cement grouts with w/c 0.6, and 0.8 and subsequently determine the rheological properties. In addition, it was observed that the pulsation of the piston pump, used for field grouting operations, can be visualized using the UVP technique. This makes it a promising tool for grout pump characterization. From the studies performed with the laboratory based set up, it was shown that it is possible to obtain the velocity profile nearly to the center of the pipe, but a change of the rheological properties over time was not observed due to the strong attenuation of the signal. Nevertheless, it can be concluded that the UVP+PD method is a promising new method for process monitoring and control of cement based grouts in the field. The future outlook of this method concerns the optimization, characterization of the ultrasound transducers for cement based grouts, observing the change of the rheological properties of cement over time and the characterization of different kind of pumps, used for grouting.

REFERENCES

- [1] Håkansson U & Rahman M: Rheological measurements of cement based grouts using UVP-PD method. Helsinki: Nordic Symposium of Rock Grouting, 2009.
- [2] Håkansson U: *Rheology of Fresh cement Based Grouts*. PhD Thesis, Stockholm: Royal Institute of Technology KTH, 1993.
- [3] Gustafson G & Stille H: Stop criteria for cement grouting. *Felsbau Rock and Soil Engineering* 3 (2005): 62-68.
- [4] Wiklund et al. "In-line rheometry of micro cement-based grouts - a promising new industrial application of the ultrasound based UVP+PD method." *Applied Rheology (submitted)*, 2012.
- [5] Håkansson et al: In-line measurements of rheological properties of cement-based grouts - Introducing the UVP-PD method. *4th International Conference on Grouting and Deep Mixing*. New Orleans, 2012.
- [6] Rahman et al: Grout pump characteristics evaluated with the Ultrasound Velocity Profiling. *EUROCK*. Stockholm, 2012.
- [7] Chhabra R & Richardson J: *Non Newtonian flow in process industry: Fundamentals and engineering applications*. Great Britain: Oxford, 1999.
- [8] Wiklund et al. Methodology for in-line rheology by Ultrasound Doppler velocity profiling and pressure difference technique. *Chemical Engineering Science* 62 (2007): 4277-4293.
- [9] Kotze et al: Rheological characterization of highly concentrated mineral suspensions using an Ultrasonic Velocity Profiling with combined Pressure Difference method. *Applied Rheology* 18 (2008).

Development of rotational rheometers by introducing UVP

Takahisa Shiratori, Ichiro Kumagai, Yuji Tasaka, Yuichi Murai and Yasushi Takeda
 Graduate School of Engineering, Hokkaido University, N13-W8, Kita-ku, Sapporo, 060-8628, Japan
 t.shiratori@ring-me.eng.hokudai.ac.jp

Most of commercial rheometers have thin measuring section to ignore spatial distribution of shear rate. The objective of this research is obtaining more information about rheological properties in shorter time by taking into account the spatial distribution of the shear rate. Velocity fields of Newtonian and non-Newtonian fluids in a rotating cylinder are measured by a UVP-Duo. The velocity fields are converted to two velocity components on the two-dimensional plane (2D2C) by a method we established. Effects of measurement errors of the UVP on the 2D2C velocity field through the conversion method are assessed quantitatively by introducing numerical simulation. The result shows that measurement errors are amplified near the wall of the cylinder. Applications of the velocity fields for rheometry are suggested. In the suggested rheometry, a strain range of linear viscoelasticity can be detected without changing the oscillation amplitude. Shear rate dependent viscosity can also be measured without changing the rotation speed.

Keywords: Rheometry, rheology, rotating cylinder, multi velocity components, polyacrylamide solution

1 INTRODUCTION

Nowadays foods are required not only to supply nutrients but to provide enjoyment through new flavors and textures. Physical factors, for example hardness, viscosity and shape, affect feeling of the people as much as chemical factors, for example sweetness, bitterness and fragrance. The physical factors are quantitatively evaluated by introducing rheological properties such as viscosity, storage modulus and loss modulus. These properties are measured by equipment called rheometer. Furthermore, rheometers are utilized in industries other than food industry. For example, rheological properties given by rheometers are helpful for quality control in polymer industry.

Existing commercial rheometers have two problems: one is a limitation of test fluids, and the second is a long measurement time. These rheometers generally have thin measuring section in order to ignore spatial distribution of shear rate in test fluids. Thus they cannot measure properties of fluids with larger ingredients than the thickness of measurement sections: for instance juice with fruit pulps. The long measurement time is also owing to the thin measuring section. Because spatial distribution of shear rate is ignored, one rotational speed corresponds to one shear rate. By taking into account spatial distribution of shear rate, viscosity under a range of shear rate is obtained from one rotational speed measurement.

Nowadays it is possible to take into account shear rate distribution with field velocimetry e.g. UVP. Thus a rheometer with a thick measurement section can be designed while taking into account shear rate distribution. Viscosity distribution due to shear rate dependent viscosity is also obtained. It means that the relationship between shear rate and

viscosity is measured simultaneously. Actually a system named UVP-PD [1] enabled to measure shear rate dependent viscosity. As described above, problems of commercial rheometers can be overcome with UVP.

According to this strategy we have developed a novel rheometry for viscoelastic [2] and multiphase [3] flows based on UVP. The rheometry requires obtaining two velocity components on two-dimensional plane (2D2C), and it has been achieved with some assumption. One of critical factors for relevance of the rheometry is effects from measurement errors of UVP on 2D2C velocity field. Thus the assessment of the error conversion is demonstrated by introducing numerical simulation as the first topic of this paper. Then applications of 2D2C velocity field to rheometry are suggested. The applications can measure shear rate dependent viscosity and perform linearity check in oscillation test simultaneously.

2 EXPERIMENT

2.1 Experimental apparatus

Figure 1 shows the experimental apparatus. It consists of a cylinder, a rectangular container, stepping motor and UVP-Duo as shown in Fig. 1 (a). The cylinder is filled with a test fluid: silicone oil (KF96-1000cs, Shin-Etsu Chemical) or 1.0 wt% polyacrylamide (PAA, AP805C, DiaNitrix) solution. The silicone oil is regarded as Newtonian fluid whose viscosity η and density ρ are 0.970 Pa·s and $0.967 \times 10^3 \text{ kg/m}^3$ respectively. The PAA solution has shear rate dependent viscosity and viscoelasticity. The detail of these properties is summarized in section 2.3. The rectangular container is partially filled with water to introduce ultrasonic pulse into the cylinder without reflection. The height H and the diameter D of the cylinder are

300 mm and 154 mm respectively as shown in Fig. 1(b). An ultrasound transducer is fixed nearby the cylinder with 150 mm in height from the bottom of the cylinder. The rotation of the cylinder is controlled by a stepping motor for being oscillatory rotation. The velocity of the wall of the cylinder is described as Eqs. (1) and (2).

$$u_{wall}(t) = U_{wall} \sin 2\pi ft. \quad (1)$$

$$U_{wall} = \pi f D \theta. \quad (2)$$

In this experiment, frequency of the rotation f is 0.5 Hz, and rotation angle θ is π . Then the maximum velocity of the cylinder U_{wall} is 760 mm/s. Time resolution Δt , channel distance Δx and velocity resolution Δu are set at 34 msec, 0.367 mm and 0.625 mm/s respectively.

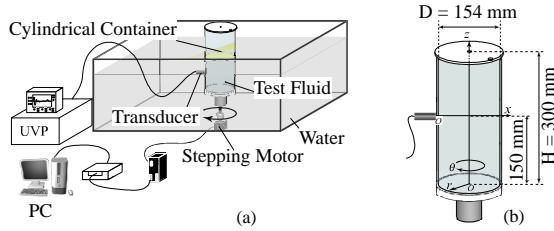


Figure 1: Diagram of (a) the overview of the experimental apparatus (b) the detail of the cylinder

2.2 Conversion method from u_x to u_θ and u_r

Tangential and radial velocity components, u_θ and u_r , respectively, are necessary to obtain rheological properties from velocity information. Thus we developed a method to determine u_θ and u_r from a velocity profile on the measurement line u_x . Figure 2 shows a top view of the cylinder. Measurement line lies on 7.0 mm from the rotation axis of the cylinder. Under the assumption of axial symmetry, u_{x+} and u_{x-} in Fig. 2 are velocity information about the same velocity vector. Thus u_θ and u_r are calculated from u_{x+} and u_{x-} by Eqs. (3) and (4) respectively.

$$u_\theta = \frac{u_{x+} + u_{x-}}{2 \cos \alpha}. \quad (3)$$

$$u_r = \frac{u_{x+} - u_{x-}}{2 \cos \alpha}. \quad (4)$$

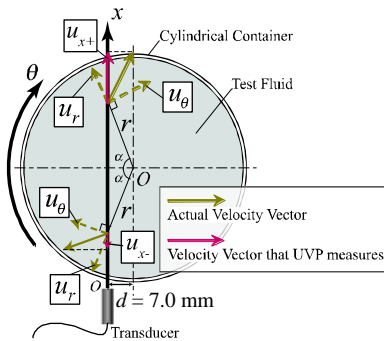


Figure 2: Top view of the cylinder

2.3 Properties of 1.0 wt% PAA solution

The PAA solution used for this experiment is one of popular non-Newtonian fluids for laboratory experiment. Rheological properties of the PAA solution, shear rate dependent viscosity and viscoelasticity, were measured with a commercial rheometer (Bohlin CVO, Malvern Instruments). The measured viscosity is plotted in Fig. 3 (a) as a function of shear rate. The shear viscosity decreases with the increase of shear rate: namely the PAA solution is a shear thinning fluid. Figure 3 (b) shows the relationship between the measured dynamic moduli, storage modulus G' and loss modulus G'' , and the applied frequency. Amplitude of stress is set as 1.0 Pa. In the frequency range of Fig. 3 (b), including the experimental condition introduced to this experiment ($f = 0.5$ Hz), G' is always larger than G'' . It is expected that the contribution from elasticity to stress is larger than that from viscosity under the experimental condition.

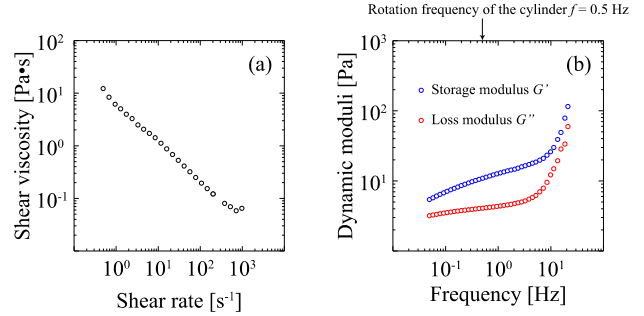


Figure 3: The relationship between (a) viscosity and shear rate, and (b) dynamic moduli and frequency

3 VELOCITY FIELDS

Spatio-temporal distributions of the velocity components are shown in Figs. 4 and 5. Spatial (horizontal) axis and temporal (vertical) axis are normalized by radius of the cylinder $D/2$ and inverse of the oscillation frequency $1/f$ respectively. Velocity components are normalized by the maximum velocity of the wall U_{wall} . Radial velocity component u_r and tangential velocity component u_θ are indicated as (a) and (b) in the figures, respectively. In the region of $r < 7.0$ mm ($2r/D < 0.09$), velocity cannot be measured because the measurement line doesn't take corresponding radial positions with this region (see Fig. 2). The distributions in Figs. 4 and 5 are obtained in case of the silicone oil and the PAA solution respectively. In both cases u_θ is about ten times larger than u_r . Thus the tangential velocity component u_θ is mainly discussed in the following sections.

4 EVALUATION OF ERROR CONVERSION

4.1 Method

The original velocity distribution obtained by UVP includes measurement errors. The errors

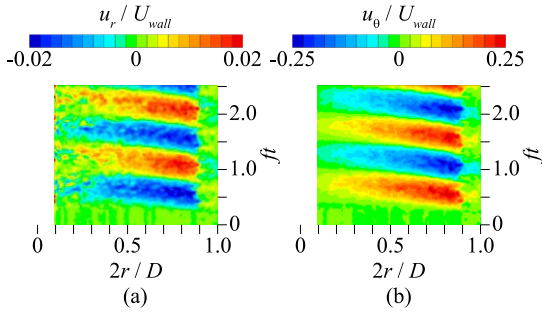


Figure 4: Spatio-temporal distribution of (a) radial velocity component and (b) tangential velocity component in silicone oil

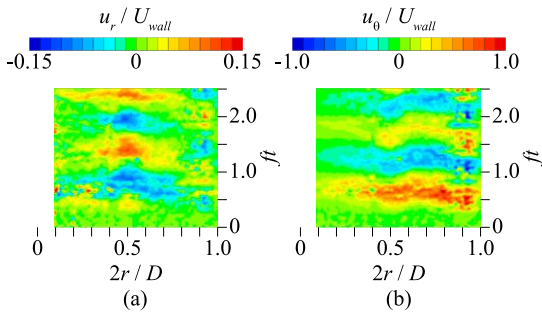


Figure 5: Spatio-temporal distribution of (a) radial velocity component and (b) tangential velocity component in PAA solution

affect the result through the conversion method from u_x to u_θ and u_r we developed. Conversion characteristics of the errors were evaluated quantitatively by performing our conversion method for the result of a numerical simulation. Equation of motion for Newtonian fluids in the tangential direction, Eq. (5), is solved numerically to obtain a spatio-temporal distribution of u_θ component.

$$\frac{\partial u_\theta}{\partial t} = \frac{\eta}{\rho} \left(\frac{\partial^2 u_\theta}{\partial r^2} + \frac{1}{r} \frac{\partial u_\theta}{\partial r} - \frac{u_\theta}{r^2} \right). \quad (5)$$

The obtained u_θ distribution is regarded as correct velocity distribution $u_{cor}(r,t)$. This velocity distribution is rearranged and projected on the measurement line x :

$$u_{cor}(x,t) = u_{cor}(r,t) \cos \alpha \quad (6)$$

where α is the center angle shown in Fig. 2. The velocity distribution measured by UVP, $u_{UVP}(x,t)$, can be expressed as

$$u_{UVP}(x,t) = u_{cor}(x,t) + Er_g(x,t), \quad (7)$$

where $Er_g(x,t)$ means that the measurement error produced by the UVP itself because of a measurement of a reflection echo or detection of Doppler shift frequency. $Er_g(x,t)$ is assumed to obey a normal distribution. The standard deviation of the normal distribution σ_g is varied from 0 to $5.0\Delta u$. Finally $u_{UVP}(x,t)$ is converted to a velocity distribution on r axis by Eq. (8) derived from Eq. (3).

$$u_{UVP}(r,t) = \frac{u_{UVP}(x+,t) + u_{UVP}(x-,t)}{2 \cos \alpha}. \quad (8)$$

A difference between $u_{UVP}(r,t)$ and $u_{cor}(r,t)$ is regarded as an error distribution on $u_{UVP}(r,t)$. This error distribution is represented by $Er(r,t)$:

$$Er(r,t) = u_{UVP}(r,t) - u_{cor}(r,t). \quad (9)$$

In other words, $Er_g(x,t)$ is converted to $Er(r,t)$ by our conversion method. Thus the relationship between them means error conversion characteristics of our conversion method. Standard deviation of $Er(r,t)$ is represented by σ , and compared with σ_g .

4.2 The results of the evaluation

At first, standard deviation σ was calculated for time series of Er on each r position in order to clarify spatial distribution of σ/σ_g ratio. The σ/σ_g ratio means how much measurement errors are amplified by the conversion. The σ/σ_g ratio for $\sigma_g = 5.0\Delta u$ is plotted in Fig. 6 (a) as a function of spatial position. Near the center of the cylinder, around $2r/D = 0.2$, σ approximately equals to σ_g . On the other hand, near the wall of the cylinder, σ is as 5 times large as σ_g . Therefore Fig. 6 (a) means that the measurement error is amplified especially near the wall of the cylinder. This amplification occurs because the center angle α is large near the wall thus the division by $\cos \alpha$ in Eq. (8) amplifies errors.

The relationship between σ and σ_g is shown in Fig. 6 (b). The relation means how errors on r - t velocity distribution changes depending on measurement errors of UVP. In Fig. 6 (b), spatial distribution of σ is not considered: a parent population of σ is all errors on spatio-temporal distribution. As σ_g increases, σ converges to the primary function shown by the green line. It means that if σ_g is large enough, σ is a constant multiple of σ_g . On the other hand, the primary function cannot explain the relationship between σ_g and σ in the region of smaller σ_g . Figure 6 (b) shows that σ has a certain value shown by the blue line when σ_g equal zero. It means that r - t velocity distribution has errors even if measurement errors of UVP do not exist.

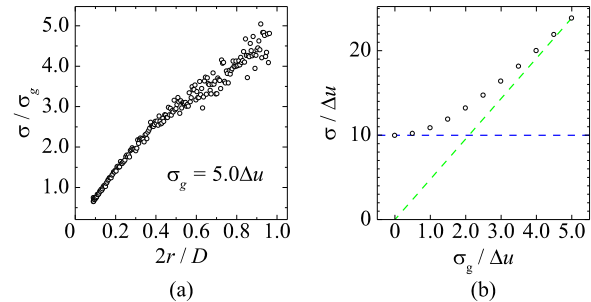


Figure 6: Standard deviation of errors on r - t velocity distribution converted from x - t velocity distribution (a) Spatial distribution (b) Dependency on standard deviation of errors on x - t velocity distribution

5 THEORIES FOR RHEOMETRY

In this section, two theories to apply 2D2C velocity field for rheometry is suggested: the first one is an evaluation of viscoelasticity under oscillatory rotations, and the second one is a measurement of shear rate dependent viscosity under steady rotations. In both cases, the experimental apparatus have to be improved to measure shear stress on the wall. Additionally fixed inner cylinder is necessary for the steady rotation test to prevent a rigid rotation.

5.1 Storage and loss moduli

By measuring a shear stress on the wall of the cylinder, strain dependency of G' and G'' can be measured simultaneously. Here a process to obtain G' and G'' is explained. The momentum conservation law in the rotating cylinder for θ component is described by Eq. (10) under the assumption of uniformity for θ and z direction.

$$\rho \left(\frac{\partial u_\theta}{\partial t} + u_r \frac{\partial u_\theta}{\partial r} + \frac{u_r u_\theta}{r} \right) = \frac{2\tau}{r} + \frac{\partial \tau}{\partial r}. \quad (10)$$

Information in the left-hand side of Eq. (10) is obtained by the conversion technique suggested in this report. Thus spatio-temporal stress distribution $\tau(r,t)$ is obtained by solving Eq. (10) numerically. Furthermore shear rate distribution $\dot{\gamma}$ and strain distribution γ are obtained from velocity distribution.

$$\dot{\gamma}(r,t) = \frac{\partial u_\theta}{\partial r} - \frac{u_\theta}{r}. \quad (11)$$

$$\gamma(r,t) = \int_0^t \dot{\gamma}(r,T) dT. \quad (12)$$

In order to obtain G' and G'' , the cylinder is controlled to rotate oscillatory. If the flow phenomenon is under the linear viscoelastic regime, a time variation of the three quantities, γ , $\dot{\gamma}$ and τ , satisfy,

$$\gamma(r,t) = \gamma_0(r) \cos 2\pi f t, \quad (13)$$

$$\dot{\gamma}(r,t) = -\dot{\gamma}_0(r) \sin 2\pi f t, \quad (14)$$

$$\tau(r,t) = \tau_0(r) \cos \{2\pi f t + \delta(r)\}, \quad (15)$$

where γ_0 , $\dot{\gamma}_0$ and τ_0 are amplitudes of strain, shear rate and stress, respectively. Eqs. (13) and (15) mean that the spatial distribution of phase difference δ is obtained by comparing $\gamma(r,t)$ and $\tau(r,t)$. Then a spatial distributions of G' and G'' are obtained as

$$G'(r) = \frac{\tau_0(r)}{\gamma_0(r)} \cos \delta(r), \quad (16)$$

$$G''(r) = \frac{\tau_0(r)}{\gamma_0(r)} \sin \delta(r). \quad (17)$$

In these equations, G' and G'' are described as the

functions of radial position r . These functions can be converted to functions of γ_0 because the relationship between r and γ_0 is given by Eq. (13). Consequently the relationship between G' , G'' and γ_0 is obtained without changing an oscillation amplitude.

5.2 Non-Newtonian viscosity

With a fixed inner cylinder, a rigid rotation is prevented and shear rate dependent viscosity can also be measured. In steady rotation test, Eq. (10) is simplified to Eq. (18) because the term of time derivative can be ignored.

$$\rho \left(u_r \frac{\partial u_\theta}{\partial r} + \frac{u_r u_\theta}{r} \right) = \frac{2\tau}{r} + \frac{\partial \tau}{\partial r}. \quad (18)$$

Spatial distribution of stress $\tau(r)$ is obtained from Eq. (18) as is the case in Eq. (10), and spatial distribution of shear rate $\dot{\gamma}(r)$ is also obtained from Eq. (11). Then the spatial distribution of viscosity is obtained by

$$\eta(r) = \frac{\tau(r)}{\dot{\gamma}(r)}. \quad (19)$$

The spatial distribution can be converted to shear rate dependency by considering Eq. (11). Therefore the technique to obtain 2D2C velocity distribution enables to measure shear rate dependent viscosity without changing a rotation speed.

6 CONCLUSION

Velocity fields of a silicone oil and polyacrylamide (PAA) solution in the rotating cylinder were measured by UVP. Under the assumption of axial symmetry, two velocity components, u_θ and u_r , were obtained on r axis (2D2C velocity field). The error conversion characteristics were assessed quantitatively. As the result, it was clarified that measurement errors are amplified especially near the wall of the cylinder. By summarizing the works mentioned above, ultrasonic rotational rheometer was suggested. In this system, it is possible to detect a strain range of linear viscoelastic region from an oscillation test without strain sweeping. Shear rate dependent viscosity can also be measured without changing the rotational speed by installing a fixed inner cylinder. In order to realize these systems, shear stress has to be measured on the wall of the inner or outer cylinder.

REFERENCES

- [1] Wiklund J *et al.* : Methodology for in-line rheology by ultrasound Doppler velocity profiling and pressure difference techniques, Chem. Eng. Sci., 62 (2007), 4277-4293.
- [2] Furuya N *et al.* : Development of Rheometry based on UVP for visco-elastic liquid, Proc. of ISUD6, (2008), 57-60.
- [3] Murai Y *et al.* : Ultrasound Doppler rheometry from spin response of viscoelastic and bubbly Liquids, Proc. of ISUD7, (2010), 9-12.

DEVELOPMENT OF AN INDUSTRIAL UVP+PD BASED RHEOMETER - OPTIMISATION OF UVP SYSTEM AND TRANSDUCER TECHNOLOGY

Johan Wiklund^a Reinhardt Kotzé^b, Rainer Haldenwang^b and Mats Stading^a

^aSIK - The Swedish Institute for Food and Biotechnology, PO Box 5401, Göteborg, Sweden.

^bFPRC - Flow Process Research Centre, Cape Peninsula University of Technology, PO Box 652, Cape Town, 8000, South Africa.

Corresponding author: johan.wiklund@sik.se

A complete UVP+PD system and methodology that meets the industrial requirements has recently been developed at SIK in collaboration with CPUT and industrial partners. The updated UVP+PD methodology and system has now been successfully installed in industry for different industrial applications including; fat crystallization, heat treatment, fiber flows, injection grouting, CIP cleaning and in-line mixing. The new industrial version of the UVP+PD system features new transducer technology, electronics, new signal processing techniques featuring multiple velocity estimation algorithms and deconvolution and also a complete UVP+PD software known as RheoFlow™. It is currently the only system capable of true non-invasive in-line flow visualization and rheometry measurements in real-time through stainless steel.

Keywords: Ultrasonic Velocity Profiling, in-line rheometry, industrial applications, ultrasonic transducer

1 INTRODUCTION AND HISTORY

Understanding the rheological behavior of industrial fluids such as concentrated suspensions is important in the analysis and control of many industrial processes. More than 95% of the fluids used in industry are structured fluids i.e. non-Newtonian fluids that exhibit complex flow behavior over wide ranges of shear rates. In addition, these fluids are almost exclusively opaque and contain a high concentration of solids/particles with size distributions ranging from microns up to several cm in length. The trend within the fluid industry is towards continuous production, leading to an increasing demand for new and improved methods that allow real-time monitoring of quality parameters and fast process control [1]. The consistency and viscosity can be described by fluid rheology and are frequently used as quality control parameters. Rheological properties can be correlated with product microstructure, they govern the performance of unit operations and detailed knowledge is fundamental for the design of new process equipment and for predicting e.g. heat transfer. The determination of rheological properties in-line, in real time, thus has a great economic impact and is important from a quality perspective for the development of innovative and competitive products. This is also a prerequisite for efficient process control.

The most promising in-line viscometer concept is based on the combination of volumetric flow rate measurements in combination with pressure difference measurements and this concept has been known for more than 100 years [1-3]. However, since instruments using this concept are based on the measurement of the average volumetric flow rate, they only provide viscosity at one shear rate, or

at most, a few shear rates. The current in-line and on-line techniques available for industrial applications are generally unable to cope with large particulate suspensions and are unreliable when non-Newtonian fluid systems are considered, according to recent reviews [1–3]. Moreover, commercial process rheometers are often based on intrusive techniques that disturb the flow, which also results in cleaning problems.

In the mid 1990's several research groups proposed to use a multi-shear rate method based on measurements of velocity profiles in combination with a pressure difference (PD) in order to estimate rheological flow properties directly in-line. Both optical techniques such as laser Doppler anemometry (LDA) and magnetic resonance imaging (MRI) were proposed, but found impractical for industrial applications due to several limitations such as; high cost, requiring transparent fluids, long acquisition times etc. The Ultrasonic Velocity Profiling (UVP) or Pulsed Ultrasound Velocimetry technique was first introduced and adapted for measurements in opaque, general fluids, in the 1980's [4]. UVP has since then been accepted as an important tool for measuring flow profiles in opaque liquids in research and engineering. The UVP technique has now been expanded to include e.g. 2D/3D-flow mapping as well as in-line tube velocimetry.

The in-line concept for enhanced tube viscometry combining the UVP technique with simultaneous Pressure Difference (PD) measurements is now known as the UVP+PD method. The UVP+PD in-line rheometer concept was proposed in the literature for the first time over 15 years ago and has been investigated by many authors [5–9]. Although the initial results demonstrated that the UVP+PD

method had the potential to become an important industrial tool for flow visualization, process monitoring and control, there still exists no commercial UVP+PD system on the market. This is due to the complexity of real industrial fluids and the harsh conditions within the fluids industry. The system must e.g. be designed to operate over wide temperatures and pressure ranges and the measurements must be non-invasive, real-time, robust and user friendly. It is thus very difficult to meet all of these industrial requirements at the same time.

A scientific collaboration was initiated in the year 2000 between SIK-The Swedish Institute for Food and Biotechnology, ETH-Zurich, Switzerland and Met-Flow SA, Lausanne, Switzerland with the aim to develop and improve a complete UVP+PD and system method for improved measurement accuracy in industrial applications. Starting in 2008, SIK found a new scientific partner in Cape Peninsula University of Technology (CPUT), Cape Town, South Africa. The projects have been very successful with several outputs: 3 PhD's, several MSc's, a large number of journal and conference articles as well as patents [10-14].

2 CURRENT LIMITATIONS WITH THE UVP+PD METHOD

2.1 Transducer technology and interfaces

According to the literature [1,5-7,10-11], the UVP+PD systems used so far were all based on traditional and simple components, such as, commercially available submersion type transducers, simple pipe flow adapter cells for housing the transducers and pulser-receivers with simple velocity estimation algorithms. The UVP+PD systems used therefore have several limitations in measurement accuracy, mainly due to the high uncertainty in the near wall region owing to the ultrasonic near field. This leads to poor accuracy of the measured velocity gradient close to pipe walls. For volumetric flow rate measurements this is not critical, but for in-line rheometry the velocity gradient in the high shear region near the walls combined with the pressure difference over a fixed distance of pipe length is used to determine the shear dependent viscosity. The measured velocity gradient must thus be correct in order to obtain the true flow curve.

2.2 Attenuation, wall effects, sound velocity etc.

Other problems include, depending on the installation method, attenuation, wall effects and the finite size of the measuring volume which partially extends over the wall interface and refraction of the ultrasonic wave (Doppler angle changes). For invasive set-up's distortion caused by cavities situated in front of ultrasonic transducers, measurement volumes overlapping wall interfaces and sound velocity variations as well as physical

changes of the ultrasonic beam shape and intensity, are also important factors leading to poor measurement accuracy [10-12].

2.3 Non-linear model fitting approach

To date, the shear viscosity and rheological parameters have been calculated from a non-linear fit of the measured velocity profiles and pressure drop data to e.g. the integrated form of the power law model. However, a model-fitting approach requires detailed knowledge about the wall positions as well as a-priori knowledge about the rheology of the fluid under investigation in order to provide realistic initial estimates. The application of a model-fitting approach for rheological characterization produces unrealistic results, as the fitted parameters are sensitive to the position of the pipe wall and vary significantly even over the minimum channel distance or i.e. the distance between the velocity sampling points [10-11]. Moreover, industrial fluids rarely exhibit single model flow behavior over a wide range of shear rates.

3 DEVELOPMENT OF AN INDUSTRIAL UVP+PD BASED RHEOMETER

3.1 The new delay line transducer concept

The near field problem was solved by the introduction of new transducers featuring a delay line. The delay line in this case is a material or several materials, attached to the front of the transducers, which are optimized for beam forming and contain the near field, thus focusing the beam on the liquid wall interface. The transducer has a curved front with angle compensation, thus perfectly matching the radius of the pipe. Experimental set-up's at SIK comprising Doppler string and needle phantoms and a robot for mechanical X,Y,Z scanning of the acoustic pressure field in front of the transducers and for estimating the physical dimensions of the sample volume along the measuring line were used to optimize the transducer performance. Fig. 1 shows the new delay line transducer and a schematic diagram of the flow adapters with delay line transducers installed. More information on the delay line transducers and the improved accuracy in the near wall region can be found in [14].

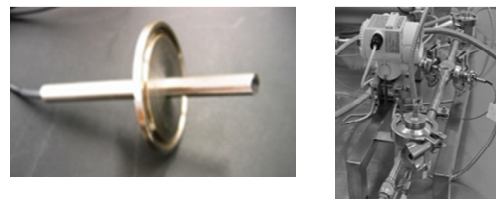


Figure 1: New delay line transducer (left) and complete UVP+PD test section with delay line transducers installed.

3.2 The new non-invasive sensor concept

Industrial unit operations often involve high temperatures and pressure levels as well as abrasive materials or corrosive fluids. Consequently, there is a large interest from industry to obtain a complete sensor unit that can be used to measure non-invasively through stainless steel pipes. Several ultrasonic time-of-flight or Doppler based flow meters of the clamp-on type have appeared on the market, but it has been shown to be very difficult to accurately measure the complete velocity profile and gradient near the wall using this set-up in combination with stainless steel pipes due to several reasons; impedance matching, attenuation, beam split modes, internal reverberation and beam refraction. To overcome previously mentioned problems, a new non-invasive sensor unit has been developed and optimized for stainless steel pipes. The sensor unit consists of a transducer, delay line, wedge, attenuators and acoustic couplants. The configuration provides optimum acoustic beam properties, such as, beam forming, focusing and coupling and impedance matching. It further provides an optimum beam path through material layers and into the fluid medium as well as sensor protection. The configuration is designed to generate or eliminate different types of waves in any solid or semi-solid materials that could be used for non-invasive measurements. The sensor "block" can either be an integral part of the material wall layer (e.g. pipe wall) or used as a clamp-on device. Fig. 2 shows a 3D-model of the non-invasive sensor unit with mounting device.

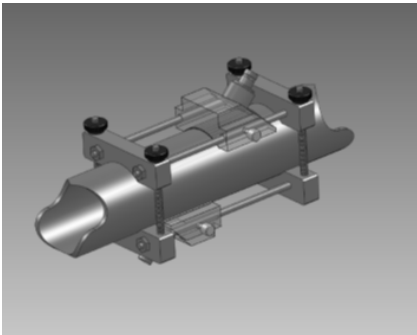


Figure 2: 3D-model of the non-invasive sensor unit with mounting device.

Fig. 3 demonstrates that it is possible to obtain accurate and identical velocity profiles in a moderately shear-thinning industrial fluid using both the new delay line transducers with a flush mounted configuration non-invasively through Plexiglas and stainless steel using the non-invasive sensor unit. Fig. 4 shows a spectral plot of a single velocity profile for an industrial detergent measured under true industrial conditions through a 51mm stainless steel (316L) pipe using the novel non-invasive sensor unit.

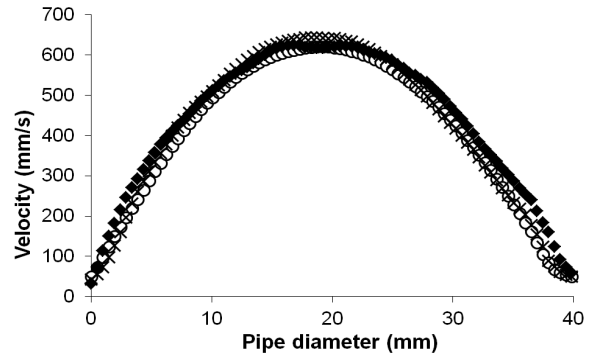


Figure 3: Velocity profiles measured using a flush mounted configuration with delay line transducers (open circles) and non-invasively through Stainless steel (crosses) and Plexiglas (filled diamonds) using the non-invasive sensor unit with mounting device.

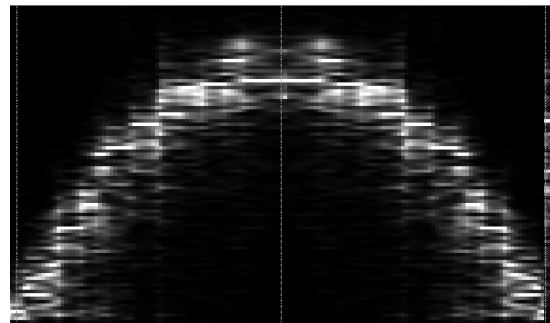


Figure 4: Spectral plot of a single velocity profile measured through 51mm stainless steel 316L pipe using novel non-invasive sensor unit.

3.3 Deconvolution & velocity estimation algorithms

The new UVP-DAQ system and software has been upgraded to include several new velocity estimation algorithms (FFT, time-domain, PBurg spectral etc.) that can be used simultaneously to improve the measurement accuracy under real industrial process conditions. Velocity data close to pipe walls, which is critical for accurate fluid characterization, are further corrected for by implementing a deconvolution procedure. More information is presented in detail in [10-14].

3.4 The non-model approach for obtaining the true shear viscosity distribution

As mentioned in Sec. 2.3 the application of a model-fitting approach for the rheological characterization produces unrealistic results due to several reasons. Therefore, an alternative method was developed in which the shear viscosities as function of shear rates are determined directly from the measured velocity profile and pressure drop data. The yield stress can be obtained once the plug radius has been automatically determined from the deconvolved velocity profile(s). Fig. 5 shows the true shear viscosity distribution of four industrial products

obtained under realistic processing conditions using the direct non-model approach/method, which was found to be both more robust and accurate as it can capture e.g. a Newtonian plateau.

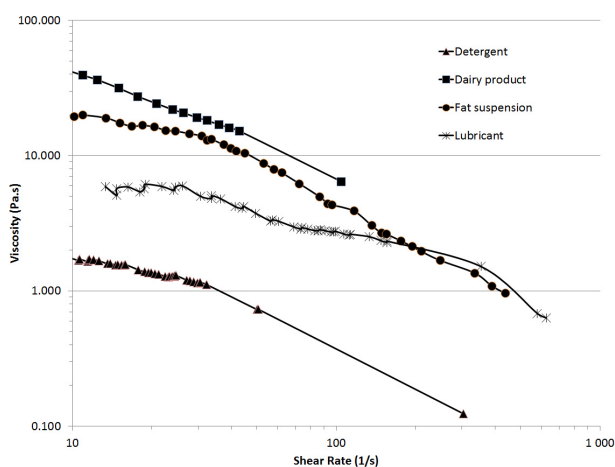


Figure 5: Shear viscosities as function of shear rates for four industrial products obtained using the non-model approach.

4 STAGE OF DEVELOPMENT

A few prototype systems have been developed and successfully installed by SIK in Europe under industrial conditions with large international companies. Additional systems have been developed and successfully used e.g. in an EU-project Healthy Structuring FOOD-CT-2006-023115. New complete sensor systems and a new integrated UVP-DAQ electronics are being developed and finalized. Both are in the final stage of development and are ready for final laboratory testing before customization. New software is currently being tested for industrial applications to be fully compatible with existing commercial systems for integrated process control.

5 SUMMARY

A new complete UVP-DAQ in-line rheometry system and methodology including unique software algorithms, together with novel sensor technology has been developed over the past 10 years and validated under real industrial process conditions. This inventive system and method can be applied to a wide range of fluids and industrial applications, e.g. oil, petroleum, food, minerals, chocolate, explosive emulsions, pharmaceutical industry and more. Our final industrial system and method will be able to accurately visualise the flow, determine the flow-rate, rheological properties and concentration of solids. Shear viscosity as a function of shear rate is determined directly from the measured data without using any model fitting procedure. The industrial system and method will be a unique product thus not directly competing with any other product on the market. It is currently the only system capable of true non-invasive in-line flow visualization

and rheometry measurements in real-time through stainless steel.

ACKNOWLEDGEMENTS

Met-Flow SA and CPUT are gratefully acknowledged for scientific collaboration. Vetenskapsrådet – The Swedish Research Council, Research Links and The National Research Foundation of South Africa (NRF), CPUT are acknowledged for funding.

REFERENCES

- [1] Roberts I. In-line and on-line rheology measurement. In: Kress-Rogers, Brimelow, editors. Instrumentation and sensors for the food industry. Abington Hall (Cambridge): Wood Head Publishing Limited; 2000. p. 1–403.
- [2] Barnes HA. On-line or process viscometry—A review. *Applied Rheology* 1999;9:102–7.
- [3] Macosko CW. Rheology—Principles, measurement and applications. New York (USA): VCH Publishers Inc.; 1993.
- [4] Takeda Y: Measurement of velocity profile of mercury flow by ultrasound Doppler shift method, *Nucl. Technol.* 79 (1987), 120-124.
- [5] Dogan N, McCarthy MJ, Powell RL. Application of an in-line rheological characterization method to chemically modified and native corn starch. *Journal of Texture Studies* 2005;36:237–54.
- [6] Wunderlich Th, Brunn PO. Ultrasound pulse Doppler method as a viscometer for process monitoring. *Flow Measurement and Instrumentation* 1999;10:201–5.
- [7] Birkhofer, B., Jeelani, S.A.K., Windhab, J. et al. (2008). Monitoring of fat crystallization process using UVP–PD technique. *Flow Measurement and Instrumentation*, 19, 163–169.
- [8] Wiklund J, Shahram I, Stading M: Methodology for in-line rheology by ultrasound Doppler velocity profiling and pressure difference techniques, *Chem. Eng. Sci.* 62 (2007) 4159-4500.
- [9] Kotzé R, Haldenwang R, Slatter P: Rheological characterization of highly concentrated mineral suspensions using an Ultrasonic Velocity Profiling with combined Pressure Difference method, *Appl. Rheol.* 18(6) (2008) 62114
- [10] Wiklund J: Ultrasound Doppler Based In-Line Rheometry: Development, Validation and Application, PhD Thesis, SIK – The Swedish Institute for Food and Biotechnology, Lund University, Sweden (2007).
- [11] Birkhofer B: Ultrasonic in-line characterization of suspensions. PhD Thesis, Swiss Federal Institute of Technology. ETH), Switzerland (2007).
- [12] Wiklund J, Stading M: Application of in-line ultrasound Doppler based UVP-PD method to concentrated model and industrial suspensions, *Flow Meas. Instrum.* 19 (2008) 171-179.
- [13] Kotzé R, Haldenwang R: Development of an ultrasonic in-line rheometer: Evaluation, optimisation and verification, 15th Int. Conf. Transport & Sedimentation Solid Particles, 15 (2011) 49-61.
- [14] Kotzé R, Wiklund J, Haldenwang R: Optimisation of Pulsed Ultrasonic Velocimetry and Transducer Technology for Industrial Applications, *Ultrasonics*, (2012)

Recent Developments in Ultrasound Imaging Velocimetry: toward Clinical Application

Christian Poelma

Laboratory for Aero & Hydrodynamics

Process & Energy Department, Faculty of Mechanical, Maritime and Materials Engineering,
Delft University of Technology, Mekelweg 2, 2628 CD Delft, The Netherlands;

E-mail: C.Poelma@tudelft.nl

An overview is given of recent progress in the field of ultrasound imaging velocimetry (UIV, also known as echo-Particle Image Velocimetry). UIV is capable of providing instantaneous velocity fields in flows that are not accessible by conventional (i.e. optical) measurement techniques. In particular, it holds great promise for non-invasive measurement of blood flow patterns and the related wall shear stress distribution. These parameters can assist in e.g. evaluating atherosclerosis risks. While some promising proof-of-principle experiments have been performed recently, quantitative clinical applicability will require significant improvement of the technique, e.g. the accuracy of near-wall velocity results and the dynamic range. The UIV technique is compared to a range of alternatives, such as MRI-based velocimetry. Finally, translation of the technique to applications other than blood flow (e.g. multiphase flows) will be briefly discussed.

Keywords: ultrasound imaging velocimetry, PIV, blood flow measurement

1 INTRODUCTION

There is a strong drive to improve the *in vivo* measurement of blood flow patterns. Better knowledge of hemodynamic conditions will facilitate fundamental studies into the role of hemodynamics in cardiovascular development and in pathologies (e.g. during the development of aneurysms or atherosclerosis). Apart from being useful for fundamental studies, access to such hemodynamic information would be an important diagnostic tool. For obvious reasons, non-invasive measurement techniques with sufficient spatial resolution are desirable. This resolution criterion also stems from the fact that often wall shear stresses need to be derived from the velocity fields. The use state-of-the-art optical flow measurement techniques, such as (microscopic) particle image velocimetry (PIV), are limited due to the opaque nature of blood and the limited optical access. Only in a limited number of cases those techniques can be applied, for instance in the embryonic chicken – a common model system for human cardiovascular development [1]. Direct application of these optical techniques is unfortunately not possible in human patients or healthy volunteers.

In recent years, ultrasound imaging velocimetry (also known as speckle velocimetry or “echo-PIV” [2-5]) has been introduced as an alternative technique that can provide the desired blood flow patterns non-invasively [6-10]. As it is largely based on existing echo-/sonography hardware and protocols, it is an accessible and relatively cheap method. The method uses cross-correlation algorithms to track features in subsequent frames of

an image sequence, similar to optical PIV. The main difference is the methodology to obtain images (using an ultrasound transducer rather than a camera). Note that in contrast to *Doppler* velocimetry, it provides instantaneous velocity fields of *two* velocity components. The related, additional benefit is that it does not rely on exact knowledge of the insonification angle; furthermore, the latter does not need to be optimized with respect to the mean flow direction, as two velocity components are available (i.e. not just the one along the direction of sound).

2 EXPERIMENTAL TECHNIQUES

2.1 Typical set-up and data acquisition method

To describe the basic techniques and procedures, a simple *in vitro* experiment is described that aims at measuring the velocity field of a steady laminar flow in a tube. More details are given by Poelma et al. (2010) [5].

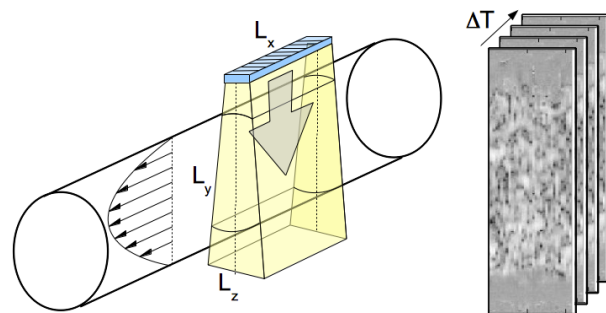


Figure 1: schematic representation of an UIV experiment (*left*) overview of geometry and orientation of the transducer (*right*) a sequence of B-mode images. Image adapted from Poelma et al., (2012) [10].

A transducer, here a linear phased array with 128 elements, is aligned with the tube axis (see Figure 1). As the working fluid by itself (water) has very little scattering efficiency, the flow must be seeded with a material with good acoustic scattering properties. “Good acoustic scattering” can be realized by using a dispersed material that has a large difference in acoustic impedance compared to the surround fluid. Here, a small amount of SonoVue contrast medium (SF_6 microbubbles) is added to the water. These scatterers are imaged in subsequent frames by the transducer, which emits at 7 MHz. Data is recorded as RF signals using an Ultrasonix RP500 system. The data can be converted (offline) to so-called B-mode images by means of envelope detection and log compression. The latter step is mainly used for visual inspection, but is not required (and often actually detrimental) for flow analysis. Image acquisition rates are typically in the tens to hundreds frames per second, see later.

2.2 Data processing

The sequence of RF data is processed using local cross-correlation, as in conventional PIV [11]: the total image is divided into smaller regions, so-called interrogation areas. The size of these interrogation areas ultimately determines the spatial resolution of the measurement. However, smaller interrogation areas also lead to a lower signal-to-noise ratio. Therefore, for each experiment (flow and imaging conditions, tracer concentration) the optimal size must be determined. Typically, areas of 16×16 to 64×64 pixels are used, with 50% overlap between neighboring areas. Cross-correlation of a pair of interrogation areas results in a “correlation plane” with a distinct peak at the location of the optimal shift of the particle image patterns, provided that there is a sufficient amount of particles that can be matched (see section 3). The cross-correlation is shown schematically in Figure 2. The red and blue objects indicate tracers at frame 1 and 2, respectively.

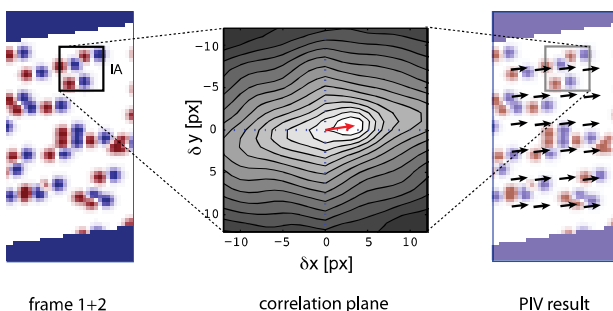


Figure 2: local cross-correlation between subsequent image frames provides the velocity field based on the mean local displacement of tracer particles (e.g. contrast bubbles).

The cross-correlation of interrogation areas is repeated for the entire image, so that a complete displacement field is generated for each image pair. The displacements can be converted to velocities by multiplication with a scaling coefficient (pixel/meter) and division by the time between subsequent frames. Note that the scaling coefficient is usually different for the x and y direction: the former is determined by the transducer pitch, while the latter is related to the wavelength of the ultrasound. The time between two subsequent frames is largely determined by the imaging acquisition rate of the ultrasound system. However, it should be noted that images are not recorded as snapshots, but are usually constructed line-by-line (sweep or ‘rolling shutter’). This means that – in the present case – any horizontal displacement will require a correction of the time between frames (ΔT); see e.g. Poelma et al. (2011) or Beulen et al. (2010) [4, 5] for a detailed discussion.

2.3 Typical results

A typical UIV result consists of one or more instantaneous two-dimensional velocity fields, describing the flow in a slice extending from the transducer (see also Figure 1). This transducer also determines the width L_x of the field-of-view (assuming that all transducer elements are used). The depth L_y is an acquisition setting. Note that larger values of L_y lead to lower frame rates (due to the finite velocity of sound, typically around 1500 m/s). The quality of the image decreases with increasing y coordinate due to attenuation and divergence of the ultrasound beams. The thickness of the measurement slice (L_z) is typically of the order of 1.5 mm and determined by the hardware design and beam focusing settings [10].

An example of a typical velocity field and a reference B-mode image are shown in Figure 3. Here, the flow in a curved, non-transparent tube has been measured; note the strong asymmetry in the flow profile - increasing with the flow from left to right - due to secondary flow patterns. The total field-of-view was $4.9 \times 2.5 \text{ cm}^2$, with an in-plane spatial resolution of 0.5 mm. Errors in the averaged flow velocities were estimated to be below 1% of the maximum velocity.

2.4 (Phase-)Averaging strategies

For steady or periodic flows it is possible to significantly enhance the signal-to-noise ratio by averaging the results. In particular, averaging the intermediate *correlation planes*, rather than the vector fields, is known to greatly improve the results [11, 12]. Averaging is often essential due to the relatively low signal-to-noise ratio of UIV images, as compared to conventional PIV images. For steady flows, the averaging is straightforward. However,

one must be careful with the interpretation of averaged PIV results from transient flows [13].

For periodic flows, the image sequence can be sorted before averaging by making use of an external trigger signal or by “self-gating”. In the latter method, a rough estimate of the flow field is used to determine the phase of the image frames; data with a similar phase is subsequently averaged [12]. For data that is sufficiently oversampled (i.e. the frame rate is relatively high compared to the highest frequencies of the flow), a sliding averaging approach can be utilized. In this method, a vector field is not obtained from a single image pair, but from a (small) series of frames (e.g. averaging frames 1-5, 3-7, 5-9, etc.). This technique can obviously be applied to any transient flow, not just periodic flows. Due to the high imaging rate requirements (discussed in the section 3), many flows studied by UIV are oversampled and thus suitable for this sliding averaging processing.

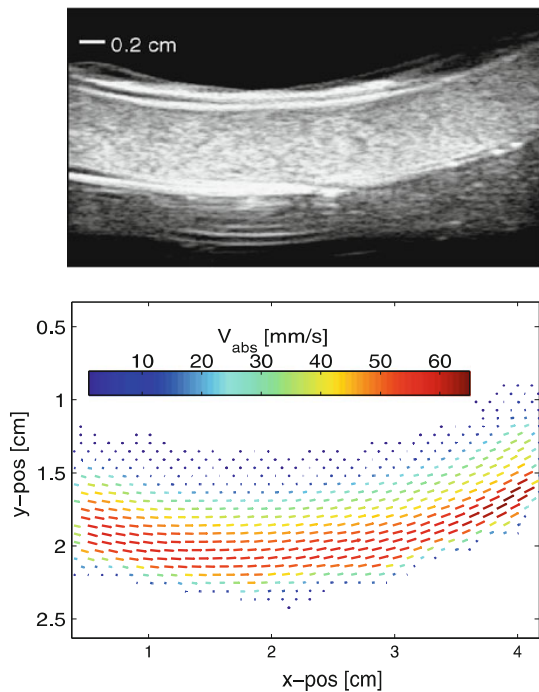


Figure 3: A typical velocity field resulting obtained with UIV; top image shows one B-mode image; the bottom figure is the corresponding mean flow pattern. Image adapted from Poelma et al. (2011) [5].

3 DISCUSSION

3.1 Resolution, dynamic range

The resolution that can be achieved by a UIV measurement depend on a number of factors: the *image* resolution in the lateral (“x”) direction is mostly dictated by the transducer design, i.e. the pitch between elements. However, the way a vertical image line is obtained (e.g. by firing multiple elements, beam forming) can lead to overlapping “cones” of neighboring imaging lines. This in turn

can introduce artifacts when one tries to achieve sub-pixel accuracy in the displacement [10]. For each velocity vector, a number of horizontal pixels is used (the width of an interrogation area), typically 8-64. This number, multiplied by the transducer pitch, serves as a good estimate of the horizontal measurement resolution.

In the axial (“y”) direction, the image resolution is determined by the frequency of the ultrasound. Higher frequencies result in a better resolution. Depending on the frequency, axial image resolutions range from 1 mm (low frequency, 2-5 Mhz) to as fine as 30 micron (high frequency, 30-50 Mhz). However, higher resolutions come at the price of higher attenuation (and thus signal degradation). In practice, one thus has to compromise between measurement depth and resolution. Typical ultrasound frequencies in the range of 2-50 Mhz are used, with corresponding penetration depths from tens of centimeters to a few millimeters. As stated earlier, the axial resolution is usually significantly better than the lateral resolution. Values of the spatial resolution of an UIV *measurement* (not *image*) as small as 0.1 and 0.4 mm respectively have been reported. This was achieved for a time-averaged flow, which permitted small interrogation areas [14].

Apart from resolution, the dynamic range of the UIV technique needs to be discussed. This range describes the minimum and maximum velocity that can be measured. The location of the displacement peak in the correlation plane (Figure 2) can in practice only be determined with a finite accuracy. This means that there is a lower limit for the velocities that can be measured. For conventional PIV, this lower limit (i.e. the random error in the displacement) is usually around 0.1 pixel for properly optimized experiments; it is questionable if the same can be achieved for UIV due to the noisy character of the data. Larger displacements will mean the relative contribution from the inaccuracy in the peak location will decrease. However, for the correlation algorithm, it is essential that features can be tracked: a certain fraction of a group of particles must remain within the interrogation area used for the correlation. For large displacements, particles will move out of the interrogation area (or even out of the total field of view)[15]. This means that the displacement must be optimized to balance between the two errors (peak location, loss of particles). In practice, a displacement of 4-8 pixels is common in PIV. This directly dictates the required time between subsequent frames – assuming that the velocity to be measured is fixed. For cardiovascular flows, which can be as fast as 1 m/s, this means that imaging rates of 100-1000 fps are required [10]. This is beyond the capabilities of many ultrasound machines. However, frame rates can be increased

by using a smaller subset of the transducer elements. Alternatively, dedicated hardware can be used, which is designed for velocimetry, rather than conventional imaging [16].

3.2 Comparison with other techniques

Ultrasound is a relatively cheap and accessible measurement technique that can provide velocity fields in applications without optical access. In recent years, other techniques have been introduced that have similar capabilities. In particular, techniques based on magnetic resonance imaging have shown to be very powerful [17]. The resolution that can be obtained is superior: for instance, Van Ooij et al. report a resolution of $0.2 \times 0.2 \times 0.33 \text{ mm}^3$ in a pc-MRI experiment using a 3T system with a 7 cm coil [18]. Furthermore, these measurements provide volumetric/3D data, something that has currently not been demonstrated using ultrasound (unless the transducer is translated [5]). Such MRI measurements require a long measurement time, however. A further drawback of MRI is the complexity of the hardware, which translates into high costs (acquisition and operating) and personnel training requirements. Finally, the strong magnetic field restricts the use of materials that can be used in/near the facility, so that experiments need to be designed carefully.

Another recent technique for flow measurement in non-transparent flow utilizes x-rays. These measurements are based on the attenuation of rays from one or more radiation sources [19]. As the attenuation represents the projection along the trajectory (i.e. the average along a line through the flow domain), some form of tomographic reconstruction is required to obtain a 3D spatial field. This means that multiple projections are necessary to reconstruct the average flow field, e.g. by either rotating the source or the actual flow geometry. If the flow is rotationally-symmetric, the flow field can be reconstructed from a single view [20]. While very promising for particular applications, the safety restrictions and hardware complexity make these techniques much less accessible than ultrasound-based techniques.

3.2 Translation to other application areas

The majority of research in UIV is performed with application to cardiovascular flow in mind. This is understandable, as the hardware that is used is already present in clinical settings. Nevertheless, it is interesting to note that one of the first flow measurements using UIV was in the field of sediment transport [21]. In this study, flow fields were studied in densely-laden liquid flows that were not accessible to optical techniques. Surprisingly, there has been little follow up with similar

applications. UIV seems a perfect fit for measurement of multiphase flows. The presence of two phases (with likely a difference in acoustic impedance, e.g. oil droplets or fibers in water) seems naturally suited for UIV. Certain conditions may need to be avoided, however: for instance, very large air bubbles will lead to strong reflections and shadowing effects. Relatively little is known how to optimize these ultrasound images for velocimetry – i.e. what kind of post-processing improves flow velocity measurement, rather than imaging? Some techniques can be borrowed (e.g. harmonic imaging), while others may need to be avoided (general “image enhancement” filtering).

A drawback that remains is the limit of maximum velocities that can be measured. In particular, this limits the application in many industrial flow applications. New hardware [16] and advanced imaging methods are presently being developed to remedy this.

4. CONCLUSIONS

Ultrasound Imaging Velocimetry can provide instantaneous velocity fields in flows without the need for optical access. This makes it possible to measure, non-invasively, in opaque flows. Compared to alternative techniques (based on MRI or x-rays), it is relatively simple, safe and cheap and can have a comparable spatial resolution. While the majority of development work so far has focused on cardiovascular flow, the technique seems very suitable to applications in other application areas. It is very likely that successful studies in e.g. process technology, food industry and other areas will be reported in the literature soon.

REFERENCES

- [1] Poelma C, Van der Heiden K, Hierck BP, Poelmann RE and Westerweel J "Measurements of the wall shear stress distribution in the outflow tract of an embryonic chicken heart" *Journal of the Royal Society Interface* 7 (42) 91-103 (2010)
- [2] Kim H, Hertzberg J, Shandas R. "Development and validation of echo PIV" *Experiments in Fluids* 36 (3) 455–462 (2004)
- [3] Zheng H, Liu L, Williams L, Hertzberg JR, Lanning C, Shandas R "Real time multicomponent echo particle image velocimetry technique for opaque flow imaging" *Applied Physics Letters* 88:261915 (2006)
- [4] Beulen B, Bijnens N, Rutten M, Brands P, van de Vosse F "Perpendicular ultrasound velocity measurement by 2D cross correlation of RF data. Part A: validation in a straight tube" *Experiments in fluids* 49(5) 1177–1186 (2010)
- [5] Poelma C, Mari JM, Foin N, Tang MX, Krams R, Caro CG, Weinberg PD and Westerweel J "3D Flow

- reconstruction using ultrasound PIV" *Experiments in Fluids* 50 (4) 777-785 (2011)
- [6] Sengupta PP, Khandheria BK, Korinek J, Jahangir A, Yoshifuku S, Milosevic I, et al. "Left Ventricular Isovolumic Flow Sequence During Sinus and Paced Rhythms New Insights From Use of High-Resolution Doppler and Ultrasonic Digital Particle Imaging Velocimetry" *Journal of the American College of Cardiology* 49(8) 899-908 (2007)
- [7] Hong GR, Pedrizzetti G, Tonti G, Li P, Wei Z, Kim JK, et al. "Characterization and Quantification of Vortex Flow in the Human Left Ventricle by Contrast Echocardiography Using Vector Particle Image Velocimetry" *JACC: Cardiovascular Imaging* 1(6) 705-717 (2008)
- [8] Kheradvar A, Assadi R, Falahatpisheh A, Sengupta PP "Assessment of Transmitral Vortex Formation in Patients with Diastolic Dysfunction" *Journal of the American Society of Echocardiography* 2011
- [9] Zhang F, Lanning C, Mazzaro L, Barker AJ, Gates PE, Strain WD, et al. In Vitro and Preliminary In Vivo Validation of Echo Particle Image Velocimetry in Carotid Vascular Imaging. *Ultrasound in medicine & biology* 37(3) 450-464 (2011)
- [10] Poelma C, van der Mijle R, Mari J, Tang MX, Weinberg PD and Westerweel J "Ultrasound imaging velocimetry: Toward reliable wall shear stress measurements" *European Journal of Mechanics-B/Fluids* 35 70-75 (2012)
- [11] Adrian R and Westerweel J "Particle Image Velocimetry" Cambridge University Press (2010)
- [12] Poelma C, Vennemann P, Lindken R and Westerweel J "In vivo blood flow and wall shear stress measurements in the vitelline network" *Experiments in Fluids* 45 (4) 703-713 (2008)
- [13] Poelma C and Westerweel J "Generalized displacement estimation for averages of non-stationary flows" *Experiments in Fluids* 50 (5) 1421-1427 (2011)
- [14] Fraser KH, Zhou B, Poelma C, Tang MX, Weinberg PD "Towards Small Animal Echo-PIV" *Bioengineering* 2012 6th - 7th September, Said Business School, Oxford
- [15] In general, the so-called "quarter-rule" indicates that the maximum in-plane tracer particle displacement must be limited to a quarter of the interrogation area size to obtain good results [Adrian & Westerweel, 2010]. Iterative analysis schemes ("window shifting") relax this limitation somewhat, but nevertheless the displacement of tracer particles must be bounded to avoid out-of-plane and flow curvature effects.
- [16] Liu L, Zheng H, Williams L, Zhang F, Wang R, Hertzberg J and Shandas R "Development of a custom-designed echo particle image velocimetry system for multi-component hemodynamic measurements: system characterization and initial experimental results" *Physics in medicine and biology* 53 1397 (2008)
- [17] Elkins CJ and Alley MT "Magnetic resonance velocimetry: applications of magnetic resonance imaging in the measurement of fluid motion" *Experiments in Fluids* 43 (6) 823-858 (2007)
- [18] Van Ooij P, Guédon A, Poelma C, Schneiders J, Rutten M, Marquering HA, Majoie CB, Van Bavel E and A. Nederveen J "Complex flow patterns in a real-size intracranial aneurysm phantom: phase contrast MRI compared with particle image velocimetry and computational fluid dynamics" *NMR in Biomedicine* 25 (1) 14-26 (2011)
- [19] Mudde RF "Bubbles in a fluidized bed: a fast X-ray scanner" *AIChE Journal* 57 (10) 2684-2690 (2011)
- [20] Irvine SC, Paganin DM, Jamison RA, Dubsky S and Fouras A "Vector tomographic X-ray phase contrast velocimetry utilizing dynamic blood speckle" *Optics Express* 18 (3) 2368-2379 (2010)
- [21] Crapper M, Bruce T and Gouble C "Flow field visualization of sediment-laden flow using ultrasonic imaging" *Dynamics of Atmospheres and Oceans* 31 (1-4) 233-245 (2000)

Time dependent 2D flow structure measurements arising from melt stirring by means of various AC magnetic fields

Sven Franke^{a,b}, Dirk Rübiger^b, Jürgen Czarske^a, Gunter Gerbeth^b and Sven Eckert^b

^a Laboratory of Measurement and Testing Techniques, Faculty of Electrical Engineering and Information Technology, Technische Universität Dresden, 01062 Dresden, Germany

^b Department Magnetohydrodynamics, Institute of Fluid Dynamics, Helmholtz-Zentrum Dresden-Rossendorf, P.O. Box 510119, 01314 Dresden, Germany

We present an experimental study concerning the flow inside an isothermal liquid metal column exposed to various magnetic field configurations. This paper is aimed at highly resolved, quantitative velocity measurements in the eutectic alloy GaInSn by means of the pulsed-wave ultrasound Doppler method. A novel ultrasound system was used to measure two-dimensional velocity fields of the secondary flow in the radial-meridional plane. The imaging system employs two arrays each of 25 transducer elements allowing for a fast electronic traversing with concurrently high spatial and temporal resolution. The study considers time-modulated fields or combinations of traveling magnetic fields (TMF) and rotating magnetic fields (RMF) revealing different flow structures and flow intensities. The results demonstrate different variants of electromagnetic melt stirring, some of them showing the potential to enhance the stirring efficiency and to optimize casting properties during solidification.

Keywords: Ultrasound Doppler method, flow field measurements, electromagnetic stirring, rotating magnetic field, magnetohydrodynamics, flow control

1 INTRODUCTION

AC magnetic fields unlock an enormous potential to realize a variety of flow structures in molten metals, which makes the electromagnetic stirring attractive for controlling the melt flow during solidification [1]. However, electromagnetically-driven melt convection may also produce segregation freckles on the macroscale [2]. The achievement of superior casting structures needs a well-aimed control of melt convection during solidification, which in turn requires a detailed knowledge of the flow structures.

Previous investigations considered the use of time-modulated rotating magnetic fields to control the heat and mass transfer at the solidification front [3]. It has been shown recently under laboratory conditions [4], that an accurate tuning of the magnetic field parameters can avoid segregation effects, however, a mismatch of the relevant modulation parameter deteriorate the results. Another idea concerns a superposition of RMF and TMF. However, a simultaneous application of RMF and TMF with comparable field frequencies generates a stationary three-dimensional force which breaks the axial symmetry of the flow [5]. Instead operating both fields at the same frequency we studied the case of a small frequency shift in the present study.

Our activities aim at an efficient strategy for adjusting the microstructure of castings by optimizing the melt convection during solidification. We propose the application of modulated or superimposed AC magnetic fields as a new approach of electromagnetic melt agitation, which should overcome the segregation effects known from the conventional electromagnetic stirring.

2 FLOW MAPPING SYSTEM

The pulsed ultrasound Doppler method has proved as a reliable and attractive flow measuring technique for non-transparent fluids as liquid metals [6]. However, a multidimensional flow mapping with a sufficient spatial and temporal resolution, as required for a detailed study of time-dependent flow structures, is distinctly limited with current ultrasound Doppler devices [7]. Hence, we developed a two-dimensional ultrasound Doppler velocimeter utilizing two linear transducer arrays [8, 9]. Each array is segmented into 25 plane transducer elements of $2.4 \times 5 \text{ mm}^2$ with an element pitch of 2.7 mm (fig. 1).

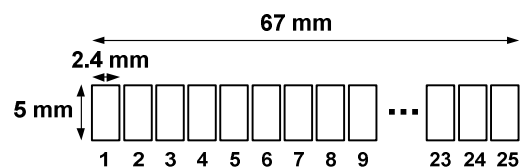


Figure 1: Design of a linear transducer array

A single array allows the flow field measurement of the velocity component perpendicular to the transducer surface. In an orthogonal arrangement of the arrays both components of the velocity field in the spanned measuring plane of $67 \times 67 \text{ mm}^2$ can be acquired [10]. Other array configurations are possible as well.

An electronic traversing by means of a specific time-division multiplex scheme provides a high spatial as well as a high temporal resolution. A suitable spatial resolution is achieved by the operation principle of segmental arrays: In operation two adjacent

transducer elements are interconnected to act as one transducer of approx. $5 \times 5 \text{ mm}^2$ resulting in a low beam divergence over the measuring depth. However, this active transducer pair, equivalent to the measuring line of the velocity profile, can be shifted by only one element pitch. In summary the lateral resolution of approx. 3 mm in the focal point is in the same magnitude as the measuring line pitch of the velocity profiles of 2.7 mm [8].

Two novel approaches are implemented to extend the temporal resolution [9, 10]. The first method concerns a multi-beam operation which is aimed at to scan as many profile measuring lines (respectively transducer pairs) in parallel as possible. There, a sufficient distance between the simultaneously excited transducer pairs is selected to reduce the crosstalk (due to the divergence of the ultrasonic beam) between the active measuring lines below a tolerable level of -40 dB [8]. The second method is related to the pulsing strategy: For the evaluation of a single velocity profile a multiplicity of typically 30 to 100 echo signals is needed. Conventional multiline systems acquire the echo signals of the separate profile lines successively resulting in a distinct time difference between the acquisition of the first and of the last measuring line meanwhile the flow structure may change distinctly. The experimental conditions of most of our small scale model experiments reveal an echo acquisition time much shorter than the pulse repetition time. Our second approach utilize this idle time to acquire the echo signals of further measuring lines. This interlaced echo signal acquisition in combination with the multi-beam operation allows to measure the entire flow field in the same time as a conventional device acquires a single velocity profile. Frame rates of flow mapping up to 30 fps are achieved typically.

The multiplex scheme involving all introduced approaches is shown in figure 2. The technical implementation of the measuring system is described in [9] and [10] in detail.

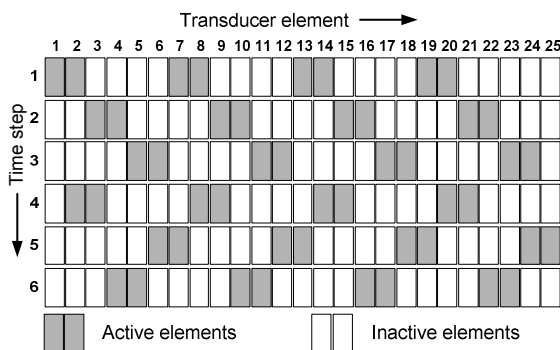


Figure 2: Multiplex scheme for single array

3 EXPERIMENTAL SETUP

A schematic view of the experimental setup is shown in figure 3. A cylindrical vessel made of perspex was used with an aspect ratio $A = H_0/2 \cdot R_0 = 1$.

The size of the inner diameter of $D = 2 \cdot R_0$ and the height H_0 was chosen to be 67.5 mm. The cylinder is closed by rigid lids and filled with the eutectic alloy GaInSn. The experiments were performed in the magnetic induction system PERM at HZDR with a bore diameter of 200 mm, wherein the fluid vessel was placed concentrically. The magnetic system consists of a circular arrangement of six induction coils and six induction coils arranged one above the other for generating a RMF or TMF, respectively. A magnetic field frequency f_{RMF} of around 50 Hz was selected being small enough to neglect any influence arising from the skin effect. In order to preclude flow artifacts arising from symmetry deviations of the experimental setup (vertical alignment, conformity of both the cylinder and the magnetic field axis), special care was necessary to ensure a precise positioning of the cylinder inside the magnetic system.

A flow mapping of the radial-meridional flow was carried out with one transducer array at the lower lid measuring the vertical velocity u_z across the meridional cross section. Due to constructive limitations the second array was not applied. For the flow investigations in this setup the second component of the measuring plane is not mandatory because of the axial symmetry of the vessel. The spatial resolution in lateral direction varies from 5 mm at the sensor over 3 mm at the focal point to approximately 7.5 mm at the lid of the fluid vessel. In axial direction a spatial resolution of about 1.4 mm was achieved. The velocity data were acquired with sampling frequencies between 0.5 and 13 Hz.

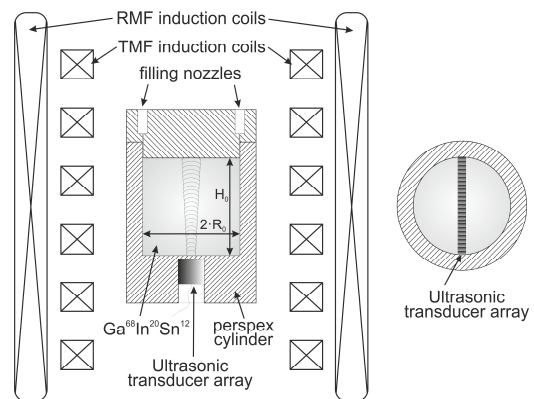


Figure 3: Schematic drawing of the experimental setup

4 RESULTS

In the first study a continuous RMF was applied generating a swirling flow in the primary azimuthal plane. Figure 4a displays a schematic drawing and figure 4b a representative snapshot of the flow structure of the secondary meridional plane occurring at a magnetic field strength of $B_0 = 0.46 \text{ mT}$. It becomes apparent that the main secondary flow structure in the form of two toroidal vortices is represented by the upward and downward flow

components, whereas Taylor-Görtler vortices can be observed additionally in the midplane on the left sidewall. In this case the magnetic field strength generates a flow structure slightly above the threshold of instability, which manifests itself in form of such vortices.

Figure 5 illustrates the transient behavior of the flow on power up the RMF ("spin-up") for $B_0 = 0.46$ mT. For evaluating the different variants of electromagnetic stirring the vertical velocity of the radial-meridional plane is averaged across the volume of the cylinder (assuming an axisymmetric flow) as a

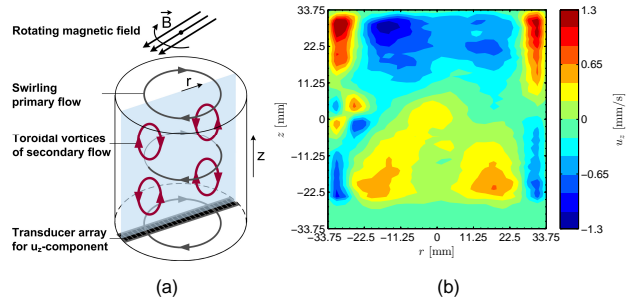


Figure 4: Schematic drawing (a) and snapshot (b) of double vortex of meridional plane at cont. RMF ($B_0 = 0.46$ mT)

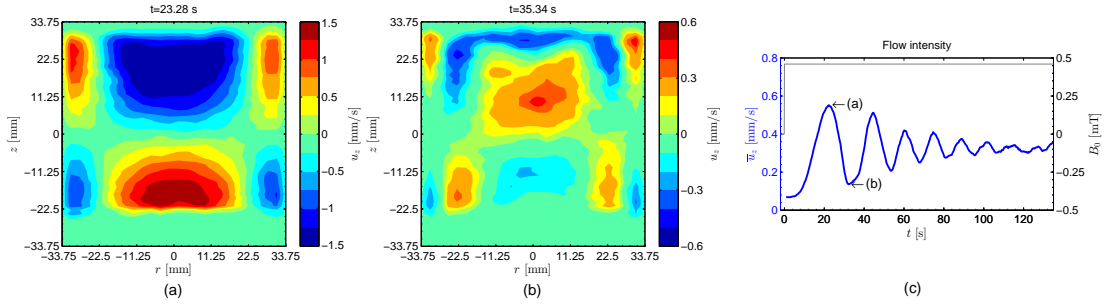


Figure 5: Flow pattern of a RMF spin-up process ($B_0 = 0.46$ mT)

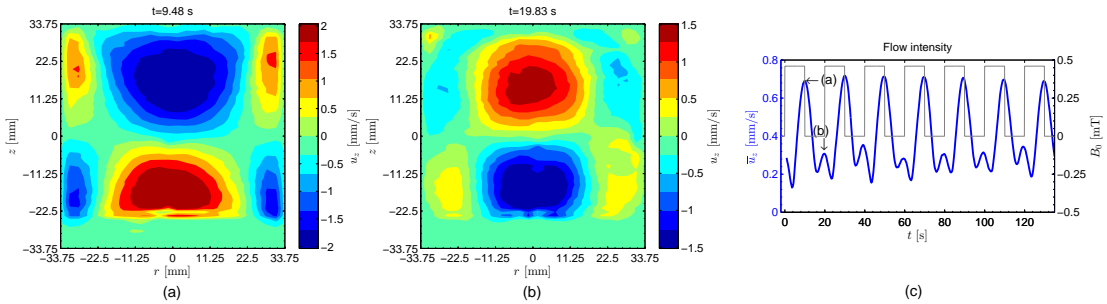


Figure 6: Flow pattern of a pulsed RMF at resonant pulse cycle duration ($T_P = 20$ s, $B_0 = 0.46$ mT)

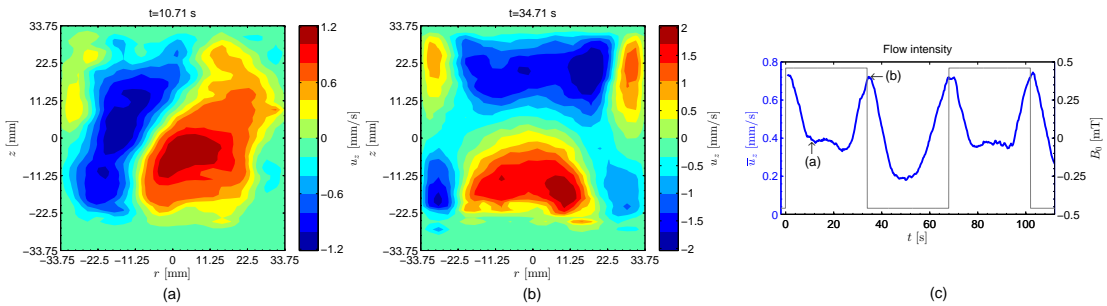


Figure 7: Flow pattern of an alternating RMF at resonant pulse cycle duration ($T_P = 68$ s, $B_0 = 0.46$ mT)

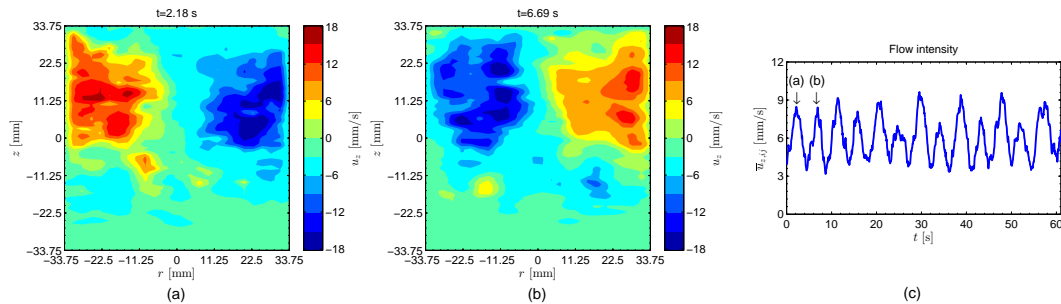


Figure 8: Flow pattern of a combined RMF and TMF ($B_{0,RMF} = 1.1$ mT, $B_{0,TMF} = 1.3$ mT, $\Delta f = 0.1$ Hz)

measure of the flow intensity:

$$\bar{u}_z = \frac{1}{H_0 R_0^2} \int_0^{H_0/2} \int_{-R_0}^{R_0} r \sqrt{u_z^2} dr dz \quad (1)$$

The time course $\bar{u}_z(t)$ of the spin-up (blue curve in figure 5c) reveals a transient oscillation with a distinct overshoot. The grey curve illustrates the course of the magnetic field. Figure 5a represents the double vortex structure occurring at the first maximum of flow intensity. At the first intensity minima a higher mode of vortex structure arises as shown in figure 5b.

The application of a pulsed RMF initiates the fluid flow to experience a sequence of spin-up and spin-down processes at particular pulse cycle durations revealing a flow pattern as shown in figure 6. The secondary flow is characterized by permanent reversals of the flow direction of the basic double vortex. Figure 6a shows the typical vortex structure where the secondary flow in the central region is directed upwards in the bottom part and downwards in the upper part of the cylinder. In contrast the snapshot in figure 6b reveals the “inverse” toroidal double vortex not arising at a continuous stirring. Figure 6c illustrates the oscillating behavior of the flow intensity showing up global and local maxima. The flow structure of figure 6a coincides to the global maxima whereas the flow pattern of figure 6b is found at the local maxima. In comparison to the continuously applied RMF a significant increase in the flow intensity especially in the central region can be noticed.

Another example for a modulated RMF is displayed in figure 7. The application of pulse sequences of alternating direction induces the formation of a big circulation role (fig. 7a) between the rising and falling edge of each pulse. At the edges the flow intensifies to its maximum resulting in a frequency doubling of the flow oscillation toward the frequency of the pulse sequence (fig. 7c). The flow structure at the edges reveals the normal toroidal double vortex (fig. 7b). At the alternating RMF, too, an intensification of the secondary flow in comparison to the permanent stirring with the same magnetic field strength is achieved.

A completely other approach is the superposition of RMF and TMF with a small difference of the respective field frequencies. It is known that a combination at the same frequency generate a strong circulation role in the meridional plane which is stable in space [5]. In case of a small difference in the frequency, this circulation role begins to rotate and generates therewith a flow with alternating flow direction, but, keeping their symmetry in the long-term average. Two snapshots of such a fluid pattern with a phase shift of 180° to each other are shown in figure 8a and 8b. The averaged midplane velocity

$\bar{u}_{z,ij}(t)$ in figure 8c illustrates the rotation of the circulation role.

5 SUMMARY AND CONCLUSIONS

In this study we investigated the impact of electromagnetic stirring by means of various AC magnetic fields on the flow structure in a metal melt. Thereto a liquid metal column of the eutectic alloy GaInSn was exposed to continuous as well as pulsed rotating magnetic fields. In addition a combination of RMF and TMF was considered. The temporal-spatial flow pattern in the column was measured with a new two-dimensional ultrasound system providing a spatial and temporal resolution previously not attained.

It was shown that a powered on RMF induce a distinct transient oscillation of flow. The enforcement of a sequence of such spin-up and spin-down processes at pulsating and alternating RMFs results in a considerable intensification of the meridional flow in comparison to a continuous RMF. A combined RMF and TMF also increases the flow intensity. Furthermore, beside the flow intensification, the continuous transitions among the flow structures (e.g among double vortex and inverse double vortex) avoid segregations and provide prospects for tailoring the microstructure of the solidifying alloy [4].

REFERENCES

- [1] Willers B et al: The columnar-to-equiaxed transition in Pb–Sn alloys affected by electromagnetically driven convection, *Mat. Sci. Eng. A* 402 (2005), 55-65.
- [2] Nikrityuk PA et al: A numerical study of unidirectional solidification of a binary metal alloy under influence of a rotating magnetic field, *Int. J. Heat Mass Transfer* 46 (2006), 1501-1511.
- [3] Eckert S et al: Efficient Melt Stirring Using Pulse Sequences of a Rotating Magnetic Field: Part I. Flow Field in a Liquid Metal Column, *Metall. Mater. Trans. B* 38B (2007), 977-988.
- [4] Willers B et al: Efficient Melt Stirring Using Pulse Sequences of a Rotating Magnetic Field: Part II. Application to Solidification of Al-Si Alloys, *Metall. Mater. Trans. B* 39B (2008), 304-316.
- [5] Cramer A et al: Experimental investigation of a flow driven by a combination of a rotating and a traveling magnetic field, *Phys. Fluids* 19 (2007), 118109
- [6] Takeda Y: Development of an ultrasound velocity profile monitor, *Nucl. Eng. Design*, 1991, 126: 277-284.
- [7] Takeda Y, Kikura H: Flow mapping of mercury flow, *Exp. Fluids* 32 (2002), 161-169.
- [8] Franke S et al: Ultrasound Doppler system for two-dimensional flow mapping in liquid metals, *Flow Meas. Instrum.* 21 (2010), 402-409.
- [9] Franke S et al: 2d-2c Ultrasound Doppler Array Velocimeter for Flow Investigations in Liquid Metals, 7th ISUD, Göteborg (2010), 89-92.
- [10] Franke S et al: Two-dimensional Ultrasound Doppler Velocimeter for Investigations of Liquid Metal Flows, 15th Int. Conference on Sensors and Measurement Technology, Nuremberg (2011), 165-170.

Application of UDV for Studying the Flow and Crystallization of Liquid Metal in the Process of Electromagnetic Stirring

Ilya Kolesnichenko^{1,2}, Ruslan Khalilov¹, Pavel Oborin¹, Alexander Pavlinov¹

¹ Institute of Continuous Media Mechanics, Ural Branch of the Russian Academy of Sciences

Korolyov str. 1, Perm, 614013, Russia

² Perm National Research Polytechnic University

Komsomolsky ave. 29, Perm, 614000, Russia

We study the operation of the MHD stirrer in a cylindrical channel with a liquid metal based on the results of experiments and 3D numerical simulations. The investigations described in this paper are focused on hydrodynamic and crystallizing processes. Experimental investigations of the velocity field and its oscillations in a cylindrical crucible filled with a gallium alloy were performed using ultrasonic Doppler velocimeter measurements. The results of testing experiment in the plane layer showed that the UDV device has the advantage of determining the solid-liquid interface without direct contact of the UDV probe with the melted metal. The results of measurements allowed us to trace the evolution of the flow velocity and solid-liquid interface.

Keywords: travelling and rotating magnetic fields, continuous casting, mixing of melting metal

1 INTRODUCTION

Many technological processes (continuous ingot casting, preparation of special alloys) are accompanied by crystallization of metal in a liquid phase. The efficiency of these processes can be essentially improved by stirring molten metals. Under real operating conditions testing of the currently used stirring regimes for adequacy is a very complicated problem. With the advent of modern, high precision devices, the analysis of these processes can be readily accomplished under the laboratory conditions. The investigations made by the author provide the basis for finding the most optimal process parameters and configuration. Experiments with metals in industrial environment requires greater effort and special equipment. Modeling of metallurgical processes in the laboratory conditions using special metal alloys with low melting point allows us to bypass the obstruction [1].

In this paper, the flow and crystallization process are studied using the gallium alloy (87.5% Ga; 10.5% Zn; 2% Sn), which is in a liquid state at room temperature. The objective of this study is to explore the process of crystallization in a liquid metal in the presence of a vortex flow and to determine the optimal conditions for effective metal stirring.

The volume of liquid metal is under the action of the alternating magnetic field. In the liquid metal the alternating magnetic field induces a vortex electric current. The interaction of the electric current with the magnetic field generates an electromagnetic force, which initiates a vortex stirring flow. Due to the non-uniform action of the electromagnetic (em-) force the initiated flow is unstable and has a complicated vortex structure. The investigations are focused on the electromagnetic and hydrodynamic

processes. The stirrer consists of ferromagnetic cores *I* (fig. 1) and a set of copper coils, which generate an alternating magnetic field inside a cylindrical volume. One part of the coils generates the rotating magnetic field (RMF) and the other generates travelling magnetic field (TMF) along the axis of the cylinder. The stirrer is also provided with an internal water cooling system *II* to avoid overheating. The entire construction is protected by a case *III* made of material, which allows a short-term contact with a melted metal. A cylindrical crucible *IV* filled with liquid metal (magnesium, aluminum, lead, tin, etc) is placed inside the cylinder.

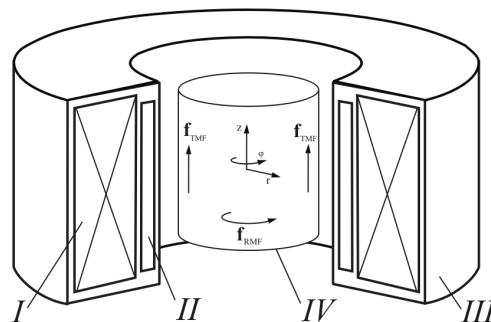


Figure 1: Sectional scheme and photo of MHD-stirrer.

2 EM-FORCE AND FLOW

We studied the forces acting on the cylinders of different height placed inside the stirrer and calculated the intensity of electromagnetic forces as a function of the value and the frequency of feeding current. The cylinders are placed inside the stirrer and have a single rotation degree of freedom coincident with the MHD-stirrer axis. Torque is defined indirectly by processing angular acceleration

measurements. It has been found that with increasing current the value of the moment grows quadratically (fig. 2). As the frequency of the electric current decreases, the moment increases (fig. 3) due to the increased penetration of the magnetic field inside the conductor – the depth of the skin layer.

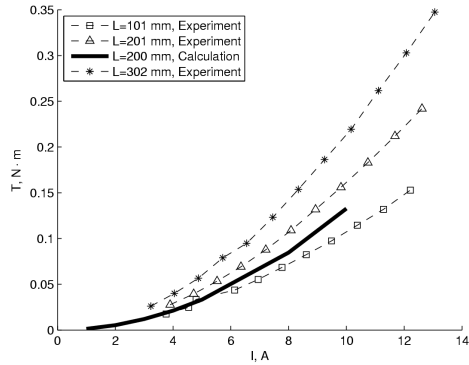


Figure 2: Torque of em-force vs coil current of RMF.

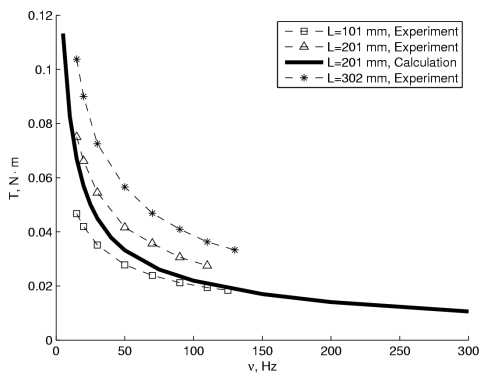


Figure 3: Torque of em-force vs frequency of RMF.

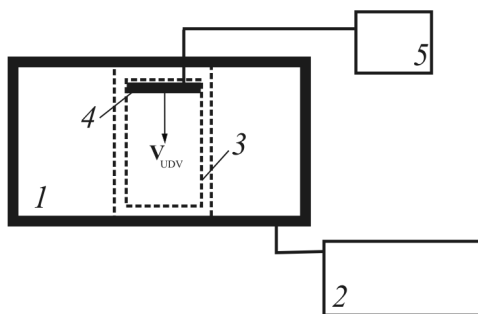


Figure 4: Scheme of the experimental setup for studying velocity.

Investigation of the velocity field was carried out in the experimental setup shown in fig. 4. The setup consists of the following part: MHD stirrer 1, power supply source for RMF and TMF coils 2, stainless steel cylindrical channel filled with liquid metal 3, UDV sensors inserted into the holder 4, and UDV 5. The vessel is filled with a gallium. To measure the velocity field we employed the UDV (DOP 2000,

Model 2125, Signal Processing, Lausanne, Switzerland). In the holder the UDV sensors 4 are arranged in row along the diameter at an equal step. This allows us to restore the flow picture in the plane [2] and to evaluate the degree of the flow symmetry. The experiment showed (fig. 5, 6) that the intensity of velocity oscillation increases with the growth of the feeding current for RMF and TMF. The errorbars are equal to rms of the velocity in fixed point. The eddies are oscillating near the equilibrium position.

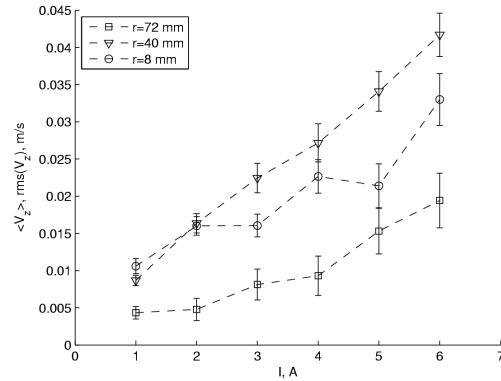


Figure 5: Mean velocity and rms vs feeding current of RMF obtained by UVD.

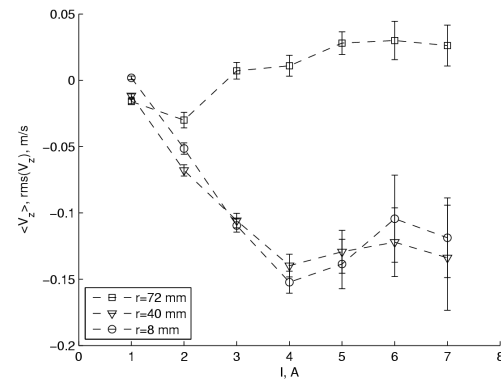


Figure 6: Mean velocity and rms vs feeding current of TMF obtained by UVD.

In calculation (fig. 7, 8) several secondary toroidal eddies are generated in the RMF case and one poloidal eddy is generated in the TMF case. The profiles have obtained for cylindrical channel of $L=0.16m$ and for $z=0.053m$. Origin point is placed on the bottom center of the cylinder. The eddies have almost the same intensity for small values of feeding current frequency. The frequency increasing leads to the growth of the eddies located close to the vertical boundary and to fading of the central eddies. The near-wall velocity increases due to the change of the em-force topology because of skin-effect. However, the flow intensity does not essentially change for the frequency values larger than 50 Hz.

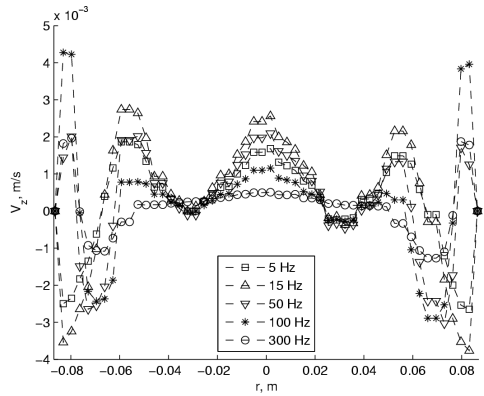


Figure 7: Numerically calculated velocity profiles for several values of RMF frequency.

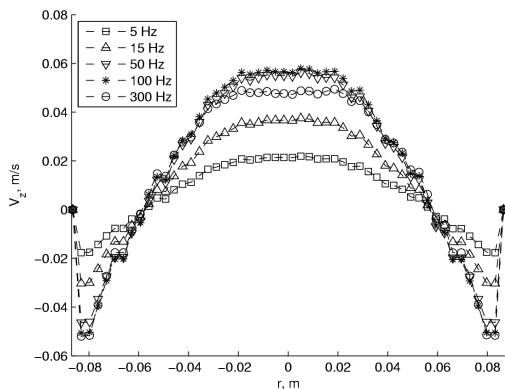


Figure 8: Numerically calculated velocity profiles for several values of TMF frequency.

3 TEST OF UDV IN THE STUDY OF PROCESS IN THE PLANE LAYER

We performed test experiment in a plane layer with free surface. The position of the interfaces obtained with UDV was compared with the interface position determined from the analysis of the obtained photographs. We investigate the flow and solidification in a thin layer of the liquid metal (fig. 9) with dimensions of 200 x 100 x 10 mm. Two opposite walls of the cell are copper heat exchangers. Two other walls, as well as the bottom of the cell are thermally insulated. The metal layer is placed into the gap of C-shaped ferromagnetic core (C-core). The bias coils place on the C-core and connect to AC power source. This leads to the generation of planar unstable vortex flow [3]. The five UDV probes were located in the hot wall. The probes emit an ultrasonic wave of a certain frequency, which falls on the solid-liquid interface. After this the wave is reflected back from the solid phase. This is clearly seen on the profile of echo signal. Using this effect it is possible to determine the solid-liquid interface in experiment.

We have tested the accuracy of the solid-liquid interface position using this technique. We studied the liquid metal layer with the free surface without MHD-stirring. The position of the interface was

defined by UDV and photo camera. The testing results show (fig. 10) that the error in the identification of the solid-liquid interface is no more than 5mm with the cell length of 200 mm. This result indicates the ability of the UDV to determine the interface without direct contact of the probe with the melted metal.

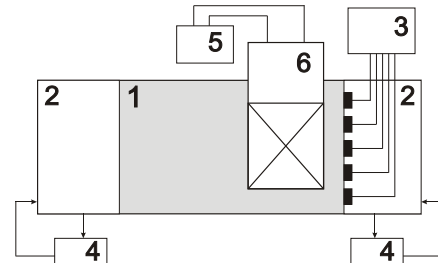


Figure 9: Scheme of the setup: 1-cell, 2- heat exchangers, 3-UDV, 4- thermostat, 5-transformer, 6-inductor.

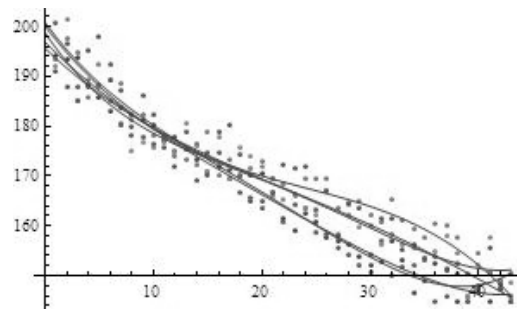


Figure 10: Evolution of the solid-liquid interface without stirring (dots – UDV data, lines – data obtained from the photo).

The investigations show, that the flow influences on the behavior and shape of the solid-liquid interface. It was found, that the crystallization rate increases with increasing intensity of stirring (fig. 11). In this case, the solid-liquid interface quickly goes to a steady state.

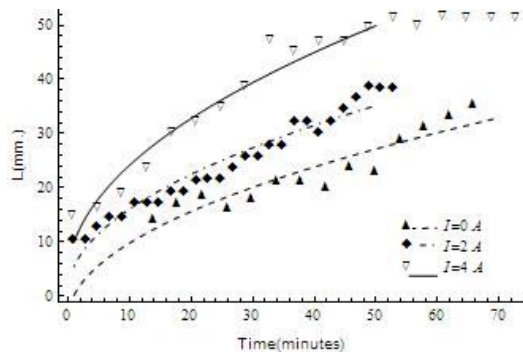


Figure 11: Evolution of the solid-liquid interface for different feeding current I of the inductor generating the flow.

4 FLOW AND CRYSTALLIZATION IN CYLINDRICAL VOLUME

To study the velocity and crystallization we have assembled the experimental setup (fig. 12). The setup consists of the following part: MHD stirrer 1, power supply source for RMF and TMF coils 2, stainless steel cylindrical channel 3 filled with gallium or gallium alloy, UVD sensors inserted into the holder 4, and UDV 5 (DOP-2000). The cold heat exchanger 6 is placed in the bottom of the cylindrical channel 3 and connected to the "cold" thermostat 7. The hot heat exchanger 8 is placed in the top of the channel and connected to the "hot" thermostat 9. When we set the temperature of the heat exchanger 6 smaller than solidification temperature the liquid metal starts to solidify. The solid-liquid interface starts to move from the bottom of the channel towards to the top. We will measure the movement of the interface as well as the evolution of the velocity profiles during solidification process. Additionally the setup includes the thermocouples, conductive velocimeters, and hall and current sensors 10 connected to multichannel data acquisition system 11. The described kit of the probes will allow us to obtain detailed information about crystallization process, evolution of the velocity, temperature, and turbulent properties of the flow. Now we are performing the experiments and calculations of the processes.

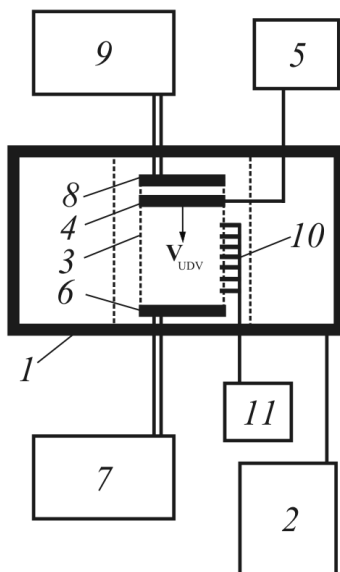


Figure 12: Scheme of the experimental setup for studying velocity and crystallization.

5 SUMMARY

We have studied the em-force, and the flow structure in liquid metal using UDV and calculations. We have measured the forces acting on the aluminum cylinders of different height inside the stirrer and calculated the intensity of em-forces as a function of the value and frequency of RMF and

TMF. The investigation of the velocity field showed that the flow was unstable already at moderate stirring. This can be seen from the low-frequency perturbations of the velocity profiles. The perturbations were caused by a drift of large-scale vortex structures through the layer of liquid metal. With the growth of the feeding current for RMF and TMF, the intensity of velocity oscillations increases. In the case of RMF, the secondary poloidal flow consists of dissimilar eddies, whereas in the case of TMF – of a single eddy. The interaction of these flows gives rise to the flow with high velocity gradients, which is an indication of intensive molten metal stirring. The obtained results allow us to proceed with studying the essentially non-stationary crystallization processes taking place in the MHD-stirrer of our design.

The results of testing experiment in the plane layer showed that the UDV device has the advantage of determining the solid-liquid interface without direct contact of the UDV probe with the melted metal. The results of measurements allowed us to trace the evolution of the flow velocity and solid-liquid interface.

This work has been supported by RFBR Grant No. 10-08-96048-r-ural-a, and by Ministry of Education of Perm Region in the frame of the project "Magnetohydrodynamical stirring of the liquid metal and its influence on the structure of solidifying alloys".

REFERENCES

- [1] Denisov S, Dolgikh V, Kolesnichenko I, Khalilov R, Khripchenko S, Verhille G, Plihon N, Pinton J.-F: Flow of liquid metal in a cylindrical crystallizer generating two-directional MHD-stirring. *Magnetohydrodynamics*, 46 (2010), 69-78.
- [2] Kolesnichenko I, Khripchenko S, Buchenau D, Gerbeth G: Flow in a square layer of conducting liquid. *Magnetohydrodynamics*, 41 (2005), 39-51.
- [3] Kolesnichenko I, Khalilov R, Khripchenko S: Vortical flow of conducting fluid driven by an alternating magnetic field in a plane channel. *Magnetohydrodynamics*, 43 (2007), 45-52.

Flow measurements in a model of the Czochralski crystal growth process

Josef Pal, Andreas Cramer and Gunter Gerbeth

Helmholtz-Zentrum Dresden-Rossendorf, P.O. Box 510119, D-01314 Dresden, Germany

An experimental study of the buoyancy-induced flow in a model of a Czochralski crystal growth system was conducted. Ultrasonic velocimetry was used to measure fluid velocities. To have similar thermal boundary conditions as in an industrial growth facility, a double walled glass crucible flown through by a heating fluid was chosen to hold the fluid. Similarity of the heat transfer conditions was achieved by selecting GalSn as liquid metal under investigation. Due to the double-walled crucible, measurements through the container wall are difficult if ever possible. Since the availability of short ultrasonic transducers it is practicable to have the sensor immersed into the fluid. Measurements of the radial velocity component shortly below the melt surface across the entire diameter of the crucible at various azimuthal angles reveal the complex flow structure of natural convection in a Czochralski crucible. As it is not to be expected to grow high quality mono-crystalline crystals from a non-axisymmetric flow, rotating magnetic fields (RMF) are often proposed to render the flow more axisymmetric. This paper also addresses the question what happens to the buoyancy-driven flow when such an RMF is applied.

Keywords: Czochralski crystal growth, Rayleigh-Bénard convection, ultrasonic flow measurement, magnetohydrodynamics, electromagnetic stirring

1 INTRODUCTION

The mass production of mono-crystalline silicon by the Czochralski (Cz) technique has initiated a huge amount of research on the convection inside the crucible. Most of the investigations are numerical 2D simulations owing to the costly calculations in the full 3D case. Experimental work, on the other hand, is basically limited by two facts. Firstly, measurements in an industrial facility are hardly possible because of the high temperatures inside the crucible and restricted accessibility. Secondly, also physical modelling is expensive. This may be seen as the reason that a lot of work has been done on systems in which simplifications often might have been over-stressed in that they eliminated exactly those effects determining essential features of the flow in industrial installations.

One of such frequently made simplifications is that the flow in a Cz crucible is physically modelled by a Rayleigh-Bénard (RB) system. A cylindrical fluid volume, homogeneous upper and lower temperature boundary conditions, and an insulated side wall comprise this generic configuration. It is possibly not so much the differing geometry, a Cz crucible has a rounded bottom, that may cause another convective pattern than that to be found in an RB system, but rather the different thermal boundary conditions. A Cz system can, to a certain extent, be seen as being similar; one is concerned with natural convection due to a vertical temperature gradient ∇T_v . The crucible is heated from below, but also the side wall is heated - with the consequence that a primary horizontal temperature gradient ∇T_h exists in the same order as ∇T_v . Moreover, the variable heat flux through the quartz crucible wall into the melt differs

substantially from the boundary conditions in the RB case. What holds for the lower boundary condition continues to be true for the upper one. In an RB system, the whole fluid surface is kept at a constant temperature, whereas the crystal in a growth facility covers only, between a quarter and a third of the diameter leaving the remaining majority of the surface open to the ambience.

Despite the lack of a deeper understanding of the flow in a Cz crucible stemming only from natural convection, means of flow control other than mechanical rotation have been subject of research for a long time - with the trend that this research is increasingly intensified. Amongst the numerous publications on RMF's being used to control the flow in a RB system [1-3] are referred to. The experimental study on the influence of an RMF in [4] was devoted to a modified RB system obeying the actual coverage of the surface by the crystal.

In its first part of the results, the present work attempts to fill the gap of missing fluid flow measurements in the mere buoyancy-driven case in a Cz crucible. Because the long-term perspective of the ongoing work is flow control by magnetic fields, the Cz model was mounted in a magnetic system providing, among others, also an RMF. The second part of the results is thus concerned with some preliminary results on the influence of electromagnetic rotary stirring on the natural convection.

2 DESCRIPTION OF THE EXPERIMENT

The flow measurements were conducted in the Czochralski-like crucible depicted in Fig. 1. Heating was established by passing a temperature-controlled fluid from a thermostat through the spacing between the inner and outer vessel, which

comprise the double-walled crucible. Extraction of heat through the growing crystal was simulated by a circular centrally mounted heat exchanger on top. Since the heat exchanger was made from copper, it imposes approximately isothermal boundary conditions in an area that corresponds to a fraction of coverage the same as in industrial installations. A sketch of the Cz setup including all relevant dimensions is also to be seen in Fig. 1. Adjustable by the filling level, the aspect ratio is determined by an effective height H_{eff} calculated from the fluid volume V and the area A in the majority of the upper part. It was $a = 0.59$ in the experiments.

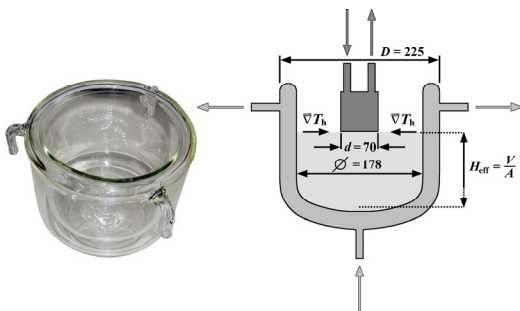


Figure 1: Photo and sketch of the Czochralski-like setup.

Flow measurements were done with a short ultrasonic transducer (8 MHz, type TR0805RS, Signal-Processing, Lausanne, Switzerland), a photo of which is provided in Fig. 2. A DOP2000 velocimeter from the same manufacturer was used to acquire the measuring data. For a description of the principle of operation of pulsed ultrasonic Doppler flow measurements, the pioneering work of Takeda is referred to [5, 6].



Figure 2: Photo of the short ultrasonic transducer that was immersed into the melt slightly below the surface to measure radial velocity sections.

Since it is hardly possible to measure through the double-wall of the crucible containing a liquid with different sound velocity and acoustic impedance, the transducer has to be immersed into the melt. In order to acquire as much of the radial profile as possible the transducer needs to be accordingly short in the measuring direction. It was then mounted on a x-y crossbar with an additional rotational unit so as to move it around the azimuth while the measuring direction was always slightly below the melt surface pointing towards the centre of the crucible.

To study the effect of an RMF on the natural convection in a Cz system, the whole apparatus was mounted inside the home-made MULTIpurpose MAGnetic field facility (MULTIMAG). This system

offers, besides an RMF, linearly travelling, single-phase alternating and static magnetic fields, the latter in homogeneous or cusp configuration. MULTIMAG is described in detail in [7].

3 RESULTS AND DISCUSSION

The first natural question about the global flow structure in an axisymmetric experimental setup is whether the developing flow is also axisymmetric. Variation of the convective pattern in RB convection, i. e. in cylindrical containers with homogeneous upper and lower temperature boundary conditions, owing to the aspect ratio a was recently studied numerically and experimentally [8]. For $a \geq 0.63$ a single roll corresponding to an azimuthal wave number of $m = 1$ was found; fluid rising in a more or less kidney-shaped region at one side, moving along the surface to the opposing side, descending there, and closing along the bottom. This flow phenomenon often termed *wind* is frequently observed in RB systems.

As mentioned, the Cz system exhibits always significantly strong primary horizontal temperature gradients owing to the only partially cooled surface. The next question therefore is, if the instantaneously developing radially inwards directed flow due to these horizontal gradients, which is axisymmetric, will survive the *wind* when the vertical gradient overcomes the critical value for the onset of RB convection. The answer for a cylindrical geometry with $a = 1$, which aspect ratio is significantly above the border even of 0.63 found in [8], is given in [4]: it does not. For all temperature differences between the bottom heating plate and the top heat exchanger the *wind* came on top. It did not just occupy a center region while there was radial and axisymmetric inward flow in an annular region adjacent to the side wall - as in the generic RB configuration with full isothermal coverage of the surface, it penetrated the whole cylinder. The findings in [4], in conjunction with the fact that the crucible dimensions in an industrial Cz facility do not reach $a = 1$ even at the maximum initial filling level, was the motivation to conduct the present experiments with a about the threshold to mono-cellular convection. A fixed value of $a = 0.59$ was chosen (c. f. Fig. 1).

If it were possible to safely measure the whole radial section of velocity across the diameter, it would have been sufficient to move the transducer over 180° since measurements from opposing directions should yield the same result. Although quite a lot of profiles were measured and averaged for each azimuthal position, measuring from the opposing side at the same locations further diminishes statistical errors. More important, it is well known that the ultrasonic beam diverges while it moves away from the emitter; the farther the measuring location, the more the lateral size of the measuring volume increases over which the local velocity is

averaged. So it is, at least, instructive to compare the results that have been obtained at, say, $0.5R$ from one side with those that were acquired at $1.5R$ from the other side.

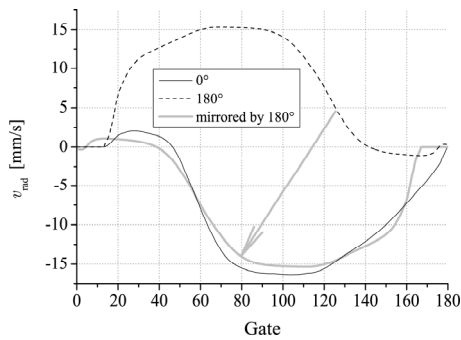


Figure 3: Radial velocity profiles across the whole diameter, measured from opposing sides with respect to the azimuthal angle.

Most important in the present case of the immersed sensor is that the sensor can not measure the location where it resides, continued by a further distance in beam direction where it does not work due to the ringing effect. This *dead zone* extends to about 15 mm, which is amply 8 % of the measuring depth. So, the information from the measurement done from the other side is vital. Fig. 3 contrasts two opposing velocity profiles acquired at 0° and 180° . The *dead zone* is obeyed by filling the missing gates with zeros.

Fig. 4 shows a series of radial velocity profiles with the azimuthal angle as parameter.

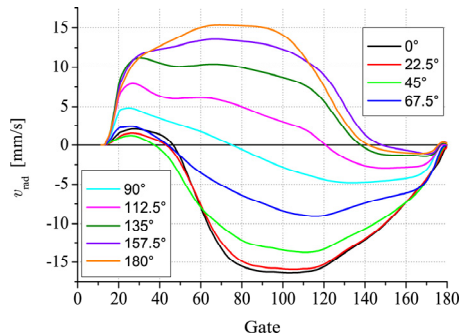


Figure 4: Radial velocity profiles across the diameter, measured in increments of 22.5° of the azimuthal angle.

If the flow in the Cz crucible were axisymmetric, all measurements at any azimuthal angle should look similar and something in between the measurements at 90° and 112.5° , crossing the $v = 0$ axis in the centre of the crucible. As this is not the case, the flow in the Cz crucible is certainly not axisymmetric, but rather three-dimensional on a global scale. What can be safely stated is, that the flow has a radially inwards directed component in an annular region adjacent to the crucible wall. Since this annular region does not penetrate the same distance from the wall towards the centre for any azimuthal angle, the observation in Fig. 4 may indicate a

superposition of several azimuthal modes, one of which is the axisymmetric $m = 0$ one.

The top-view visualization in Fig. 5 attempts to give a pictorial impression of the convective pattern which is better suited to reveal insight into the complex flow structure in the Cz crucible.

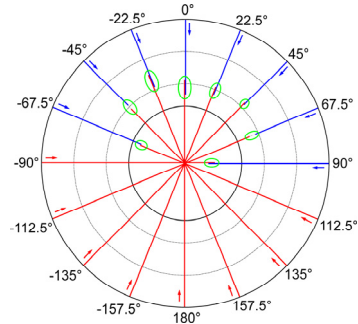


Figure 5: Top-view visualization of the flow structure in the Czochralski crucible. The details of how this plot was generated are described in the narrative.

Dropping the quantitative information from the velocities, a line is drawn from the crucible wall towards the centre for each measured azimuthal angle. The arrows indicate that the direction of flow is inwards there. The length of the lines is the distance from the wall until the velocity reverses sign. Blue is the colour for those lines, the distance up to the change of sign of velocity of which is less than the radius. In the case that the velocity changes sign in a distance longer than the radius, the line for that azimuthal angle is plotted in red. Consequently, each line from one side of the crucible wall to the opposing side of the crucible wall consists of two parts. The joint region of these two parts is encircled with an ellipse. Both profiles measured from opposing sides do not have the change of sign in velocity necessarily at precisely the same location due to some remaining uncertainties in the measurements. There can be a gap as in the case of the pair $-45^\circ/135^\circ$, or both parts of the profiles can overlap as in the case $0^\circ/180^\circ$.

Since the ellipses are stagnation points of the radial velocity component and the flow is radially inwards directed away from the crucible wall everywhere, the region covered by these ellipses should fairly coincide with a downstream. Fig. 5 suggests that there is a mono-cellular $m = 1$ mode (wind) in the centre of the crucible superimposed to the axisymmetric mode described above. The mean direction of that *wind* is from in between -157.5° and 180° towards in between 0° and 22.5° . As the innermost black circle is the region of the top heat exchanger, the superimposed *wind* seemingly extends outside the crystal dummy towards the crucible walls, at least in its mean flow direction.

With the hindsight of knowledge about such a flow structure it becomes obvious why the crucible and

the crystal in a growth facility are rotated; it should be difficult to grow a circular high quality single crystal from such an asymmetric flow. Since the temperature field is coupled to the flow field, means have to be sought which render the temperature distribution more axisymmetric. Instead of rotation of the crystal and the crucible another such means might be to rotate the melt by a rotating magnetic field, which is the next subject.

Describing the driving action of an RMF by the Taylor number [4, 7], two different RMF's were applied to the melt volume.

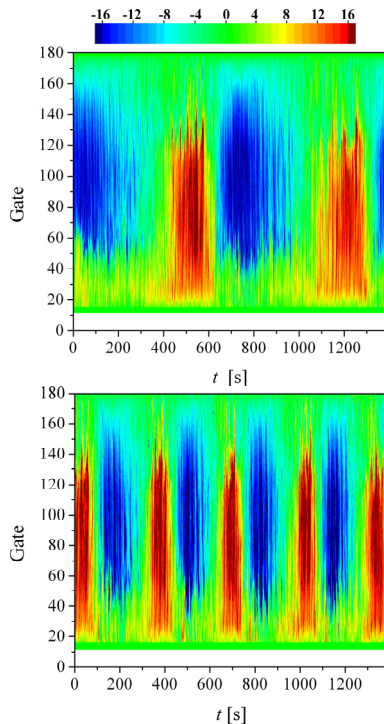


Figure 6: Time series of the radial velocity component measured at the azimuthal angle of 0° . The values of the legend of the velocities are mm/s. To the top $Ta = 1.1 \cdot 10^6$ and $Ta = 2 \cdot 10^6$ on the bottom.

In a first series, the Taylor number was kept at $1.1 \cdot 10^6$, a choice which was motivated by the parameters in [4]. In the modified RB system in [4], a cylinder with a partially cooled surface (crystal dummy), this Ta was in a range where the *wind* and rotary flow coexisted at all vertical temperature gradients. The top part in Fig. 6 shows that the *wind* rotates extremely slow at that Taylor number with about 670 seconds for one revolution of the fluid.

In the bottom part of Fig. 6, Ta was risen to $2 \cdot 10^6$. In [4] the mean temperature gradients were governed by the swirling flow evoked by the RMF. Here, the velocity time series show an increased rotational speed of the liquid metal, however, the strength of the *wind* is seemingly not affected by the swirling flow. The question about the correlation between the mean temperature gradients, which are an important parameter in crystal growth, and the flow field must remain open for the time being since temperatures

have not been measured yet. Simultaneous flow and temperature measurements will be subject of ongoing work.

4 SUMMARY

Subject of investigation was the natural convection in a Czochralski crystal growth model, for which reliable velocity data have not been available to the best of our knowledge. Velocity profiles acquired across the melt surface at various azimuthal angles indicate that the convective pattern is a superposition of an axisymmetric $m = 0$ mode and a mono-cellular $m = 1$ mode. The latter, often called *wind*, is restricted to the central region of the crucible.

When applying a rotating magnetic field, the *wind* rotates slowly. The revolution rate increases with the strength of the magnetic field, however, it does not lose vigour at field strength where the temperature distribution is strongly affected by the swirling flow. Future work will thus address two issues: (i) Simultaneous temperature measurements are needed to shed some light onto the correlation between temperature gradients in the growth zone and the flow. (ii) Increased field strengths have to be investigated to answer the question whether it is possible to suppress the buoyant convection by rotary stirring completely, that is to say whether it is possible to render the flow axisymmetric.

ACKNOWLEDGEMENTS

This work was financially supported by "Deutsche Forschungsgemeinschaft" in the framework of the Collaborative Research Centre SFB 609.

REFERENCES

- [1] Friedrich J, Lee Y S, Fischer B, Kupfer C, Vizman D, Müller G: Experimental and numerical study of Rayleigh-Bénard convection affected by a rotating magnetic field, *Phys. Fluids* 11 (1999), 853-861.
- [2] Volz M P, Mazuruk K: An experimental study of the influence of a rotating magnetic field on Rayleigh-Bénard Convection, *J. Fluid Mech.* 444 (2001), 79-98.
- [3] Grants I, Gerbeth G: The suppression of temperature fluctuations by a rotating magnetic field in a high aspect ratio Czochralski configuration, *J. Cryst. Growth* 308 (2007), 290-296.
- [4] Cramer A, Röder M, Pal J, Gerbeth G: A physical model for electromagnetic control of local temperature gradients in a Czochralski system, *Magnetohydrodynamics* 46:4 (2010), 353-361.
- [5] Takeda Y: Velocity profile measurement by ultrasound Doppler shift method, *Int. J. Heat Fluid Flow* 7:4 (1986), 313-318.
- [6] Takeda Y: Development of ultrasound velocity profile monitor, *Nucl. Eng. Des.* 126 (1990), 277-284.
- [7] Pal J, Cramer A, Gundrum Th, Gerbeth G: MULTIMAG - A MULTIpurpose MAGnetic system for physical modelling in magnetohydrodynamics, *Flow. Meas. Instrum.* 20 (2009), 241-251.
- [8] Hébert F, Hufschmid R, Scheel J, Ahlers G: Onset of Rayleigh-Bénard convection in cylindrical containers, *Phys. Rev. E* 81 (2010), 046318.

Flow measurements in a continuous casting model using a low temperature liquid metal

Klaus Timmel, Michael Röder, Sven Eckert, Gunter Gerbeth
Helmholtz-Zentrum Dresden-Rossendorf; Institute of Fluid Dynamics, Germany

This paper describes experimental investigations of flow structures and related transport processes in the continuous casting mould under the influence of an external DC magnetic field at laboratory scale. Experimental results will be presented here which have been obtained using a physical model (mini-LIMMCAST) operating with the low melting point alloy GaInSn. The Ultrasound-Doppler-Velocimetry (UDV) was applied for measurements of the flow pattern in the mould. An array of ten transducers was attached to the narrow mould side, measuring the horizontal velocities in the region around the liquid metal jet. Further, with two sensors on the mould top, vertical velocities were recorded successively in the whole mould width. According to the concept of the electromagnetic brake the impact of a DC magnetic field on the outlet flow from the Submerged Entry Nozzle (SEN) has been studied up to Hartmann numbers of about 400. The effect of the magnetic field on the flow structure turned out to be manifold and rather complex. The magnetic field causes a deflection of the jet, at which the respective exit angle from the nozzle ports becomes more flat. Thus, both the penetration depth of the discharging flow into the lower part of the mould and the impinging velocity of the jet onto the side wall are reduced. A significant return flow occurs in the adjacent regions of the jet. Specific vortices are formed with axes being aligned with the magnetic field direction. Such vortical structures are typical for quasi-two-dimensional magneto-hydrodynamic (MHD) flows. The flow measurements do not manifest a general braking effect which would be expected as an overall damping of the flow velocity and the related fluctuations all-over the mould volume. Variations of the wall conductivity showed a striking impact on the resulting flow structures.

Keywords: Continuous steel casting, Liquid metal model, electromagnetic brake (EMBr)

1 INTRODUCTION

Magnetic fields are established in the continuous casting process for years for the purpose of flow control [1]. However, the turbulent flow of molten steel in a continuous casting mould under the influence of a DC magnetic field appears to be very complex and is not sufficiently understood yet. The impact of an electromagnetic brake (EMBR) on the mould flow was addressed by many numerical studies considering various magnetic field configurations or examining the influence of variations of different casting parameters on the magnetic field effect. However, a serious deficit of experimental data is noticed which could be employed for numerical code validations. Model experiments using low melting point alloys (e.g. [2]) are an important tool to provide a substantial database for the validation of respective numerical simulations [3], [4]. The main value of “cold” laboratory experiments consists in the capabilities to obtain quantitative flow measurements with a reasonable spatial and temporal resolution.

2 EXPERIMENTAL SET-UP

The continuous casting process was studied by means of the small-scale model facility mini-LIMMCAST [5]. The eutectic GaInSn-alloy was used

as model fluid which is liquid at room temperature. The experimental mockup contains a tundish in the shape of a circular vessel made of stainless steel. A submerged entry nozzle (SEN) with an inner diameter of 10 mm was attached at the bottom of the cylinder. The liquid metal was poured through the SEN into a rectangular mould made of acrylic glass with a cross section of 140 x 35 mm² and a length of about 300 mm. Fig. 1 shows the setup of the mini-LIMMCAST facility.

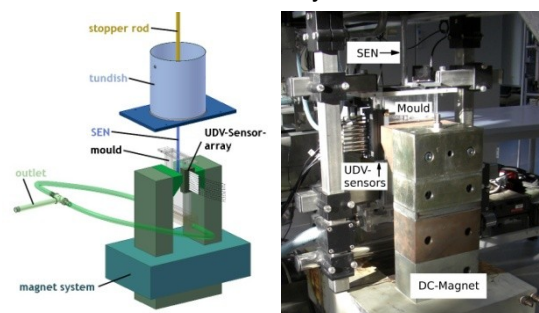


Figure 1: Sketch and photograph of the experimental setup mini-LIMMCAST showing the installed magnetic system and the ultrasonic sensors for flow measurements.

The experiments were conducted with a ruler type magnetic brake, which covers the whole width of the mould. The magnet was positioned in a height,

where the liquid jet discharges from of the nozzle ports. Three cases were considered within this paper: a reference measurement without magnetic field and the application of the magnet field with either isolating or electrically conducting walls of the mould. To realize the situation of the conducting walls in the acrylic glass mould, thin brass plates were attached to the inner wide side of the mould. The narrow walls had to be kept free in order to enable the undisturbed application of the ultrasonic measurement technique. The thickness of the brass plates was chosen in such a way, that the wall conductance ratio C_W corresponds to the real case of the solidified steel strand in the continuous casting mould [6]. Further details about the experimental equipment can also be found in [6].

The liquid metal flow in the mould was measured by means of the Ultrasonic Doppler Velocimetry (UDV). This method is capable to measure the fluid flow around the discharging jet from the nozzle ports with a reasonable temporal and spatial resolution [6]. The UDV-method was applied non-invasively through the narrow mould wall. Ten transducers were mounted having a distance in between of 10 mm for detecting the horizontal velocities in the region of the nozzle ports.

In further experiments one sensor was placed on the top of the mould top at each side of the nozzle, to capture the vertical velocities. In contrast to the horizontal measurement through the wall, these sensors are dipped into the liquid metal. The sensors were shifted in steps of 7 mm yielding in 8 measuring lines.

Another UDV configuration consists of two ultrasonic transducers, placed opposite at the narrow side walls. The height was chosen in such a way, that the measuring line crosses the liquid metal jet.

The DOP2000 velocimeter (Signal Processing, Lausanne, Switzerland) was used in combination with 4 MHz ultrasonic transducers (TR0405LS, same producer). Velocity profiles delivered by the transducers were recorded in multiplexer mode.

3 RESULTS

3.1 Vertical Flow Field

The averaged vertical mould flow in the mid plane is depicted in Fig. 2. The magnitude of the velocity is plotted according to a colour scale (red corresponds to a downward flow meanwhile blue represents an upward flow). The position of the DC-magnet is indicated by the horizontal green lines. These lines represent the upper and lower edges of the pole faces.

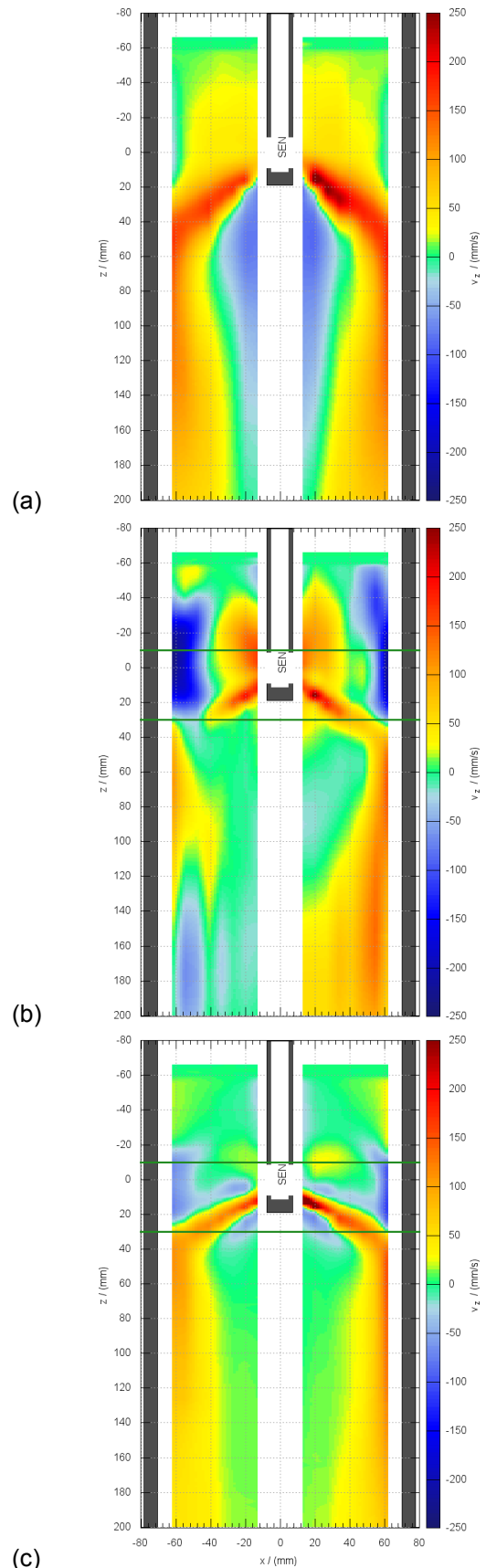


Figure 2: Mean vertical velocity without field (a); with applied DC-magnetic field between the horizontal green lines for isolating walls (b) and conducting walls(c).

The typical double roll flow pattern, which is usually the desired flow pattern, can be observed in the situation without applied magnetic field in the uppermost plot. The jet is exiting from the ports and is directed towards the narrow mould wall, where it splits into an upper and lower roll.

The flow undergoes a tremendous change as soon as a DC-magnetic field is applied. The mean flow becomes clearly asymmetric between the left and right mould sides with electrically isolating walls. An additional small roll is created just below free surface.

The installation of conducting walls at the wide sides of the mould results in another flow regime. A small roll is created just below and above the jet and near the nozzle, resulting in a return flow in the vicinity of the jet. The roll below the free surface is still present, as in the case with isolating walls. These features are related to the transition from a double roll structure to a multi roll pattern in the mould. The new flow structure is caused by the alignment of eddies parallel to the magnetic field direction and the creation of return flows close to a free liquid metal jet in the case of a DC-magnetic field [7]. In the lower parts of the mould a plug flow is generated showing rather low velocity values.

The application of a DC-magnetic field at the marked position obviously destroys the double roll flow pattern. Further eddies were created with isolated walls as well as with conducting walls. The zone of the jet appears rather confined and a perceptible reduction of the flow intensity in the jet cannot be recognized.

3.2 Two-dimensional velocity vectors

The combination of horizontal and vertical measurements allows for the calculation of velocity vectors at the intersection points. The result of the 80 intersection points is depicted in Fig. 3, again for all three investigated conditions. The location of the DC-magnets pole faces is highlighted in green.

The jet emanating from the SEN and the downward flow near the narrow wall is clearly visible in all three cases. The return flows of the lower and the upper roll can be well observed in the reference case without magnetic field. The upward stream of the upper roll is concentrated close to the narrow wall and merely adequately caught by the measurement.

The application of a static magnetic field enforces a recirculation zone close above the jet under isolating conditions. Actually, velocities are increased in this region, contrary to the usual expectations with respect to the action of an electromagnetic brake.

The placement of conducting walls damps the recirculation zone above the jet. A further recirculation zone below the jet becomes visible. These recirculation zones can also be identified in

Fig. 2(c) as blue stripes directly beside the liquid metal jet.

In addition, the exit angle of the jet was flattened and the impinging point was shifted upwards in presence of a magnetic field.

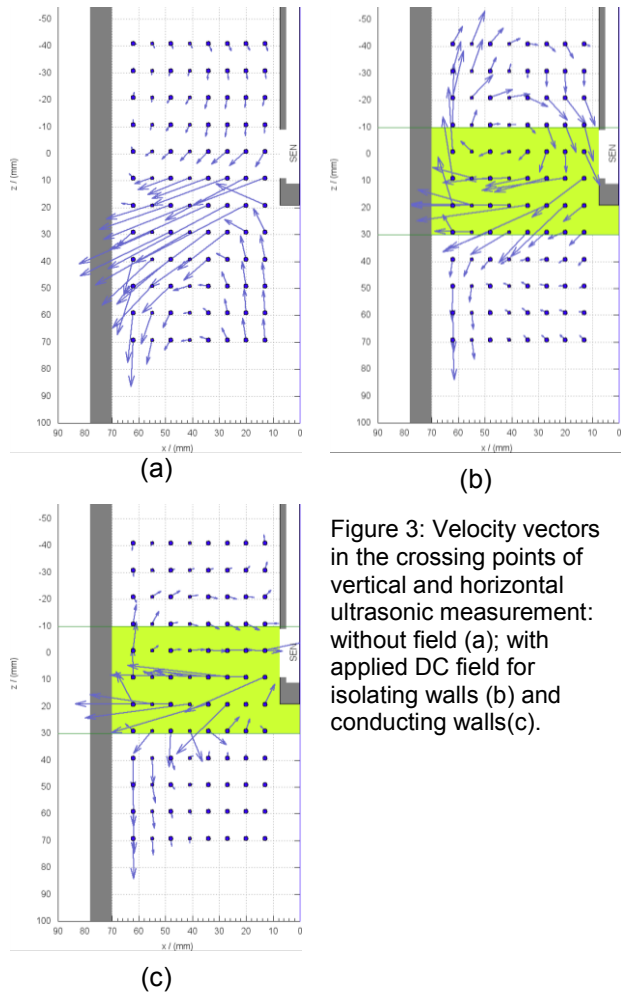


Figure 3: Velocity vectors in the crossing points of vertical and horizontal ultrasonic measurement: without field (a); with applied DC field for isolating walls (b) and conducting walls(c).

3.3 Time dependent flow

The time dependent flow profiles of the oppositely placed ultrasonic transducers can be viewed in Fig. 4. The horizontal velocity is plotted over the measuring depth and time. Positive values (red colours) indicates a flow towards the middle of the mould, meanwhile negative velocities (blue colours) represent a flow towards the narrow walls. The crossing of the jet trough the measuring line can be observed very well in all diagrams.

The impact of the wall conductivity becomes especially manifested by analysing the transient behaviour of the mould flow. The magnetic field triggered low frequent flow oscillations in case of isolating mould walls. The jet is disappearing from the measuring line temporarily and a reversal of flow direction can be detected (Fig. 4(b)). This is related to an up and down bending of the jet [6] and the creation of recirculation zones, as already described before. The oscillation seems to be linked between

the two mould halves to appear opposite in phase, with a prominent jet on the one side and a damped jet, or even flow reversal, on the other side. The unequal temporal distribution of the flow regimes between the mould halves is the reason for the asymmetry in the averaged flow field, like in Fig. 2(b).

The low-frequent oscillations are damped, when the conducting brass plates have been inserted into the acrylic glass mould (Fig. 4(c)). In addition the liquid metal jet was constricted concerning his extension. A change in flow direction was observed near the SEN, which is again a sign for the creation of recirculation zones.

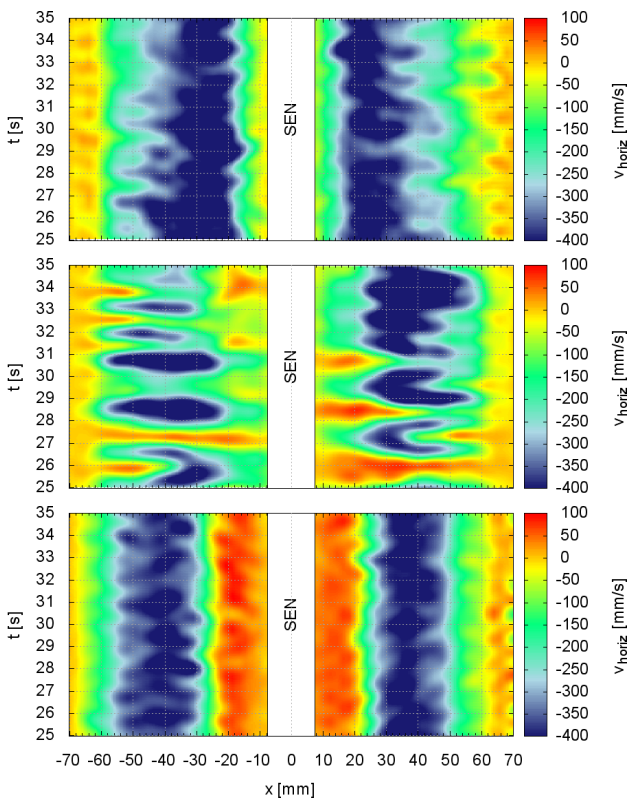


Figure 4: Time series of the horizontal velocity in the jet region ($z=+19\text{mm}$) without field (a); with applied DC-magnetic field and isolating walls (b) and conducting walls(c).

SUMMARY

The liquid metal models proved to be an appropriate and important tool for the investigation of flow phenomena occurring in the continuous casting process. In particular, the application of the Ultrasonic Doppler Velocimetry method allows for the observation of global flow structures, profiles of the local velocity and flow fluctuations. Moreover, the combination of such liquid metal models and measurement techniques are inevitable for the analysis of the magnetic field effects on the flow behaviour.

The applied DC-magnetic field causes strong

modifications of the flow structure in the continuous casting mould. An overall damping of the mean flow was not observed in our experiments. The magnetic field may reduce the flow locally, but contrary to that the flow is accelerated at other locations or inversions of the flow direction occur. Another finding is that a steady magnetic field may give rise to flow oscillations in the mould.

The measurements illustrated the importance of the electrical boundary conditions. The electrical conductivity of the mould wall had a dramatic influence on the temporal behaviour of the flow. This feature has to be considered accurately in numerical modelling.

The experimental results provide a valuable database for a validation of numerical models and enable a better understanding of the mould flow and the related phenomena.

ACKNOWLEDGEMENT

The LIMMCAST programme is part of the collaborative research centre SFB609 "Electromagnetic Flow Control in Metallurgy, Crystal Growth and Electrochemistry", which is funded by the Deutsche Forschungsgemeinschaft (DFG). The authors would like to thank the DFG for the granted support.

REFERENCES

- [1] H. Yasuda, T. Toh, K. Iwai, K. Morita: Recent Progress of EPM in Steelmaking, Casting, and Solidification Processing, *ISIJ Int.* 47 (2007), 619-626.
- [2] H. Harada, T. Toh, T. Ishii, K. Kaneko, E. Takeuchi: Effect of magnetic field conditions on the electromagnetic braking efficiency, *ISIJ Int.* 41 (2001), 1236-1244.
- [3] X. Miao, K. Timmel, D. Lucas, Z. Ren, S. Eckert, G. Gerbeth: Effect of an Electromagnetic Brake on the Turbulent Melt Flow in a Continuous Casting Mold, *Metallurgical and Materials Transactions* 43B (2012), 954-972.
- [4] R. Chaudhary, C. Ji, B.G. Thomas, S.P. Vanka: Transient Turbulent Flow in a Liquid-Metal Model of Continuous Casting, Including Comparison of Six Different Methods, *Metallurgical and Materials Transactions B* 42 (2011), 987-1007.
- [5] K. Timmel, S. Eckert, G. Gerbeth, F. Stefani, T. Wondrak: Experimental Modeling of the Continuous Casting Process of Steel Using Low Melting Point Metal Alloys - the LIMMCAST Program, *ISIJ Int.* 50 (2010), 1134-1141.
- [6] K. Timmel, S. Eckert, G. Gerbeth: Experimental investigation of the flow in a continuous casting mould under the influence of a transverse DC magnetic field, *Metallurgical and Materials Transactions B* 42 (2010) 68-80.
- [7] P. A. Davidson: Magnetic damping of jets and vortices. *J. Fluid Mech.* 229 (1995), 153-186

Random reversals of flow direction in Rayleigh-Bénard convection of liquid metal under a uniform magnetic field

Takatoshi Yanagisawa¹, Takehiro Miyagoshi¹, Yasuko Yamagishi¹, Yozo Hamano¹, Ataru Sakuraba², Yuji Tasaka³, and Yasushi Takeda³

¹Institute for Research on Earth Evolution (IFREE), Japan Agency for Marine-Earth Science and Technology (JAMSTEC), Yokosuka, Japan

²Department of Earth and Planetary Science, University of Tokyo, Tokyo, Japan

³Division of Energy and Environmental Systems, Hokkaido University, Sapporo, Japan

We performed laboratory experiments of Rayleigh-Bénard convection by using liquid gallium, in the range of Rayleigh number (Ra) from critical value to 100 times above it, under various intensities of a uniform horizontal magnetic field B . The range of Chandrasekhar number (Q) is from 0 to 1000. The vessel we used has a square geometry with aspect ratio five. Flow patterns were visualized by ultrasonic velocity profiling method, and time variations of convective flow structure were clearly observed. We recognized five flow regimes depending on Ra and Q , that is, (1) isotropic large-scale cell pattern, (2) anisotropic cell with larger flow velocity perpendicular to B , (3) short-period oscillatory behavior of rolls aligned in the direction of B , (4) rolls with random reversals of the flow direction, and (5) steady 2-D rolls. In the regime (4), a roll-like structure is dominant for most of the duration and the flow keeps its two-dimensionality, while an emergence of new circulation near the wall triggers the global reorganization of the pattern causing reversal of the flow direction. The reversals of the flow occur randomly with the typical time interval between reversals much longer than the circulation time.

Keywords: Rayleigh-Bénard convection, liquid metal, horizontal magnetic field, flow reversal

1 INTRODUCTION

The study on the nature of thermal convection in liquid metals is essential for the dynamics of Earth's outer core and many engineering topics, and the behavior of turbulent flow under a magnetic field is very important. In highly conductive (low Prandtl number (Pr)) fluids like liquid metals, theoretical studies propose following features [1-2]. (a) Two-dimensional steady roll structure emerging at the onset of convective flow easily becomes time-dependent just above the critical Rayleigh number (Ra) at the condition without external magnetic field, and producing oscillatory instability such as "traveling-wave convection" in the direction of the roll axis. (b) Under a horizontal magnetic field, the axis of the roll structure at the onset of convection is forced to align in the direction of the magnetic field, and the Ra for transition to time-dependent flow regime is increased. (c) At much higher Ra where turbulence is developed, suppression of turbulence and formation of anisotropic flow structure are expected under a magnetic field. These features are confirmed in our laboratory experiments by visualizing flow patterns in liquid metals [3-5].

On the other hand, 'flow reversals' in Rayleigh-Bénard convection has been an active topic in this decade [6]. The occurrence of spontaneous reversals of the mean flow direction in turbulent thermal convection in water and gas is established. The observed reversals occur at irregular intervals, with the time-scales much longer than the turnover

time of the convection [7-8]. Most experimental investigations on flow reversals are made in cylinders or rectangular boxes with small aspect ratios, in which the flow pattern is basically a single circulation and is strongly restricted by the sidewalls of the vessels. Experiments with larger aspect ratio geometries would be helpful to understand, whether flow reversals can occur in situations with several horizontal coexisting circulations. The working fluids in the reported experiments have mainly been water and gas, whose Pr are around one. Liquid metals were used in some experiments [9], but obvious flow reversals have not been established with liquid metals. Here, we report several regimes of flow pattern including newly found flow reversals in liquid metal layer of larger aspect ratio, under the effect of horizontal magnetic field. We classified the flow regimes and clarified the condition for the occurrence of reversals in this system.

2 APARATUS AND SETTING

The vessel we used has a square geometry with aspect ratio five (Fig. 1) [10]. The top and bottom plates are made of copper, and the temperature of each plate is maintained by circulating water. Liquid gallium is used as the working fluid. Ultrasonic transducers for the UVP are set in holes in the Teflon sidewalls, and are in direct contact with the liquid gallium. The flow velocities of the gallium were measured along four lines from the ultrasonic transducers (uv1-uv4); these four transducers were switched on in order for 1.25 s periods, and the

sampling for the lines was taken place at 5 s intervals. The UVP measures the projected flow velocity along each line. We used a Helmholtz coil system to apply a uniform magnetic field. The direction of magnetic field is horizontal in this study, and its intensity is controlled by an electric power supply.

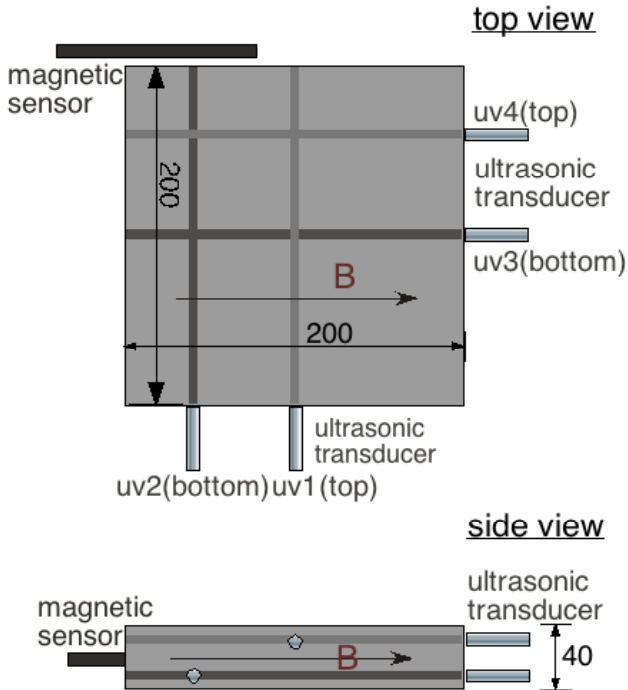


Figure 1: Geometry of the vessel and measurement lines with ultrasonic beam. Liquid gallium is filled in the vessel. The numbers are the dimensions in mm.

3 RESULTS

We found five flow regimes depending on Ra and the intensity of applied magnetic field B . Intensity of the magnetic field can be evaluated by Chandrasekhar number (Q), which is proportional to the square of B . Q is identical to the square of Hartmann number (Ha). At a fixed value of Ra with the increase in Q , those regimes are, (1) isotropic large-scale cell pattern, (2) anisotropic cell with larger flow velocity in the direction perpendicular to B , (3) short-period oscillatory behavior of rolls aligned in the direction of B , (4) random reversals of the flow direction with very long time-scale, and (5) steady 2-dimensional rolls. We note the detail of each regime. In the following figures, the direction and magnitude of the flow velocity are shown in color, blue (minus) shows a flow toward each transducer and red (plus) flow away from it. Ra is fixed at 1.4×10^4 , about one order above the critical Ra , in the following examples.

3.1 Isotropic large-scale cell

This regime is observed for the case without magnetic field or under a weak magnetic field. The flow is strongly time-dependent, and there is no obvious structure in time-averaged field. Flow

velocities are the same order in both directions as shown in Fig. 2. It is a kind of organized flow pattern in turbulence for low Pr fluid.

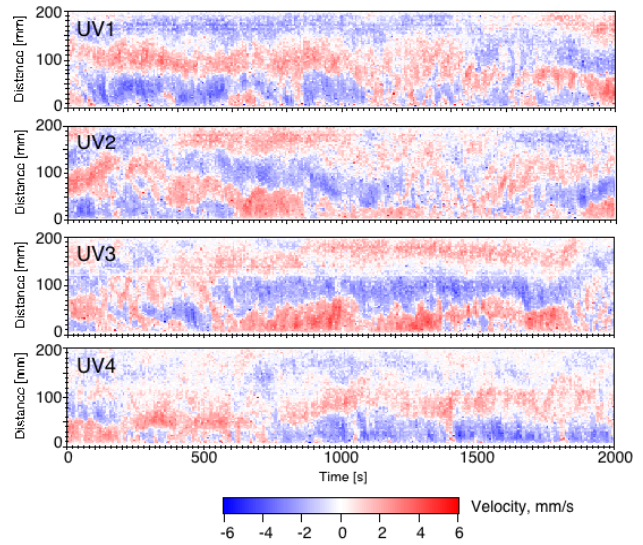


Figure 2: Time-space map of the horizontal flow velocity at $Ra=1.4 \times 10^4$ with $Q=0$, for 2000 seconds. Isotropic large-scale cell pattern.

3.2 Anisotropic cell with larger flow velocity perpendicular to B

In this flow regime, the average velocity is larger for $uv1-2$ than $uv3-4$, which is the effect of the applied magnetic field, but no clear roll-like structure exists (Fig. 3). The flow pattern is broader than four-roll structure in the next regime, and it shows large amplitude of fluctuations. Three-dimensionality of the flow structure is strong. This regime can be thought as a transition state between isotropic cells and aligned rolls.

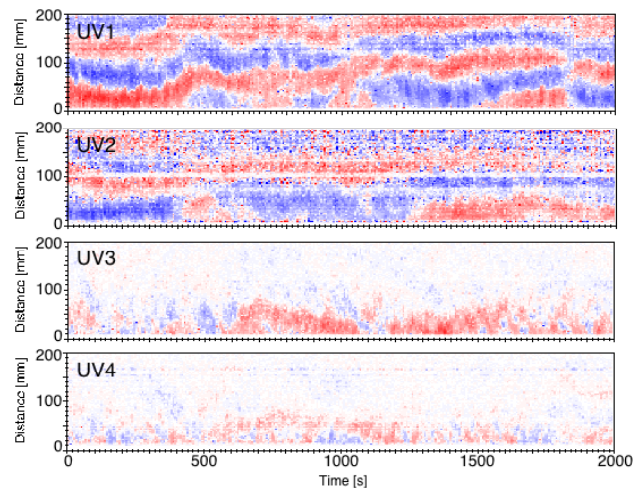


Figure 3: $Ra=1.4 \times 10^4$ with $Q=7.7 \times 10^1$. Anisotropic cell pattern.

3.3 Rolls with short-period of oscillation

More organized, roll-like pattern emerges at moderate values of Q as shown in Fig. 4. Four clusters of velocities are observed with opposite

signs in uv1 and uv2 (due to the different height of them, uv1: top, uv2: bottom), which suggests the existence of a nearly two-dimensional roll-like structure with the axis parallel to the direction of the applied magnetic field. In this example, the sign of the flow velocity indicates that there exist upwelling flows at both sidewalls and in the central part of the vessel. One noteworthy feature of these profiles is that the pattern shows periodic fluctuations, suggesting the presence of oscillation of the roll structure. Its typical period is about 70 s for the case here. The period does not depend on Q much, as far as the oscillatory behavior of four-roll is observed, but the spatial range of its horizontal fluctuation gets shorter as Q increases. As the circulation time of the flow for a roll is 30-40 s (length of one circulation for four roll structure ~ 180 mm, and the typical flow velocity 5-6 mm/s), this oscillation period is about two times of the circulation time. This time ratio is almost equal for the other cases with different Ra .

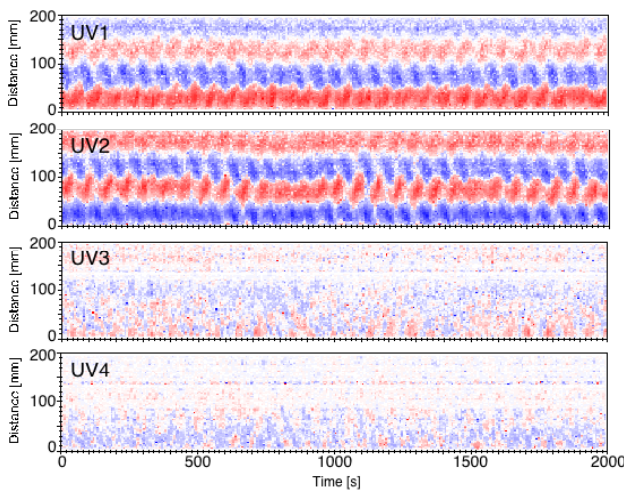


Figure 4: $Ra=1.4 \times 10^4$ with $Q=1.5 \times 10^2$. Rolls with short-period of oscillation. The mean direction of the roll is parallel to B.

3.4 Rolls with random reversals of flow direction

The pattern in Fig. 5 shows the regime with irregular reversals of the flow direction. A four-roll structure with axis parallel to the magnetic field is dominant, but the profiles show two reversals of flow direction with non-periodic intervals. Reversals repeat throughout the duration of the experiment (longer than 20,000 s). One flow structure dominantly observed is the four-roll pattern with red patches around 0-50 mm in uv1, which shows upwelling flows at both sidewalls and the center as indicated in Fig. 6 (a). The other dominant flow structure is also a four-roll pattern with the flow direction opposite to this (Fig. 6 (b)). The fraction of time that the flows show either of these four-roll states is relatively large, and the transition between the two patterns occurs over a shorter time than the four-roll state is maintained. Flow velocities in uv3-4 become larger at the timing of reversals; hence two-

dimensionality of the flow structure becomes weaker. The transition proceeds as follows: a small circulation emerges at a corner of the vessel in either sidewall. It grows up to the fifth roll, and expands horizontally for a while, then the global flow reverses with a reorganization of the whole pattern. In this case with 20,000 s of the duration, the average time between intervals is 800 s. The average intervals of the flow reversal are much longer than the circulation time.

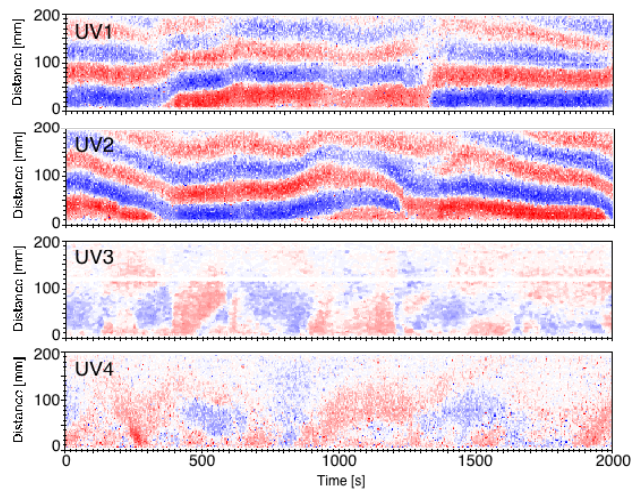


Figure 5: $Ra=1.4 \times 10^4$ with $Q=1.0 \times 10^3$. Random reversals of the flow direction.

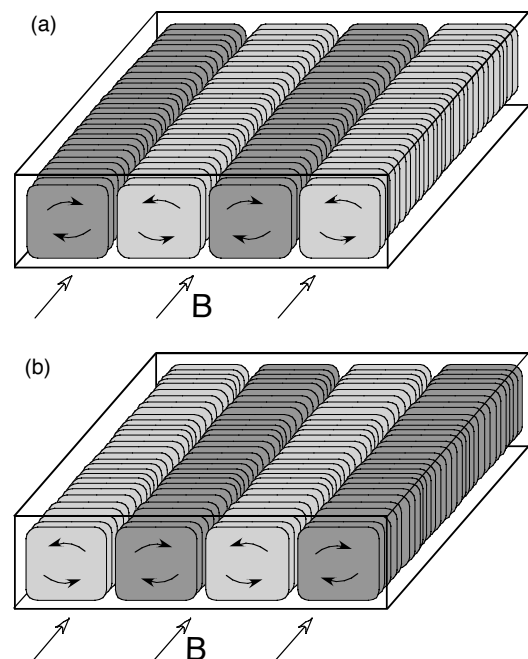


Figure 6: Schematic view of the flow patterns with four rolls. These patterns correspond to (a) $t \sim 600$ s, and (b) $t \sim 1500$ s in Fig. 4.

3.5 Steady 2-D rolls

With a higher intensity of B, the flow pattern keeps almost steady roll structure whose axis is parallel to the magnetic field. Either pattern in Fig. 6 (a) or (b) lasts for a long time.

4 DISCUSSIONS

A regime diagram of convection patterns under a horizontal magnetic field is established in relation to Ra and Q . These flow regimes can be classified by the ratio of buoyancy force to the Lorentz force. If buoyancy force is much larger than Lorentz force, the flow is turbulent and isotropic structure is dominant. Short-period of oscillation is observed where this ratio is lower than 100. Random reversals are observed at lower ratio.

The geometry of the vessel is also important for the occurrence of flow reversals; we did not observe spontaneous flow reversals in a narrower vessel. Fluctuations of flow pattern in a narrower vessel are limited to induce oscillatory behavior of roll-like structure [5], but fluctuations in a wider vessel can cause global reorganizations of the flow pattern as shown in the present experiments. This may be due to the larger variation of the flow in a wider vessel, such as the emergence of new circulations.

Applying a horizontal magnetic field of adequate intensity for horizontally wide fluid layer may be essential for the occurrence of flow reversals in liquid metal Rayleigh-Bénard convection.

REFERENCES

- [1] Chandrasekhar S: Hydrodynamic and Hydromagnetic Stability, Oxford University Press, New York (1961).
- [2] Davidson PA: An Introduction to Magnetohydrodynamics, Cambridge University Press, Cambridge (2001).
- [3] Tasaka et al.: Ultrasonic visualization of thermal convective motion in a liquid gallium layer, Flow Meas. & Inst., 19 (2008), 131.
- [4] Yanagisawa T et al.: Structure of large-scale flows and their oscillation in the thermal convection of liquid metal, Phys. Rev. E, 82 (2010), 016320.
- [5] Yanagisawa T et al.: Detailed investigation of thermal convection in a liquid metal under a horizontal magnetic field: Suppression of oscillatory flow observed by velocity profiles, Phys. Rev. E, 82 (2010), 056306
- [6] Ahlers G et al.: Heat transfer and large scale dynamics in turbulent Rayleigh-Bénard convection, Rev. Mod. Phys., 81 (2009), 503-537.
- [7] Niemela JJ et al.: The wind in confined thermal convection, J. Fluid Mech., 449 (2001), 169-178.
- [8] Sreenivasan KR et al.: Mean wind and its reversal in thermal convection, Phys. Rev. E, 66 (2002), 056306.
- [9] Mashiko et al.: Instantaneous measurement of velocity fields in developed thermal turbulence in mercury, Phys. Rev. E, 69 (2004), 036306.
- [10] Yanagisawa T et al.: Spontaneous flow reversals in Rayleigh-Bénard convection of a liquid metal, Phys. Rev. E, 83 (2011), 036307

Inertial wave observations in liquid metal by means of ultrasound Doppler velocimetry

Dirk Rübiger^a, Tobias Vogt^a, Sven Franke^{a,b}, Sven Eckert^a, Gunter Gerbeth^a and Jürgen Czarske^b

^a Helmholtz-Zentrum Dresden-Rossendorf, PO Box 510119, 01314 Dresden, Germany

^b Technische Universität Dresden, Helmholtzstrasse 18, 01069 Dresden, Germany

This experimental study considers the transient flow inside a liquid metal column exposed to a pulsed rotating magnetic field. To measure two-dimensional velocity fields of the secondary flow in the radial-meridional plane a novel ultrasound Doppler system was used. A linear ultrasound transducer array equipped with 25 transducer elements is used to measure the flow field in a square plane of 67 x 67 mm². The application of advanced processing techniques like a simultaneous excitation of multiple transducer elements and a segmented array technique enable high data acquisition rates as well as a high spatial resolution. The measurements revealed transient flow regimes showing distinct inertial oscillations and coherent vortex structures.

Keywords: Ultrasound Doppler method, flow field measurements, electromagnetic stirring, rotating magnetic field, inertial waves, flow control

1 INTRODUCTION

Electromagnetic stirring during solidification has been proved to be a striking method for achieving a purposeful alteration of the microstructure of casting ingots, such as grain refinement or the promotion of a transition from a columnar to an equiaxed dendritic growth (CET). However, the imposition of a rotating (RMF) or a travelling magnetic field (TMF) also causes problems like the occurrence of typical segregation pattern or a deflection of the upper free surface. A permanent radial inward (RMF and downward TMF) or outward (upward TMF) flow along the solidification front is responsible for the transport of solute to the axis or the wall of the ingot resulting in typical freckle segregation pattern filled with alloy of eutectic composition [1, 2]. Several studies have been devoted to overcoming the handicaps of rotary stirring with the specific goal to generate a vigorous stirring in the bulk without considerable deformations of the free surface [3-5]. It was shown recently, that the application of modulated AC magnetic fields offers considerable potential for optimizing the melt stirring [6, 7]. It became apparent that a careful adjustment of the modulation parameters is required in order to create intense secondary flows with periodic reversals of the flow direction. Especially, the secondary flow can be organized in such a way that periodic reversals of the flow direction occur adjacent to the solidification front, which has been experimentally verified as an important method to prevent flow-induced macrosegregation [8].

Within this paper we especially consider the effect of a modulated RMF on the isothermal liquid metal flow inside a circular cylinder, whereas the RMF is

applied in form of successive rectangular pulses. Previous investigations revealed the existence of an optimal pulse length T_P , where a maximum intensity of a periodic meridional flow can be observed [7]. In that case the corresponding pulse frequency f_P relates to the eigenperiod of inertial waves in a developed regime, as given by Greenspan [9].

2 EXPERIMENTAL SET-UP

A schematic view of the experimental setup is shown in figure 1. A cylindrical vessel made of Plexiglas was used with an aspect ratio $A = H_0/2 \cdot R_0 = 1$. The size of the inner diameter of $D = 2 \cdot R_0$ and the height H_0 was chosen to be 67.5 mm. The cylinder is closed by rigid lids and filled with the eutectic alloy GalnSn. The experiments were performed in the magnetic induction system PERM at HZDR with a bore diameter of 200 mm, wherein the fluid vessel was placed concentrically. In order to preclude flow artifacts arising from symmetry deviations of the experimental setup (vertical alignment, conformity of both the cylinder and the magnetic field axis), special care was necessary to ensure a precise positioning of the cylinder inside the magnetic system. The homogeneity of the magnetic field was checked using a 3-axis Gauss meter (Lakeshore model 560, sensor type MMZ2560-UH). Within a radius of 35 mm, which approximately corresponds to the radial dimension of the container, the variance of the magnetic field strength was found to be smaller than 3%.

The ultrasound Doppler velocimetry (UDV) was used to perform measurements of the fluid flow inside the cylinder. Details with respect to the

measuring principle can be found in [10]. The DOP2000 velocimeter (model 2125, Signal Processing SA, Lausanne) equipped with an 4 MHz transducer (TR0405LS, acoustic active diameter 5 mm) was applied to measure the primary azimuthal flow at two vertical positions. By attaching the ultrasonic transducer to the wall of the fluid container, the acoustic coupling between sensor and fluid was realized through the curved cylindrical surface. Moreover, a flow mapping of the meridional flow was realised by using a new measuring system. Details of the measuring system are given in [11]. The system operates with a linear array of 25 single transducers attached to the plane-parallel bottom wall of the flow container (see figure 1) and work with a frequency of 8 MHz. Each single transducer element has an active area of 2.5 x 5 mm. The segmental array is actuated in groups of two elements to achieve a low beam divergence. This square transducer can be traversed by half of its edge length that corresponds to one element pitch to achieve a small distance of the measuring line of 2.5 mm. A high temporal resolution can be realized by a parallel operation of four transducer pairs. To minimize the crosstalk between the active elements to a tolerable level four inactive array elements between are required. The spatial resolution in lateral direction varies from 5 mm at the sensor to approximately 7.5 mm at the lid of the fluid vessel. In axial direction a spatial resolution of about 1.4 mm was achieved. The velocity data were acquired with sampling frequencies between 0.5 and 6 Hz. The accuracy of the velocity data can be assessed to be better than 0.15 mm/s.

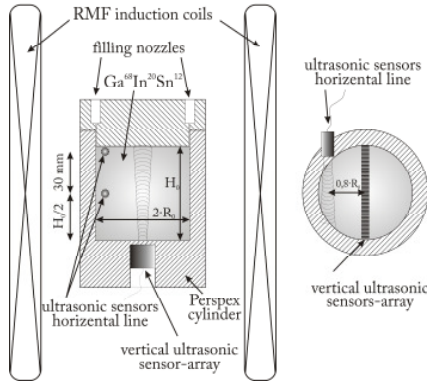


Figure 1: Schematic view of the experimental setup

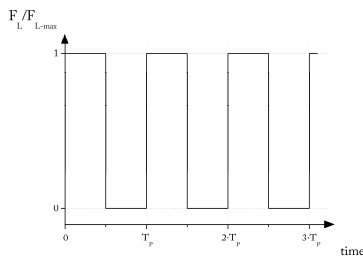


Figure 2: Modulation scheme of the Lorentz force F_L .

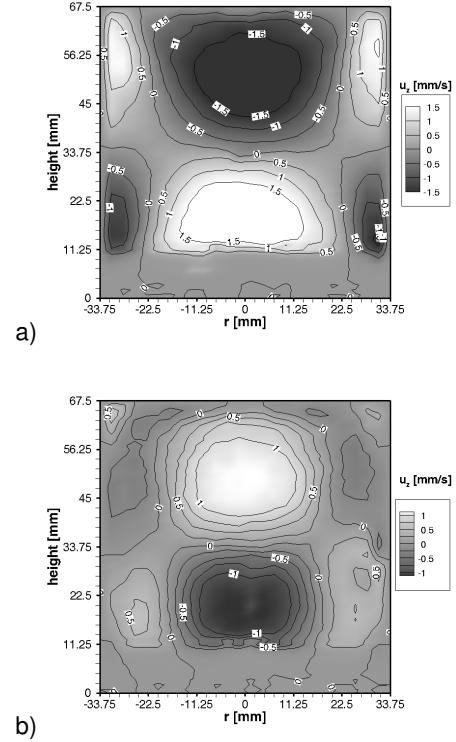


Figure 3: Snapshots of the vertical velocity across the vertical mid-plane of the cylinder recorded by the US sensor array for $T_P = 20$ s at $B_{RMF} = 0.46$ mT: (a) typical double vortex of the secondary flow; (b) “inverse” double vortex

3 RESULTS

The modulation scheme of the pulsed RMF as considered within this study is displayed in figure 2. As a consequence the fluid flow experiences a sequence of spin-up and spin-down processes. The duration of the particular pulse cycles T_P turns out to be a crucial control parameter. Measurements of the secondary flow have been carried out for different values of T_P . Figure 3 shows two snapshots of the flow pattern obtained for $B_0 = 0.46$ mT and a pulse cycle of $T_P = 20$ s. The typical structure of the toroidal double vortex can be detected in figure 3(a).

The secondary flow in the central region is directed upwards in the bottom part and downwards in the upper part of the cylinder, respectively. In figure 3(b), an inversion of the flow direction can be observed. A so-called “inverse” double vortex is formed at lower intensity. The mean values of the vertical velocity u_z averaged over both the total measuring time and the vertical cylinder cross section, which can be calculated at follows:

$$\bar{U}_z = \frac{1}{T \cdot H_0 R_0^2} \int_0^T \int_{H_0/2}^{H_0} \int_{-R_0}^{R_0} r \sqrt{u_z^2} dr dz dt \quad (1)$$

Respective results are drawn in figure 4 vs. the pulse duration cycle T_P for magnetic fields of 0.46 mT and 2.25mT.

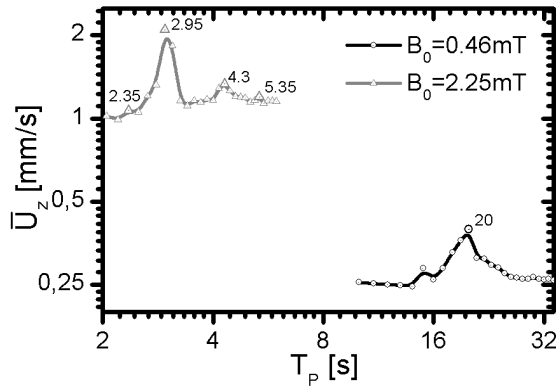


Figure 4: Dependence of the intensity of the secondary flow on the duration of the pulse cycle

It becomes obvious that the intensity of the secondary flow for $B_{RMF} = 0.46$ mT exhibits a pronounced maximum around $T_P = 20$ s, where distinct periodic reversals of the secondary flow have been observed. This resonance peak is shifted to lower T_P with increasing magnetic field strength, in particular the maximum is found at $T_P = 2.95$ s for $B_{RMF} = 2.25$ mT. Moreover, further maxima of the magnitude of the averaged secondary flow appear at larger pulse durations. Figure 5 shows snapshots of the vertical flow obtained for pulse durations which correspond to the four marked points in figure 4. It is interesting to note that the new flow pattern is characterized by an increment of vortex cells in radial or axial direction.

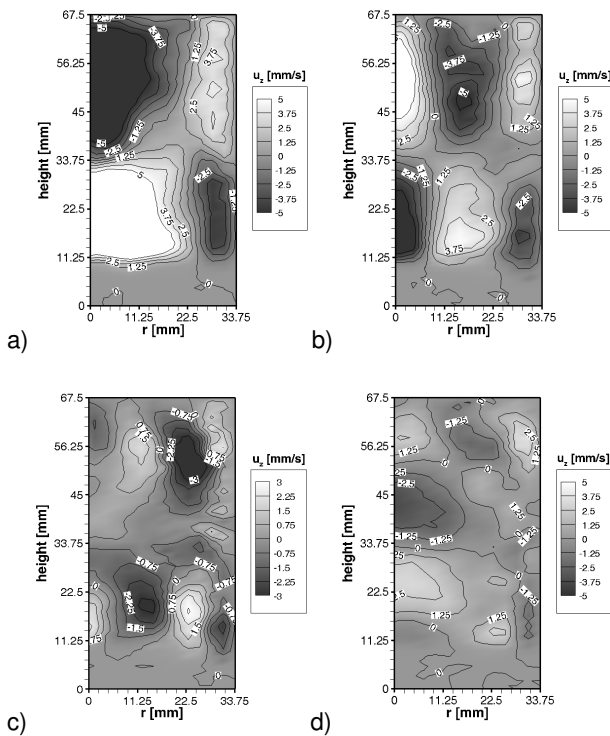


Figure 5: Snapshots of the vertical velocity across the vertical mid-plane of the cylinder recorded by the US sensor array at $B_{RMF} = 2.25$ mT: (a) $T_P = 2.95$ s, (b) $T_P = 4.3$ s; (c) $T_P = 5.3$ s and (d) $T_P = 2.35$ s

Figure 5(a) show the well-known double vortex flow structure for the maxima in the flow intensity for $T_P = 2.95$ s. For higher pulse durations we find two (figure 5(b)) and three (figure 5(c)) vortices in radial direction, respectively, which corresponds to the minor maxima in figure 4 at pulse duration times of $T_P = 4.3$ s and $T_P = 5.35$ s, respectively. Figure 5(d) shows the flow structure for a lower pulse duration time. In this case four vortices in axial direction are visible. This flow structure corresponds to the small peak at $T_P = 2.35$ s in figure 4.

All these differences in the flow intensity and structure must be reflected by the azimuthal velocity component. Figure 6 shows the time series of the azimuthal velocity for two positions and three pulse durations. The vertical position is in the midplane and in the near of the upper horizontal boundary layer (see figure 1). The pulse duration matches with the main maximum in the flow intensity, the second maximum at $T_P = 4.3$ s and a pulse duration between these distinguished points. By the switch-on and switch-off of the electromagnetic force a pulsation of the azimuthal velocity in the midplane is generated and can be observed for all three pulse durations. In the vicinity of the horizontal boundary the pulsation is also visible but with a remarkable phase shift in comparison to the midplane. For the two maxima a reversal of the vertical gradient in the azimuthal flow is observable which does not exist for the pulse duration of $T_P = 3.7$ s. These strong periodic changes in the vertical gradient of the azimuthal velocity generate an oscillation of the meridional flow and vice versa the oscillation of the meridional flow influences the transport of angular momentum.

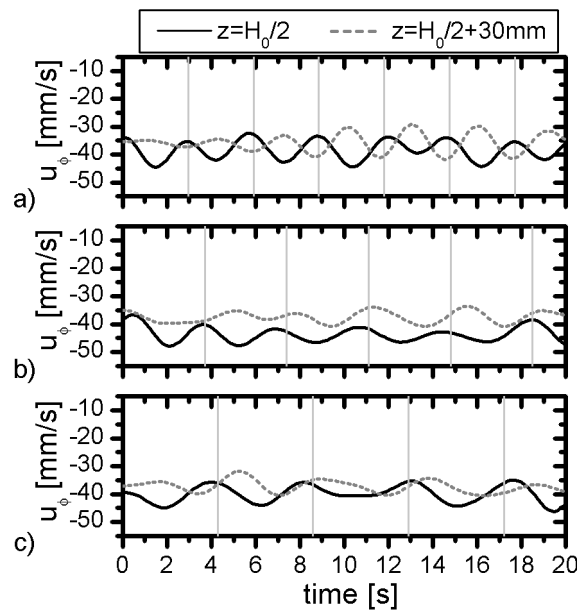


Figure 6: Time series of the azimuthal velocity in the midplane and in the near of the horizontal boundary at $B_{RMF} = 2.25$ mT: (a) $T_P = 2.95$ s, (b) $T_P = 3.7$ s and (c) $T_P = 4.3$ s

4 DISCUSSION

The present study concerns a liquid metal flow being exposed to a pulsed RMF. The alternating power-on and power-off of the magnetic field generates successive spin-ups and spin-downs of the rotating fluid flow. Abrupt changes in the energy injection rates promote the propagation of inertial waves through the interior of the fluid [12, 13]. Such waves were derived for the case of small perturbations in a fluid which rotates as solid body [9]. The Coriolis force balances the pressure gradients and generates the restoring force for the inertial waves. Theoretical eigenvalues of the inertial waves are given in the book of Greenspan (page 82) [9]. Considering the axisymmetric inertial mode $k = 0$, $n = 2$, $m = 1$ we obtain eigenperiods of 20.6 s and 3.1 s for magnetic field intensities of 0.46 mT and 2.25 mT, respectively. These results agree very well with the experimentally identified T_P values for the respective main resonance peaks. The parameter region around these resonance frequencies of the driving force appears as an optimal operating range for an efficient electromagnetic stirring, because the intensity of the secondary flow reaches a distinct maximum here. Moreover, the permanent reversals of the flow direction make this flow regime promising for applications in directional solidification processes.

A prolongation of the pulse duration T_P at 2.25 mT produces minor maxima of the magnitude of the secondary flow. Using the equation from Greenspan's book we yield eigenperiods of 4.6 s and 6.4 s for higher radial modes and 2.3 s for higher axial mode, which corresponds fairly good to the minor peaks in figure 4. These higher modes manifest themselves in new secondary flow pattern showing an incremented number of vortex cells in radial or axial direction (see figure 5).

5 CONCLUSION

In this present study, we have discussed the impact of a discontinuous applied rotating magnetic field with subsequent equidistant pulses. A new ultrasound Doppler array measurement technique was used and a two-dimensional-one-component flow mapping of transient flows with a high time resolution was realized. Other groups measured 2D flow structures before [14,15] but only the time-averaged pattern. For the case of time modulated magnetic fields and the resultant discontinuous fluid flow the possibility of highly time-resolved flow measurements is indispensable to understand the flow structure.

The electromagnetic stirring method that uses a modulated RMF offers a considerable potential to enhance the stirring efficiency and to optimize the properties of castings by a well-aimed flow control during solidification. Further investigations are

necessary to improve the understanding of the development of various flow regimes under the influence of a time-modulated driving force.

This work was financially supported by Deutsche Forschungsgemeinschaft (DFG) in form of the collaborative research centre SFB 609 "Electromagnetic Flow Control in Metallurgy, Crystal Growth and Electrochemistry".

REFERENCES

- [1] Medina M, Du Terrai Y, Durand F, Fautrell Y: Channel Segregation during Solidification and the Effects of an Alternating Traveling Magnetic Field, *Metall. Mater. Trans. B*, 2004, 35B: 743-755.
- [2] Nikrityuk PA, Eckert K, Grundmann R: A numerical study of unidirectional solidification of a binary metal alloy under influence of a rotating magnetic field, *Int. J. Heat Mass Transfer*, 2006, 49: 1501-1511.
- [3] Vives C: Elaboration of Metal Matrix Composites from Thixotropic Alloy Slurries Using a New Magnetohydrodynamic Caster, *Metall. Trans. B*, 1993, 24B: 493-510.
- [4] Taniguchi S, Mataike K, Okubo M, Ando T, Ueno K: Proc. of the 4th Int. Conf. on Electromagnetic Processing of Materials (EPM), Sendai 2003: 339-343.
- [5] Spitzer K-H, Reiter G, Schwerdtfeger K: Multi-Frequency Electromagnetic Stirring of Liquid Metals, *ISIJ Int.*, 1996, 36: 487-492.
- [6] Kojima S, Ohnishi T, Mori T, Shiwaku K, Wakasugi I, Ohgarni M: Application of advanced mild Stirring to a new bloom caster, Proc. of the 66th Steelmaking Conf., Atlanta 1983: 127-131.
- [7] Eckert S, Nikrityuk PA, Rübiger D, Eckert K, Gerbeth G: Efficient Melt Stirring Using Pulse Sequences of a Rotating Magnetic Field: Part I. Flow Field in a Liquid Metal Column, *Metall. Mater. Trans. B*, 2007, 38B: 977-988.
- [8] Willers B, Eckert S, Nikrityuk PA, Rübiger D, Dong J, Eckert K, Gerbeth G: Efficient Melt Stirring Using Pulse Sequences of a Rotating Magnetic Field: Part II. Application to Solidification of Al-Si Alloys, *Metall. Mater. Trans. B*, 2008, 39B: 304-316.
- [9] Greenspan HP: The theory of rotating fluids, Breukelen Press, Brookline 1990
- [10] Takeda Y: Development of an ultrasound velocity profile monitor, *Nucl. Eng. Design*, 1991, 126: 277-284.
- [11] Franke S, Büttner L, Czarske J, Rübiger D, Eckert S: Ultrasound Doppler system for two-dimensional flow mapping in liquid metals, *Flow Meas. Instrum.*, 2010, 21: 402-409.
- [12] Nikrityuk PA, Ungarish M, Eckert K, Grundmann R: Spin-up of a liquid metal flow driven by a rotating magnetic field in a finit cylinder: A numerical and an analytical study, *Phys. Fluids*, 2005, 17: 067101.
- [13] Rübiger D, Eckert S, Gerbeth G: Measurements of an unsteady liquid metal flow during spin-up driven by a rotating magnetic field, *Exp. Fluids*, 2010, 48: 233-244.
- [14] Takeda Y, Kikura H: Flow mapping of mercury flow, *Exp. Fluids* 32 (2002), 161-169.
- [15] Andreev O, Kolesnikov Y, Thess A: Application of the ultrasonic velocity profile method to the mapping of liquid metal flows under the influence of a non-uniform magnetic field, *Exp. Fluids* 46 (2009), 77-83.

Investigation of flow structure in electromagnetically driven liquid metal confined in an annulus by Ultrasonic Doppler Velocimetry

- ISUD8 2012 -

F. Samsami*, A. Thess†

* Institute of Thermo- and Magnetofluidynamics
Ilmenau University of technology
Am Helmholtzring 1 ,98693 Ilmenau, Germany
e-mail: farzaneh.samsami@tu-ilmenau.de, web page:<http://www.tu-ilmenau.de/lorentz-force>

† Institute of Thermo- and Magnetofluidynamics
Ilmenau University of technology
Am Helmholtzring 1 ,98693 Ilmenau, Germany
e-mail:andre.thess@tu-ilmenau.de - Web
page:<http://www.tu-ilmenau.de/fakmb/Prof-Andre-Thess.4115.0.html>

ABSTRACT

Electromagnetic driving of the fluids as the driving mechanism in electromagnetic pumps is of great interest in industry. On the other hand the fluid flow in annulus has its own place in investigating the channel flow structure in the sense that we can use it as a model for a very long channel. It means that we can have the same flow structure in a confined area without wasting too much energy and effort to build up a long channel. Although the combination of electromagnetic force with toroidal geometry sounds efficient and practical, but lots of questions will arise when we do combine them. These questions are mainly about the formation of Hartmann layer and its role on transition to turbulence. During the last decades several numerical and experimental investigations were aimed to determine the instability criteria of this problem. In the previous experiments the potential drop across the annular channel has been used as a measure to show the transition to turbulence. Since these voltage drops can't give us any information about the structure of the flow, we decided to spot the possibility of using UDV to detect this structure. A rectangular channel with 10mm \times 67mm cross section and an inner radius of 40mm is used in this investigation. The channel is filled up with eutectic alloy GaInSn. Two insulating Hartmann walls and two conducting side walls which are 10mm apart (in the radial direction) are the special boundary conditions in our case. Side walls are parallel to the magnetic field. Our facilities let us test 500mT as maximum magnetic field and 2000A as the maximum driving current. An ultrasonic 8 MHz sensor with the aid of DOP2000 is used for this investigation. Here we will represent the results of our experiments and compare them with the theoretical predictions of the reference literatures. This will help understanding the role of Hartman layer on transition to turbulence.

REFERENCES

- [1] A. Cramer, C. Zhang, S. Eckert *Local flow structures in liquid metals measured by ultrasonic Doppler velocimetry*, Flow Measurement and Instrumentation **15-3**, 145-153, 2004.
- [2] P. Moresco, T. Alboussiere *Experimental study of the instability of the hartmann layer*, J. fluid Mech. **504**,167-181, 2004.

A new fully digital UVP enabling quantitative in-line rheometry

A. Debacker¹, B. Birkhofer^{2*}, D. Lootens¹, R. Bourquin¹, S. Ricci³ and P. Tortoli³

¹Sika Technology AG, ²Sika Services AG, ³Dept. of Electronics and Telecommunications, Florence University, Italy

^{1,2}Tüffenwies 16, CH-8048 Zurich, Switzerland (*Corresponding author: birkhofer.beat@ch.sika.com)

The performance of a newly developed fully digital UVP-PD (Ultrasonic Velocity Profiling with Pressure Drop) electronics is tested and validated with a Non-Newtonian model solution. For this purpose, a piston setup is used to create well defined flow conditions to enable a comparison of theoretical and measured velocity profile. The rheometric parameters are estimated in-line with UVP-PD by using three different approaches and compared with those obtained from off-line rotational rheometer. Considering the shear rate range available in the pipe flow, a good agreement of in- and off-line results is found.

Keywords: in-line rheometry, non-Newtonian fluids, ultrasonic velocimetry, pipe flow

1 Introduction

The idea to derive information on the flow behavior of liquids from the velocity profile measured by ultrasound — in other words, the use of Doppler velocimetry as in-line rheometer — is older than 30 years. In this period, several research groups worked on this concept: Kowalewski [9], Müller et al. [10], Ouriev and Windhab [11], Wiklund et al. [18], Wiklund and Stading [17], Birkhofer et al. [2], Fischer et al. [5], Wassell et al. [16], Dogan et al. [3, 4], Kotze et al. [8], Petit et al. [12], Birkhofer [1]. A feasibility study in highly filled adhesives presented in former work [12], proved that the UVP-DP can be used in industry for a quantitative analysis of the rheological properties of complex fluids. In order to adapt the setup to industrial requirements, a new electronic device [15], based on former work [13, 14] has been developed. The accuracy and limitations of the new UVP-PD device and technique itself are first evaluated with a well defined Non-Newtonian model liquid and flow conditions. For this purpose, a solution of polyethylene oxide polymers is pumped with a piston setup and the velocity profiles, pressure drops and temperatures are recorded. The resulting rheological parameters are then extracted, using different rheometric characterization approaches and compared with the results obtained from off-line rotatory rheometry measurements.

2 Material and methods

2.1 Polyox solution

A Solution of 2% by weight of polyethylene oxide with a molecular mass of 1 000 000 is dispersed with 0.2% of Acticide (preservative) in water to obtain a stable, shear thinning fluid.

2.2 Flow setup

The tailored flow setup has been built with a linear piston which allows to pump the fluid through a pipe of 25 mm inner diameter. A continuous flow rate ranging from 10 ml/min to 2 l/min can be obtained with this setup, allowing a well defined continuous flow of the fluid in the instrumented pipe section. This section also comprises two absolute pressure sensors and two temperature sensors.

2.3 Electronics and transducer

The electronics used in this work [15] has been developed by the University of Florence based on a previous research board [13] in collaboration with Schmid-Engineering (Münchwilen, Switzerland), Sika Technology AG and Sika Services AG. The system is connected to a custom made 5 MHz pencil transducer, excited with a 5 cycle Hanning windowed pulse of 5 MHz. The data received from the transducer in each pulse repetition interval (PRI) are sampled at 74.3 MS/s, with a 16 bit resolution. The signals are coherently demodulated, decimated to 18.6 MS/s (corresponding to a gate resolution in water ($c = 1480$ m/s) of 79.7 μ m) by the on board FPGA and stored to a 64 MB SDRAM. The data is transferred via an ethernet connection to a PC, where it is visualized and saved in a file for further post processing. Typically 4096 PRIs are acquired for each measurement. The electronics also allows the simultaneous acquisition of pressure and temperature data. As an additional feature it is also possible to obtain the unprocessed radio frequency data, which are useful for the investigation of artifacts and the optimization of ultrasound parameters such as the amplification.

2.4 Signal processing

The velocity profile is estimated through a weighted mean of the Doppler power spectra from each depth [12]. This approach avoids the necessity of a deconvolution [7, 6]. In the model systems it is possible to obtain the full profile over the complete pipe diameter, but the second half of the profile, opposite to the transducer, is disturbed by internal reflections. For this reason, only the first half is used for the data analysis.

2.5 Rheometry

The conventional approach to extract rheometric information from the velocity profile is a nonlinear least square fitting, using equation 1. The equation describes the velocity profile for power law fluids, defined by $\eta = K\dot{\gamma}^{n-1}$, where η is the viscosity, K the power law coefficient, $\dot{\gamma}$ the shear rate and n the power law exponent.

$$v(r) = \frac{Q}{\pi R^2} \frac{3n+1}{n+1} \left(1 - \left(\frac{r}{R} \right)^{\frac{n+1}{n}} \right) \quad (1)$$

Q : flow rate, R : radius, r : radial distance from the pipe center.

A simplified technique is the use of the relation of the maximum velocity and n as shown in equations 2 and 3.

$$v_{\max} = \frac{Q}{\pi R^2} \frac{3n+1}{n+1} \quad (2)$$

which can be transformed to:

$$n = \frac{v_{\max} - a}{3a - v_{\max}}; \quad a = \frac{Q}{\pi R^2} \quad (3)$$

Compared to the fitting approach, the complexity and computational weight of the maximum velocity based approach is extremely reduced, which makes it interesting for the implementation in an embedded system.

For both approaches the power law coefficient K can be calculated in a second step, using equation 4, which requires a pressure drop (ΔP) measurement over a certain length (L).

$$K = \frac{\Delta P}{2L} \left(\frac{Q}{\pi} \frac{3n}{n} R^{\frac{-3n-1}{n}} \right)^n \quad (4)$$

Compared to the classic technique, where n and K are fitted simultaneously [2] this two-step approach allows to clearly distinguish problems originating from the profile shape and the pressure drop measurement.

The wall shear rate, used as maximum shear rate of the in-line measurements in the comparison with the off-line rheometry, is calculated using equation 5.

$$\dot{\gamma}_w = \frac{3n+1}{4n} \frac{4Q}{\pi R^3} \quad (5)$$

Finally, a third approach, the so called gradient method [10], is used. For this method the local shear stress τ is $\Delta Pr/2L\dot{\gamma}$ and $\dot{\gamma}$ simply the first derivation of the velocity profile, thus $\dot{\gamma} = dv/dr$.

3 Results and discussion

3.1 Rotational rheometry

The off-line rheometry measurements are made as triple determination with an Anton Paar Physica MRC301 rheometer, using a cone/plate geometry with a 2° angle and 25 mm diameter. The Polyox solution shows a shear thinning behaviour (fig. 1), which can be approximated with the power law model. The corresponding fits are also shown in figure 1 in dashed and dotted lines. The plot shows that the shear thinning is more pronounced at higher shear rates. The temperature influence between 20 and 25 °C is rather insignificant and nearly in the precision of the measurement.

3.2 In-line rheometry

The presented results are based on 56 measurements made with flow rates varying from 100 to 3000 ml/min at fluid temperatures between 23.5 and 24.5 °C. For the measurements only the pulse repetition frequency is adjusted to the flow rate, all other measurement and processing parameters are identical over all measurements.

Figure 2 shows the intensities of the power spectra for a representative example, where the black line is the estimated profile. This profile, also shown in thin line in figure 3, is then used for the fitting (thick line in the same figure), the estimation of the maximum velocity and the determination of the first derivative for the gradient method.

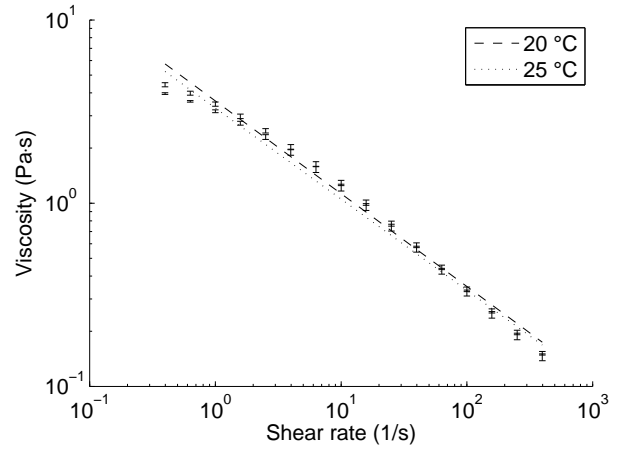


Figure 1: Viscosity of Polyox (0.125%) as function of the shear rate at 20 °C and 25 °C measured with a rotational rheometer. Error bars indicate the $\pm 2\sigma$ range from the triple determination.

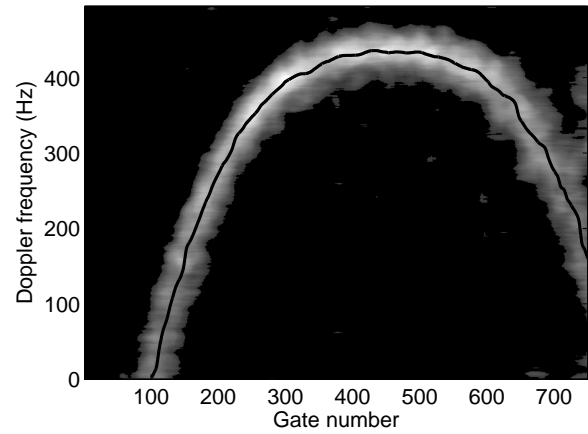


Figure 2: Spectral intensities represented as surface plot and the estimated profile in black line. The flow rate is 2500 ml/min.

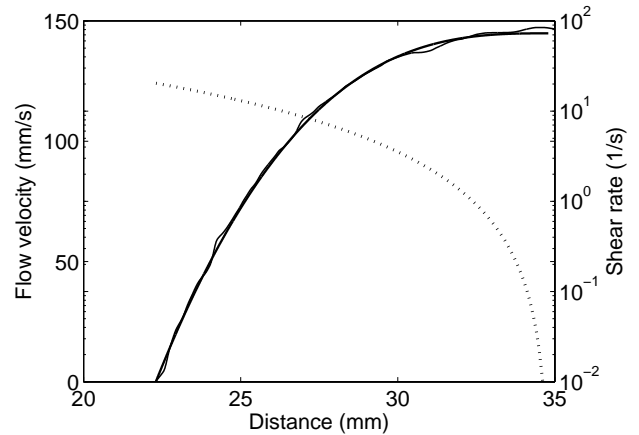


Figure 3: The estimated flow velocity profile from figure 2 in thin line, the fitted power law profile in thick line and the local shear rate in dotted line.

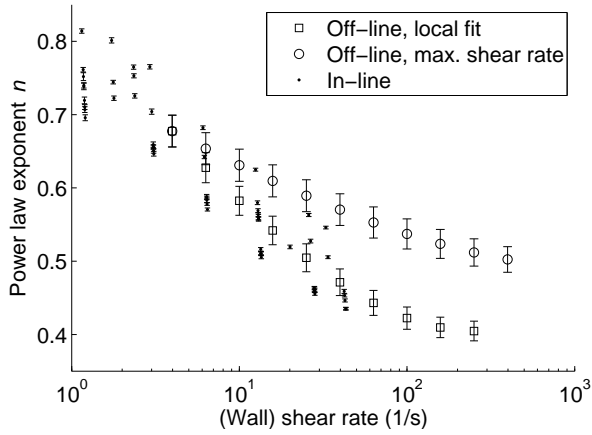


Figure 4: A comparison of the power law exponent n determined by two different approaches from the off-line rheometer data and the in-line measurements. The error bars indicate the 95% confidence interval from the fitting.

3.2.1 Power law model fitting

As shown in section 3.1, the Polyox solution is not a perfect power law fluid: the shear thinning behaviour, characterized by the power law exponent n , increases with shear rate. Nevertheless, a meaningful fit is possible because the relevant shear rate range over the pipe radius, with its maximum at the pipe wall, is limited to one or two decades (fig. 3, dotted line). The coefficient of determination (R^2) for the fit with equation 1 is at least 0.9932. Figure 4 shows the power law exponent n extracted in 3 different ways as a function of the shear rate: (1) from the rotational rheometer data using 6 consecutive measurement points («local fit»), corresponding approximately to one decade, (2) also from the off-line rheometer, using the data from the minimum shear rate to the shear rate on the x-axis («max. shear rate»), also with a minimum of 6 points, and (3) the in-line data with the points shown on the x-axis at their wall shear rate.

An alternative comparison of the in- and off-line data is shown in figure 5 where the in-line results are represented with the shear rate dependent viscosity determined over one decade based on the fitted power law parameter n and K . The agreement observed is good and the in-line data also shows the increase of the shear thinning behaviour with increasing shear rate.

3.2.2 Maximum velocity based analysis

Equation 3 can be used to calculate the power law exponent n directly from the maximum velocity of the flow velocity profile. Figure 6 shows the correlation of the two different calculation methods. The fitted line has a slope of 0.94 and an offset of 0.0063. The n determined from the maximum velocity is always larger than the n determined from the fitting. This can easily be explained with the stronger influence of the behaviour at low shear rates in the pipe center.

3.2.3 Gradient method

The results of the gradient method are shown in figure 7. Applying more smoothing and filtering it would be possible to achieve better result, but then the degree of complexity increases with-

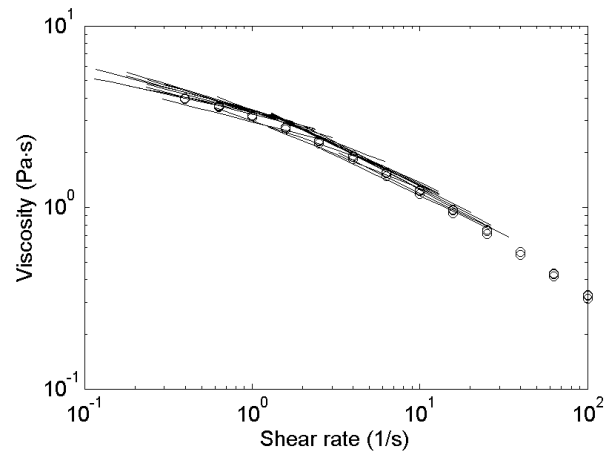


Figure 5: Viscosity as function of shear rate measured by the rotational rheometer shown in circles. The lines are based on the power law parameters n and K determined in-line.

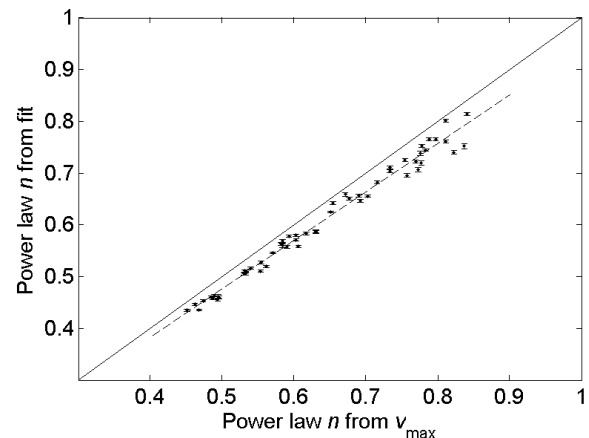


Figure 6: Comparison of the power law exponent n determined by two different methods: fitting and extraction from the maximum flow velocity. The solid line shows the 1:1 correlation, the dashed line the linear approximation of the points.

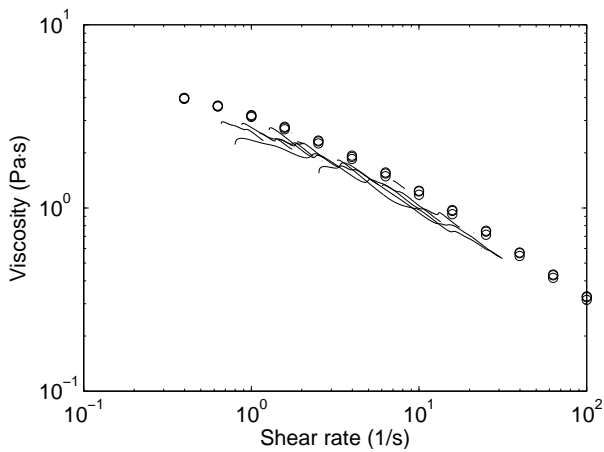


Figure 7: Viscosity as a function of the shear rate determined by the off-line rotational rheometer (circles) and the gradient method (one curve per measurement).

out additional information compared to the power law fitting approach. The main problem of this method is the strong impact of minor artifacts in the shape of the measured velocity profile on the derived local shear rate.

4 Summary and conclusions

The presented first series of measurements made on a simple Non-Newtonian fluid prove, that UVP-PD can be used to obtain accurate and quantitative measurement of the flow properties. It is important to consider the shear rate range in the pipe flow. As it is usually limited to one or two decades, it is possible to use the power law fluid model as an approximation for a fluid, which is not perfectly described by the power law model. It is also possible to use simply the maximum velocity for the rheological characterization. The gradient method also gave an acceptable agreement between in- and off-line measurements, but it showed no advantages compared to the power law model approach.

References

- [1] B. Birkhofer. *Practical Food Rheology: An Interpretive Approach*, chapter Doppler Ultrasound-Based Rheology, pages 29–60. Wiley-Blackwell, 2011.
- [2] B. H. Birkhofer, S. A. K. Jeelani, E. J. Windhab, B. Ouriev, K.-J. Lisner, P. Braun, and Y. Zeng. Monitoring of fat crystallization process using UVP-PD technique. *Flow Measurement and Instrumentation*, 19(3-4):163–169, 2008. doi: 10.1016/j.flowmeasinst.2007.08.008.
- [3] N. Dogan, M. J. McCarthy, and R. L. Powell. Comparison of in-line consistency measurement of tomato concentrates using ultrasonics and capillary methods. *Journal of Food Process Engineering*, 25:571–587, 2003. doi: 10.1111/j.1745-4530.2003.tb00652.x.
- [4] N. Dogan, M. J. McCarthy, and R. L. Powell. Measurement of polymer melt rheology using ultrasonics-based in-line rheometry. *Measurement Science and Technology*, 16(8):1684–1690, 2005. doi: 10.1088/0957-0233/16/8/021.
- [5] P. Fischer, B. Ouriev, and E. J. Windhab. Macroscopic pipe flow of micellar solutions investigated by ultrasound Doppler velocimetry. *Tenside Surfactants Detergents*, 46(3):140–144, 2009.
- [6] P. E. Hughes and T. V. How. Quantitative measurement of wall shear rate by pulsed Doppler ultrasound. *Journal of Medical Engineering & Technology*, 17(2):58–64, 1993.
- [7] J. E. Jorgensen and J. L. Garbini. An analytical procedure of calibration for the pulsed ultrasonic Doppler flow meter. *Transactions of the ASME/Journal of Fluids Engineering*, 96:158–167, 1974.
- [8] R. Kotze, J. Wiklund, R. Haldenwang, and V. G. Fester. Measurement and analysis of flow behaviour in complex geometries using ultrasonic velocity profiling (UVP) technique. *Flow Measurement and Science Journal*, 22(2):110–119, 2011. doi: 10.1016/j.flowmeasinst.2010.12.010.
- [9] T. A. Kowalewski. Velocity profiles of suspension flowing through a tube. *Archives of Mechanics*, 32(6):857–865, 1980.
- [10] M. Müller, P. Brunn, and C. Harder. New rheometric technique: The gradient-ultrasound pulse Doppler method. *Applied Rheology*, 7(5):204–210, 1997.
- [11] B. Ouriev and E. J. Windhab. Rheological study of concentrated suspensions in pressure-driven shear flow using a novel in-line ultrasound Doppler method. *Experiments in Fluids*, 32:204–211, 2002. doi: 10.1007/s003480100345.
- [12] P. Petit, B. Birkhofer, and D. Lootens. Wall shear measurement based on ultrasonic velocimetry for process in-line rheometry. In J. Wiklund, E. L. Bragd, and S. Manneville, editors, *Proceedings of the 7th International Symposium on Ultrasonic Doppler Methods for Fluid Mechanics and Fluid Engineering*, pages 17–20, 2010.
- [13] S. Ricci, E. Boni, F. Guidi, T. Morganti, and P. Tortoli. A programmable real-time system for development and test of new ultrasound investigation methods. *IEEE Transactions on Ultrasonics, Ferroelectrics, and Frequency Control*, 53(10):1813–1819, 2006. doi: 10.1109/TUFFC.2006.113.
- [14] S. Ricci, B. Birkhofer, D. Lootens, and P. Tortoli. In-line rheometry for highly filled suspensions through doppler ultrasound. In *2010 IEEE Ultrasonics Symposium (IUS)*, pages 2044–2047, 2010. doi: 10.1109/ULTSYM.2010.5935438.
- [15] S. Ricci, M. Liard, B. Birkhofer, D. Lootens, A. Brühwiler, and P. Tortoli. Embedded Doppler system for industrial in-line rheometry. *IEEE Transactions on Ultrasonics, Ferroelectrics, and Frequency Control*, 59(7):1395–1401, 2012. doi: 10.1109/TUFFC.2012.2340.
- [16] P. Wassell, J. Wiklund, M. Stading, G. Bonwick, C. Smith, E. Almiron-Roig, and N. W. G. Young. Ultrasound Doppler based in-line viscosity and solid fat profile measurement of fat blends. *International Journal of Food Science and Technology*, 45(5):877–883, 2010. doi: 10.1111/j.1365-2621.2010.02204.x.
- [17] J. Wiklund and M. Stading. Application of in-line ultrasound Doppler-based UVP-PD rheometry method to concentrated model and industrial suspensions. *Flow Measurement and Instrumentation*, 19(3-4):171–179, 2008.
- [18] J. Wiklund, I. Shahram, and M. Stading. Methodology for in-line rheology by ultrasound Doppler velocity profiling and pressure difference techniques. *Chemical Engineering Science*, 62:4277–4293, 2007.

Characteristic Velocity Distribution of Rectangular Duct Flow of a Magnetic Fluid under Magnetic Field

Masaaki MOTOZAWA¹, Tsukasa SEKINE¹, Tatsuo SAWADA² and Yasuo KAWAGUCHI¹

¹Department of Mechanical Engineering, Tokyo University of Science
2641 Yamazaki, Noda 278-8510, Japan

²Department of Mechanical Engineering, Keio University
3-14-1 Hiyoshi, Kohoku-ku, Yokohama 223-8522, Japan

Velocity distribution of rectangular duct flow of a magnetic fluid was measured using Ultrasonic Velocity Profiling (UVP) method and influence of magnetic field on the velocity distribution was investigated. Velocity profile measurements have been performed in both laminar flow and turbulent flow and we paid attention to the effects of external magnetic field intensity ranging from 0 mT to 700 mT. As a result of the measurements, characteristic velocity distribution was obtained. In the case of laminar flow, when the magnetic field is applied to this magnetic fluid flow, the flow velocity at the center of the rectangular duct decreases and the velocity gradient in the near-wall region increases. On the contrary, in the case of turbulent flow, not only velocity gradient but also flow velocity near the center of the duct increases with applying magnetic field. This fact indicates that the characteristic anisotropy exist in the velocity distribution related to the magnetic field direction.

Keywords: Magnetic fluid, Rectangular duct flow, UVP, Uniform magnetic field.

1 INTRODUCTION

After development of the UVP method [1], measurement of velocity distribution in many kinds of opaque fluid could be realized. In this study, we focused on the magnetic fluid flow. Magnetic fluid is a stable colloidal dispersion of rather small surfactant-coated magnetic particles in a liquid carrier, such as water or kerosene [2]. These particles are about 10 nm in size and have magnetic single domain structure. Magnetic fluid can be treated as a Newtonian fluid under no magnetic field. However, when magnetic field is applied to magnetic fluid, several interesting flow behavior, which are not seen in a Newtonian fluid, can be observed because of its strong magnetism.

Because magnetic fluid has very unique characteristics under magnetic field, magnetic fluid is applied to many industrial technologies [3]. In addition, in order to better understand these characteristic properties, the internal velocity field is one of the very important information. However, in spite of the importance of the measurement of the internal velocity field, it is very difficult to measure the velocity distribution of a magnetic fluid. Because magnetic fluid is opaque and a kind of a solid-liquid two-phase flow, the optical methods such as LDV (Laser Doppler Velocimetry) or PIV (Particle Image Velocimetry), and the electrical method such as hot-wire anemometer can not apply to measure the velocity field in magnetic fluid flow. As mentioned above, the UVP method realized the measurement of the velocity field of magnetic fluid flow.

There are a few studies on the velocity distribution

of a magnetic fluid flow by the UVP method. Kikura et al. [4] measured the velocity distribution of the Taylor vortex flow of a magnetic fluid and discussed the influence of non-uniform magnetic field. They reported that when the magnetic field is applied the velocity magnitude decreases, and wavelength of Taylor vortex flow also decreases with increasing magnetic field intensity. In our previous study [5], we apply the UVP method to the oscillating pipe flow of a magnetic fluid. As a result of this measurement, the Annular effect, which is the characteristic reversed flow phenomenon in the center region of the pipe in the oscillating flow of the Newtonian fluid, can be observed under no magnetic field. In contrast, when the magnetic field is applied to the oscillating pipe flow of magnetic fluid, this Annular effect disappears. Thus, these experimental studies have shown the efficiency of the UVP method for velocity profile measurement of magnetic fluid.

In our previous study [6], we investigated the forced convective heat transfer in the rectangular duct flow of a magnetic fluid in a laminar flow. The result showed the heat transfer was enhanced locally in the region in which the magnetic field existed. In order to better understand the reason of this heat transfer enhancement, the internal velocity fields should provide useful information. Therefore, in this study, we measured the velocity distribution of the rectangular duct flow of a magnetic fluid. Experiments were performed in both laminar magnetic fluid flow and turbulent magnetic fluid flow. The magnetic field intensity can be varied from 0 mT to 700 mT. On the basis of the experimental results, the influence of magnetic field on the velocity distribution was discussed.

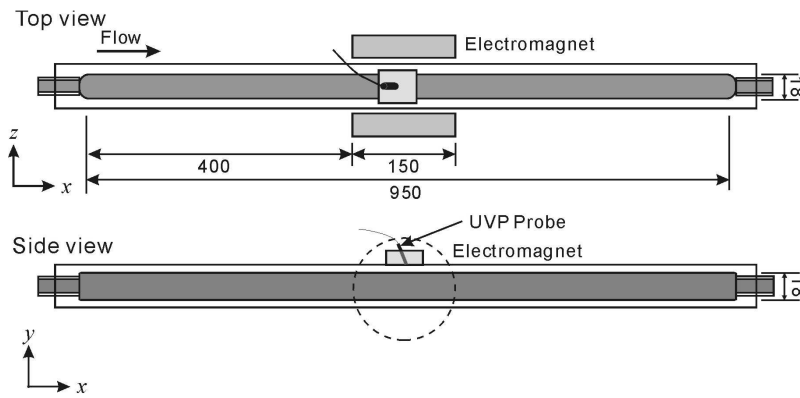


Figure 1: Detailed structure of the rectangular duct.

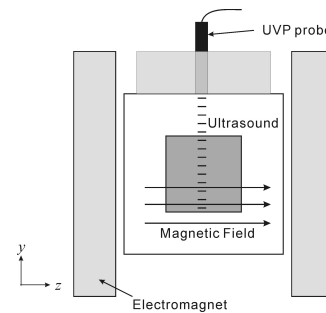


Figure 2: Cross-section of the duct.

2 EXPERIMENT

2.1 Experimental apparatus

Figures 1 and 2 showed the detailed structure of the rectangular duct and the cross-section of this duct at the center position. Experiment was performed with a closed circuit loop with this rectangular duct as a test section. This rectangular duct was made of a transparent acrylic resin, having 18 mm × 18 mm in cross-section and 950 mm in length. The hydraulic diameter D_h of this duct is 18 mm. We defined the Cartesian coordinates as shown in Figs. 1 and 2 (i.e. x : Streamwise direction, y : Direction of normal to the bottom wall, z : Spanwise direction). A thermocouple was set at the inlet of this duct. Therefore, we could measure the inlet temperature of the flow liquid T_{in} . A storage tank on the flow loop was equipped with a heater and a cooler to keep T_{in} at a constant level. An electromagnet was located at the center of the test section. This electromagnet could apply a uniform magnetic field to the magnetic fluid flow and the magnetic field could be varied from 0 mT to 700 mT. In this experiment, the Reynolds number based on the bulk mean velocity and hydraulic diameter was set to 960 (laminar magnetic fluid flow) and 2830 (turbulent magnetic fluid flow).

UVP probe was set on the center of the rectangular duct and at the position where magnetic field is applied to the magnetic fluid. Therefore, we can measure the velocity distribution in the x - y plane at the center of the duct. The UVP probe was fixed on the outer wall of the duct with an angle of 14°. The UVP monitor is XW-PSi model manufactured by Met-Flow SA. In order to obtain reflected echo signal, we added the polymethylmethacrylate particles (MBX-100 produced by Sekisui Plastics Co., Ltd.) as tracer particles. These particles have 115 μ m in mean diameter.

2.2 Magnetic fluid

We used a water-based magnetic fluid named W-40 produced by Taiho Industries Co., Ltd. as the test magnetic fluid. W-40 was 40 % weight concentration of fine magnetite particles (Fe_3O_4) in water. However, because W-40 is too dense for this

experiment, we diluted this magnetic fluid to 70 volume % with water as a test fluid. The density and viscosity of this test magnetic fluid were 1.301 kg/m³ and 8.0 mPa·s, respectively.

2.3 Sound velocity in magnetic fluid

When we measure the velocity profile by UVP method, the sound velocity in the test fluid is needed for the detection of velocity profile information, such as the position from where the ultrasound is reflected and instantaneous velocity at each position. Therefore, we need to measure the sound velocity in a magnetic fluid before the velocity profile measurement by UVP method. Moreover, it is necessary to investigate the influence of magnetic field on the sound velocity in magnetic fluid.

In our previous study [7], we constructed the experimental apparatus for precise measurement of the sound velocity in a magnetic fluid under magnetic field. Details of the measurement technique can be found in Motozawa et al. [7]. Then, we measured the sound velocity in magnetic fluid and investigated the influence of magnetic field on the sound velocity in magnetic fluid. The results showed when a magnetic field is applied to a magnetic fluid, the sound velocity slightly changes with magnetic field intensity and the length of time the magnetic field is applied to magnetic fluid. Regarding magnetic fluid, the inner particles coagulate and form a chain-like cluster under a magnetic field. This change of the sound velocity in magnetic fluid seems to be caused by chain-like cluster formations. However, because the change in the sound velocity is rather small (less than 0.1 % in the case of test magnetic fluid of this study), this change does not influence UVP measurements. The sound velocity in the test magnetic fluid was $c = 1429$ m/s.

3 RESULTS AND DISCUSSION

3.1 Laminar flow

Figure 3 shows the velocity distribution of a rectangular duct flow of a magnetic fluid with and

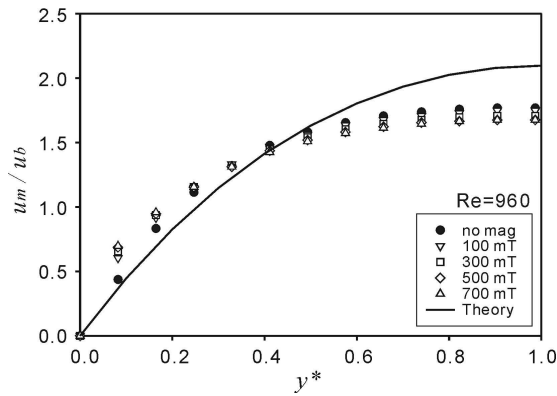


Figure 3: Influence of magnetic field on velocity distribution of laminar magnetic fluid flow ($Re = 960$).

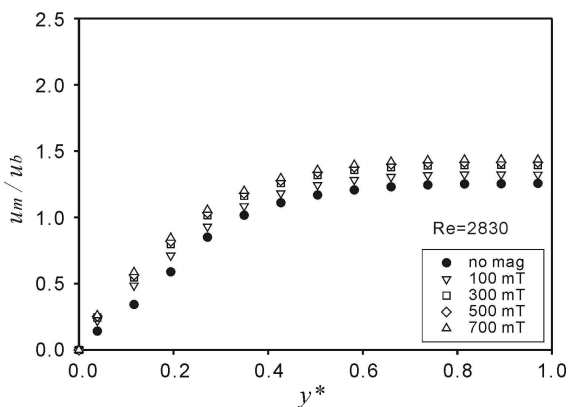


Figure 4: Influence of magnetic field on velocity distribution of turbulent magnetic fluid flow ($Re = 2830$).

without magnetic field at $Re = 960$ (Laminar flow). In this figure, the closed circle plots and solid line indicate the velocity distribution of the magnetic fluid flow under no magnetic field, and Newtonian fluid calculated by the theory, respectively. The horizontal axis is the distance from the bottom wall normalized by the half of the duct and the vertical axis is the mean velocity u_m normalized by the bulk mean velocity u_b .

Though magnetic fluid can be treated as a Newtonian fluid under no magnetic field, the configuration of the measured velocity distribution is different from that of the Newtonian fluid. This is due to a problem in the experimental system. In this experiment, we measured the velocity distribution at the developing region. Therefore, the magnetic fluid flow was not developed enough and the velocity distribution of magnetic fluid under no magnetic field was different from that of the Newtonian fluid.

On the other hand, when the magnetic field is applied to magnetic fluid, this figure indicates that the mean velocity in the center region of the duct decreases and the velocity gradient increases near the wall. The decrement of the mean velocity and increment of velocity gradient becomes larger with increasing magnetic field.

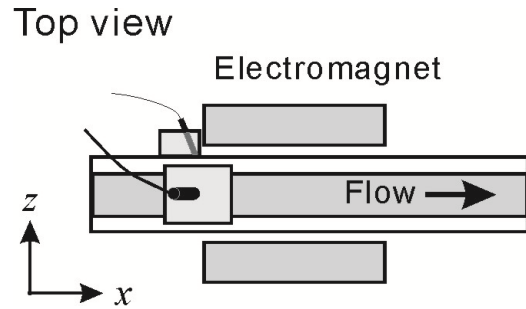


Figure 5: Measurement of velocity distribution in both x - y plane and x - z plane at entrance region of the magnetic field.

Generally, when the magnetic field is applied to magnetic fluid, the apparent viscosity increases with increasing magnetic field. Therefore, because the apparent viscosity suddenly increases in the region where the magnetic field exists, it seems that the mean velocity near the center of the duct decreases.

3.2 Turbulent flow

In contrast, Fig. 4 shows the influence of the magnetic field on the velocity distribution of the turbulent magnetic fluid flow at $Re = 2430$ (Turbulent flow). In the case of the turbulent flow, characteristic velocity distribution was obtained. When the magnetic field is applied to a magnetic fluid, not only the velocity gradient near the wall but also the mean velocity near the center of the duct increases with increasing magnetic field intensity. In this study, experiments carried out under a constant flow rate under magnetic field. Therefore, this fact indicates that the velocity distribution in the x - y plane is different from that in the x - z plane and characteristic anisotropy of the velocity distribution exists related to the magnetic field direction. In addition, although the result is not shown in this paper, the streamwise velocity fluctuation was greatly suppressed with increasing magnetic field intensity.

3.3 Measurement at entrance of magnetic field

It is impossible to measure the velocity distribution in the x - z plane at the same position because of the existence of the iron-core of the electromagnet as shown in Fig. 1. Hence, we try to measure the velocity distribution in the x - y plane and the x - z plane at the entrance region of the magnetic field. Fig.5 shows the position of the UVP probes for this measurement. UVP probes were set just before the iron-core of the electromagnet and ultrasound from the UVP probe should propagate the magnetic fluid flow in the region where the magnetic field exists.

Figures 6 and 7 shows the influence of the magnetic field on the velocity distribution in the x - y plane and the x - z plane respectively at $Re = 2430$ (Turbulent

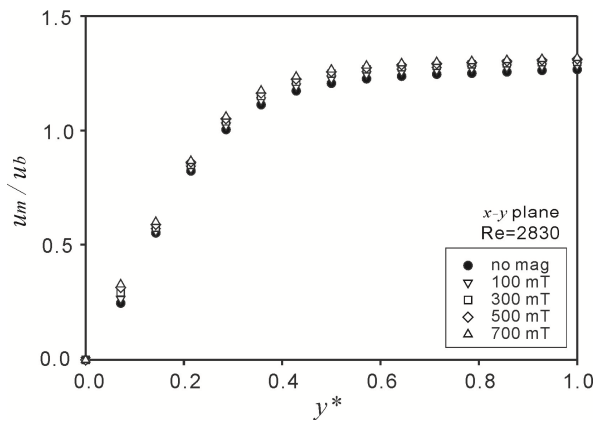


Figure 6: Influence of magnetic field on velocity distribution in x - y plane at $Re = 2830$ (Turbulent magnetic fluid flow).

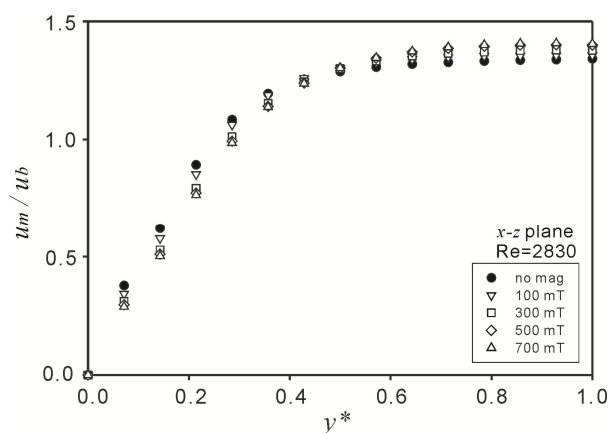


Figure 7: Influence of magnetic field on velocity distribution in x - z plane at $Re = 2830$ (Turbulent magnetic fluid flow).

flow). Fig. 6 indicates that although the change in the velocity distribution is smaller comparing with Fig. 4, same tendency could be observed. On the other hand, regarding the velocity distribution in the x - z plane, the mean velocity near the side wall decreases but the mean velocity near the center of the duct increases with applying magnetic field as shown in Fig. 7. Therefore, characteristic anisotropy of the velocity distribution evidently exists. It seems that this anisotropy of the velocity distribution is caused by the anisotropy of the shear stress related to the magnetic field direction.

5 CONCLUSION

Velocity distribution of the rectangular duct flow of a magnetic fluid was measured by using UVP method and the influence of the magnetic field on the velocity distribution was investigated. We performed the experiments in both laminar flow and turbulent flow of magnetic fluid.

In the case of laminar flow, when the magnetic field is applied to magnetic fluid flow, the mean velocity at the center of the duct decreases with increasing magnetic field intensity and velocity gradient slightly increases near the wall.

On the contrary, in the case of turbulent flow, when the magnetic field is applied to magnetic fluid, the mean velocity near the center of the duct slightly increases with increasing magnetic field intensity. This fact indicates that characteristic anisotropy exists in the velocity distribution related with the magnetic field direction. We confirmed this anisotropy experimentally by the measurement at the entrance region of the magnetic field.

ACKNOWLEDGEMENT

This study was partly supported by a Grant-in-Aid for Young Scientists (B) of the Japan Society for Promotion of Science.

REFERENCES

- [1] Takeda Y: Velocity profile measurement by ultrasound Doppler shift method, *Int. J. Heat and Fluid Flow*, 7 (1986), 313-318.
- [2] Rosensweig R. E: *Ferrohydrodynamics*, Cambridge University Press, New York (1985), Chap. 2.
- [3] Ohno K, Suzuki H and Sawada T: Analysis of liquid sloshing of a tuned magnetic fluid damper for single and co-axial cylindrical containers, *J. Magn. Mater.* 323 (2011), 1389-1393.
- [4] Kikura H, Takeda Y and Durst F: Velocity profile measurement of the Taylor vortex flow of a magnetic fluid using the ultrasonic Doppler method, *Exp. Fluids*, 26 (1999), 208-214.
- [5] Motozawa M, Hasegawa R and Sawada T: Influence of inner structure on oscillating pipe flow of a magnetic fluid, *Trans. JSME, B*, 73 (2009), 1013-1020 (Japanese).
- [6] Motozawa M, Chang J, Sawada T and Kawaguchi Y: Effect of magnetic field on heat transfer in rectangular duct flow of a magnetic fluid, *Phys. Procedia*, 9 (2010), 190-193.
- [7] Motozawa M, Iizuka Y and Sawada T: Experimental measurements of ultrasonic propagation velocity and attenuation in a magnetic fluid, *J. Phys.: Cond. Matter*, 20 (2008), 204117.

Heat and momentum transfer of a buoyant blob in low Prandtl number fluids

Kazuto Igaki, Ryuta Abe, Yuji Tasaka, Ichiro Kumagai and Yuichi Murai
 Graduate School of Engineering, Hokkaido University, N13-W8, Kita-ku, Sapporo, 060-8628, Japan
 e-mail: igaki@ring-me.eng.hokudai.ac.jp

The motivation of this study is obtaining characteristic features of heat and momentum transfer in low Pr fluids through a detailed measurement using UVP. As a preliminary study, two types of experiments were conducted with liquid gallium. One is with respect to “thermal”, instantaneous release of a thermal blob into the ambient fluid, and the other is an experiment of a starting plume. In the former experiments, we found that thermal buoyancy affects the convective behavior of the blob, even though the characteristic time for thermal diffusivity in liquid gallium is large. It was observed that the vortex structure in the buoyant blob remains or decays, depending on the direction of the working buoyant force. In another experiment, we succeeded in observing the motion of the thermal plume in liquid gallium. From simultaneous measurement of velocity and temperature field, we visualized some features of a laminar starting plume such as translational velocity and entrainment.

Keywords: Heat and momentum transfer, Low Prandtl number, Liquid metal, Thin container, Ultrasonic velocity profiling

1 INTRODUCTION

Thermal plumes are seen in wide range of field from natural convections to industries. The convective elements driven by thermal buoyancy are generally believed to make large scale convections such as Rayleigh-Benard convection [1]. Accordingly, investigations of their generation and rising motions have significant rolls in basic study of thermal convection. Their convective motions are often described by Rayleigh number (Ra) and Prandtl number (Pr). There are many experiments and studies with interests in thermal convection regarding fluids at higher Pr than unity [2-3]. On the other hand, the thermal convection in low Pr fluids such as liquid metals (where Pr approximately range from 0.01 to 0.1) has not been investigated enough compared to that of higher Pr fluids. However, the heat transfer in lower Pr fluids is believed to be very different from higher Pr fluids [4-5]. The reason why the experimental studies on low Pr fluids are so few is that their convective motions cannot be visualized optically. In recent years, the advancement of measurement techniques using ultrasonic waves makes it possible to obtain a spatio-temporal velocity field even for opaque fluids.

Our group is applying the Ultrasonic Velocity Profiling (UVP) on thermal convections in low Pr fluids. In the past, we conducted UVP measurement on thermal plumes in a circular cylinder. However, we could do little meaningful discussion since velocity measurement using the UVP is a line measurement. Then, we employed a thin container which can restrain the complexity of the three dimensional flow and exploit the capabilities of the UVP. In addition, Thermo-chromic Liquid Crystals (TLCs) was pasted on an inner wall of the container

to visualize the temperature field on the basis that the temperature difference is small in the depth direction. Therefore, this thin container has enabled us to obtain the velocity and temperature as a field simultaneously.

It may be guessed that buoyancy effects in low Pr fluids decays rapidly, considering its large thermal diffusivity. Beginning with this question, we conducted two types of experiments in the thin container as a preliminary study for a thermal plume. These experiments aim to investigate how buoyancy works on the heat and momentum transfer in low Pr fluids. First, we ran experiments of “thermal”, instantaneous release of a thermally buoyant blob. We injected small quantity of fluid with temperature difference among the ambient fluid layer. Then, we observed how the vortex structure in a buoyant blob decays, where buoyancy effects were expected to emerge. Second, we conducted a brief experiment of a cold plume. The fluid layer was cooled from above. In this trial, we succeeded in measuring the behavior of a starting plume in low Pr fluid.

2 APPARATUS AND METHOD

2.1 Working fluid

Liquid gallium whose melting point is 30°C was used as a working fluid because it is easier to treat in laboratory experiments than other liquid metals such as sodium or mercury. Its kinematic viscosity and thermal diffusivity are $3.2 \times 10^{-7} \text{m}^2/\text{s}$ and $1.2 \times 10^{-5} \text{m}^2/\text{s}$ respectively, so that Pr of liquid gallium equals 0.025. Sound speed in liquid gallium we applied for UVP measurement is around 2860 m/s. The sound speed has different values depending on working temperature, but this effect is enough small for our experiments to disregard it.

2.2 Experimental set-up and method

The experiments were conducted in a thin acrylic container illustrated in Figure 1 whose size is 150mm×270mm×15mm. The container was filled with liquid gallium up to 205mm in height. A nozzle with a film of latex membrane stretched tightly on the outlet is mounted on top part of the container. As soon as the membrane is broken by a needle, the liquid gallium which has temperature difference among the fluid layer is introduced into the container by gravity force. The height of fluid level in the nozzle (which is described by h) is 35mm. Cross-sectional dimensions of the nozzle are 20mm×8mm.

Three ultrasonic transducers (A, B and C) were installed on the container to measure velocity distributions as shown in Figure 1. Their basic frequency is 4MHz. Transducer A is for the measurement on the vertical axis to observe the advection of the injected liquid gallium blob, and the other transducers are for the horizontal axis to determine the vortex structure of the blob. Only two transducers A-B or A-C were used for simultaneous measurements to reduce interferences. The system used for signal processing was UVP, UVP monitor model Duo (Met-Flow S. A.). As ultrasonic reflection particles, fine powder of ZrB_2 was suspended in the liquid gallium. This tracer particle has $50\mu\text{m}$ in diameter and 6.17kg/m^3 in density.

To visualize the temperature field, TLCs whose range of color developing temperature is from 35°C to 40°C was painted on the surface of the inner plane. The color variation of TLCs which represents the temperature near the inside wall, was recorded by a high-speed video camera placed in front of the container. The white light created by metal halide lamp illuminated the wall.

The container is set in a temperature-controlled bath to regulate the ambient temperature. The experimental conditions regarding temperature are listed on Table 1. Here, T_0 means initial temperature of the fluid layer. In Exp. (a), experiments of "thermal", T_b represents initial temperature of a blob at the nozzle. The initial temperature difference between a blob and the ambient is defined as $\Delta T (=T_0-T_b)$. In the experiment of a starting plume (Exp. (b)), T_s means temperature of a cooling source. The nozzle with frozen water was mounted above the fluid layer, not for injection of fluids but as a cooling source.

Table 1: Experimental conditions regarding temperatures

	T_0 ($^\circ\text{C}$)	T_b ($^\circ\text{C}$)	$\Delta T (=T_0-T_b)$ ($^\circ\text{C}$)
Exp. (a1)	47	32	15
Exp. (a2)	32	47	-15
	T_0 ($^\circ\text{C}$)	T_s ($^\circ\text{C}$)	$\Delta T (=T_0-T_s)$ ($^\circ\text{C}$)
Exp. (b)	42	0.0	42

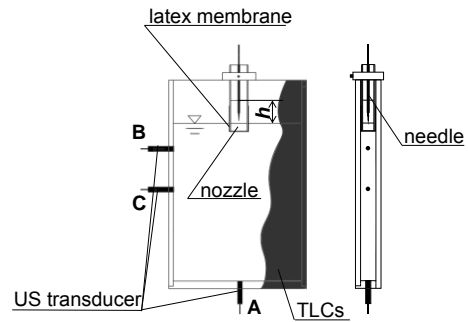


Figure 1: Schematic diagram of experimental container

3 RESULTS AND DISCUSSION

3.1 Exp. (a): Injection of a buoyant blob

Figure 2 shows the temperature field just after an injection in Exp. (a1). The gray scale color represents *Hue* information extracted from raw images with RGB brightness components. *Hue* refers to a pure color divided from other elements of color, so that it is advantage in analyzing color. More detail information of treatment with color is introduced in Dabiri, *et al.* (1991) [6]. Here, temperature rises as *Hue* approaches to 240 degrees. As shown in the figure, just after the injection was started, a thermally buoyant blob rolled up the shear layer and, in result, formed a pair of vortex structures. From the figure, it was confirmed that the buoyant blob had gained an initial circulation and buoyancy.

Spatio-temporal velocity field on measurement line A was obtained as shown in Figure 3(a). To compare the translational behavior among the two temperature conditions: $\Delta T=15$ ($T_0>T_b$) and $\Delta T=-15$ ($T_0<T_b$), we picked up the peak velocity locations and they were plotted in Figure 3(b). As shown in Figure 3(b), there are no remarkable differences found among the two conditions in terms of vertical velocity distribution.

On the horizontal axis, however, spatio-temporal velocity distributions of the two temperature conditions have notable disparity. Figure 4 and Figure 5 show velocity distributions on horizontal axis; Figure 4 was obtained in Exp. (a1) and Figure 5 was in Exp. (a2). In the each figure, (a) is velocity distribution on measurement line B and (b) is that on measurement line C. In Figure 4, clear velocity patterns of vortex structure could be observed. Here, vortex structure was confirmed from the characteristics of the velocity field. The feature of the velocity field is that the relation of the opposite signed peak of temporal velocity distribution reverses as time passed. In Figure 4 (a) and (b), those clear velocity patterns of vortex in both measurement line (B and C) indicate that a buoyant blob remain and expand its vortex structure. This insight is illustrated in Figure 4 (a') and (b'). On the other hand, velocity distribution with opposite temperature condition ($T_0<T_b$) had similar but quite

different patterns as shown in Figure 5. In terms of measurement line C, the velocity pattern was similar to Figure 4 but latter half does not have clear peak velocity locations. The moderately sloped velocity distribution in latter half of a blob shows us that the blob has stretched structure as shown in Figure 5(b'). Those differences are due to following reasons. In these experiments, whether a blob remains vortex structure or not is attributed to the relation between the direction of buoyancy and advection. In experiment (a1), the thermally buoyant force worked downward which was the same direction to its translational direction. Contrary to that case, the buoyancy worked upward in the opposite temperature relation, in experiment (a2). Thus, buoyancy caused stretching or decaying the vortex structure. It is considered that when the direction of buoyancy corresponds to the local flow direction, the effects of buoyancy force easily emerge. Consequently, the stretching of the structure is observed in the latter half of the blob.

It was maintained, so far, that buoyancy worked on the behavior of the blob. To validate the buoyancy effects, we estimated the order of time scale for thermal diffusion using the thermal diffusivity. Here, the time scale τ_d is defined as $\tau_d=L^2/\kappa$, where L is representative length, derived from the cubic root of the volume for the injected blob. The value of L is 18mm. Therefore, τ_d equals 27s. Considering the time scale of these experiments, about 2s or 3s, the value of τ_d indicates thermal buoyancy sufficiently has potential to influence on the behavior of the blob.

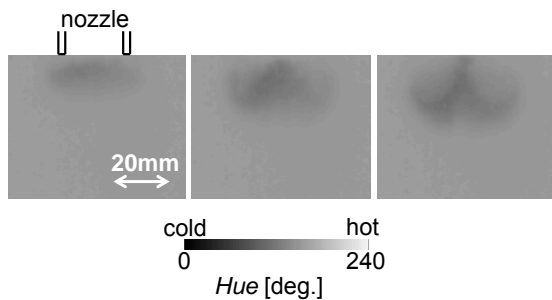


Figure 2: Formation of a pair-vortex structure

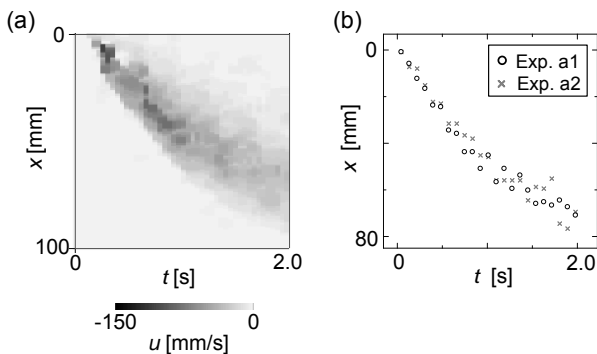


Figure 3: (a) Velocity distribution on vertical axis and (b) temporal locations of peak velocity

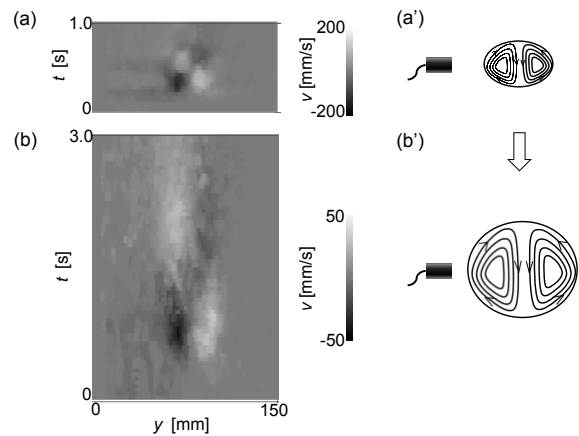


Figure 4: Velocity distributions obtained in Exp. (a1) and schematic images of the structure in the blob: (a-a') on measurement line B, (b-b') on measurement line C

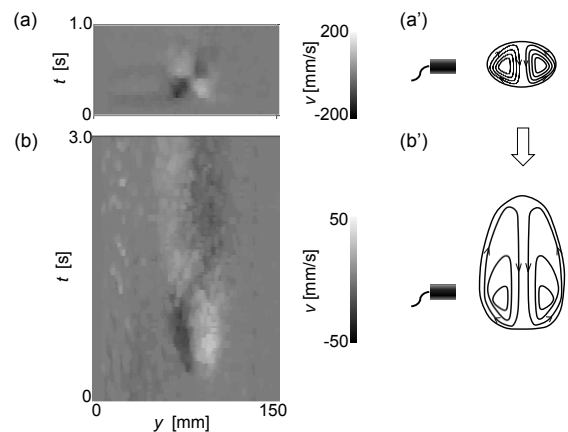


Figure 5: Velocity distributions obtained in Exp. (a2) and schematic images of the structure in the blob: (a-a') on measurement line B, (b-b') on measurement line C

3.1 Exp. (b): Starting plume cooled from above

The experiment of the cold plume was conducted in the same container as described previously. Figure 6(a) shows the temperature field represented by *Hue* information. In the figure, the behavior of a cold plume was observed in temperature field. Then, we detected the head of a plume and calculated its translational velocity from the images. At first, the time line image in Figure 6(b) was prepared. In Figure 6(b), the gradient of the time development image of *Hue* information means the velocity of heat transfer. The gradient was calculated in the time range from $t=10s$ to $t=30s$ and the value was 4.3 mm/s. This velocity is defined as u_h . On the other hand, Figure 7 shows a spatio-temporal velocity distribution on the measurement line A which is for vertical axis. The gradient of peak velocity locations is seen in the figure, which indicates the motion of plume head. Thus, the gradient means the velocity of momentum transfer. We estimated the velocity u_m , which was about 4.0 mm/s. Here, the u_m was smaller than u_h . It can be said that the speed of heat transfer is faster than that of momentum transfer.

Then, we performed order estimation of the velocity scale of thermal diffusion. Here, the velocity scale U_d is defined as $U_d=L/\kappa$. The value of L is 20mm, width of the cooling source. Consequently, U_d computed in 0.6mm/s. Given U_d can be calculated from $\Delta u (=u_h-u_m)$, the $U_d (=0.6\text{mm/s})$ and $\Delta u (=0.3\text{mm/s})$ have reasonable agreement. It should be considered that the starting plume descended with an angle due to experimental difficulties. Additionally, the u_h reflected only the large valued Hue information, so that the small variation of Hue was disregarded.

Figure 8(a) shows a velocity distribution on measurement line C which is for horizontal axis. The flow structure indicating entrainment at plume head was seen in the figure, though the latter half part of the plume head was not so distinct. In the figure, around $t=10\text{s}$, negative velocity was seen in wide range for space, compared to positive velocity. This is because the plume head entered in the measurement line not orthogonally but with an angle. In addition, the latter half or stem of the plume slid forward on y axis, horizontal axis. A schematic image in Figure 8(b) is a possible example of these interpretations of the velocity distribution. Also in temperature field, these features of the starting plume behavior, such as descending obliquely and shifting toward y direction, were observed as shown in Figure 6(a).

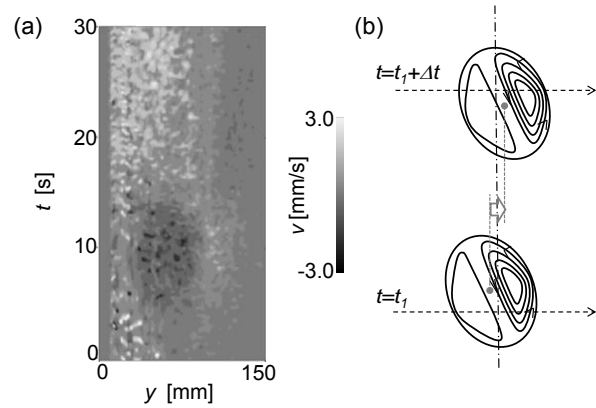


Figure 8: (a) Velocity distribution of a starting plume on measurement line C (for horizontal axis) and (b) a schematic image of swaying forward on y axis

4 CONCLUSION AND REMARKS

Two types of experiments were conducted in order to investigate whether buoyancy works or not and how buoyancy affects the convective motions in low Pr fluids. From measurements of spatio-temporal velocity field and temperature field by means of UVP and TLCs, following insights were obtained.

In Exp. (a), buoyancy effects on decaying the vortex structure was confirmed. When the direction of buoyant force was opposite to that of the advection of the blob its vortex structure decayed rapidly. Furthermore, the buoyancy effects emerged not in the translational behavior but in the extension of the vortex structure.

In Exp. (b), though it is necessary to take account of several experimental matters, we have succeeded in measurement of the features of the starting plume, such as translation and entrainment. From the perspective of flow visualization for thermal plumes in low Pr fluids, these experimental results are meaningful examples in the study of the thermal convection. Accordingly, detailed experimental study of thermal plumes in low Pr fluids is our next step.

REFERENCES

- [1] J. Zhang, *et al.*: Non-Boussinesq effect: Thermal convection with broken symmetry, *Phys. Fluids*, 9 (1997), 1034-1042.
- [2] G. Zocchi, *et al.*: Coherent structures in turbulent convection, and experimental study, *Physica A*, 166 (1990), 387-407.
- [3] T. S. Pottebaum, *et al.*: The pinch-off process in a starting buoyant plume, *Exp. Fluids*, 37 (2004), 87-94.
- [4] R. Verzicco, *et al.*: Prandtl number effects in convective turbulence, *J. Fluid Mech.*, 383 (1999), 55-73.
- [5] C. A. H. Majumder, *et al.*: Four dynamical regimes for a starting plume model, *Phys. Fluids*, 16 (2004), 1516-1531.
- [6] D. Dabiri, *et al.*: Digital particle image thermometry: The method and implementation, *Exp. Fluids*, 11 (1991), 77-86.

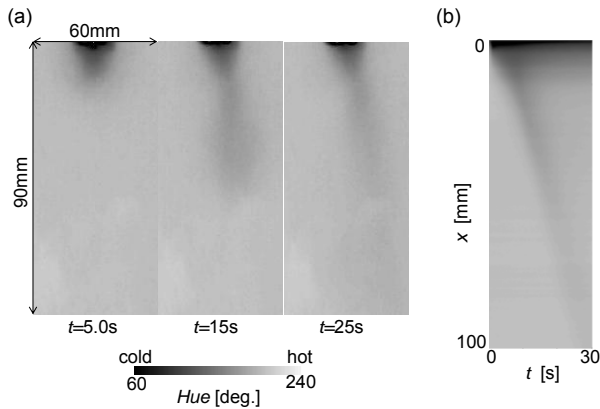


Figure 6: Plume motions observed in Hue information

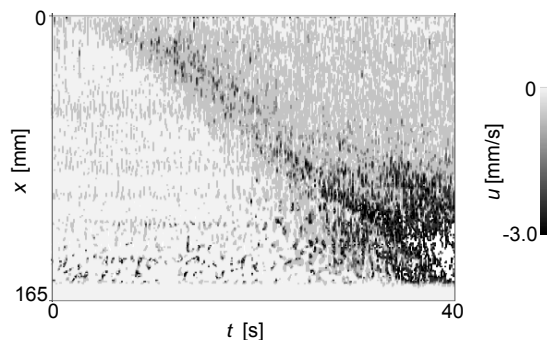


Figure 7: Velocity distribution of a starting plume on measurement line A (for vertical axis)

Applicability of Ultrasonic Pulsed Doppler for Fast Flow-Metering

Stéphane Fischer⁽¹⁾, Claude Rebattet⁽²⁾, Thibault Lalande⁽²⁾, Damien Dufour⁽¹⁾,
Nicolas Bachellier⁽¹⁾

(1) Ubertone SAS, Strasbourg, France, www.ubertone.com

(2) CREMHyG Lab, INP, Grenoble, France

Measurement of fluctuating flows in hydraulic machines is an ongoing challenge for which classical flow meter technologies (Differential pressure, Magnetic, Turbine and Propeller) are not well adapted. The ultrasonic pulsed Doppler technique allows to measure instantaneous velocity profiles in a very short time. This paper presents the performances of the ultrasonic velocity profiler UB-Lab to achieve faster velocity flow measurement through hydraulic pipes. The system has been optimized (transducer frequency, beam angle, parameters of sequencing) in order to reduce effect of wall echoes, to keep a good velocity range and to minimize the effect of secondary currents. The paper presents the measurement system with UB-lab's software module dedicated to fast flow-metering, the velocity profile measurement in a mixing tank, the bench demonstrator, the results and the perspectives of development of such solutions.

Keywords: hydraulic machines, fast measurement, velocity, flow modulation.

1 INTRODUCTION

Measurement of fluctuating flows in hydraulic machines is an ongoing challenge because of the need to study, quantify, and improve their performances and reliabilities. Indeed, unsteady flows have an impact on the machine working. Moreover, these effects often appear with a high frequency with possible circuit coupling effects. Therefore, to study them correctly, a high frequency flow measurement system is necessary.

Classical flow meter technologies (Differential pressure, Magnetic, Turbine and Propeller) are not well adapted for such kind of measurements. The ultrasonic pulsed Doppler technique allows to measure velocity profile in a more acceptable time range. It has been particularly used to observe coherent structures at high frequency in costal [1] and river flows [2]. This technique has also shown excellent performances to measure flow rate, especially on transient flows [3].

The ultrasonic profiler UB-Lab, developed by Ubertone, measures velocity profiles at high resolution in laboratory and industrial flows. This application-oriented instrument has a flexible architecture, it is compact and adapted to industrial conditions. In order to allow fast measurement of velocity profiles we have rewrite the core of the driver of UB-Lab. This has been done by using multi-threading and TCP-IP transfer optimization.

This paper presents the collaborative development of Ubertone SAS and Cremhyg Lab of Grenoble University, to develop and improve the performances of the ultrasonic velocity profiler data acquisition system to achieve faster velocity flow measurement through hydraulic pipes and turbomachineries.

2 INSTRUMENT SETUP

2.1 Specification

This technology will be tested on bench, at Cremhyg Lab, which enables to create high frequency flow modulation through several hydraulic components. Thanks to an oscillating piston, this bench can produce discharge and pressure fluctuations with a frequency range from 5 and 50Hz. The velocity oscillations are presently measured in a straight DN40 pipe with indirect 3-pressure method. The main velocity is about 2 m/s. Results may be available at the end of a PhD program and may be analyzed and published within next year.

As an example of typical modulation, the figure 1 shows the modulation of pressure signals measured by 3-pressure piezoelectric sensor (A1, A2, A3) located on pipe closed to exciter piston.

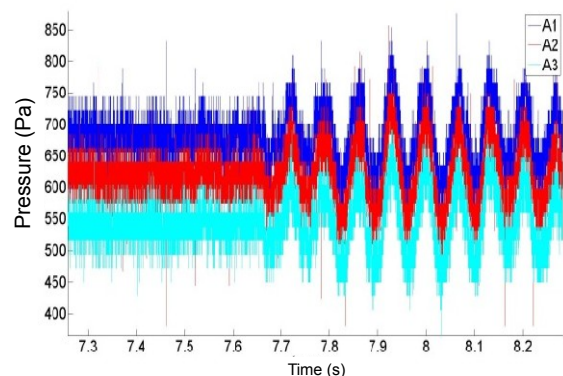


Figure 1 : modulation of pressure signals near the piston.

Fluctuations of discharge flow are represented on figure 2, the different curves demonstrate the influence of location of the section of measurement on pipe and distance to piston.

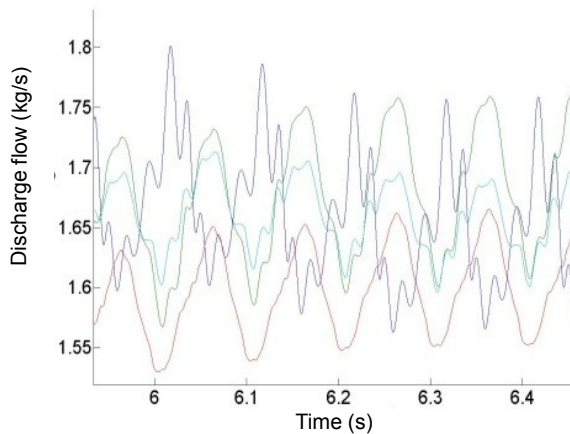


Figure 2 : Fluctuations of discharge flow at different locations.

The final objective is to measure the amplitude modulation of flow along any section on the main axis of pipe. The ultrasonic flow must be sufficiently fast to capture information of propagative flow waves. The measurement accuracy is a secondary endpoint and will be evaluated on this experimental test bench with reference to other flow measurement methods.

2.2 Technological constraints

The use of pulsed ultrasounds allows to observe a velocity profile along an acoustic beam sliced in many measurement cells. With the coherent pulse Doppler method used in the UB-Lab, the estimation of the velocity [4] is obtained with a low variance. This estimation is done, after sending N_{pp} ultrasonic pulses at a specific PRF (pulse repetition frequency), by computing the autocorrelation of the signal. Thus, the measurement frequency of the velocities is given by :

$$f_s = \frac{N_{pp}}{PRF} \quad (1)$$

This gives two parameters that can be changed to set this sampling frequency f_s . On the other side, the variance of the estimation is proportional to the signal to noise ratio [5] and inversely proportional to N_{pp} .

The coherent pulse Doppler method induce a velocity range limitation [6] expressed by :

$$\left[0 .. \frac{c^2 \tan \beta}{4 f_0 d} \right] \quad (2)$$

For the given pipe diameter d and a sound velocity c , this range limitation will influence the set of the parameters : the PRF, the beam angle β and the emitting frequency f_0 .

2.3 Geometry sizing

Only one transducer is used in order to get the maximum sampling rate on velocity measurement by avoiding channel switch time. In order to reduce effects of parasite echoes, the spatial range will integrate two wall reflections (see figure 3). We also set the beam angle (β) to 60° in order to minimize the influence of radial velocity component (average and fluctuating) but still keeping a comfortable velocity-depth range. This sets the spatial range to 115 mm along the acoustic beam.

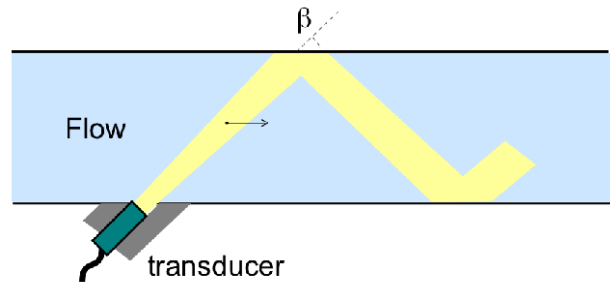


Figure 3: Transducer insertion in the pipe. The spatial range will integrate two wall reflections.

2.3 Transducer Sizing

The velocity range is set to $[0..3\text{m/s}]$ in order to take account of the turbulence of the flow. The velocity-depth constraint imposes a maximum frequency of 3.2 MHz (obtained from the equation 2).

We choose a transducer centered on 3 MHz with a 6 dB bandwidth ranging from 2 to 4 MHz. This will allow, for maximum flexibility, to improve sensitivity (with higher frequencies) or to increase the velocity-depth range (with lower frequencies).

2.4 Ultrasonic pulses sequencing

The minimum spatial range for the ultrasonic velocity profile is 115 mm. This corresponds to a maximum PRF of 6435 Hz and to a range of theoretical instantaneous velocity of $[0 .. 3.15 \text{ m/s}]$.

3 HARDWARE IMPROVEMENTS

3.1 Data transmission

On the first version of the UB-Lab, the maximum frequency acquisition of velocity profile was about 1Hz. To reduce the response time, we choose a multi-thread approach allowing the management of different tasks and the optimization of computing resources. These improvements allow the device to measure and transfer a velocity profile each 5ms (200Hz, limited to 30 cells) or each 10ms at full capacity (100Hz, 62 cells). Moreover, to reduce the size of data flow, the new TCP-IP protocol does not transfer raw Doppler signal; conversely, it only transfers velocity profiles, variances and correlations.

3.2 Operating modes

There are two operating modes implemented in the driver :

⤴ The “continuous mode” is able to measure and transfer up to 200 profiles per second. It is designed to study high frequency flows and to observe evolutions of the flow in real time. Moreover it is possible to record and post-process the data for further study.

⤴ The “bloc mode” measures several profiles like the continuous mode but will only transfer the average profile of these data. Duration and period of these measurements are specified by the user. Mostly designed for long-term studies, the device can be installed for several days or weeks.

These operating modes allow acquiring a large range of velocity profiles in different conditions.

3.3 Communication protocol

To improve data exchange and automated measurement routines with homemade or licensed software like Matlab or Labview, a TCP-IP communication protocol with the driver was created. Once the client software is connected to the device, the user can load a configuration and start measurement with one of the two operating modes described above (continuous or bloc).

When the continuous mode is started, the driver sends the desired number of instantaneous profiles in a data-stream. An “end flag” is send to close the data-stream.

In the bloc mode, the driver computes the average on the number of asked profiles. During the processing of the bloc mode, the user can ask for an instantaneous profile or a moving average. If this profile is available, it is sent to the user; otherwise an empty profile is sent. The device does not send the same profile twice.

Routines can be stopped at any time by a “stop command”.

4 FIRST TECHNICAL RESULTS

Experiments were carried out in a mixing tank that contains about 20 liters of water and few grams of corn farina. The tank has a diameter of 36 cm. A vortex is created inside the tank by a mixer rotating with an adjustable speed. The transducer connected to the UB-Lab device is set to measure the velocities along the diameter of the mixing tank.

The velocity profiles are measured continuously during several minutes. We used a frequency f_0 of 4.17 MHz, a PRF of 3 kHz and 128 samples (N_{pp}) are used for each profile. This lead to a velocity sampling frequency f_s of 23.4 Hz (23 velocity profiles

measured per second). Cells size and intervals are set to 4 mm.

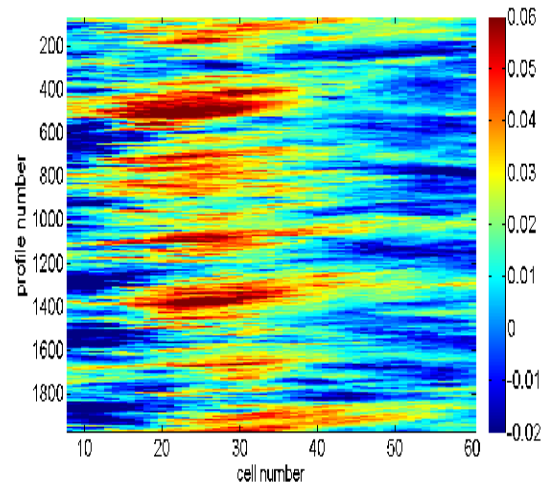


Figure 4: spatio-temporal view of the velocities in the vortex of the mixing tank (23.4 Hz sampling frequency) .

Figure 4 shows the velocity values according to the cell number (X axis, referring to the depth) and the profile number (Y axis, referring to time). The blues zones correspond to negative velocities and the red ones to positive velocities. The evolution of velocities across time and depth shows the turbulence due to the mixer.

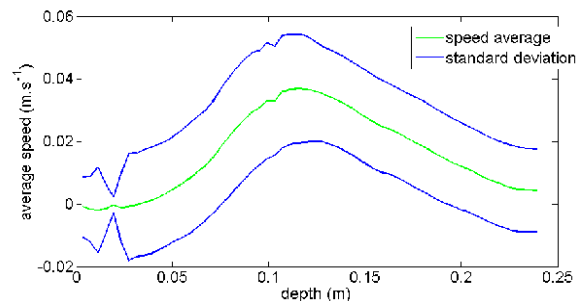


Figure 5: Mean velocity profile through the vortex.

The temporal average of the velocities (Figure 5) shows a smooth variation of the mean velocity along the depth as the transducer axis did not cross the center of the vortex. This graph shows that the standard deviation is constant except for one point at a depth of 0.019. This breakdown of the standard deviation is due to a parasite echo that leads to a low SNR (signal-to-noise ratio).

Figure 6 compares the evolution of velocities during time in cells located at 0.092 m, 0.119 m and 0.139 m of the transducer. Depending on the position of the vortex relatively to the cells, the velocities in these cells follow sometimes the same variations.

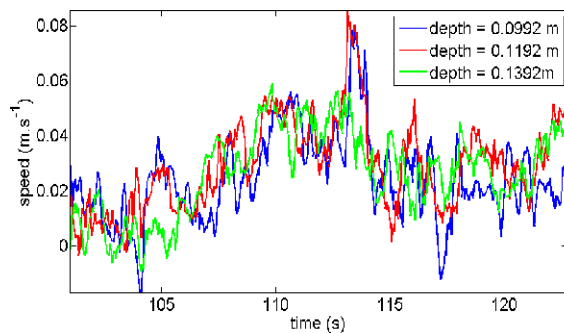


Figure 6: evolution of the velocity in three different cells.

The spectral analysis of the velocities shows the distribution of the turbulent energy (figure 7). Two cells in the same area (homogeneous turbulence is assumed) but with different SNR are compared.

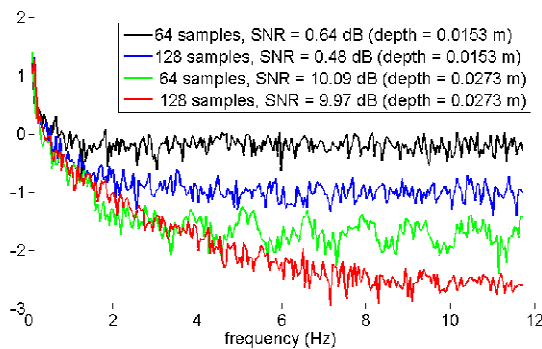


Figure 7: power spectrum of velocities (in dB).

The turbulent energy is present at low frequencies and decrease progressively. The variance of the velocity estimation appears as white noise. The level of this noise depends on the signal-to-noise ratio and on the number of samples used for one velocity estimation.

These results shows that while increasing the sampling frequency from 23.4 to 46.9 Hz (with $N_{pp}=64$), the noise level grows of about 1.2dB. On the other side, the SNR decreases the noise level, allowing to see the turbulent energy on a wider frequency range.

5 BENCH DEMONSTRATOR

The aim of the test bench is to permit measurement with monitored flow oscillation at different amplitude and frequency ranges. This bench has been designed initially to study the impact of flow fluctuation on several hydraulic components such as cavitating pumps and cavitating radial chamber systems, both with impedance influence coupled with pipe arrangement circuit. The possibility to equip the pipes with different instrumentations and to modulate the flow through variable hydraulic components offer a possibility to characterize the speed, the accuracy and the flexibility of US high

speed methods.

6 CONCLUSION AND PERSPECTIVES

The presented system of high speed flow measurement has been developed for further hydraulic applications on hydraulic circuit and turbomachineries. Because of high speed oscillation due to acoustic propagation in water channel, it is necessary to improve both the methodology and the instrument technology to access the flow modulation. Coupled with pressure measurement, it is possible to quantify the unsteady flow in pipes of circuit and access to the transfer function of hydraulic components. During this year, the Cremhyg test bench had been developed to generate such calibrated oscillation with an exciter piston. In the same time, Ubertone had developed new functionality and improved the acquisition system to measure fluctuation of discharge flow. The combination of R&D and availability of operational test circuit may permit to achieve test validation during next year to demonstrate the capability of Ubertone's profiler in fast flow metering.

ACKNOWLEDGEMENT

Ubertone is supported by the French Ministry of Research through the "Concours National d'Aide à la Création d'Entreprises de Technologies Innovantes".

REFERENCES

- [1] Hurther D., Thorne P.D.: Suspension and near bed load sediment transport processes above a migrating, sand rippled bed under shoaling waves, journal of geophysical research 116 (2011)
- [2] Bagherimiyab F.: Coherent structure and particle turbulence interaction in suspended sediment-laden laboratory open-channel flows, 34th IAHR World Congress (2011) 3354-3361
- [3] Mori M., Tezuka K., Tezuka H., Furuichi N., Kikura H., and Takeda Y.: Industrial application experiences of new type flowmetering system based on ultrasonic doppler flow profile measurement, 3th International Symposium on Ultrasonic Doppler Methods for Fluid Mechanics and Fluid Engineering (2002)
- [4] Miller, K.S., Rochwarger, M.M.: A covariance approach to spectral moment estimation, IEEE Transactions on Information Theory, 18 (1972) 588-596.
- [5] Abeysekera S.: Performance of pulse-pair method of Doppler estimation. Aerospace and Electronic Systems, IEEE Transactions, 34 (1998) 520-531.
- [6] Takeda Y.: Velocity profile measurement by ultrasonic Doppler method, Experimental Thermal and Fluid Science 10 (1995) 444-453.

Contactless Inductive Flow Tomography: A Liquid Metal Flow Measuring Technique Complementary to UDV

Frank Stefani, Gunter Gerbeth, Thomas Gundrum, and Thomas Wondrak
Helmholtz-Zentrum Dresden-Rossendorf, P.O. Box 510119, D-01314 Dresden, Germany

The aim of the Contactless Inductive Flow Tomography (CIFT) is the reconstruction of flow structures in metal and semiconductor melts. It relies on the induction of electric currents in moving conductors exposed to magnetic fields. The flow induced deformations of various applied magnetic fields can be measured in the exterior of the melt and utilized for the reconstruction of the velocity field. After a presentation of the principles of CIFT, first applications and possible extensions of the method are discussed and put into the context with traditional measuring techniques such as UDV.

Keywords: Contactless inductive flow tomography, Steel casting, Crystal growth

1 INTRODUCTION

Ultrasound Doppler Velocimetry (UDV) is nowadays the most appropriate measuring technique when it comes to flow field determinations in opaque fluids for which optical methods like Particle Image Velocimetry (PIV) or Laser Doppler Velocimetry (LDV) are not applicable. Since the pioneering work of Takeda [1], UDV has been established as a standard technique for flow field determinations in liquid metals, in particular. Great effort is presently being spent on extending the range of UDV to higher-dimensional flow mappings [2], and to high temperature applications by the use of waveguides between the transducer and the liquid [3].

Yet, there are some particular measuring tasks for which the application of UDV is hard to imagine. One example is the casting of steel which works at temperatures around 1500°C. Another one is the growth of silicon mono-crystals in the Czochralski process in which the use of UDV is not only prevented by the high temperatures (around 1400°C) but also by the demand that the silicon melt must be clean and free of any tracer particles. Hence, for those technologies there is an urgent need for alternative flow measuring techniques. Fortunately, most of the hot fluids to be monitored are liquid metals or liquid semiconductors, both characterized by a relatively high electrical conductivity in the order of 10⁶ S/m. The movement of such good electrical conductors under the influence of externally applied magnetic field is known to induce electrical currents which are, in turn, the source of induced magnetic fields. When measuring these flow induced magnetic fields in the exterior of the melt, one can try to extract information about the velocity field. This is the basic idea of the Contactless Inductive Flow Tomography (CIFT), to be discussed in this paper.

2 BASIC THEORY

When an electrically conducting medium, moving with the velocity \mathbf{u} , comes under the influence of a

magnetic field \mathbf{B} , an electromotive force (emf) $\mathbf{u} \times \mathbf{B}$ is induced that drives an electric current with density

$$\mathbf{j} = \sigma(\mathbf{E} + \mathbf{u} \times \mathbf{B}), \quad (1)$$

where σ is the electrical conductivity of the melt and \mathbf{E} is the electric field. In the stationary case, we can express \mathbf{E} in terms of the gradient of the electric potential, $\mathbf{E} = -\text{grad } \phi$. Then, Biot-Savart's law gives the following expression for the induced magnetic field \mathbf{b} :

$$\mathbf{b}(\mathbf{r}) = \frac{\sigma\mu_0}{4\pi} \int_D \frac{(\mathbf{u}(\mathbf{r}') \times \mathbf{B}(\mathbf{r}')) \times (\mathbf{r} - \mathbf{r}')}{|\mathbf{r} - \mathbf{r}'|^3} dV' - \frac{\sigma\mu_0}{4\pi} \iint_S \phi(\mathbf{s}') d\mathbf{S}' \times \frac{\mathbf{r} - \mathbf{s}'}{|\mathbf{r} - \mathbf{s}'|^3}. \quad (2)$$

Note that the surface integral term on the left hand side of Eq. (2) results from converting an equivalent volume integral with $\text{grad } \phi$ in the integrand. Note further that this term must not be neglected (as was done, e.g., in earlier attempts for a magnetic flow tomography [4]), since it can attain the same order of magnitude as the first term, possibly cancelling it completely for special flow and magnetic field configurations. By applying the divergence operator to Eq. (1) we obtain the Poisson equation for the electric potential, $\Delta\phi = \text{div}(\mathbf{u} \times \mathbf{B})$, whose solution can be shown to fulfill the boundary integral equation

$$\phi(\mathbf{s}) = \frac{1}{2\pi} \int_D \frac{(\mathbf{u}(\mathbf{r}') \times \mathbf{B}(\mathbf{r}')) \cdot (\mathbf{s} - \mathbf{r}')}{|\mathbf{s} - \mathbf{r}'|^3} dV' - \frac{1}{2\pi} \iint_S \phi(\mathbf{s}') d\mathbf{S}' \cdot \frac{\mathbf{s} - \mathbf{s}'}{|\mathbf{s} - \mathbf{s}'|^3}. \quad (3)$$

The two integral equations (2) and (3) are valid for rather general induction processes, and can also be employed to solve dynamo problems in which a magnetic field self-excites under the influence of a velocity field, without applying any external magnetic field. For many industrial problems, however, the ratio of the induced field \mathbf{b} to an externally applied field \mathbf{B}_0 is typically smaller than one, so that the total

field $\mathbf{B}=\mathbf{B}_0+\mathbf{b}$ under the integrals in Eqs. (2) and (3) can be replaced by the applied magnetic field \mathbf{B}_0 alone. It is this replacement that makes the inverse problem of reconstructing the velocity field from the induced electro-magnetic fields a linear one, which is much easier solvable than the full-fledged non-linear problem with $\mathbf{B}_0+\mathbf{b}$ under the integrals.

In a very first attempt [5,6] we had shown that, with a vertical field $\mathbf{B}_{0,z}$ being applied, the velocity structure of the flow can be roughly reconstructed from the external measurement of the induced magnetic field in the exterior and of the induced electric potential at the boundary of the fluid. There remains, however, a non-uniqueness concerning the exact radial distribution of the flow, a fact that can be made plausible by representing the fluid velocity by two defining scalars (for the poloidal and the toroidal velocity component), living both in the whole fluid volume. Then it is clear that two quantities measured only on a two-dimensional covering of the fluid cannot give enough information for the reconstruction of the two desired 3D-quantities.

Later, then, we had developed a completely contactless method, CIFT, to avoid the electric potential measurement at the fluid boundary [7]. The main idea was to apply the external magnetic field in two different, e.g. orthogonal, directions and to utilize both corresponding sets of induced magnetic fields for the velocity field reconstruction.

3 A FIRST DEMONSTRATION EXPERIMENT

The goal of a first demonstration experiment [8] for CIFT was the reconstruction of a propeller-driven three-dimensional flow of the eutectic alloy GaInSn in a compact cylindrical vessel with a ratio of height to diameter close to one (Fig. 1). In order to determine both the poloidal (in r and z) and the toroidal (in φ) flow component, we applied subsequently a vertical ($\mathbf{B}_{0,z}$) and a horizontal ($\mathbf{B}_{0,x}$) magnetic field, either produced by Helmholtz-like coil pairs. In this experiment, the switching between the two fields occurs every 3 seconds, so that after 6 seconds all the magnetic field information is available for the velocity reconstruction. Note that, in principle, this rather poor time resolution can be significantly enhanced, with a physical limitation given by the magnetic decay time $\mu_0\sigma R^2$, which is in the order of 0.05 s for the demonstration experiment.

For each of the two applied fields, $\mathbf{B}_{0,z}$ and $\mathbf{B}_{0,x}$, the induced fields are measured by Hall sensors at 48 positions, which are rather homogeneously distributed all around the surface of the cylindrical vessel. The rather small ratio of around $10^{-3}\dots 10^{-2}$, between the induced and the applied fields, demands for a very stable current source of the Helmholtz-like coils, for a very stable relative position of Hall sensors and coils, and for significant effort to compensate drift and sensitivity changes of

the Hall sensors (e.g., due to varying temperature).

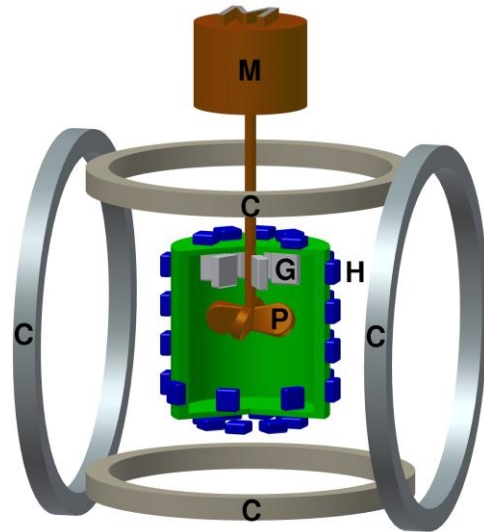


Figure 1: Schematic sketch of the demonstration experiment for the validation of CIFT at a propeller-driven 3D flow of GaInSn. M - Motor, C - Coils, P - Propeller, G - Guiding blades, H - Hall sensors.

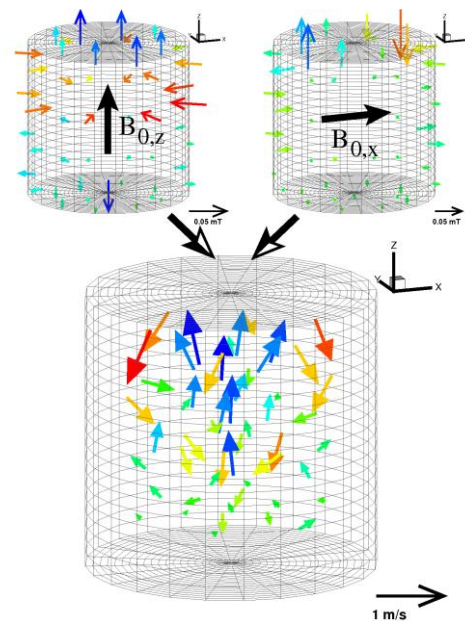


Figure 2: Velocity field for upward pumping (below), as reconstructed by the externally measured induced magnetic fields for applied $\mathbf{B}_{0,z}$ and $\mathbf{B}_{0,x}$ (above). The color scale of the induced fields indicates the normal component relative to the nearest surface point, the color scale of the velocity vectors indicates the z -component.

For the reconstruction of the velocity field we solve the Gauss normal equations that minimize the mean quadratic deviation of the measured from the modeled induced magnetic fields. The intrinsic non-uniqueness problem concerning the detailed depth-dependence of the velocity is overcome by utilizing the so-called Tikhonov regularization by minimizing,

in parallel to the magnetic field deviations, also the kinetic energy of the flow or other appropriate quadratic functionals of the velocity. This numerical scheme can easily be extended to incorporate further a-priori information, e.g. the divergence-free condition of the velocity field, or velocity components and mass flow rates known from other measuring techniques.

In this experiment it was possible to distinguish clearly between upward and downward pumping of the propeller, with the rotational component being reduced by guiding blades in the case of upward pumping. For the latter case, Fig. 2 shows the induced fields for applied $\mathbf{B}_{0,z}$ und $\mathbf{B}_{0,x}$, respectively, and the velocity field as reconstructed from this information. The comparison with UDV measurements has shown a good coincidence of the resulting velocity fields (see [8]).

3 APPLICATION TO CONTINUOUS CASTING PROBLEMS

In the continuous casting of steel, the liquid metal flows from a tundish through a Submerged Entry Nozzle (SEN), with typically two ports at the lower end, into the mould where it starts to solidify at the water-cooled copper walls. The quality of the produced steel depends critically on the detailed flow structure in the mould. What is desirable here is a so-called double-roll structure, with the two jets that emanate from the SEN ports first reaching the narrow-faces of the mould and then splitting into upward and downward directed branches. In contrast to that, the so-called single-roll structure, with the jets being sharply bent upward after leaving the SEN ports, is considered dangerous since it could lead to entrainment of casting powder into the steel.

Any sort of online-monitoring of the detailed roll-structure in the mould would allow for an active control of the casting process, with the prospect to increase the possible casting speed significantly. As a contactless method, CIFT suggests itself for such monitoring, although the problem of the copper-mould oscillations makes its implementation in the industry still a formidable task. As a first step in this direction, we have installed a simplified CIFT system at our small continuous casting model Mini-LIMMCAST, working also with the GaInSn alloy [9]. The simplification concerns the restriction of the CIFT system to only one magnetic field coil which produced a mainly vertical magnetic field. This configuration is sufficient for the determination of the velocity component parallel to the wide faces of the mould [10], which is the dominant one for the slab-casting as modeled in Mini-LIMMCAST. The induced fields are now measured by Fluxgate sensors positioned at the narrow faces of the mould, typically at 7-9 positions on either side.

In addition to CIFT, we have utilized a Mutual

Inductance Tomography (MIT) system for determining the conductivity distribution in the SEN, which allows visualizing the details of the two-phase GaInSn/Argon flow. The simultaneous utilization of CIFT and MIT leads to a detailed understanding of the two-phase flow in the SEN and of the resulting flow in the mould [11]. Figure 4 illustrates various flow structures that had been detected during one run of the experiment, including double-roll and single roll structures occurring on different sides of the mould.

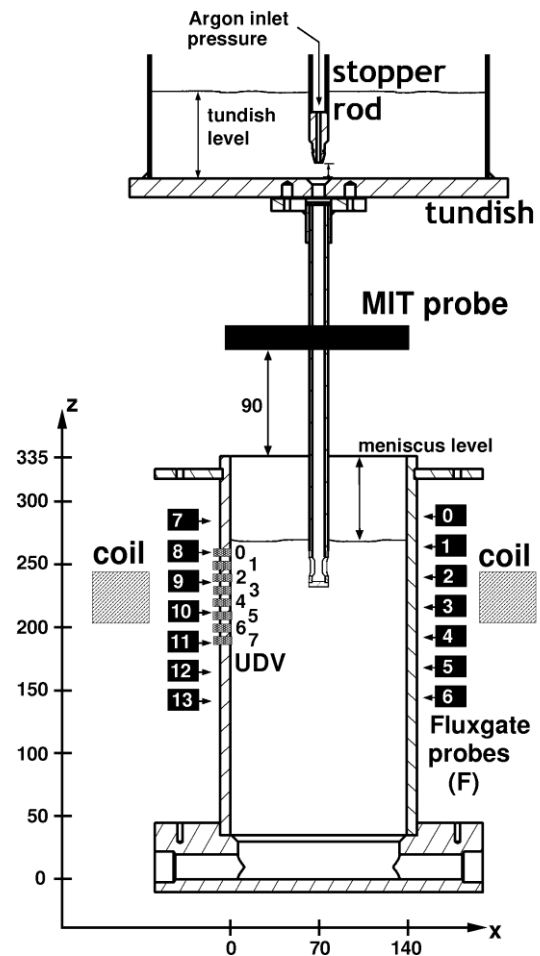


Figure 3: Schematic sketch of the Mini-LIMMCAST facility and the employed CIFT, UDV and MIT technique. The use of one coil is sufficient for the reconstruction of the basically 2-dimensional flow field in the mould. Lengths are in mm.

It might be interesting to see, in particular for the audience of the ISUD workshop, how CIFT compares with traditional UDV measurements. For this purpose, we show in Fig. 5 the x-component of the velocity as determined both by CIFT and UDV at a height of $z=210$ mm over the course of one run. Despite some slight quantitative differences, the general agreement between the two results is quite convincing.

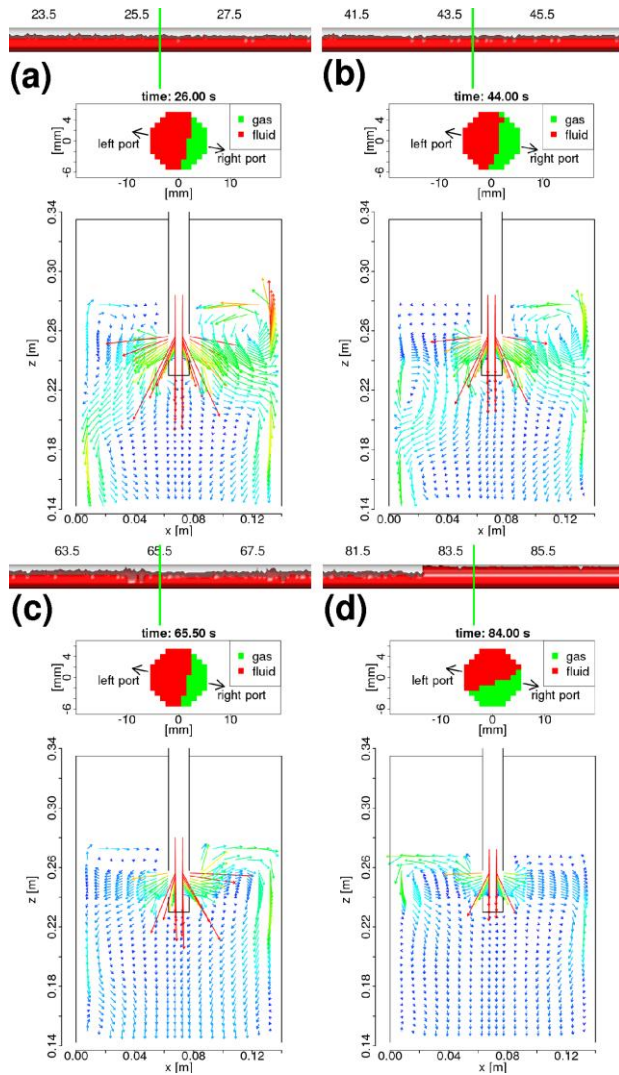


Fig. 4. CIFT reconstructed velocity in the mould , and MIT reconstructed metal distribution in the SEN at four instants (a - 26 s; b - 44 s; c - 65.5 s; d - 84 s) during one two-phase experiment with an argon flow rate of 500 cm³/min. Different flow structures (a,b – double roll, c,d – single roll on different sides) are clearly visible.

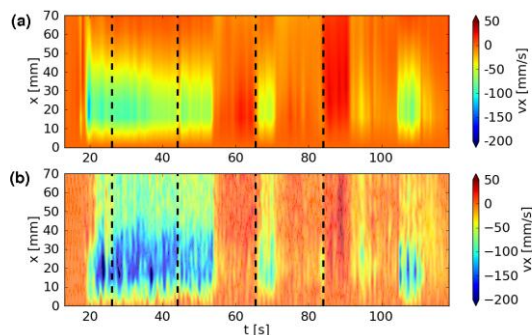


Figure 5: Comparison of the CIFT reconstructed (a) and the UDV determined (b) v_x component at $z=210$ mm in dependence on time and x -coordinate. The dashed lines indicate the snapshots illustrated in Fig. 4.

6 SUMMARY AND OUTLOOK

In this paper, we have summarized the recent efforts in the development of the Contactless Inductive Flow Tomography, and put them into the context of established flow measurement techniques like UDV. While CIFT, as a global reconstruction technique with an intrinsic non-uniqueness, will never attain the precision of UDV measurement, the avoidance of any contact with the melt makes it promising for some special measurement tasks in very hot and/or chemically aggressive and/or extremely clean metallic and semiconducting melts. Presently, work is going on to make the method more robust (by using AC measuring fields and gradiometric coils) for its envisioned industrial deployment.

REFERENCES

- [1] Takeda Y: Measurement of velocity profile of mercury flow by ultrasound Doppler shift method, Nucl. Technol. 79 (1987), 120-124.
- [2] Franke S et al.: Ultrasound Doppler system for two-dimensional flow mapping in liquid metals, Flow Meas. Instrum. 21 (2010), 402-409.
- [3] Eckert S et al.: Velocity measurement techniques for liquid metal flows, In: S. Molokov, R. Moreau, H.K. Moffatt (eds.) Magnetohydrodynamics – Historical Evolution and Trends, Springer (2007), pp. 275-294.
- [4] Baumgartl J et al.: The use of magnetohydrodynamic effects to investigate fluid flow in electrically conducting melts, Phys. Fluids A 5 (1993), 3280-3289.
- [5] Stefani F and Gerbeth G: Velocity reconstruction in conducting fluids from magnetic field and electric potential measurements, Inverse Problems 15 (1999), 771-786.
- [6] Stefani F and Gerbeth G: On the uniqueness of velocity reconstruction in conducting fluids from measurements of induced electromagnetic fields, Inverse Problems 16 (2000), 1-9.
- [7] Stefani F and Gerbeth G: A contactless method for velocity reconstruction in electrically conducting fluids, Meas. Sci. Techn. 11 (2000), 758-765.
- [8] Stefani F et al.: Contactless inductive flow tomography, Phys. Rev. E. 70 (2004), 056306.
- [9] Timmel K et al.: Experimental modeling of the continuous casting process of steel using low melting point alloys - the LIMMCAST program, ISIJ International 50 (2010), 1134-1141.
- [10] Wondrak T et al.: Contactless inductive flow tomography for a model of continuous steel casting, Meas. Sci. Techn. 21 (2010), 045402.
- [11] Wondrak T et al.: Combined electromagnetic tomography for determining two-phase flow characteristics in the submerged entry nozzle and in the mould of a continuous-casting model, Met. Mat. Trans. B 42 (2011), 1201-1210.

Effects of analysis algorithms and number of repetition pulses on velocity data by using ultrasonic Doppler method

Hideki Murakawa, Ryosuke Sakagami, Katsumi Sugimoto and Nobuyuki Takenaka
Department of Mechanical Engineering, Kobe University

1-1 Rokkodai, Nada, Kobe, 657-8501 Japan

An ultrasonic velocity profile (UVP) method is mainly based on the pulse Doppler method. In order to improve the time resolution, number of pulse repetition, N_{pulse} , must be reduced. However, the appropriate N_{pulse} changes with algorithms of the frequency analysis and signal-noise-ratio (SNR). In this study, appropriate algorithms of the frequency analysis and N_{pulse} were investigated with changing of the SNR by simulation and experiments. As a result, N_{pulse} could be set at the lowest by using autocorrelation method if the SNR was high. With decreasing of the SNR, results calculated by FFT became better. Furthermore, wavelet transform (WT) was hard to be affected by noises, and it is one of choice for measuring flow field if on-time measurement isn't required.

Keywords: Autocorrelation, FFT, Wavelet transform, Doppler method, UVP

1 INTRODUCTION

An ultrasonic velocity profile (UVP) method is mainly based on the pulse Doppler method although a cross-correlation method has been proposed [1,2]. Echo signals reflected from moving particles include Doppler frequency, f_d , depending on the velocity. However it is difficult to obtain f_d directly from an echo signal because the f_d is much smaller than the basic frequency of the ultrasonic, f_0 . Therefore multiple echo signals are usually used for the calculation. If fast Fourier transform (FFT) is used for analyzing the echo signals, factorial of 2 time repetitions are required. Frequency resolution of the f_d becomes worth with decreasing the number of repetition pulse, N_{pulse} . Therefore, fewer N_{pulse} for improving the time resolution is difficult. The autocorrelation method [3] calculates the phase change at least 2 pulses, but several number of echo signals are required in real situation because of noises and an assumption of the calculation. Wavelet transform (WT) is one of the frequency analysis methods. Some attempts using WT for the Doppler method was carried out in medical field [4, 5]. However, effect of noises on the measurement data has not been investigated. In this study, effects of the frequency analysis algorithms and N_{pulse} on the velocity data with changing of signal-noise-ratio (SNR) are investigated compared with the FFT, autocorrelation and WT methods.

2 PULSE DOPPLER METHOD

2.1 Principle

Schematic of the ultrasonic Doppler method is shown in Fig.1. The ultrasonic transducer emits a pulse with basic frequency of f_0 . If the pulse reflects on a reflector, the echo signal $z(t)$ is expressed as

$$z(t) = A \cos 2\pi(f_0 + f_d)t, \quad (1)$$

where A is amplitude of the signal. Multiple ultrasonic pulses are emitted and received for obtaining the velocity in each measurement position. Time delay, $t_{h,i}$, in pulse of h th and measurement position of i can be expressed as

$$t_{h,i} = hT_{prf} + \frac{2l_i}{c} \quad (2)$$

Here, time of the first pulse emission is referred to as 0. Where T_{prf} is interval time of the pulse emissions, and expressed as $T_{prf} = 1/f_{prf}$ using pulse repetition frequency, f_{prf} . Echo signal, $s_{h,i}(t)$, can be shown as

$$s_{h,i}(t) = A_{h,i} \cos 2\pi(f_0 + f_d) \left(t - t_{h,i} + \frac{2\Delta x h}{c} \right) \approx A_{h,i} \cos 2\pi \left\{ f_0(t - t_{h,i}) + f_d h T_{prf} \right\} \quad (3)$$

Here, the reflector moves Δx during T_{prf} . Velocities in each measurement position can be obtained from calculating the phase change of the consecutive echo signals.

Figure 2 represents block diagram of the measurement system. Echo signals are received at a pulser/receiver, and the signals are digitized by a

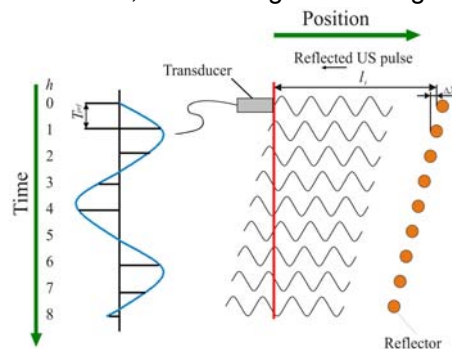


Figure 1 Schematic of detecting the Doppler frequency

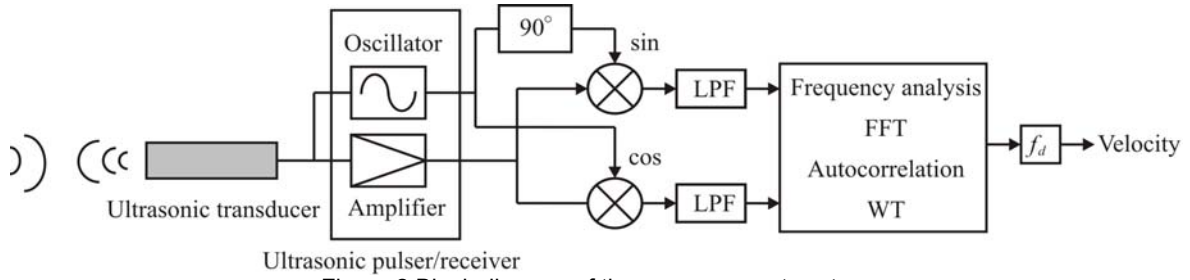


Figure 2 Block diagram of the measurement system

high-speed digitizer. Quadrature detection is applied to the signals, and it makes possible improve the SNR and detect the direction of the moving reflector. Above procedures are sampled at $t_{n,i} = nT_{prf} + T_i$, $x_{c,i}[n]$ and $x_{s,i}[n]$ are obtained as follow:

$$\begin{aligned} z_i(t) &= \left\{ s_{hi}(t) \cdot 2e^{j2\pi f_d t} \right\}_{LowPass} = x_{c,i}[n] - jx_{s,i}[n] \\ x_{c,i}[n] &= A_{ni} \cos(2\pi f_d n T_{prf} - \varphi_i) \\ x_{s,i}[n] &= A_{ni} \sin(2\pi f_d n T_{prf} - \varphi_i) \end{aligned} \quad (4)$$

φ_i is the differential phase between the initial phase. Applying frequency analysis to the signals, Doppler frequency in each position, $f_{d,i}$, can be obtained, and velocities are calculated as follow:

$$v_i = \frac{c f_{d,i}}{2 f_0} \quad (5)$$

2.2 Frequency analysis

FFT and autocorrelation method [3] is usually used for calculating the Doppler frequency from Eq.(4). A time-frequency window with fixed length which depends on the N_{pulse} is used for calculating the FFT analysis. Therefore, the time-resolution and frequency-resolution are incompatible. If we want to reduce the time-resolution, the N_{pulse} must be reduced. Which means the frequency-resolution becomes worth although an interpolation method is usually applied between the discrete spectrums. Hence, the N_{pulse} must be set at higher value appropriately, and time-resolution has limitation to be reduced. In this study, a threshold is used for eliminating the uncertain data. If the maximum value of power spectrum density (PSD) is higher than the threshold, the data is considered as effective. Otherwise, the data is recorded as invalid data.

Autocorrelation method utilizes the autocorrelation function to obtain the phase change between two consecutive echo signals, and expressed as

$$R_i(\tau) = \int z_i(t) \times \overline{z_i(t + \tau)} dt \quad (6)$$

Substituting $\tau = T_{prf}$ into Eq.(6),

$$\begin{aligned} R_i(T_{prf}) &= \int z_i(t) \times \overline{z_i(t + T_{prf})} dt \\ &= R_{x,i}(T_{prf}) + jR_{y,i}(T_{prf}) \end{aligned} \quad (7)$$

Doppler frequency $f_{d,i}$ can be expressed as

$$f_{d,i} = \frac{I}{2\pi T_{prf}} \tan^{-1} \frac{R_{y,i}(T_{prf})}{R_{x,i}(T_{prf})} \quad (8)$$

Velocity is obtained theoretically from 2 echo signals, and it is high time-resolution. However, this includes an assumption that either velocity component of going away from the transducer or toward the transducer is 0. In addition, ultrasonic has wide spectrum, and it includes noises. Several times repetition is required to obtain velocity accurately.

WT uses flexible time-frequency window. Mother wavelet changes with scaling parameter. If the frequency is high, the time-resolution becomes better. In this study, Gabor was used for the mother wavelet.

3 SIMULATION USING PSEUDO DOPPLER SIGNALS

3.1 Simulation method

Time series of velocity data was measured by using laser Doppler velocimetry (LDV) at a position in a horizontal duct. Pseudo Doppler signal was calculated by the frequency modulation of the LDV data. In order to simulate the noises, white noises with SNR of 20dB and 5dB was added to the signal. Velocities were obtained by applying the Doppler analysis on the signals, and compared with the LDV data (true velocity).

3.2 Simulation results

Time series of velocity data are compared with true velocity (measured by LDV) and analyzed velocities as shown in Figure 3. Figure 3(a) is the case of $N_{pulse}=4$, and (b) is the case of $N_{pulse}=16$. Results calculated from with and without noises are shown in each case. If there are no noises, the smaller N_{pulse} is, the better results are obtained. With decreasing of the N_{pulse} , high-frequency velocity fluctuations could be analyzed. This is because of time resolution. With increasing of N_{pulse} , the time resolution becomes worth, and the velocity data is averaged during the longer time. Therefore, it can be said that the N_{pulse} must be set at the lowest if the signal doesn't include noises.

However, if noises exist in the signal, the results changed. In case of $N_{pulse}=4$, the analyzed velocity has larger fluctuation than the true velocity. In this case, it is expected that the velocity standard

deviation is overestimated. On the other hand, the difference of velocity between without and with noises is small in the case of $N_{pulse}=16$. In this case, the velocity standard deviation is underestimated.

In order to evaluate the instantaneous velocity

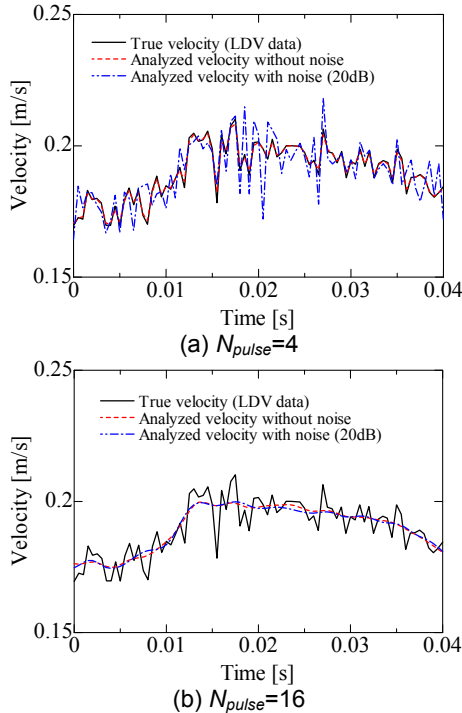


Figure 3 Time-series of velocity data compared between with and without noises. (Autocorrelation method)

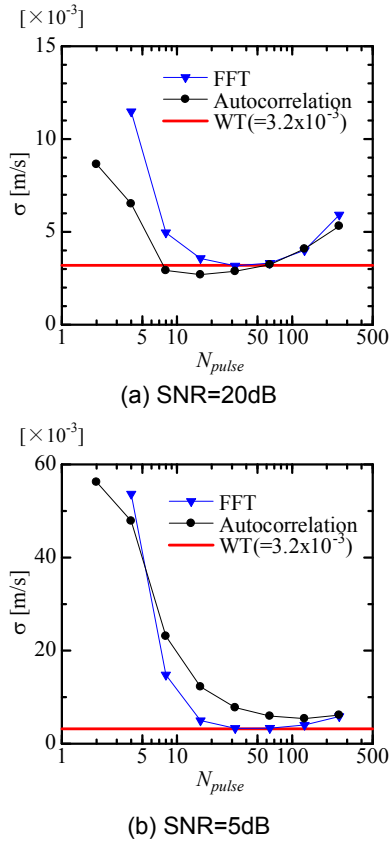


Figure 4 Difference between real and analyzed velocities

difference between true velocity (v_1 , LDV data) and analyzed velocity v_2 , root-mean-square of the velocity, σ , is calculated as follow:

$$\sigma = \sqrt{\frac{\sum \{v_1(t) - v_2(t)\}^2}{N}} \quad (8)$$

Figure 4 represents change of σ with N_{pulse} in each noise condition. Note that σ by WT is constant with N_{pulse} because the time-frequency window doesn't change. σ becomes worth with decreasing of the N_{pulse} under noise condition. Therefore, optimal values for decreasing the σ exist in both autocorrelation and FFT. Furthermore, the optimal analysis method and N_{pulse} changes with the SNR. Autocorrelation give us a good result under lower noise lever (SNR = 20dB). On the other hand, FFT is better under higher noise level (SNR = 5dB). This is because the threshold works well to remove the invalid data. Furthermore, the optimal N_{pulse} increases with the noises.

In case of WT, it can be confirmed that the effect of noise is relatively small, and the values are almost the same at between the SNR = 5 and 20dB. It can be said that the WT is hard to be affected by noises.

4 EXPERIMENTS

4.1 Experimental method

In order to confirm the optimal analysis method and N_{pulse} in Doppler method, experiment was carried out at the horizontal duct with 50 mm width and 25 mm height (H). Working fluid was tap water kept at 19 to 21 °C, and the Reynolds number was 8,000. Ultrasonic transducer with 4 MHz basic frequency was set at outer surface of the top wall with inclined angle of 45°. The f_{prt} was set at 4 kHz. During the experiment, multiple echo signals were continuously recorded as much as possible in a data file, and calculation were carried out after the experiment. Therefore, the same wave data were used for the calculation with changing analysis methods and N_{pulse} . Gain of the pulser/receiver was set at 30dB and 20dB. Changing of the gain setting, SNR could be changed. The 30dB was the best for the measurement. Therefore, SNR at 20dB was worth than that at 30dB.

4.2 Experimental results

Figure 5 indicates time-average velocity distributions calculated by autocorrelation method with $N_{pulse} = 8 \sim 128$ and wavelet analysis at 30dB. The horizontal axis indicates the distance from the wall, y , divided by H . It is confirmed that there is little difference between them, and average velocity can be obtained accurately from even $N_{pulse} = 8$ except near wall region. Because ultrasonic has relatively large measurement volume, velocity measurement near the wall where velocity gradient is steep is difficult.

Velocity standard deviations, u'_{+45} , are strongly affected by the N_{pulse} . It can be seen that $N_{pulse} = 8$ in

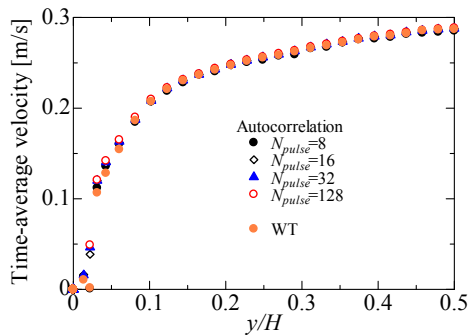


Figure 5 Time-average velocity distribution (Gain=30dB)

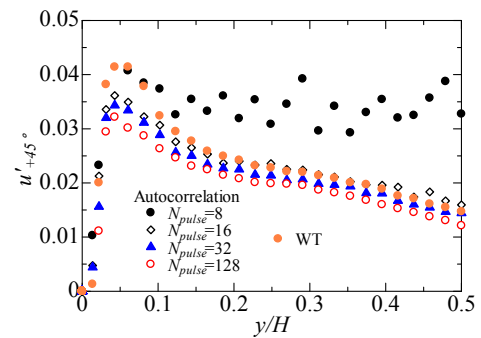
autocorrelation method couldn't measure it accurately. Even at $N_{pulse} = 16$, the fluctuation can be confirmed at $y/H > 0.4$. With increasing of the N_{pulse} , the u'_{+45} decreases all over the positions. This is reasonable result. The standard deviation calculated by WT takes values between $N_{pulse} = 8$ and 16.

In case of 20dB, the u'_{+45} becomes worth in autocorrelation method. Accuracy of u'_{+45} were low at $N_{pulse} = 32$, and it is confirmed that the N_{pulse} must be increased with increasing of the noises. The u'_{+45} at $N_{pulse} = 64$ increases with distance from the wall. It means that the accuracy of u'_{+45} becomes worth with the distance. This is because the SNR of ultrasonic echo signal becomes worth with the distance from the transducer. However, it can be confirmed that the WT is hard to be affected by noises. This result is good agreement with the simulation results shown in Figure 4.

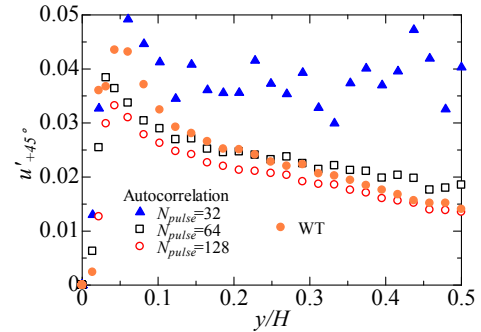
Comparing the results under lower SNR by autocorrelation and FFT, the results in autocorrelation are better at the same N_{pulse} . However, if appropriate N_{pulse} is chosen in FFT, u'_{+45} around $y/H=0.1$ can be obtained more accurately than that in autocorrelation. This tendency is similar with the results by WT. In case of WT, time-frequency window changes with the velocity. Therefore, the WT is more convenient than the FFT. However, the calculation-time takes much longer than the other methods. It means the WT is one of the methods for measuring velocity distributions because the SNR continuously changes with measurement positions, if on-time measurement is not required.

5 SUMMARY

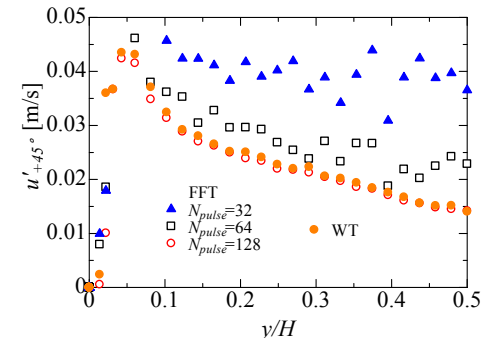
Effects of algorithms and N_{pulse} on velocity measurement by using pulse Doppler method were investigated by simulation and experiments. N_{pulse} could be set at the lowest by using autocorrelation method if the SNR was high. With increasing of the SNR, results by FFT became better. However, N_{pulse} must be chosen appropriately depending on the SNR. WT is relatively hard to be affected by noises. Therefore, WT is one of choice for measuring velocity distributions if on-time measurement isn't



(a) Autocorrelation (Gain=30dB, High SNR)



(b) Autocorrelation (Gain=20dB, Low SNR)



(c) FFT (Gain=20dB, Low SNR)

Figure 6 Velocity standard deviation along the transducer direction (u'_{+45})

required.

REFERENCES

- [1] Ozaki Y, Kawaguchi T, Takeda Y, Hishida K and Maeda M: High time resolution ultrasonic velocity profiler", *Exp Thermal Fluid Sci.* 26 (2002), 253–258.
- [2] Yamanaka G, Kikura H and Aritomi M: Study on the development of novel velocity profiles measurement method using ultrasonic time-domain cross-correlation, In *Proc. of 3rd Int. Symp. Ultrasonic Doppler methods for fluid mechanics and fluid engineering*, (2002). 109–114.
- [3] Kasai C, Namekawa K, Koyano A and Omoto R: Real-time two-dimensional blood flow imaging using an autocorrelation technique, *IEEE Trans. Sonics and Ultrasonics*, SU-32 (1985), 458-464.
- [4] Matani A, Oshiro O and Chihara K: Doppler signal processing of blood flow using a wavelet transform, *Jpn. J. Apply. Phys.* 35 (1996), 3131-3134.
- [5] Zhang Y, Guo Z, Wang W, He S, Lee T and Loew M: A comparison of the wavelet and short-time fourier transforms for Doppler spectral analysis, *Medical Engineering & Physics* 25 (2003), 547-557.

Ultrasonic Flow Field Measurement of a Rotating Flow with Free Surface

Yuji Tasaka¹, Yuichi Murai¹ and Makoto Ima²

¹Laboratory for Flow Control, Hokkaido University, Sapporo 060-8628, Japan

²Department of Mathematical and File Science, Graduate School of Science, Hiroshima University, Hiroshima 739-8526, Japan

We developed a measurement technique to achieve the both of the interface detection and the flow field measurement simultaneously using UVP. The technique was adopted to investigate a temporally irregular surface switching of rotating fluids to clarify the mechanism of the phenomenon. Interface detection and estimation of two-dimensional velocity field from spatio-temporal velocity distributions successfully represented the development of the surface switching; change of the surface shape from circle to bow-tie shape via ellipsoid, and corresponding flow circulations on the velocity vector field.

Keywords: Flow field, Free surface, Rotating flow, Ultrasonic echo intensity

1 INTRODUCTION

Flow field measurement around largely deformed free surface has been desired in many research and development scenes, for instance in fundamental fluid physics, chemical engineering and civil engineering, etc. Traditional measurement tools, however, cannot provide detailed information about the both of the surface position and the flow field. Image-processing-based velocimetry such as PIV achieves that with high accuracy but has difficulties on industrial use because of limitations on the setup. In contrast with this UVP has some advantages for industrial use: UVP does not require transparency for fluids and walls of test sections; a non-invasive technique, spatio-temporal velocity measurement, etc. Recently, some works to enrich the measurable information on the UVP measurements have performed. There exist ultrasonic displacement meters and it is possible to add this function of the interface detection into UVP. We perform the interface detection on the results of UVP measurement, i.e. ultrasonic echo information and spatio-temporal velocity distribution [1].

Flows accompanied by a largely deformed free surface are one of the interesting problems in the fluid mechanics. Those motions are difficult to be analyzed and predicted by numerical analyses and theoretical ways. Good experimental works sometime provide a breakthrough to overcome difficulties to clarify the complex phenomenon. Here we utilize the developed technique to investigate recently discussed phenomenon, temporally irregular surface switching of rotating fluids [2,3]. The surface shape and the flow field around the deformed free surface in the surface switching are determined by UVP, and the development of the surface switching is represented.

2 IRREGULAR SURFACE SWITCHING OF ROTATING FLUIDS

Typical sequence of the surface switching of rotating

fluids is shown in Fig. 1, where the top schema represents the top view of the surface shape with contours of surface height, and bottom photos are side view of the surface extracted from a movie. The process is summarized as follows: At the beginning of the process, (a)-(b) in the figure, a symmetry breaking of the free surface occurs, and the shape of the surface in the horizontal cross-section changes from an axisymmetric state to a line-symmetric state, elliptic in this step; then the line-symmetric surface has two humps at the bottom of the surface in the development of the deformation ((b)-(c)); after that the surface detaches from the disk ((d)); the detached free surface starts vertical oscillations and takes irregularly the axisymmetric state again; the axisymmetric surface sometime reattaches to the disk ((a)), but usually takes the symmetry breaking before that. Previous works clarified that the surface switching accompanies laminar-turbulent flow transition, namely the flow state for the axisymmetric surface is laminar and the turbulent for the line-symmetric surface. Reason of the elevation of the free surface in the surface switching may be a change of the pressure balance in the radial direction due to the turbulent flow mixing; turbulence transfers faster fluids near the lateral wall into the central part and vice versa.

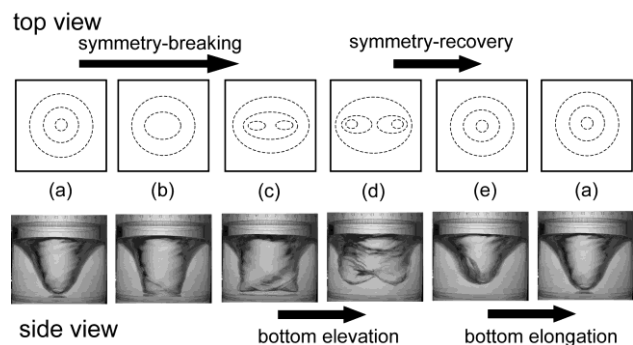


Figure 1: Typical sequence of the switching process; (top) illustrations for the top view of the free surface (bottom) side view of the free surface [3]

3 EXPERIMENTAL SETUP AND INTERFACE DETECTION

3.1 Experimental setup

Schema of the experimental setup for the interface detection and the flow field measurement is shown in Fig. 2(a). A cylindrical open vessel made of acrylic resin with $R = 42$ mm in radius has a glass disk as its bottom. There is a certain lateral clearance, $\Delta R = 0.3$ mm, between the cylinder and the disk. Tap water is used as the test fluid and the depth of the water layer in the vessel is $H = 40$ mm at rest; the corresponding aspect ratio becomes $\Gamma = H/R = 0.95$. The bottom disk is rotated by a motor with a constant speed of rotation, $\Omega = 13.2$ Hz. For this value, the Reynolds number, $Re = 2\pi\Omega R/\nu$ (ν is kinematic viscosity of water), is 1.46×10^5 .

UVP was utilized to obtain spatio-temporal velocity profiles and ultrasonic echo information. An ultrasonic transducer (TDX) with 4 MHz in the resonance frequency was mounted on the side wall of the cylinder with 8 mm in height from the disk. The TDX faced the center of the cylinder and the UVP measured time variation of the radial velocity component along the radial direction, i.e. $u_r(r, t)$. UVP monitor model Duo recorded and processed ultrasonic echo information. Time and space resolutions of the measurement are 13 ms and 0.74 mm. Particles of porous resin (50-60 μm in diameter and 1020 kg/m^3 in density) were seeded into the water as the flow tracers for the UVP measurement.

A halogen ramp illuminated fluid layer from the side, and the back-lighting images of the free surface were recorded by a digital video camera with 29.97 fps. Samples of the obtained images are shown in Fig. 2(b), where the black lines in the figure indicate measurement line of the UVP.

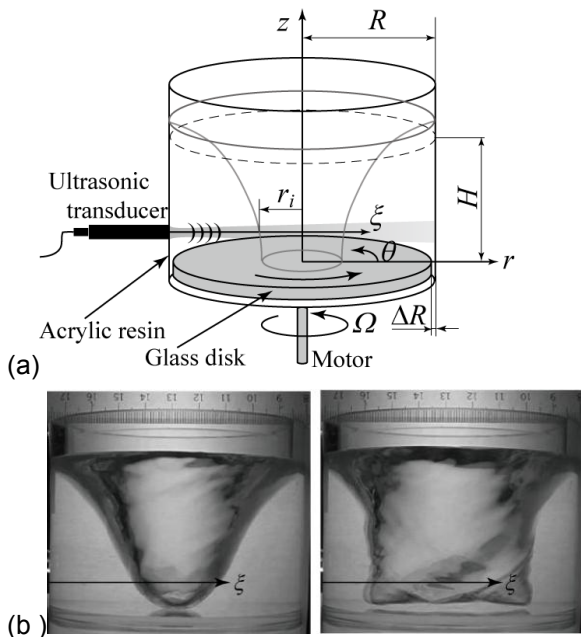


Figure 2: (a) Schema of experimental setup and (b) examples of surface shape

3.2 Interface detection

To achieve the interface detection together with the velocity field measurement, two methods, Doppler method and echo intensity method, are utilized. These have different disadvantages on the interface detection and thus are used in a complementary style. Figure 3(a) shows original, spatio-temporal velocity distribution in the development of the symmetry breaking, corresponding to (a)-(b)-(c)-(d) in Fig. 1, measured by UVP. The symmetry breaking of the rotating free surface provides periodic variation of the velocity, and the magnitude of the variation increases with time. With the development, discontinuous lines appear in the radial direction because of reflection of ultrasonic wave at the interface. Sobel filter, a kind of differential filter, enhances the 'discontinuous edge' as shown in Fig. 3(b), and we can detect interface position by finding the edges. This method, however, does not work at which the flow direction greatly changes, local minimal or maximal points on the variation of the interface position in this case. On the other hand, the ultrasonic echo intensity indicates higher values only at the extremal points as shown in Fig. 3(c). It is because the inclination angle of the surface is much larger than the divergence angle of the ultrasonic wave, 5 deg. in this case, without the extremal points on the variation of the surface position, and thus the ultrasonic transducer cannot receive the echo reflected at the interface.

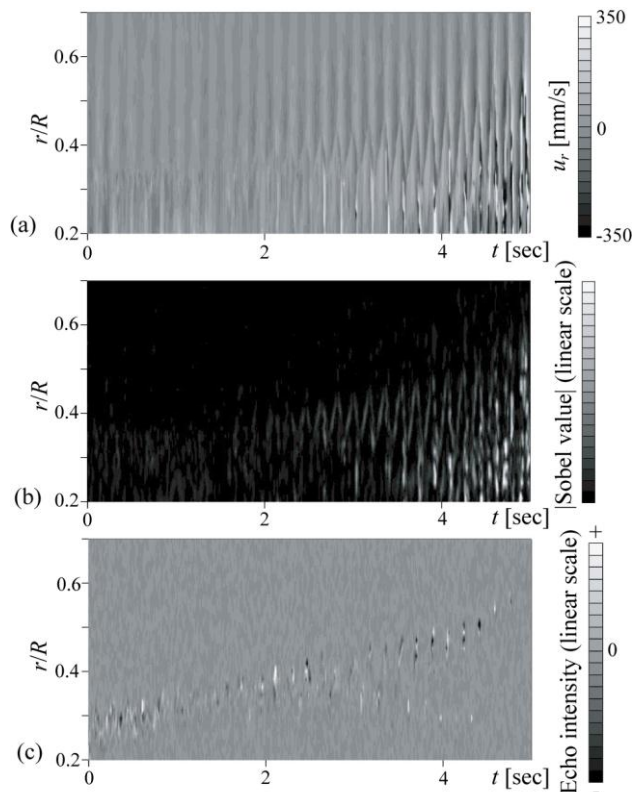


Figure 3: (a) Original velocity distribution, (b) Sobel-filtered value of the velocity, (c) variation of the corresponding ultrasonic echo information [1]

A variation of the free surface position in the radial direction, r_i , detected by above two methods is shown in Fig. 4, where the surface height at the center of the vessel, h , determined from the movie simultaneously taken and the intensity of the spatial velocity fluctuation, $u_{r,rms}$, are also shown. The black and gray lines in the figure indicate original data and moving-averaged one, respectively. There seems strong correlation between the development of the surface deformation and the increase of the velocity fluctuation. The variations represent process of the symmetry breaking and detachment of the free surface: The surface deformation due to the symmetry breaking proceeds increase of the velocity fluctuation that provides the flow mixing; when the fluctuation becomes large enough, the free surface detaches from the bottom; the surface deformation and the increase of the velocity fluctuation are further enhanced.

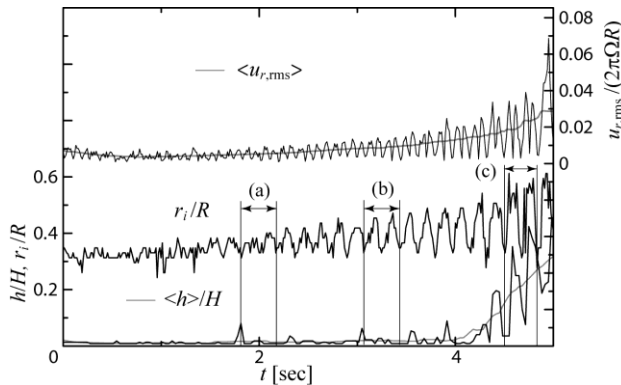


Figure 4: Variations of the surface height, h , radial position of the interface, r_i , and the intensity of the velocity fluctuation, $u_{r,rms}$, where the black and gray lines represent original data and moving-averaged one

4 RESULTS AND DISCUSSIONS

4.1 Surface shape

According to the observation of the free surface shape in the sequence of the surface switching (see Fig. 1), surface shape on the horizontal cross-section changes from circle to ellipsoid. It is, therefore, reasonable to assume that two cycles of the variation on r_i shown in Fig. 4 corresponds to the whole periphery of the free surface; namely the local minimal and maximal positions on r_i correspond to the minor and major axes of the ellipsoidal free surface. By giving period of the rotation T , $r_i(t)$ can be converted into $r_i(\theta)$, where the T is not constant and changes with respect to the surface deformation. Figure 5 shows the result of the conversion, i.e. estimated surface shape expressed in the polar coordinates, where the diagonal crosses represent the obtained surface position in the radial direction and the lines connecting these points are given by closed B-Spline interpolation. Here we also converted spatio-temporal distribution of the radial velocity component, $u_r(r, t)$ into $u_r(r, \theta)$ in the same way of the conversion from $r_i(t)$ to $r_i(\theta)$ by applying

Taylor's frozen hypothesis that assumes the local flow structure doesn't change against the advection.

Three circular distributions in the Fig. 5 represent the surface shape and the radial velocity distribution at the beginning of the symmetry breaking (a), the adjacent (b) and immediate (c) states for the detachment of the free surface from the rotating disk. Corresponding time series of r_i , the surface height h and the velocity fluctuation $u_{r,rms}$ for these states are indicated in Fig. 4. In Fig. 5(a) the surface deformation is small and its shape is still circular. The radial velocity due to the surface deformation is also small. In the adjacent state for the surface detachment from the disk, Fig. 5(b), the surface largely deforms and its shape becomes ellipsoid. The radial velocity is enhanced and the flow direction changes around the minor and major axes

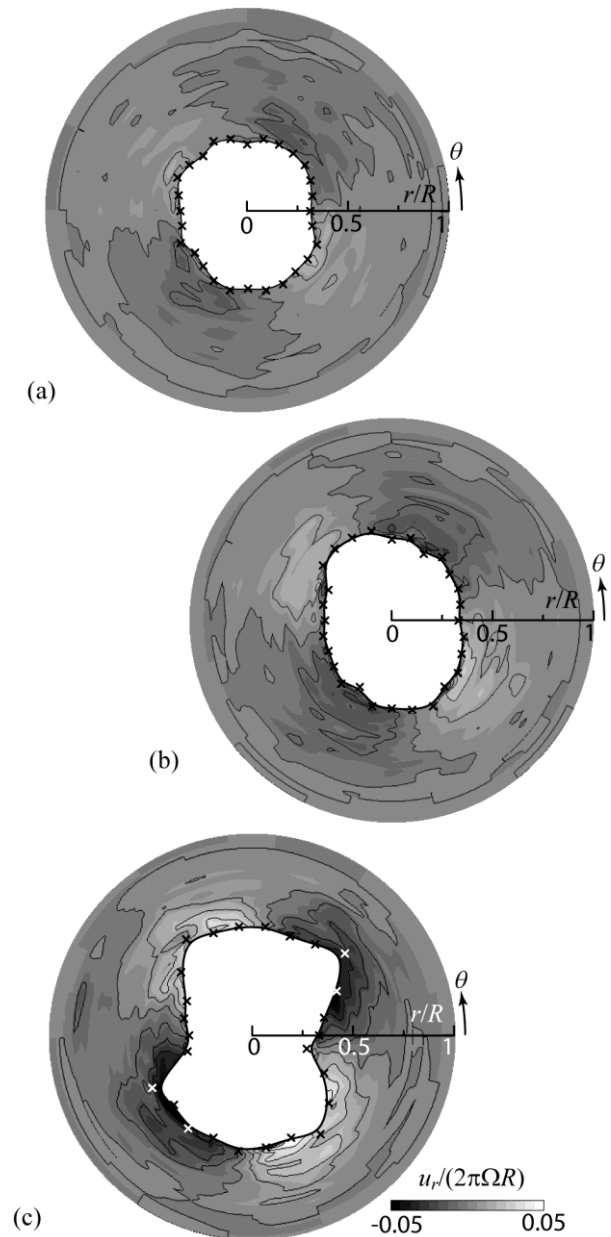


Figure 5: Estimated surface shapes $r_i(\theta)$ and distribution of the radial velocity component $u_r(r, \theta)$ in polar coordinates; original data for figs are indicated in Fig. 4.

points. After the free surface detaches from the bottom, surface deformation is further developed and the shape is no longer ellipsoid: Smaller curvature sides of the ellipsoid are concaved and four apexes appear like a bow tie. The flow seems to be pushed out by two facing apexes.

4.2 Estimation and evaluation of the flow field

To evaluate the flow field around the free surface that deforms with time, we estimate the distribution of the tangential velocity component u_θ from $u_r(r, \theta)$ and form the two dimensional velocity vector field. By assuming that the axial velocity is small enough in comparison with u_r and u_θ , u_θ is derived from the two-dimensional equation of continuity in the polar coordinate as

$$u_\theta(r, \theta) = u_\theta(r, 0) - \int_0^{2\pi} \frac{\partial}{\partial r}(ru_r) d\theta \quad (1)$$

Here giving $u_\theta(r, 0)$ to above equation is impossible on the present data set. But using the whole circumference average of $u_\theta(r, \theta)$,

$$\begin{aligned} u'_\theta(r, \theta) &= u_\theta(r, \theta) - \langle u_\theta \rangle_\theta(r) \\ &= \frac{1}{2\pi} \int_0^{2\pi} \int_0^\phi \frac{\partial}{\partial r}(ru_r) d\theta d\phi - \int_0^\theta \frac{\partial}{\partial r}(ru_r) d\theta, \end{aligned} \quad (2)$$

where the brackets, $\langle \rangle_\theta$, mean the whole circumference average. To prevent noise amplification due to the numerical difference, median filtering with 3 times 3 lattice size has been applied on the original data of $u_r(r, \theta)$ before the estimation. The trapezium scheme is used for numerical integration.

Figure 6 shows the results of the estimation; (a) at the beginning of the symmetry breaking, (b) at the immediate state of the surface detachment. Corresponding radial velocity distributions for these figures are (a) and (c) in Fig. 5. As expected in the radial velocity distribution, variation on the velocity field around the circular free surface is extremely small (Fig. 6(a)). It means the flow field is axisymmetric. On the other hand for the largely deformed free surface, there exists a typical flow structure due to surface deformation, even though the error vectors appear near the deformed, bow-tie-shaped free surface (Fig. 6(b)). Four large circulations are formed around the apexes of the surface, and these circulations may modify the pressure distribution and provide the strange surface shape at the bottom as shown in Fig. 2(b).

5 CONCLUSION

We developed a non-invasive technique to measure the both of the surface shape and the flow field around the free surface by utilizing UVP. The technique was applied to determine the behavior of the free surface and the surrounding fluid motion in the temporally irregular surface switching of a rotating fluid. Doppler method that utilizes

characteristic velocity variation around the free surface on the results of the UVP measurements, and echo intensity method were employed to detect the free surface position. These methods act to redeem their disadvantages each other. Obtained results represent the development of the free surface and corresponding flow field as well; the free surface deformation from circle to bow-tie shape via ellipsoid. Velocity vector fields estimated from the radial velocity component with applying Taylor's frozen hypothesis show four local circulation of the flow for the bow-tie shaped surface.

ACKNOWLEDGEMENT

This study is partially supported by Core Research for Evolutional Science and Technology (CREST) No. PJ74100011.

REFERENCES

- [1] Murai Y, *et al.*: Ultrasonic detection of moving interfaces in gas-liquid two-phase flow, *Flow Meas. & Inst.* 21(2010), 356-366.
- [2] Suzuki T, Ima M, Hayase Y: Surface switching of rotating fluid in a cylinder, *Phys. Fluids* 18(2006), 101701.
- [3] Tasaka Y and Ima M: Flow transition in the surface switching of rotating fluid, *J. Fluid Mech.* 636(2009), 475-484.

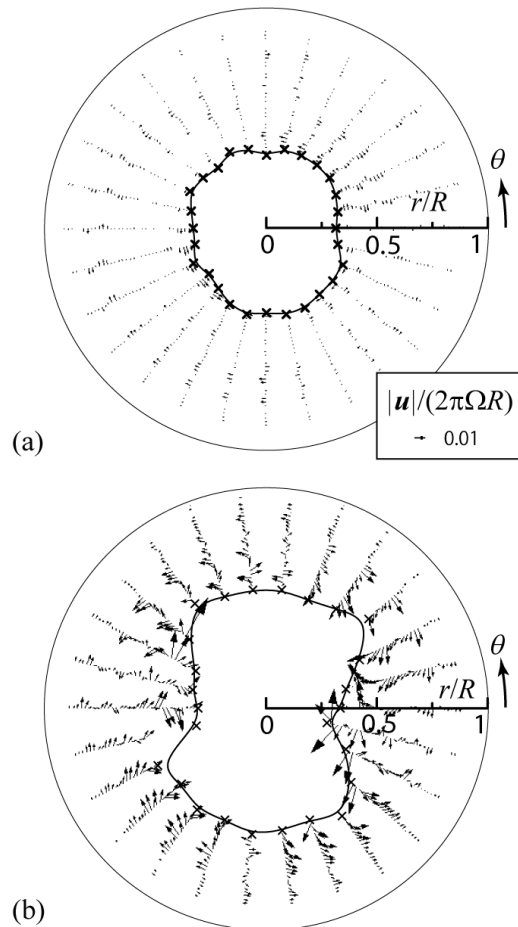


Figure 6: Estimated velocity vector field around the rotating free surface; corresponding radial velocity distributions are shown in Fig. 5(a) and (c)

Ultrasonic flow measurements in a downscaled water mockup of a large scale precession driven dynamo experiment

Thomas Gundrum, Frank Stefani, Canlong Ma, Yunhan Sun, André Giesecke, Thomas Albrecht, and Gunter Gerbeth
Helmholtz-Zentrum Dresden-Rossendorf, P.O. Box 510119, D-01314 Dresden, Germany

The DREsden Sodium facility for DYnamo and thermohydraulic studies (DRESHDYN) is planned to become a platform both for large scale experiments related to geo- and astrophysics as well as for experiments on thermo-hydraulic and safety aspects of liquid metal applications in energy related technologies. The most ambitious project in the framework of DRESHDYN is a homogeneous hydromagnetic dynamo driven solely by precession. The detailed knowledge of the flow structure in the precessing cylindrical vessel is of key importance for the prediction of the dynamo action. In this paper we present UDV measurements of the velocity field in a 1:6 downscaled water mock-up.

Keywords: Ultrasound Doppler Velocimetry, Precession, Dynamo

1 INTRODUCTION

Although most theories of the geodynamo rely basically on a flow driven by thermal and/or compositional buoyant force [1], precession has been discussed since long as a complementary energy source [2,3,4]. This idea seems to be supported by paleomagnetic measurements that have revealed a modulation of the geomagnetic field intensity by the 100 kyr Milankovic cycle of the Earth's orbit eccentricity and by the corresponding 41 kyr cycle of the Earth's axis obliquity [4]. Although the observed 100 kyr signal might be biased by climate-driven lithological variations, it reappears in the more robust reversal statistics of the geomagnetic field [5]. Most interesting in this respect is the correlation of geomagnetic field variations with climate changes, as hypothesized for the sequence of ice ages [6], demonstrated for variations during the last 5000 years [7], and perhaps also existing for the recently discovered 60 years cycle of the climate [8,9]. Yet, it is still a puzzling question how exactly the variation of orbital parameters affects both the climate and the geomagnetic field. In the standard scenario, pioneered by Doake [10], growing or melting ice sheets are thought to change the moment of the inertia of the Earth, thereby influencing the geodynamo by a modified rotation period. However, the recently revealed role of the solar and geomagnetic field as possible climate drivers due to their varying shielding effect on galactic cosmic ray particles [11] makes it worthwhile to consider also the reversed causal direction: What if the changing orbital parameters would *first* influence the geodynamo and *then and thereby* the climate by preventing cosmic rays from triggering cloud formation?

Aside from those questions of general geophysical interest, precession driven dynamo action is also interesting from the narrower magnetohydrodynamic

point of view. For more than a decade now, the experimental study of dynamo action in the liquid metal laboratory has made great progress [12]. In a sequence with the previous experiments in Riga [13], Karlsruhe [14] and Cadarache [15], a precession driven dynamo experiment would represent a logical next step towards a real homogeneous dynamo. With just a fluid rotating around two axes, it would neither contain any propeller, as in Riga, nor any assembly of guiding tubes, as in Karlsruhe, nor any soft-iron material (which is crucial for the low critical magnetic Reynolds number and the close to axisymmetric eigenmode) as in the Cadarache experiment [16].

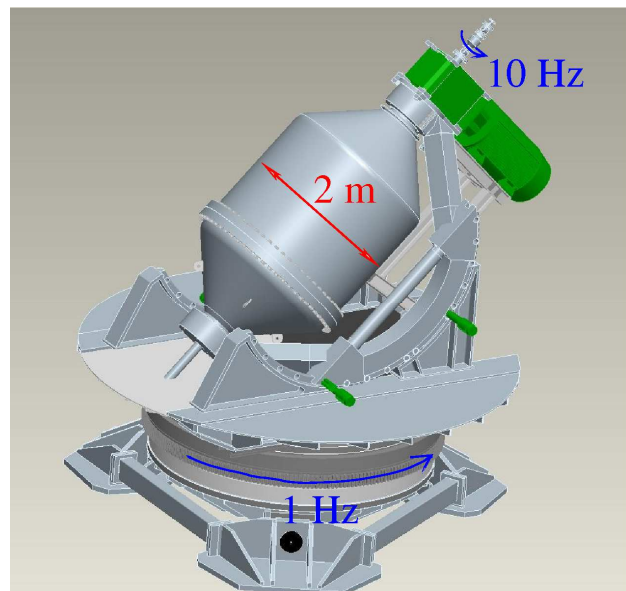


Figure 1: Preliminary draft of the planned large scale precession driven dynamo experiment. The angle between rotation and precession axes can be varied between 90° and 45°.

The precession driven dynamo experiment that is

planned to be set-up in the framework of the DREsden Sodium facility for DYNamo and thermohydraulic studies (DRESdYN) will be a cylindrical vessel of approximately 2 m diameter and length, rotating with up to 10 Hz around its symmetry axis, and with up to 1 Hz around the precession axis whose angle to the symmetry axis can be varied between 90° and 45° (see Fig. 1 for a preliminary draft). An inner cylindrical copper shell is immersed into a slightly larger cylindrical stainless container with conical end parts. With the indicated rotation and precession rates, this precessing vessel would exert a huge gyroscopic moment of around 5×10^6 Nm on the ground which requires the construction of a very solid basement.

2 THE WATER MOCKUP AND THE ULTRASONIC DOPPLER SYSTEM

Despite some numerical evidence for the possibility of dynamo action in a precessing cylinder [17], many aspects are still in need of further investigation. In order to figure out optimal design and process parameters for the later large-scale liquid sodium experiment, we have started a series of experiments at a smaller, 1:6 down-scaled, water precession experiment that is shown in Fig. 2.

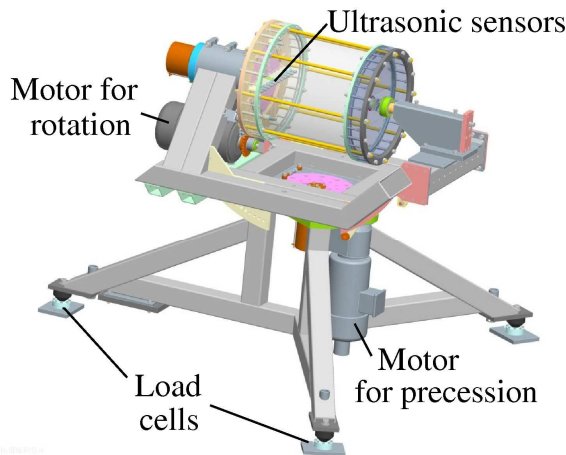


Figure 2: Drawing of the 1:6 downscaled water precession experiment for the determination of velocity fields, motor powers, and torques on the basement for various driving conditions.

This small water experiment is quite similar to the ATER experiment guided by J. Léorat [18], but allows for choosing different angles between the rotation and the precession axes. The installed measurement equipment enables the determination of the torques and motor powers needed to drive the rotation of the cylinder and the turntable, and of the gyroscopic torques acting on the basement.

Concerning the flow field determination, we have installed a number of ultrasonic sensors for the determination of the axial velocity component (Fig. 3

and 4). While the facility can run with rotation rates of 10 Hz and precession rates of 1 Hz, the well-known relation $d v_{\max} = c^2 / (8 f)$ between signal depth d and maximal velocity v_{\max} , for given sound velocity c and frequency f , restricts the UDV measurements to rather low rotation rates.



Figure 3: Photograph of the rotating cylinder and of the UDV sensors for the measurement of the axial velocity.

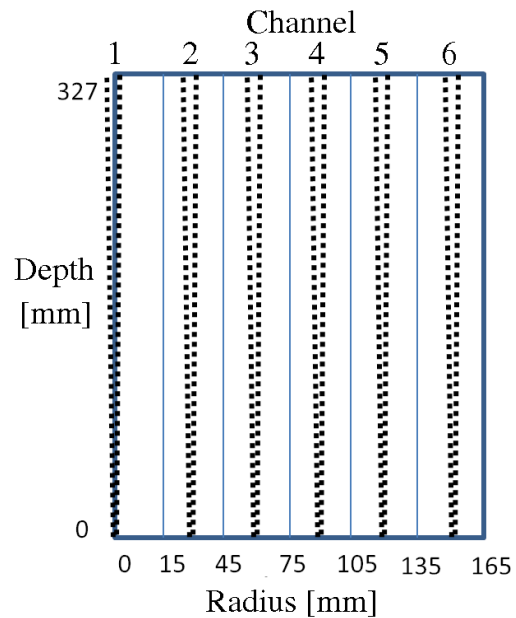


Figure 4: Sketch of the UDV sensor configuration and of the covering of the volume by the ultrasound beams.

3 FIRST RESULTS

For a rather low rotation rate of 0.2 Hz and a precession rate of 0.01 Hz, Fig. 5 shows the results of the axial velocity measured by UDV for an angle between the two axes of 90°. Hereby, the upper panel shows the raw data, and the lower panel shows the low-pass filtered data. The oscillatory sequence of positive and negative values is a typical indication for the first non-axisymmetric Kelvin mode with an azimuthal wave number $m=1$. The observed frequency of ~ 0.2 Hz indicates also that this mode is essentially fixed in the frame of the turntable, so that the UDV sensor rotating with the cylinder at 0.2 Hz experiences a changing v_z component of the

precession mode along the azimuthal angle of the cylinder.

When scaled to the planned 10 Hz rotation rate, and to the 6 times larger sodium facility, the observed velocity of 40 mm/s would correspond to a value of around 12 m/s.

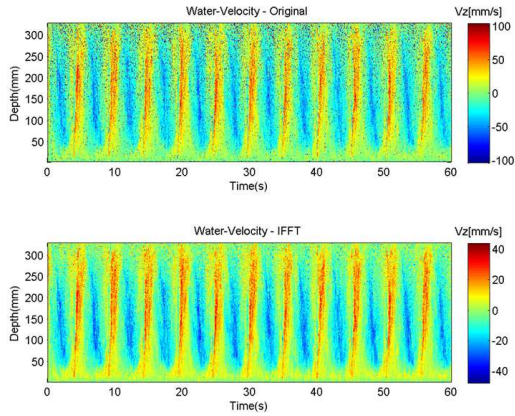


Figure 5: Axial velocity component at sensor 6 for a rotation rate of 0.2 Hz and a precession rate of 0.01 Hz. The $m=1$ Kelvin mode is fixed to the turntable frame.

It is a typical feature of precessing flows in cylinders that they show quiet different flow patterns in dependence on the precession ratio ϵ , i.e. the ratio of the precession frequency to the rotation frequency. With the details depending slightly on the aspect ratio of height to diameter of the cylinder, we first observe a laminar flow with only a few non-axisymmetric modes which changes suddenly, at a critical value ϵ^* , to a turbulent flow. It is at this point, that the torque necessary for driving the rotation, and therefore the motor power, jumps significantly.

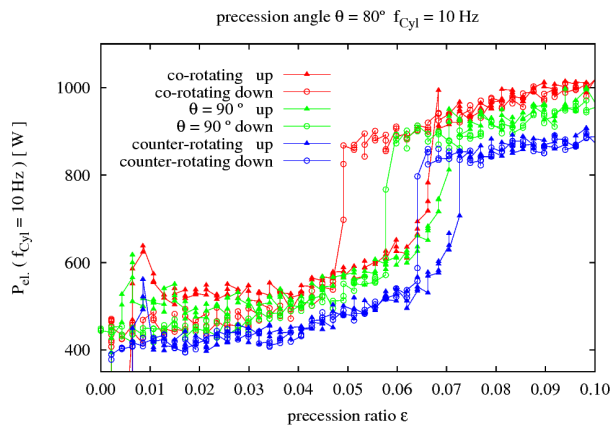


Figure 6: Motor power in dependence on the precession ratio for three different configurations between the axes.

This behaviour is illustrated in Fig. 6 which shows, now for a cylinder rotation rate of 10 Hz and for

three different configurations, sudden jumps of the electrical motor power. The green lines are for the case of angle of 90° . Interestingly, we observe a slight hysteresis, i.e. for increasing precession ratio the upward jump occurs approximately at $\epsilon \sim 0.07$, while for decreasing precession ratio the downward jump occurs at $\epsilon \sim 0.06$.

The critical precession ratio changes slightly when we modify the angle between the axes to 80° . Then we have to distinguish between the co-rotating case (red lines) and the counter-rotating case (blue lines). It seems that the hysteresis becomes broader for the co-rotating case, and narrower for the counter-rotating case, although this needs further confirmation.

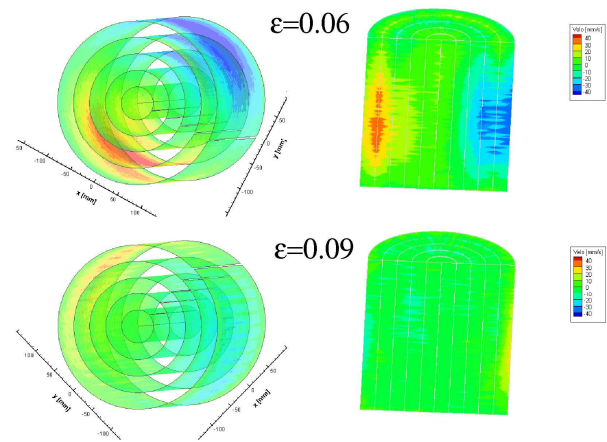


Figure 7: Axial velocity component measured by the 6 sensors for two different precession ratios in the laminar case ($\epsilon=0.06$) and in the turbulent case ($\epsilon=0.09$).

Figure 7 illustrates the physical mechanism that leads to the transition from a laminar to a turbulent flow. For a rotation rate of 0.2 Hz and an angle of 80° it shows the different flow structure for $\epsilon=0.06 < \epsilon^*$, and for $\epsilon=0.09 > \epsilon^*$. The left panel in either case shows the axial velocity as measured by the 6 UDV sensors in dependence on the azimuthal position and the depth, the right panel shows a cut in the meridional plane with the highest velocity contrast. Evidently, the clear $m=1$ mode that is dominating in the laminar case ($\epsilon=0.06$), is significantly weakened in the turbulent case ($\epsilon=0.09$).

6 SUMMARY AND OUTLOOK

In this paper, we have motivated the set-up of a large-scale liquid sodium dynamo experiment that is exclusively driven by precession. For the detailed characterization of the fluid flow in a precessing cylinder at different precession ratios, we have carried out a variety of experiments at an 1:6 downscaled water mock-up. The power

measurements have confirmed the existence of a critical value of the precession ratio at which a transition between a laminar and a turbulent flow occurs. The UDV flow measurements were up to present restricted to rather small rotation rates, partly due to the well known maximum product of depth and velocity, but partly also by the disturbing effect of sound reflections at the opposite cylinder wall. By using sound absorbing material at this wall we hope to overcome this problem and to extend the flow measurement to up to 1 Hz rotation rate. A further goal for the future UDV measurements concerns the identification of the few large-scale helical eddies as they were identified by Particle Image Velocimetry (PIV) at the ATER experiment in Meudon [19].

A major step will then be to assemble the acquired information about the stationary and fluctuating parts of the velocity field into an appropriate form that can then be utilized in dynamo codes to determine in detail the conditions and optimal parameters for magnetic field self-excitations in the precession driven dynamo.

REFERENCES

- [1] Wicht J and Tilgner A: Theory and Modeling of Planetary Dynamos, *Space Sci. Rev.* 152 (2010), 501-542.
- [2] Malkus WVR: Precession of Earth as cause of geomagnetism, *Science* 160 (1968), 259-264.
- [3] Gans RF, On hydromagnetic precession in a cylinder, *J. Fluid Mech.* 45 (1970), 111-130.
- [4] Tilgner A: Precession driven dynamo, *Phys. Fluids* 17 (2005), 034104
- [5] Consolini G and De Michelis P: Stochastic resonance in geomagnetic polarity reversals, *Phys. Rev. Lett.* 90 (2003), 058501
- [6] Courtillot V et al.: Are there connections between the Earth's magnetic field and climate? *Earth Planet. Sci. Lett.* 253 (2007), 328-339.
- [7] Knudsen MF and Riisager P: Is there a link between Earth's magnetic field and low-latitude precipitation? *Geology* 37 (2009), 71-74.
- [8] Scafetta N: A shared frequency set between historical mid-latitude aurora records and the global surface temperature *J. Atmos. Sol.-Terr. Phys.* 74 (2012), 145-163
- [9] Roberts PH et al.: On the 60-year signal from the core, *Geophys. Astrophys. Fluid Dyn* 101 (2007), 11-35.
- [10] Doake CSM: Possible effect of ice ages on Earth's magnetic field, *Nature* 267 (2007), 415-417.
- [11] Scherer K et al.: Interstellar-terrestrial relations: Variable cosmic environments, the dynamic heliosphere, and their imprints on terrestrial archives and climate. *Space Sci. Rev.* 127 (2006), 327-465.
- [12] Stefani F et al.: Magnetohydrodynamic experiments on cosmic magnetic fields, *Z. Angew. Math. Mech.* 88 (2008) 930-954.
- [13] Gailitis A et al.: Detection of a flow induced magnetic field eigenmode in the Riga dynamo facility, *Phys. Rev. Lett.* 84 (2000), 4365-4368.
- [14] Stieglitz R and Müller U: Experimental demonstration of an homogeneous two-scale dynamo, *Phys. Fluids* 13 (2001), 561-564.
- [15] Monchaux et al.: Generation of a magnetic field by dynamo action in a turbulent flow of liquid sodium, *Phys. Rev. Lett.* 98 (2007), 044502.
- [16] Giesecke A et al.: Role of soft-iron impellers on the mode selection in the von Kármán-sodium dynamo experiment, *Phys. Rev. Lett.* 104 (2010), 044503.
- [17] Nore C et al.: Nonlinear dynamo action in a precessing cylindrical container. *Phys. Rev. E* 84 (2011), 016317.
- [18] Léorat J: Large scales features of a flow driven by precession, *Magnetohydrodynamics* 42 (2006), 143-151.
- [19] Mouhali W: Etude d'un écoulement en précession. Transition vers la turbulence et application à l'effet dynamo, PhD Thesis, Université Paris-Diderot - Paris VII (2010)

Experimental Investigation of Flow Structure of a Density Current Encountering a Basal Obstacle

¹Ehsan Khavasi, ²Hamidreza Jamshidnia, ^{3,*}Bahar Firoozabadi and ⁴Hossein Afshin

¹ PhD student, ³Professor, ⁴Assistant Professor: School of Mechanical Engineering, Sharif University of Technology, Tehran, Iran, * Corresponding author (email: firoozabadi@sharif.edu)

² Visiting Assistant Professor, Department of Engineering and Science, Sharif University of Technology, International Kish Campus, Kish Island, Iran.

Due to the significance of density currents and with regards to the control of such important flows the flow structure of a density current encountering a basal obstacle in a rectangular channel is investigated experimentally by a 3D Acoustic Doppler Velocimeter. It was shown that the obstacle causes the distribution of turbulent kinetic energy of the flow to be changed significantly such that at its downstream the turbulent intensity profiles appears to have a non-uniform distribution over the height. Also it was shown that the turbulent kinetic energy has larger magnitude in downstream of the obstacle. In addition, in the presence of the obstacle, the variation of the local Froude number seems to be more significant over the channel length at its downstream which is compatible with the changes in turbulent kinetic energy. Moreover, it was quantitatively confirmed that in the absence of the obstacle, as the inlet Froude number increases from subcritical to the supercritical flow, the turbulent intensities along the channel seem to increase.

Keywords: Density current, flow structure, turbulent intensity, Froude Number, Obstacle, ADV.

1 INTRODUCTION

Many geophysical flows are classified as gravity or density currents, as they occur due to a density difference with the surrounding environment [1]. Density currents can be considered observed manifestations of interactions between an ambient flow and a horizontal buoyant intrusion [2] and are produced where gravity acts upon a density difference between two fluids. In the case of suspension currents such as turbidity currents, density excess is provided by suspended solid particles.

Density currents are of considerable importance from many perspectives as they play a major role in the transport of sediment on land, in lakes, seas and into the deep oceans [3] and thus their control is of significance. They pose various potential hazards such as submarine cable breakage, destroying sea-floor equipments etc. [4]. They also pose danger to submarines and therefore should be properly predicted to provide information on the safe navigation path for them.

Specifically, in an environmental context, turbidity currents are responsible for much of the sedimentation in reservoirs [5], with consequent loss of water storage capacity [6]. Therefore, turbidity currents also provide an important mechanism for transfer of sediments. One application of the control of such flows can be the ultimate goal of controlling or management of sedimentation in dams. There are some methods to control the density currents, amongst them using the standing barriers have been regarded as a way to control them. The dynamics of deposition in quasi-steady or steady

turbidity currents can be usually controlled by the topographic obstacles in the flow path [7]. It is noted that sea-floor topographies can also influence the pattern of sedimentation in ocean or sea floors [8].

With regards to the utilization of obstacles for density current control, some investigations have been performed in the literature. For example, Oehy and Schleiss [9] examined the placement of an obstacle before a reservoir to control the sedimentation in a reservoir. Their findings show that turbidity currents could be affected well by appropriately designed constructive measures. Kneller & Buckee [10] reviewed some studies on the structure and fluid mechanics of turbidity currents, saying that when sediment gravity flows face with the topography which is not completely flat, the topography influences deposition significantly.

Therefore, it is also important to reveal how such barriers affect the turbulent structure of the flow since the turbulent structure could influence the deposition behavior of turbidity currents (e.g. resuspend sediments) [11]. As this effect has not been explored very systematically, therefore, in this paper the effect of a triangular obstacle on the flow structure of a density current is experimentally investigated by using a 3D Acoustic-Doppler-Velocimeter (ADV) which is capable of measuring the instantaneous velocity at each point in space in three directions. The main focus will be the turbulent structure of the turbidity current and the effect of the inlet Froude number.

2 EXPERIMENTS

2.1 Experimental setup

All the experiments have been performed in a rectangular channel flume specially designed for the generation of density currents resulting from the release of turbid water on a sloping surface in a 12 m long, 0.2 m wide and 0.6 m high channel of fresh water with a glass side walls to provide visualization of the flow. The schematic view of the experimental set-up is shown in Fig. 1.

The channel is divided into two sections in the longitudinal direction using a separating Plexiglas sheet. The shorter upstream section accumulates dense fluid with a sluice gate in its rectangular bottom. The adjustable opening gate allows changing the inlet velocity of the particle-laden fluid which is prepared in the supply tank using a mixture of water and Kaolin particles ($d_{50}=18\mu\text{m}$) with density of 2650 kg/m^3 . The channel was previously filled with fresh water and its temperature was the same as the laboratory temperature. At the beginning of the tests, by removing the gate the particle-laden fluid is continuously fed into the accumulator through the gate and then it flows down the sloping bottom under the fresh water. The slope of the channel is kept constant at 1%. The sediment-laden density current gradually spreads under the fresh water.

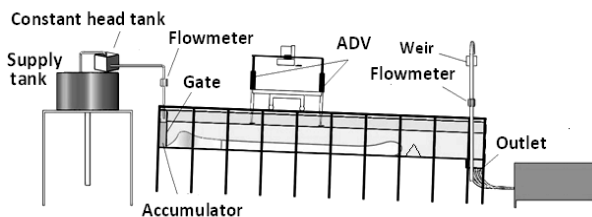


Figure 1: Schematic side view of the experimental setup

2.1 Experimental procedures

The velocities at each measurement point have been measured on the central longitudinal plane by a 3D ADV. This device is based on the principle of Doppler shift of a wave reflected from particles suspended in the fluid flow. Data can be available at an output rate of 25 Hz. The small sampling volume is located away from the sensor to undisturbed measurements resulting in accurate velocity measurements. Two down-looking probes of 10MHz-ADV have been utilized to measure the instantaneous velocities at various depths at several longitudinal sections along the channel.

Velocity profiles were measured at 5 sections along the channel located at $x = 3.5\text{m}$, 4.25m , 4.5m (obstacle position), 4.75m and 5.25m . x is the distance of from the inlet. Measurements started at the top part of the current and continued by dipping the probes until all the desired positions were covered. About 14 positions were considered to obtain the velocity profile at each station. The schematic view of the measuring sections is shown in Fig. 2.

First, the flow is measured for the case that there is no obstacle. In the next stages an isosceles triangular made of Plexiglas with the height of $S_o=6\text{ cm}$ is positioned at $x=4.5\text{m}$ as an obstacle. At each stage experiments were performed for three inlet conditions: ($F_{in}=1.55$, $F_{in}=1$, $F_{in}=0.6$).

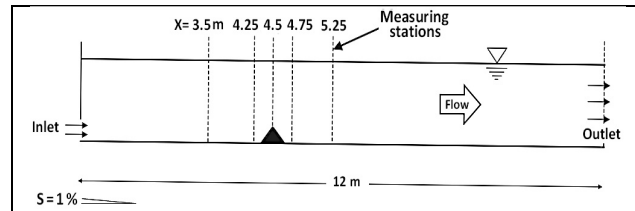


Figure 1: Schematic of measuring stations (numbers are in meter)

3 RESULTS AND DISCUSSION

3.1 General perspective of turbidity current facing with the obstacle

Turbidity current enters and flows through the channel and continues its path over implanted obstacle. While the head of the dense fluid faces the obstacle, it undergoes some changes in its shape. This phenomenon has been qualitatively shown in Figure 3-a, to 3-f which demonstrates some captured images of the sequences in a typical experiment. When the dense fluid passes over the obstacle (3-a to 3-e), it takes several minutes for the flow to reach the quasi-steady condition and the measurements start. Figure 3-f shows the quasi-steady condition for the mentioned experiment. Also in Fig. 4 a typical longitudinal velocity distribution has been show quantitatively.

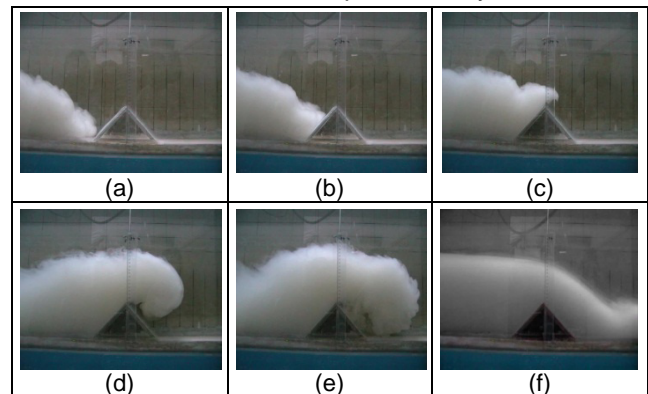


Figure 3: (a) to (e): Dense layer behavior passing over the obstacle, (f): The quasi-steady condition

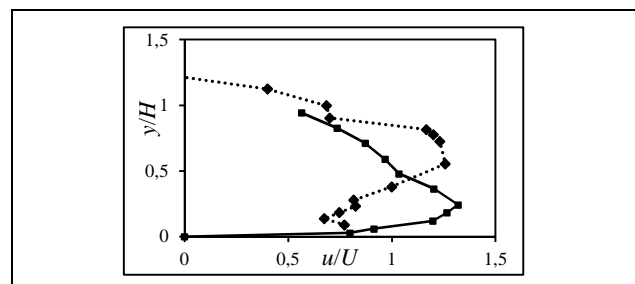


Figure 4: Longitudinal velocity profiles non-dimensionalized by layer-averaged velocity at a typical

station ($x = 4.75$ m from the inlet), when, $F_{in}=1.55$. Solid line (no-obstacle) and dashed line (obstacle) experiment.

3.2 Effect of obstacle on the turbulent structure

In order to investigate the effect of the obstacle on the turbulent structure of the flow, turbulent kinetic energy has been considered at measurement stations. Turbulent kinetic energy per unit mass denoted by k is defined as

$$k = \frac{1}{2}(\overline{u'^2} + \overline{v'^2} + \overline{w'^2}) \quad (1)$$

where u' , v' , w' are the fluctuations of the velocity components in streamwise, normal and lateral directions, respectively. These fluctuations were obtained by ADV. Detailed investigation of turbulent structures in turbidity current flow requires precise evaluation of the friction velocity, U^* . This parameter is the most fundamental velocity scale. In the present research, turbulent kinetic energies have been normalized with this velocity scale. As a result, the friction velocity can be computed as:

$$U^* = \sqrt{\frac{\tau_w}{\rho_m}} \quad (2)$$

τ_w is the wall shear stress and ρ_m is the mixture density.

Distribution of the turbulent kinetic energy at various stations for no obstacle experiments ($F_{in}=1.55$, $F_{in}=1$, $F_{in}=0.6$) have been calculated and shown in Fig. 5. In all the figures, heights are non-dimensionalized with the layer-averaged height (H) which is defined later. There are also dashed lines, these lines indicate the current height (the current height is chosen as a height of the dense layer where the velocity becomes $\frac{1}{4}$ maximum velocity or briefly $z_{1/4}$ (Firoozabadi *et al.* [12]) which is non-dimensionalized with the layer averaged height. As can be observed from the figure, in the absence of an obstacle the kinetic energy does not vary significantly throughout the channel, for each inlet Froude number; however, an increase in the value of the inlet Froude number raises the corresponding kinetic turbulent energy.

It is noticeable that as shown in Fig. 6 in the absence of any obstacle, the turbulent intensities along the channel seem to increase when the inlet Fr. number increases from subcritical to the supercritical value.

Implanting an obstacle causes the turbulence structure of the flow to change significantly. Fig. 7 shows the normal distribution of the turbulent kinetic energy for $F_{in}=1.55$, and for the case that a 6 cm-high obstacle has been installed. It is observed that at upstream of the obstacle the turbulent kinetic energy profiles are approximately the same as the no obstacle case with the same inlet condition. But, at downstream of the obstacle the turbulent kinetic energy seems to be about 2-3 times larger than its value at the upstream. This behavior could be as a

result of the circulations that occur in the density current when it is going downward the obstacle. This change is very similar to the change of the local Froude number of the current which is shown for both experiments in figure 4. It is noted that the local Froude number at each station is calculated as follows:

$$F_{loc} = \frac{U}{\sqrt{g'H}} \quad (3)$$

where $U = \int u(y)^2 dy / \int u(y) dy$ and $H = (\int u dy)^2 / \int u^2 dy$ [13] and $g' = g \Delta\rho / \rho_a$. Also,

$C = \int c(y)u(y)dy / \int u(y)dy$ and $\Delta\rho = \rho_m - \rho_a \approx C$ in which ρ_a is ambient fluid density. Here, $u(y)$ and $c(y)$ are velocity and concentration distribution in the streamwise direction at distance y above the channel's bed which are obtained by ADV.

This similarity is predictable as the (local) Froude number is (locally) the proportion of inertia force which in turn makes the current more unstable, to the buoyancy force which stabilizes it. In no obstacle flow, the changes in the local Froude number appear not to be so much but for the other experiments with the obstacle the variation of the local Froude number seems to be more significant over the height which is compatible with the changes in turbulent kinetic energy.

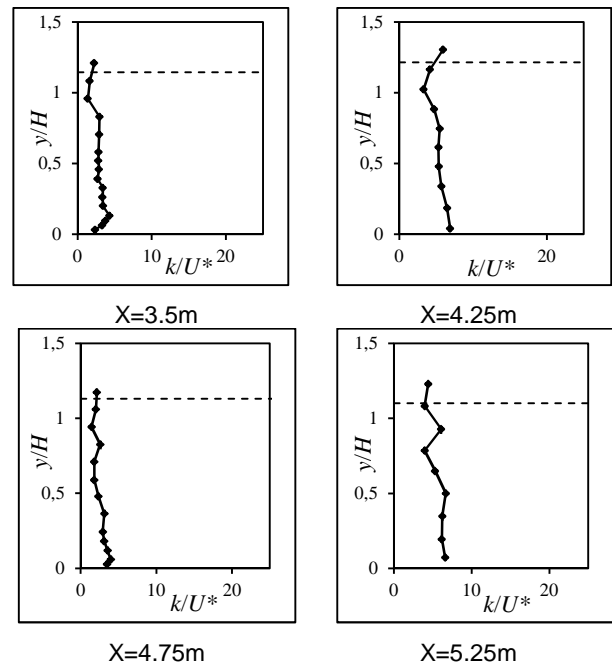


Figure 5: Typical profiles of the turbulent kinetic energy in normal direction for no-obstacle experiment for $F_{in}=1.55$. Dashed lines represent the currents height with respect to the layer averaged height.

In figure 8 the distribution of the local Fr Number in the absence and presence of the obstacle has been presented.

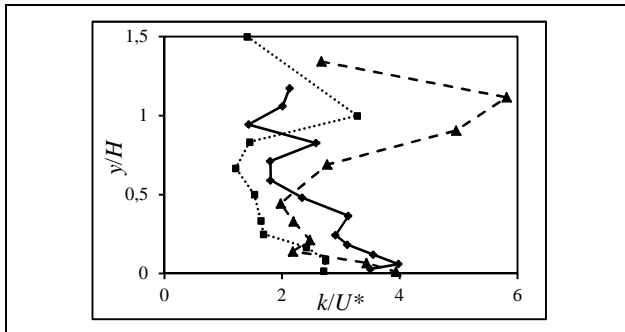


Figure 6: The comparison of the turbulent kinetic energy in normal direction for no-obstacle experiment: $F_{in} = 1.55$ (solid line with diamonds), $F_{in} = 1$ (dash line with triangles), $F_{in} = 0.6$ (dot line with circles) at a typical section ($x = 4.75$ m from the inlet)

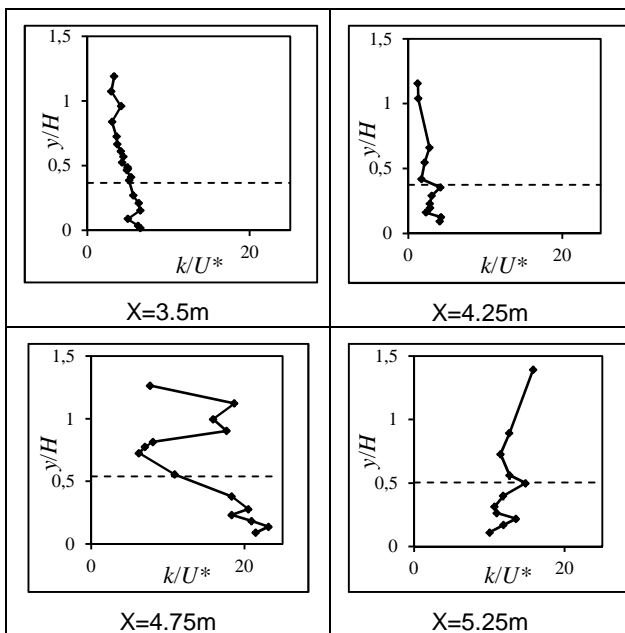


Figure 7: Typical profiles of the turbulent kinetic energy in normal direction for experiments with the obstacle: $F_{in} = 1.55$, dashed lines shows the obstacle height with respect to the layer-averaged height.

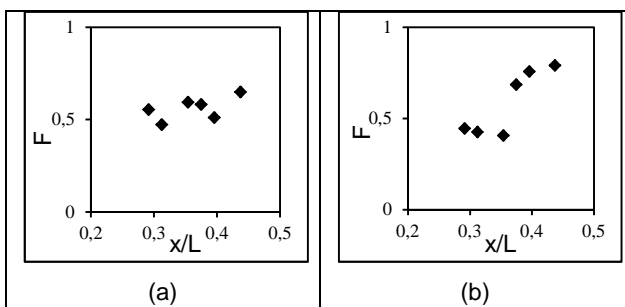


Figure 8: A typical distribution of the local Fr numbers over the channel length for (a) no-obstacle experiments: $F_{in} = 1.55$ and (b) with obstacle experiments: $F_{in} = 1.55$.

6 SUMMARY

The flow structure of a density current encountering a basal obstacle is investigated experimentally in a rectangular channel using a 3D ADV. Based on the obtained results of this investigation, the following conclusions can be made:

1. It was quantitatively confirmed that when there is no obstacle, the turbulent intensities along the channel seem to increase with the inlet Fr. number from sub-critical to the supercritical flow regime.
2. It was found that the obstacle causes the distribution of turbulent intensity profile to be changed. At the downstream of the obstacle the turbulent intensity profiles appears to have a non-uniform distribution over height. Also the turbulent kinetic energy seems to increase compared to its value at the upstream.
3. In the absence of any obstacle, the changes in the local Froude number of the flow appear not to be very considerable but in the presence of the obstacle the variation of the local Froude number seems to be more significant over the channel length at its downstream which is compatible with the changes in turbulent kinetic energy.

The result of this investigation could in turn be helpful in the prediction of the behavior of turbidity current facing with an obstacle.

REFERENCES

- [1] Simpson, J. E., (1987), Gravity currents in the environment and the laboratory, Ellis Harwood, Chi Chester, U.K.
- [2] Jirka G.H., Arita M., (1987), Density currents or density wedges: boundary-layer influence and control methods, *J. of Fluid Mechanics*, 177, pp. 187-206.
- [3] Middleton, G.V., (1993), Sediment deposition from turbidity currents, *Journal of Annu. Rev. Earth Planet. Sci.* 21, pp. 89–114.
- [4] Kneller B., Buckee C., (2000), The structure and fluid mechanics of turbidity currents: a review of some recent studies and their geological implications, *Journal of Sedimentology*, 47, pp. 62-94.
- [5] De Cesare G., Schleiss A., Hermann F., (2001), Impact of turbidity currents on reservoir sedimentation, *Journal of Hydraulic Eng.*, 127, pp. 6–16.
- [6] Meiburg E. and Kneller B, (2010), Turbidity Currents and Their Deposits, *Annu. Rev. Fluid Mech.*, 42, pp. 135–56.
- [7] Bursik, M., I., Woods, A., W., The effects of topography on sedimentation from particle-laden turbulent density currents” *Journal of Sedimentary Research*, 70, No. 1 (2000) 53-63.
- [8] Alexander, J., Morris, S., Observation on experimental, nonchannelized, high-concentration turbidity currents and variations in deposits around obstacles, *Journal of Sedimentary Research*, A64, No. 4 (1994) 899-909.
- [9] Oehy, C., Schleiss, A., Control of turbidity currents in reservoirs by solid and permeable obstacles *Journal of Hydraulic Engineering ASCE*, 133, No. 6 (2007) 637-659.
- [10] Kneller, B.C., Buckee, C., The structure and mechanics of turbidity currents: a review of some recent studies and their geological implications”; *Int'l Association of Sedimentologists, Sedimentology*, 47, No. 1 (2000) 62-94.
- [11] Toniolo H., Lamb M., Parker G., (2006), Depositional turbidity currents in diapiric minibasins on the continental slope: formulation and theory, *Journal of Sedimentary research*, 76, pp. 783-797.
- [12] Firoozabadi, B., Afshin, H., Sheikhi, J., (2009). Experimental Investigation of Single Value Variables of Three-dimensional Density Current. *Canadian Journal of Physics*, 87, 125-134.
- [13] Ellison, T.H., Turner, J.S., (1959), Turbulent entrainment in stratified flows. *Journal of Fluid Mech.* 6(3), 423–448.

UVP measurement of low speed natural convection in the internally heating rectangular cavity

Tatsuya Kawaguchi

Department of Mechanical and Control Engineering, Tokyo Institute of Technology.

Addresses: Ookayama 2-12-1 Meguro Tokyo, Japan

Rayleigh-Bénard convection is one of the fundamental and significant flows of the chaotic and transitional fluid phenomena. The objective of the present study is to analyze a natural convection in a square cavity with Joule heating. Also the ultrasound velocity profiler (UVP) for the lower velocity fields was developed that enabled to measure the velocity below 1 mm/s. Cross correlation method in conjunction with an appropriate function fitting was employed to determine the local velocity. Temperature of the top of the cavity was fixed by the electrically insulated copper plate. The other five surfaces were adiabatic thermal boundary condition. A pair of opposed horizontal carbon plates was used as the electrode. The mixture of tap water and glycerol was used as a working fluid, LiCl was added as an electrolyte. Maximum Rayleigh number with internal heating was $Ri=2.2 \times 10^{10}$. Velocity magnitude in the vicinity of the cooled surface was less than 10 mm/s, the disordered detachment of the thin thermal boundary layer was observed.

Keywords: natural convection, internal heating, cavity flow, cross correlation, cosine fitting.

1 INTRODUCTION

Natural convection with internal heat source is the flow due to the temperature difference within the enclosure. In many applications, the possible energy source of the internal heating is electric current for Joule heating, absorption of electromagnetic wave and such molecular or atomic reactions as chemical reactions and nucleorrhexis. For example, a mantle convection is one of the applications of the natural convection with internal heating^[1]. Glass injection molding manufacturing as well as the vitrification of high-level radioactive waste is another industrial application of natural convection of molten glass with internal heat source. The numerical prediction and relevant experiments of the physics of a natural convection in a cavity has been investigated by many groups. Liaquat and Baytas^[2] have numerically investigated the heat transfer characteristics of internally heated liquid in a cavity at high Rayleigh numbers from 10^7 to 10^{12} . They concluded that the flow pattern with lower Rayleigh number showed periodic oscillation whereas the higher Rayleigh number caused non-periodic time-dependent behavior. Since the instability of the flow field is essentially present and the considerable range of Rayleigh number is widely varied, the verification of each numerical model is complicated without the detailed and precise experimental data. Natural convection could be scaled by Grashof number, Prandtl number and Damköhler numbers in the presence of the internal heat source.

$$Ri = Pr \cdot Gr \cdot Da = \frac{g\beta q L^5}{k\nu\alpha} \quad (1)$$

Characteristic length, L , is equal to the size of the channel. q is calculated from the input energy

density per unit volume. g represents gravitational acceleration. β , ν , α , and k are the thermal expansion coefficient, kinematic viscosity, thermal diffusivity and thermal conductivity of liquid respectively. The dimensionless parameter contains the intensity of the volumetric heating instead of a temperature difference between horizontal Dirichlet boundaries. Since the parameter increases directly with the fifth power of the characteristic length, the growth of the cavity size significantly affects the internal fluid behavior of cavity. The objective of the present study is to analyze a natural convection in a rectangular cavity with Joule heating by means of ultrasound velocity profiler. Moreover the improvement of the ultrasound velocity profiler was introduced for the sake of the measurement of the lower magnitude of velocity.

2 EXPERIENTS AND RESULTS

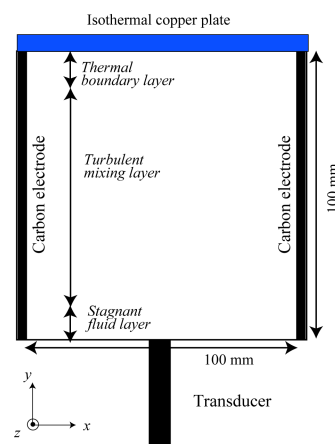


Figure 1. Simplified illustration of the experimental rig.

Figure 1 illustrates the simplified set up of the ultrasound measurement that consisted of a square transparent acrylic open channel with a pair of carbon plates as electrode, and a copper plate as a constant temperature ceiling. The size of the cubic cavity was 100 mm on a side, which is equal to L in equation (1). Copper plate with internal water channel was mounted on the top of cavity. The channel was connected to the heat exchanger with an automatic temperature control system. The temperature fluctuation of the plate was less than 0.1 K during the following experiments. The other five surfaces were assumed to be adiabatic by which the heat fluxes through the surfaces were equal to zero. The alternating current was applied for the energy source of the Joule heating. The frequency of the alternating current was 50 Hz due to the commercial electric supply. As the electric conductivity of the carbon graphite is 10^6 S/m that is sufficiently larger than that of the working fluid, the electric potential in the carbon electrode was assumed to be constant. The 50 % mixture of glycerol and ion-exchanged water was used as a working fluid and LiCl was added as an electrolyte. The copper plate surface was protected by the insulating coating in order to avoid the undesired potential distribution in the test section. Sound speed of the glycerol and water mixture was $c=1700 \text{ m/s}$ that is assumed to be independent of the temperature of liquid. The arithmetic mean diameter of tracer particle was 0.1 mm. Relation between LiCl concentration and electric conductivity was calibrated in advance. Electric conductivity of working fluid was set to 0.2 S/m, mean electric current was 1.5 A. Consequently the density of internal heating by electric current was 135 kW/m^3 assuming that the electrical energy supply per unit volume was spatially homogeneous. Temperature of liquid was measured by the electrically-insulated thermocouples. Rayleigh number was 2.2×10^{10} . The resultant difference of local temperature between top and bottom of cavity was 40°C .

For the velocity profile measurement, cross correlational ultrasound velocity profiler method^[3,4] was used to obtain the fluid behavior of the natural convection. Conventional pulse Doppler ultrasound velocity profiler was also used. Velocity resolution of the latter system is 0.7 mm/s under the standard configuration that is not sufficient for the measurement of the natural convection with higher viscosity of liquid. Therefore the advanced cross correlation method was proposed that was explained in the following sentence. The frequency of the ultrasound was 4 MHz. For the echo signal monitoring, LeCroy 9360 storage oscilloscope was used. Simultaneously the PCI-bus connected high-speed 100 MHz analog to digital(A/D) convertor with on-board fast RAM was employed by which the triggered echo signal could be directly stored into the memory in computer. The captured consecutive

echo signal was analyzed by the cross correlational technique. In the previous study^[4], the aim of the development was the improvement of the temporal resolution. In contrast to the former study, the present contribution would focus on the extension for the low-speed measurement of the ultrasound technique. The present signal processing technique employed the appropriate infinite impulse filter as well as the new fitting function for the accurate determination of the sub-pixel displacement of sinusoidal waves.

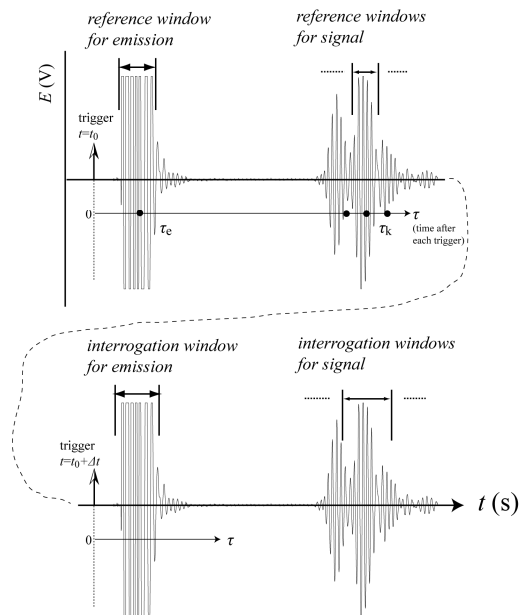


Figure 2. Definition of the post-trigger temporal axis, τ , and windowing scheme for the velocity distribution measurement by cross correlation technique. Not only the displacement of the reflected echo but also the fluctuation of the emission wave were considered between consecutive echo signals.

Figure 2 illustrates the example of the captured two successive echo signals. The definition of two temporal axes, t and τ , and the windowing position for the cross correlation technique was depicted. Each echo signal was consisted of the primary emission signal which is followed by the modulated sinusoidal echo. Since the input range of the analog to digital convertor was usually optimized for the echo signal that was extremely inferior to the emission signal, the emission signal was the rectangular shape due to the saturation of the converter. The DFT based coarse pre-processing followed by the fine direct cross correlation computation was performed. By the cross correlational UVP method, local velocity was determined by the displacement of the echo as $u = c \Delta\tau / 2 \Delta t$. Therefore the calculation accuracy of $\Delta\tau$ directly affects the determination of velocity. The sizes of reference and interrogation windows for the real-domain correlational computation were 100 and

110 respectively. If the velocity magnitude of the fluid flow is sufficiently larger, the displacement of the local echo signal is several pixels, and the measurement error due to the sub-pixel interpolation is negligible. However the fluid investigation with very low velocity magnitude, the amount of the displacement is less than a pixel and the determination of the sub-pixel displacement is significantly important.

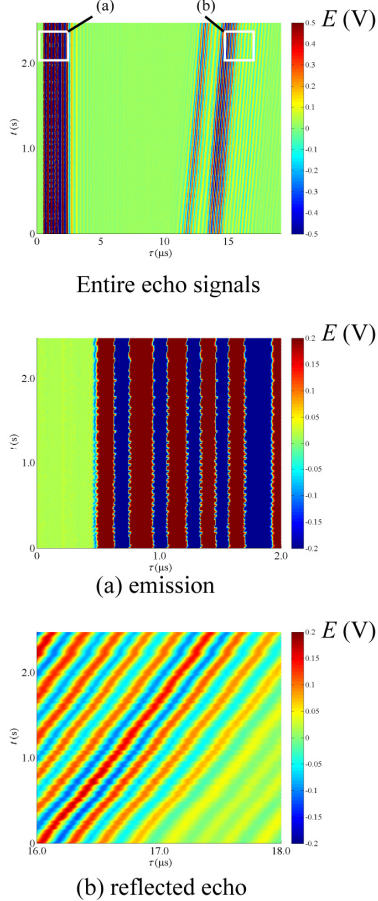


Figure 3. The example of the captured intensity of the entire echo signals from the moving solid wall with constant velocity during 2.5 sec. The denotations (a) and (b) represent the magnified area of emission signal and reflected signal from the moving solid wall respectively.

Figure 3 depicts the acquired electrical voltage that is equivalent to the intensity of the received ultrasound. The horizontal axis is equal to the actual temporal domain, τ , of the digitizer. On the other hand, the vertical axis, t , corresponds the triggering intervals of the ultrasound emission, which is equivalent to the sampling frequency of the velocity profile measurement. This two-dimensional echo plot contains the entire information of the velocity profile along the measurement line. The denotation (a) and (b) in figure 3 shows the detailed echo signals of the emission region and of the reflected echo from the fluid flow respectively. Since the start trigger of the A/D converter was electrically

synchronized with the emission circuit of the ultrasound, the waveforms of the captured emission signal were quite similar and their phases were nearly fixed. However, the cycle-by-cycle instability of the emission signal is still remained that causes the bias error of the velocity profile. Although the noise reduction was partially considered as "emission trigger" in the previous study^[4], the actual effect of the removal was not clarified. In order to determine the displacement of the reflected sinusoids accurately, the jitter noise was firstly estimated by the cross correlation methods with a triangular wave interpolation that is equivalent to the auto correlation function of the emission signal.

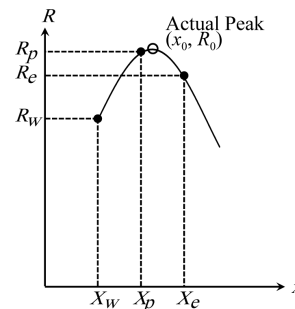


Figure 4. Sub-pixel estimation of the actual maximum of the cross correlation function by means of a function fitting.

The second improvement of the study is to employ the cosine function instead of the Gaussian curve for the sub-pixel interpolation. Figure 4 shows the fundamental scheme of the function fitting for the cross correlation coefficients. From the sampled echo signals by A/D converter, only the discrete correlation coefficients, R , are calculated. By using the neighboring three correlation coefficients, the actual peak location of function, x_0 could be determined by a function fitting. The cross correlation function of cosine waves must be cosine wave as well, not a Gaussian function but a cosine function is appropriate as follows.

$$x_0 = X_p - \tan^{-1} \left(\frac{R_w - R_e}{2R_p \sin(\omega)} \right) / \omega, \omega = \cos^{-1} \left(\frac{R_w + R_e}{2R_p} \right) \quad (2)$$

Since the fitting method could be applied with the arbitrarily-chosen three points to determine the peak location of correlation function, the least square value of the x_0 was calculated from the various combinations of the successive three coefficients. The multi-point peak estimation enabled to determine the precise peak location of cross correlation function and to determine the local velocity of fluid flow accurately as well.

As a preliminary experiment, the developed system was verified by the measurement of moving solid wall running at fixed low speed. Figure 5 compared

the probability density distribution of measured 2000 velocity data. Relative velocity, U_{ref} , between transducer and solid wall as a reflector was varied, the emission interval of ultrasound, Δt , was considered as the parameter. When the velocity is equal to zero, the mean velocity was almost zero. The variation was, however, significantly affected by the change of Δt . With the smaller Δt , the value of Δr is also small, therefore the relative error of the velocity determination was increased. The result showed that if the sampling interval of velocity profile is 100 ms, the standard deviation of velocity was 0.05 mm/s in the present configuration.

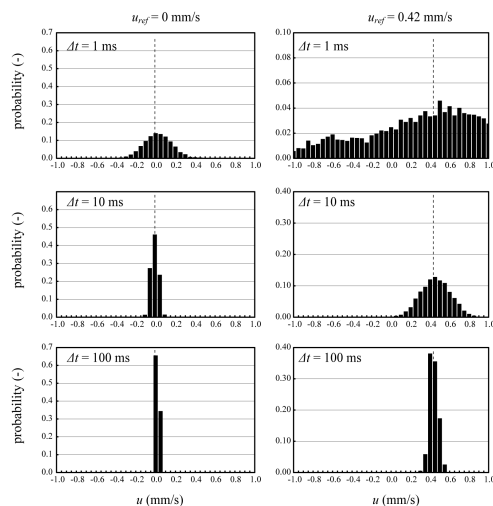


Figure 5. Comparison of the probability density functions of the measured velocity in terms of the frequency of the ultrasound emission. Dashed lines are the reference velocity of transducer at 0mm/s and 0.42 mm/s.

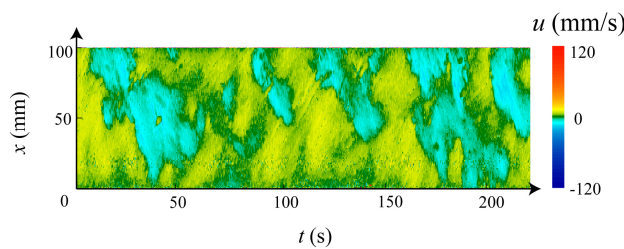


Figure 6. Velocity transition at the center vertical axis of the cavity during 220 sec by pulse Doppler technique. The upward and downward flows were alternately appeared. Cooled ceiling is located at $x=100$ mm.

The spatio-temporal velocity profile at the central vertical axis of the cavity was depicted in figure 6. The profile was obtained by the pulse Doppler method. The duration of the profile was 220 sec, sampling frequency of the velocity was 15 Hz approximately. The profile shows that the downward plume due to the detachment of the thermal boundary layer in the vicinity of the cooled surface was periodically occurred. However, no explicit cycle appeared in the term. Moreover the absolute

value of velocity was quite small and it was difficult to analyze the detailed fluctuation of local velocity.

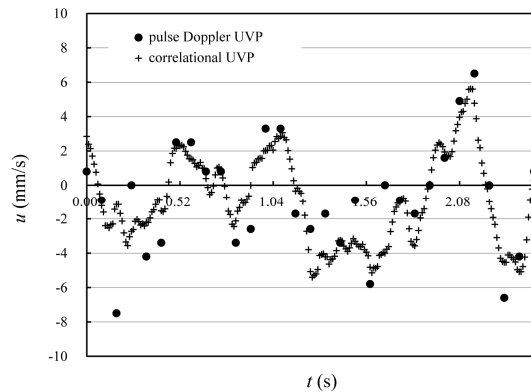


Figure 7. Comparison of measured velocity profile in the vicinity of the cooled surface at $x=95$ mm. Both conventional pulse-Doppler UVP system and present correlational techniques were compared. Resolution of the velocity was 1 mm/s by the pulse Doppler UVP, whereas that of the correlational technique was 0.05 mm/s.

Figure 7 compare the velocity profile obtained by the pulse Doppler method and by the advanced correlational techniques. Velocity profiles at $x=95$ mm were depicted. By the present measurement technique, not only the sampling frequency but also the velocity resolution was drastically improved and the detailed structure of the velocity fluctuation was obtained.

CONCLUSION

Natural convection in a square cavity with internal Joule heating was experimentally investigated by means of the advanced ultrasound velocity profiler. The flow field with the vertical temperature gradient due to the homogeneous internal heating and a low temperature ceiling is essentially unstable. The instability of the thermal boundary layer induces the characteristic downward flow in a cavity and the turbulent mixing around the the center of cavity was significantly affected by the convective behavior of fluid. By the present technique, the standard deviation of the velocity measurement was 0.05 mm/s.

REFERENCES

- [1] Turcotte D L and Schubert G: Geodynamics 2nd edition, Cambridge Univ. Press (2001)
- [2] Liaqat A and Baytas A C: Heat transfer characteristics of internally heated liquid pools at high Rayleigh numbers, Heat and Mass transfer, 36 (2000), 401-405.
- [3] William D B et al.: A New Time Domain Technique for Velocity Measurements Using Doppler Ultrasound, IEEE Trans. Biomedical Engng., BME-32, 3 (1985), 213-229.
- [4] Ozaki Y et al.: High time resolution ultrasonic velocity profiler, Experimental Thermal and Fluid Science, 26 (2002), 253-258.

Improvement of the acoustical characterization of suspended particles in wastewater

Philippe SCHMITT¹, Anne PALLARES¹, Marie-Noëlle PONS²

¹Institut de Mécanique des Fluides et des Solides, Université de Strasbourg,

2, rue Boussingault, F-67000 Strasbourg, France

²Laboratoire Réactions et Génie des Procédés - CNRS, UP3349, Université de Lorraine, INPL

1, rue Grandville, BP 20451, F-54001 Nancy cedex, France

The interpretation of acoustic measurements in wastewater has to come up against the huge variety of encountered particles. Previous work showed that a good representative of the organic fraction is potato starch. Thus, this work focuses on the acoustical characterization of potato starch in order to evaluate acoustically its concentration and particle size distribution. The theoretical aspects and a methodology for the determination of the averaged form function $\langle f \rangle$ and the normalized total scattering cross section χ_m are given for potato starch suspension. The final aim of this work is an identification method of the particle size distribution in wastewater.

Keywords: Acoustic, suspended particles, scattering

1 INTRODUCTION

Over the past two decades the understanding of small scale sediment transport processes has strongly increased with the use of acoustic instrumentation. This technology was first used by the sedimentological community because of its potential to measure non-intrusively, with high temporal and spatial resolution, the velocity, size and concentration profiles of sediments over the seabed [1]. It also allows the mapping of the bedform morphology. Indeed, the use of multi-frequency Acoustic Backscattering Systems (ABS) allows the measurement of particle size and concentration over sandy beds. These systems typically operate at frequencies in the range 0.5 – 5MHz, which fits with the sand particles diameter, and in transceiver mode, which permits the measurement of the backscattering and attenuation characteristics of the suspended sediments.

Our application, urban wastewater, is a complex medium mixing mineral and organic elements with variable characteristics. Within the common particles found in wastewater, only the sands have been exhaustively studied by acoustics. A recent study [2] showed that the percentage of organic matter varies with the type of wastewater and can reach routinely 50%. Preliminary work on various materials like paper pulp, loess, garden earth, soups and excrements was already carried out. It showed that none of these materials has an identical behavior to sand.

Some aspects of our previous work [3] focused on the suspended solids standard characterization. After the evaluation of the composition of standard wastewaters in terms of total suspended solids (TSS), amount and nature, we tried to define stable representative compounds of wastewater. Different kind of starches were studied (corn, wheat, rice,

potato), to represent the organic fraction in wastewater. Potato starch was found to be a good candidate.

The aim of the present work focuses on the acoustical characterization of potato starch in order to evaluate its concentration and particle size distribution. The general principle of the method will be presented, as well as some measurement results. The goal of this approach is to develop an identification methodology in order to establish a suspended particle size distribution in an unknown fluid mixture.

2 BACKGROUND SCATTERING THEORY

2.1 Incoherent backscattering

In a medium insonified by a piston transceiver, if we assume that the attenuation over a bin range is not substantial [4] and that the phase of the backscattered signal from the suspended particles is randomly distributed between 0 and 2π , then the recorded root-mean-square backscattered voltage can be written [1] at a range r as follows:

$$V_{rms} = \frac{k_s k_t}{r \psi} M^{1/2} e^{-2\alpha r} \quad (1)$$

with

$$k_t = RT_v P_0 r_0 \left\{ \frac{3\pi}{16} \right\}^{1/2} \frac{0,96}{ka_t} \quad (2)$$

$$k_s = \frac{\langle f \rangle}{(\rho_s \langle a_s \rangle)^{1/2}} \quad (3)$$

$$\alpha = \alpha_w + \alpha_s = \alpha_w + \frac{3}{4\rho_s r} \int_0^r \frac{\chi_m}{\langle a_s \rangle} M(r') dr' \quad (4)$$

V_{rms} is an average over a number of backscattered

returns. An individual backscattered signal is Rayleigh distributed.

k_t is an acquisition system constant for a given setting. P_0 is the reference pressure, normally defined at $r_0=1m$, R is the receiver sensitivity, T_v is the voltage transfer function of the system, τ is the pulse duration, c is the velocity of sound in water, k is the wavenumber for sound in water ($k=2\pi/\lambda$, λ is the wavelength of sound in water), and a_t is the radius of the transducer.

k_s represents the sediment backscattered properties, with $\langle f \rangle$ the averaged form function which describes the backscattering characteristics of the particles, ρ_s the sediment density, $\langle a_s \rangle$ the mean particle radius.

ψ stands for the near field correction, M is the sediment concentration, α_w is attenuation due to the water absorption and α_s is the sediment attenuation mainly due to scattering for noncohesive particles insonified at megahertz frequencies ultrasound.

As shown, α_s is related to the normalized total scattering cross-section χ_m .

2.2 Form function and scattering cross-section

The averaged form function $\langle f \rangle$ and the normalized total scattering cross-section χ_m characterize the behavior of an insonified particle in a fluid. The form function is used to describe the intrinsic scattering properties of an element. The normalized scattering cross-section is related to the sound attenuating properties of particles in a suspension [5].

The behavior of these two functions are well-described by the variable $x = k\langle a_s \rangle$, which is the ratio between the particle circumference and the wavelength of the sound in water. There are no general solutions for the scattering behavior of irregularly shaped particles, but some estimates can be made for the asymptotes.

For $x \ll 1$, the so-called Rayleigh regime, the wavelength of sound is much greater than the particle circumference and thus the scattering is considered to be independent of the particle shape. Thereby, the Rayleigh scattering for a sphere can be kept and this implies that $\langle f \rangle \propto x^2$ and $\chi_m \propto x^4$. For $x \gg 1$, the geometric regime, the wavelength of sound is smaller than the particle circumference, and the scattering cross-section is directly related to the particle's geometry. In this case, for a rigid sphere, $\langle f \rangle$ and χ_m tend to a constant value of unity. For irregularly shaped particles $\langle f \rangle$ and χ_m will tend to a constant value slightly greater than unity.

2.3 Analysis in homogenous solutions

Eq.(1) can be rewritten under its logarithmic form:

$$\ln(V_{rms} r \psi) = \ln \left(k_t \langle f \rangle \sqrt{\frac{M}{\rho_s \langle a_s \rangle}} \right) - 2r \left(\alpha_w + \frac{3\chi_m M}{4\rho_s \langle a_s \rangle} \right) \quad (5)$$

For a homogeneous suspension (for which the concentration won't vary with the range), this becomes a linear equation in $\ln(Vr\psi)$ and r , and we obtain:

$$\eta = \ln \left(k_t \langle f \rangle \sqrt{\frac{M}{\rho_s \langle a_s \rangle}} \right) \quad (6a)$$

$$\kappa = 2(\alpha_w + \alpha_s) = 2 \left(\alpha_w + \frac{3\chi_m M}{4\rho_s \langle a_s \rangle} \right) \quad (6b)$$

where η and κ are respectively the intercept and the slope obtained from the measurements as expressed in Eq.(5). This allows the characterization of the behavior of an insonified particle by specifying its form function $\langle f \rangle$ and its normalized total scattering cross-section χ_m .

3 PARTICLE CHARACTERISTICS

The present study focuses on the acoustical characterization of potato starch in order to evaluate its concentration and particle size distribution. Concerning its density, the literature on the subject seems quite concordant and gives a density of potato starch ranging from 1.53 to 1.552.

A density measurement of the used potato starch (S4251, Sigma-Aldrich) was also performed and gave a coherent result:

$$\rho = \frac{m}{V} = 1,470 \pm 0,087 \text{ g / ml} = 1470 \text{ kg / m}^3$$

The dimension and the shape of the potato starch has been studied optically (figure 1). Its size distribution was also determined using a Malvern Mastersizer 2000 (figure 2).

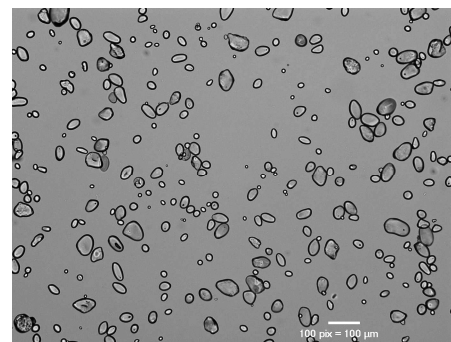


Figure 1: Optical microscopy view of potato starch

One can see that potato starch has wide spread shapes and sizes. However the mean observed size is around 50 μm with particle size ranging from 24 to 80 μm . Knowing that the particle sizes of less than a few microns are invisible at the used ultrasonic frequencies, we can assimilate these samples of potato starch to a unimodal distribution with a mean value of $\langle a_s \rangle \sim 24 \mu\text{m}$.

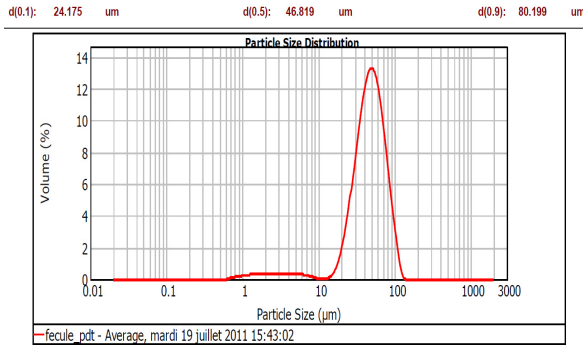


Figure 2: Laser diffraction potato starch size distribution

4 MEASUREMENTS AND ANALYSIS

4.1 Measurement bench

All measurements on potato starch were performed at room temperature in a 50 L water tank (figure 3). The suspension of the starch was obtained by continuous stirring with a propeller whose frequency was adjusted to insure homogeneous slurry.



Figure 3: Water tank and instrumentation

The measurements were performed with an UB-Lab system and several stand-alone transducers allowing measurements at different frequencies growing from 600kHz up to 7,5MHz. Care was taken on the pulse repetition frequency adjustment in order to allow the sound from one emission/reception cycle to dissipate before the following cycle. A temperature sensor completes the test-bench in order to compensate temperature effects.

4.2 Potato behavior

For all the measurements, a common procedure was applied. The tank was filled with water from the main supply, and the propeller was activated during a period of several hours in order to allow the air bubbles to leave the water. This procedure was monitored and lasted until the signals recorded by the instrument reduced to background levels. Water-saturated potato starch was then added at a concentration of 1,3g/l and, after homogenization of the suspension, a run of five hundred profiles was realized, each one composed of two hundred samples. This procedure was applied for every used ultrasound frequency utilized. An example of the raw data collected by the instrument is presented in figure 4.

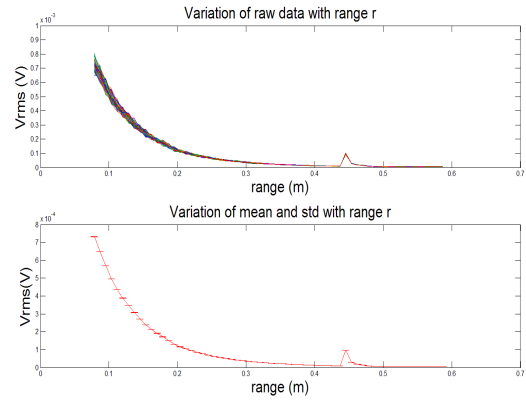


Figure 4: Raw data, mean and standard deviation on measurements on potato starch

The peak at ~45 cm corresponds to the inner wall of the tank.

4.3 Scattering cross-section extrapolation

The UB-Lab instrument was used to carry out the measurements at different frequencies. To obtain the information about the form function and the total scattering cross section, the expressions in Eqs. (6a&b) were used. Figure 5 shows an example of analyzed data, it shows the variation of $\ln(Vr_{ij})$ as a function of the range r from the transducer. Note that the analyzed data correspond to a measurement zone situated between the end of near field and the echoes of the inner wall of the tank.

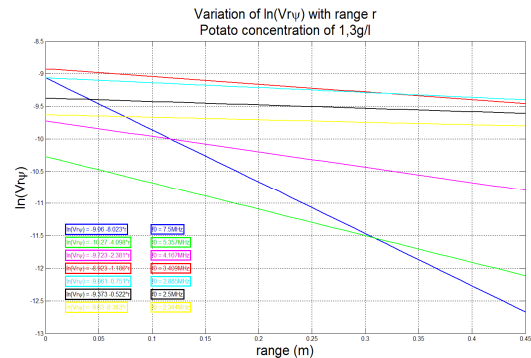


Figure 5: Graphical display of Eq. (5) for several frequencies generated by the UB-Lab

One can see in Eq.(6b) that the attenuation is directly and exclusively related on the suspension characteristics. The water attenuation reliance on temperature and ultrasound frequency is well-known [6]. Considering that the potato starch density, its mean size and its concentration are well-known in our tank, we can evaluate the normalized total scattering cross-section χ_m at different ultrasound frequencies. Tab. 1 shows the normalized total scattering cross-section χ_m obtained from the measurements as a function of the variable $x = k <a_s>$. The frequencies available on the UB-Lab allow only measurements in the Rayleigh regime and in a part of the intermediate regime for the potato starch. It should be noted that for small

values of x , nominally $x \ll 1$, the value for χ_m might have a high degree of uncertainty because in this case $\kappa \approx 2\alpha_w$. Nevertheless, several measurements were done on frequencies between 3,125MHz and 7,5MHz and show a small dispersion of 2 to 4 %.

Table 1: Normalized total scattering cross-section χ_m and variable $x = k\langle a_s \rangle$ as a function of the UB-Lab ultrasound frequencies.

Frequency (MHz)	$k\langle a_s \rangle$	χ_m
7,5	0,764	0,0993
5,357	0,545	0,0506
4,167	0,424	0,0291
3,409	0,347	0,01179
3,125	0,318	0,008795
2,885	0,294	0,006842
2,500	0,255	0,004321
2,344	0,239	0,002369

Figure 6 show a fit of the points of χ_m from Tab. 1.

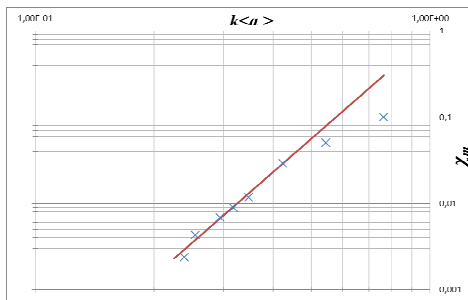


Figure 6: Graphical display of χ_m versus $k\langle a_s \rangle$ in the Rayleigh regime

The data show a constant increase in magnitude of χ_m with x , as expected. The fit allows the extraction of the dependence of χ_m with x and gives:

$$\chi_m = 0,85(k\langle a_s \rangle)^4 \quad (7)$$

This result shows that for $x \ll 1$, the Rayleigh regime, the measurements are in close agreement with the theoretical description, which predict reliance in $(k\langle a_s \rangle)^4$. The slope coefficient is higher than the one of the sand, which is close to 0,26. A reason can be that for a given concentration, the density and the radius of potato starch particles are smaller than for sand, and imply that there are much more particles. Currently, the evaluation of the form function is not possible because this needs a complete system calibration for every used frequency. However this work is on the run.

4.4 Concentration measurements

In order to evaluate the possibility of measuring particle concentrations with the UB-Lab instrument in this configuration, several experiences were carried out with various starch concentrations. Figure 7 shows the analyzed data which allows the

estimation of χ_m for every concentration. A difference of less than 2% was notice between the measured and expected values.

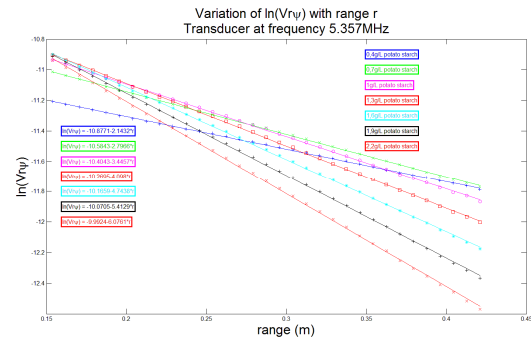


Figure 7: Analyzed data's of ultrasound measurements for different starch concentrations.

6 SUMMARY

The present study focused on the examination of the scattering properties of suspension of potato starch. It is a part of a larger work which includes the evaluation of $\langle f \rangle$ and χ_m in both Rayleigh and geometric regimes, and this for different test particles. This can then allow the possibility to classify suspensions in particle sizes by classes by the use of several different ultrasound frequencies.

Nevertheless, the current state of our work allows the measurement of the particle size or concentration. If one of these two parameters and density is known, this method can even bring knowledge on the concentration gradient in an unhomogeneous suspensions.

7 ACKNOWLEDGEMENT

This work was partly supported by GEMCEA, Groupement pour l'Evaluation des Mesures en Continu dans les Eaux et en Assainissement, France.

REFERENCES

- [1] Thorne P.D., Hanes D.M.: A review of acoustic measurement of small-scale sediment processes, Cont. Shelf Res. 22 (2002), 603-632.
- [2] Sophonsiri C., Morgenroth E.: Chemical composition associated with different particle size fractions in municipal, industrial, & agricultural wastewaters, Chemosphere 55 (2004), 691.
- [3] Schmitt P. et al.: Suspended particles in wastewater: acoustical characterization and modeling, ISUD7 Proceedings (2010), 43-46.
- [4] Hay A.E.: Sound scattering from a particle-laden, turbulent jet, J. Acoust. Soc. Am. 90 (1991), 2055-2074.
- [5] Thorne P.D., Meral R.: Formulations for the scattering properties of suspended sandy sediments for use in the application of acoustics to sediment transport processes, Cont. Shelf Res. 28 (2008), 309-317.
- [6] Admiraal D.M., Garcia M.H.: Laboratory measurement of suspended sediment concentration using an Acoustic Concentration Profiler (ACP), Experiments in Fluids 28 (2000), 116-127.

Sound velocity measurements in fluids using echo signals from scattering particles

Michael Lenz¹, Martin Bock¹, Elfgard Kühnicke¹, Josef Pal² and Andreas Cramer²

¹ Technische Universität Dresden, Institut für Festkörperelektronik, Helmholtzstraße 18, D-01062 Dresden, michael.lenz@tu-dresden.de

² Helmholtz-Zentrum Dresden-Rossendorf, Bautzner Landstraße 400, D-01328 Dresden, Germany, a.cramer@hzdr.de

A novel approach for measuring the speed of sound in fluids with scattering particles is presented. Potential fields of application for sound velocity measurements in fluids are process control, environmental measurement technology and medicine, where sound velocity can be used as an indicator of temperature, concentration or mass density. Similar to the pulsed Doppler application, the method also works non-invasively and uses the echo signals from scattering particles suspended in the fluid. The basic idea is that the ultrasonic time of flight to the focus position z depends on the speed of sound c in a well-defined way. The time of flight to the focus can be extracted from the echo signals, because the stray echo is strongest for the scattering particles being located in the sound focus and can thus be used to determine the speed of sound. Results are shown for different homogeneous fluids with sound velocities between 1116 m/s (ethanol, 50°C) and 2740 m/s (eutectic GalSn). Measurements have shown that a statistical measurement uncertainty of about 0,1% was achieved with the underlying set-up. Further results of recent measurements in water having a temperature gradient show that the method is even capable of measuring the sound velocity with local resolution.

Keywords: speed of sound, material characterisation, scattering particles, annular array

1 INTRODUCTION

Ultrasonic measurements are widely used for flow measurements in scientific and industrial applications. Their advantages primarily lie in measurements in opaque fluids, where optical methods such as PIV cannot be applied.

A large number of ultrasonic measurements are based on the Doppler method, which analyses the stray echoes originating from scattering particles suspended in the fluid. While the current method is comparable to Doppler methods in that it uses the same echo signals, it is, however, not intended to measuring mass transport, but rather the speed of sound. By that way, it enables access to an additional measuring variable that is otherwise measurable solely with invasive methods such as bringing reflectors of known position into the fluid and measuring the time of flight between these reflectors. In a way, the method thus addresses to the result of mass transport rather than the process itself.

An interesting application from the point of view of fluid mechanics, is the measurement of concentration of a two-phase metal melt with two constituents having different sound velocities

2 FUNCTIONAL PRINCIPLE

2.1 Basic idea

The functional principle is based on the fact that the focus position (and related to that the time of flight to the ultrasonic focus – the variable that is accessible by measurement) depends on the speed of sound in

the medium and on the transducer.

This concept is visualised in Fig. 1, where the simulated sound fields of a focusing transducer in the fluids ethanol, water and eutectic GalSn are plotted versus the corresponding measurements of the echo signal amplitudes. For clarity, the measured times of flight were converted into the corresponding focus distance to the transducer using the known sound velocities of fluid and the acoustic lens that the transducer was equipped with for focusing purposes.

2.2 Theoretical calibration curve for a circular piston transducer

The basic idea can be understood analytically for a circular piston transducer. For this kind of transducer, the focus position is given by

$$z_{\text{foc}} = \frac{D^2}{4\lambda} = \frac{D^2 \cdot f_{\text{US}}}{4c} \quad (1)$$

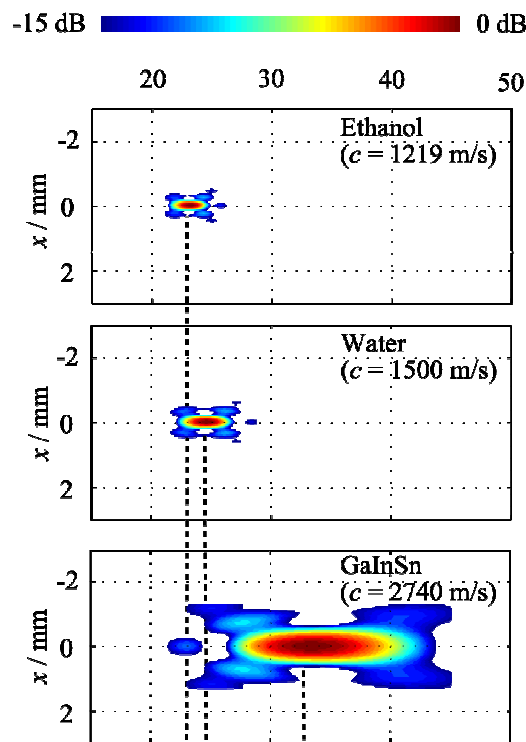
with the transducer diameter D , the wavelength λ the ultrasonic frequency f_{US} and the sound velocity c . Considering that

$$z_{\text{foc}} = \frac{1}{2} c t_{\text{SFM}} \quad (2)$$

with the two-way time of flight t_{SFM} to the sound field maximum, this leads to the theoretical calibration curve

$$c = \sqrt{\frac{D^2 \cdot f_{\text{US}}}{2 \cdot t_{\text{SFM}}}} \quad (3)$$

a) Calculated sound pressure fields



b) Measured echo amplitudes

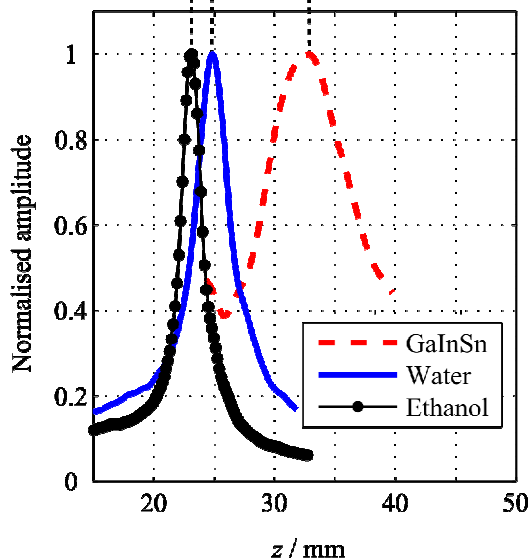


Figure 1: The maximum position of the echo signal amplitude curve indicates the position of the sound field maximum in the fluid. (a) Sound field simulations for different propagation media. (b) Time-averaged echo signal amplitude using the focusing ultrasonic transducer in media with different sound velocities. The measured times of flight have been converted into the corresponding measurement depth for easier comparison between measurements and simulations. Figure source: [1].

of the circular piston transducer. Since for most transducer geometries, analytical solutions are not

available, numerical simulations were used, here.

3 DESCRIPTION OF EXPERIMENTS

Two different experiments were carried out: (i) an experiment with a focusing transducer equipped with a ceramic lens, and (ii) experiments with a sparse annular having six active elements – an annular array with ring elements of equal size and passive gaps between the elements.

(i) The measurements with the focusing transducer equipped with a lens were done in media with sound velocities between 1116 m/s (ethanol, 50°C) and 2740 m/s (eutectic GalnSn) listed in Tab. 1.

Table 1: Fluids used in the measurements with the focusing transducer equipped with a lens.

Fluid	Temp./ °C.	c/(m/s)
Ethanol 95%	50	1116
Ethanol 95%	36	1169
Ethanol 95%	20.7	1219
Ethanol 70%	23.9	1377
Tap water	6	1431
Ethanol 50%	25.8	1499
Tap water	30	1509
Tap water	60	1551
Glycerine 39%	23.8	1685
Glycerine 59%	23.8	1785
Glycerine 85%	22.3	1879
GalnSn	20	2740

(ii) The measurements with the sparse annular array were carried out in ethanol and water. To change the focus position by signal processing, which is an important premise for achieving a local resolution of the sound velocity, the receiving signals of the different array elements were time-shifted to compensate the differing path lengths between the respective array element and the focus (focusing in receive mode).

Measuring the band-pass filtered high frequency signals and averaging their envelopes (absolute values of the Hilbert transformation) over a multitude of measurements finally led to the curves shown in Fig. 1b. Further details about the experimental-setup and the simulation method can be found in [1-2].

3 MEASUREMENT RESULTS

The experiment (i) using the focusing transducer equipped with a ceramic lens primarily confirms the underlying concept and experimentally proves its validity for a sound velocity range between 1116 m/s and 2740 m/s. The results are shown in Fig.2. Note that Fig.2 can be considered to be a calibration curve, which comprises the characteristics of the specific transducer. The deviation between

measured and simulated curves in Fig.2 is about 3%.

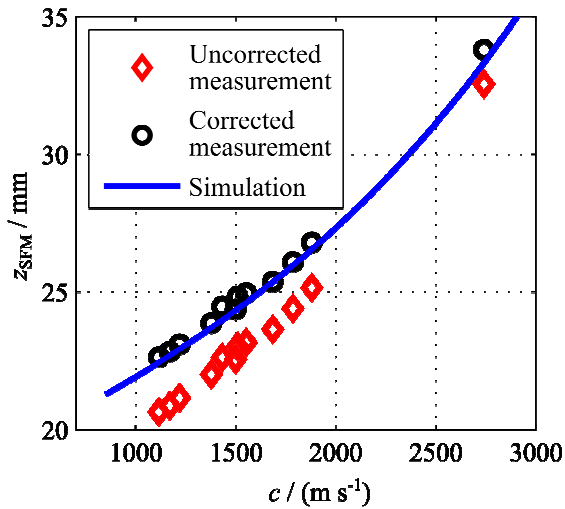


Figure 2: Calibration curve for the focusing transducer equipped with a lens. The correction considers the different speeds of sound in the ultrasonic lens and the propagation medium. Figure source: [1].

In a more detailed measurement described in [1], water of different temperatures was used to precisely adjust the sound velocity and test the statistical uncertainty of the method. A statistical deviation between measurements and fit curve for that method of about 1,41 m/s (0,1%) was found. This means that the largest part of the 3% uncertainty consist of systematic uncertainties such as an uncertainty in the knowledge of the true sound velocity and the parameters for the lens material and geometry.

Experiment (ii) using the annular array proofs that the calibration curves depend on the sound velocity of the propagation medium. Two calibration curves of the annular array are shown for $c=1200$ m/s and 1430 m/s. The measurements were done in *focusing in receive mode*.

4 ONGOING RESEARCH

Current research concentrates on the following aspects:

- reducing the statistical uncertainty of the determination of the focus position,
- measurement of the local distribution of sound velocity, and
- influence of sound propagation on focus determination.

The reduction of the statistical uncertainty for the determination of the focus position is mainly done by focusing in *send and receive mode*. This means that both the emitted ultrasonic wave and the receiving signals are focused. This makes the ultrasonic focus smaller than for focusing in just one direction and contributes to a larger signal to noise ratio.

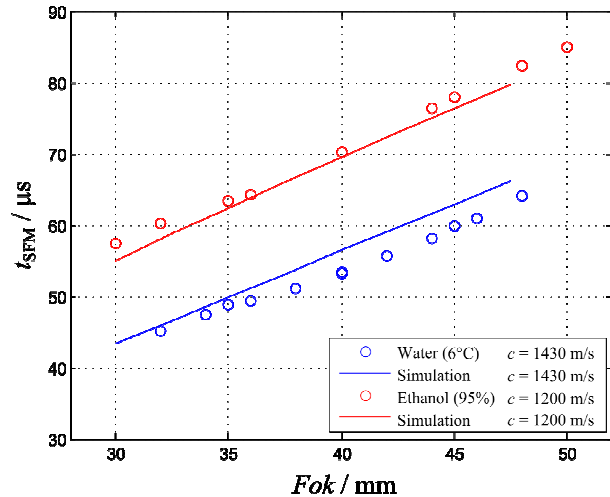


Figure 3: Calibration curves for the sparse annular array in ethanol ($c = 1200$ m/s) and water ($c = 1430$ m/s).

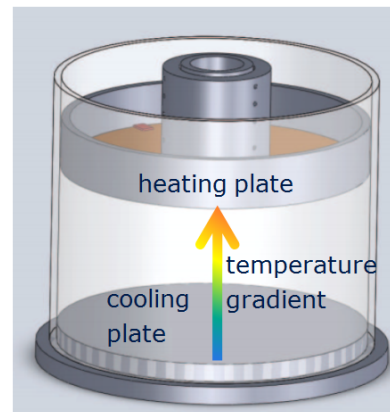


Figure 4: Set-up for generating a temperature gradient. The cooling plate needs to be on the bottom to avoid convection.

Measurement of the locally and temporarily resolved sound velocity is one of the main topics for future applications in flow research. Up-to-date measurement results will be shown for measurements in water having a temperature gradient between 10°C and 60°C, which is equivalent to a sound velocity gradient of between 1450 and 1550 m/s. The gradient generation is done with the set-up shown in Fig.4. Recent measurements have verified that the method is capable of achieving a local resolution for the sound velocity. However, a dependence of curvature of the piezoelectric element on the fluid temperature was found, which affects the focusing behaviour of the transducer and needs to be suppressed (or studied in more detailed) before final results can be given.

Further attention is also being paid to the influence of the attenuation of the propagation medium on the measurement results. In fluids with high attenuation, the measured ultrasonic focus (defined as the location exhibiting the highest sound pressure) tends to be located closer to the transducer than the locating with maximum constructive interference.

5 SUMMARY

The presentation introduces a novel approach for non-invasive sound velocity measurements in fluids that is based on the echo signals of scattering particles suspended in the fluid. Experimental proof is shown for fluids covering the wide range of sound velocity between 1116 and 2740 m/s.

The possibility to change the focus depth via time-shifted superposition of the echo signals belonging to the elements of an annular array allows to measure the sound velocity with local resolution without the need for any movement of the transducer. First sound velocity gradients measured in water exhibiting a temperature gradient are shown, and different aspects on improving the method and making it a useful tool for flow research are discussed.

REFERENCES

- [1] Lenz M, Bock M., Kühnicke E, Pal J. Cramer A.: Measurement of the sound velocity in fluids using the echo signals from scattering particles, *Ultrasonics* 52:1 (2012), 117-124. DOI: 10.1016/j.ultras.2011.07.003.
- [2] Lenz M, Kühnicke E: Nichtinvasive Schallgeschwindigkeitsmessung in Fluiden auf Basis von Streupartikelechos, *tm – Technisches Messen* 79:1 (2012), 23-28. DOI: 10.1524/teme.2012.017
- [3] Marczak W.: Water as a standard in the measurements of speed of sound in liquids, *J. Acoust. Soc. Am.* 102:5 (1997) 2776–2779. DOI: 10.1121/1.420332

Uncertainty analysis of flowrate measurement using UVP

Noriyuki Furuichi

National Institute of Advanced Industrial Science and Technology (AIST), National Metrology Institute of Japan (NMIJ), Tsukuba Central 3, Umezono 1-1-1, Tsukuba, 305-8563, Japan

A fundamental uncertainty analysis of a flowrate measurement using UVP is carried out according to GUM. Dominant uncertainty factors are a resolution of a velocity and an inclination angle of an ultrasonic transducer. The expanded uncertainty whose coverage factor is 2 is estimated as 0.4%~1.0% depending on the inclination angle of a transducer. The actual flow calibration is also carried out in national standard of flowrate (NMIJ). The combined uncertainty of the calibration, deviation from reference flowrate and reproducibility is inside of the analytical uncertainty.

Keywords: Flowrate, Velocity profile, Calibration, Uncertainty

1 INTRODUCTION

A study of a flowrate measurement using UVP has started by Takeda et al.[1]-[3] from about twenty years ago. Since the principle of this method is based on a direct integration of a velocity profile, a correction factor which is almost used for a commercial flow meter is not necessary. By this feature, this method can be applied to a flowrate measurement of many industrial fields without any influences of an upstream pipe condition such as an elbow, wall roughness and so on. In the field of metrology, this flowrate measurement is considered as most appropriate for a master meter for on-site calibration of flow meters installed in an existing pipeline. In that calibration, the uncertainty of the master meter (here, UVP method) is very important. In previous studies, accuracy of this method is considered as around 1% in theoretically[4][5]. Many actual flow calibration works have also carried out and deviations from the reference flowrate in each calibration are within about $\pm 0.5\%$ [2]. However, there is difficulty to obtain an actual accuracy of this method since a pipe condition is very different for each measuring target as case by case.

On the other hand, a fundamental uncertainty analysis for this flowrate measuring method by UVP has still not been carried out enough. It is very important to do the fundamental analysis of the uncertainty since those results might be necessary to calculate an uncertainty for the actual measurement. In this paper, the fundamental uncertainty analysis of a flowrate measurement of UVP based on GUM[6] is estimated.

Moreover, a calibration by a static weighing tank method is carried out to verify the uncertainty analysis. This calibration work is carried out in NMIJ's facility which is a national standard of flowrate in Japan. Under a careful arranged flow condition such as a fully developed flow, enough reflector and so on, the calibration is carried out for various flowrate and evaluate the uncertainty of the flowrate measurement by UVP method.

2 UNCERTAINTY ANALYSIS

2.1 Analysis model of flowrate measurement

In this paper, the uncertainty analysis is carried out according to GUM[6]. GUM is recognized as the most global uncertainty analysis method as describing in international standard (ISO). In the metrology field, the uncertainty of a measurement device is normally estimated according to GUM.

Theoretically, flowrate is estimated by equations (1) - (3) which means an integration of a velocity profile as shown in Fig.1.

$$Q_U = Q_C + \sum_{i=1}^{72} Q_{Ri} \quad (1)$$

$$Q_C = \frac{\pi \Delta r^2}{4} v_0 \quad (2)$$

$$Q_{Ri} = 2\pi \Delta r v_i r_i \quad (3)$$

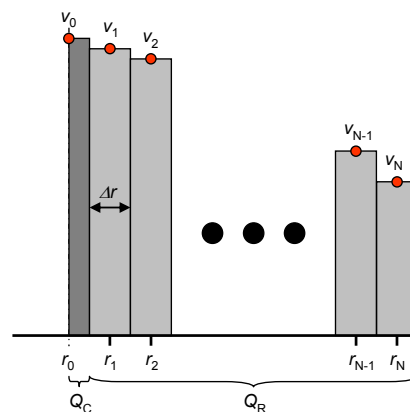


Figure 1: Integration model

Here Q_C is flowrate at the center of pipe, Q_{Ri} is flowrate at each measuring point, Δr is a split width, r_i is a radial position, v_i is velocity at each measuring point. Assumptions in this equation are following. The flow field in the measurement area is axisymmetric fully developed. The radial position described by $r_N + \Delta r/2$ is completely fitted to the inner

pipe wall. The pipe is completely circle. The velocity component of the radial direction is negligible small and an ultrasonic transducer alignment is immersion.

More assumptions to estimate an uncertainty are following. Measuring points are over 100[4]. Reflectors in the flow are satisfied to obtain a correct velocity. Then, an uncertainty of flowrate is estimated by the next equation.

$$u(Q_U) = u(Q_C) + \sum_{i=1}^N u(Q_{Ri}) \quad (4)$$

Here, the correlation coefficient is considered as 1. The relative standard uncertainty for Q_C and Q_{Ri} are described by next equations.

$$\begin{aligned} \frac{u(Q_C)}{Q_C} &= \sqrt{\sum_j \left(\frac{\partial Q_C}{\partial x_j} \right)^2 \left(\frac{u(x_j)}{Q_C} \right)^2} \\ &= \sqrt{\left(\frac{2u(\Delta r)}{\Delta r} \right)^2 + \left(\frac{u(v_0)}{v_0} \right)^2} \end{aligned} \quad (5)$$

$$\begin{aligned} \frac{u(Q_{Ri})}{Q_{Ri}} &= \sqrt{\sum_j \left(\frac{\partial Q_{Ri}}{\partial x_j} \right)^2 \left(\frac{u(x_j)}{Q_{Ri}} \right)^2} \\ &= \sqrt{\left(\frac{u(\Delta r)}{\Delta r} \right)^2 + \left(\frac{u(v_i)}{v_i} \right)^2 + \left(\frac{u(r_i)}{r_i} \right)^2} \end{aligned} \quad (6)$$

Here, u means a standard uncertainty. As showing formula, uncertainty factors are A: split width and radial position, B: velocity.

A. Split width and radial position

The split width and the radial position is calculated by next equations.

$$\Delta r = \frac{\Delta \tau}{2} C \cos \theta, \quad r_i = \frac{\tau_i}{2} C \cos \theta \quad (7)$$

Here, $\Delta \tau$ is a delay time of pulse, C is a sound speed, θ is an inclination angle of transducer. Since these equations are completely same, the uncertainty estimation will be only carried out for the split width. The relative standard uncertainty of the split width is estimated by the next equation.

$$\frac{u(\Delta r)}{\Delta r} = \sqrt{\left(\frac{u(\Delta \tau)}{\Delta \tau} \right)^2 + \left(\frac{u(C)}{C} \right)^2 + (|\tan \theta| u(\theta))^2} \quad (8)$$

The uncertainty of $\Delta \tau$ is depending on the accuracy of the clock of the processor installed in UVP. Since the uncertainty of time measurement is relatively smaller than other factors, it is normally negligible.

The sound speed is set manually in UVP. Since the sound speed is a function of a temperature and a pressure, the uncertainty caused by the measurement of these values and the equation to estimate the sound speed should be estimated.

Moreover the uncertainty caused by a resolution should be included, when normal UVP such as UVP-Duo is used.

The uncertainty caused by the inclination angle of the transducer is very different whether the transducer setting is an immersion or a clamp-on method. In this paper, actual uncertainty estimation showing next section will be carried out for the immersion type to know the fundamental uncertainty.

B. Velocity measurement

The velocity in UVP measurement is calculated by the next equation considering with the inclination angle of the transducer.

$$v_i = \frac{C f_{PRF}}{512 f_0} \frac{v_{Ti}}{\sin \theta} \quad (9)$$

Here, f_{PRF} is a repetition frequency of a pulse, f_0 is a basic frequency of the transducer, v_{Ti} is a digitized raw velocity component outputted from UVP. The relative standard uncertainty is following.

$$\begin{aligned} \frac{u(v_i)}{v_i} &= \\ &= \sqrt{\left(\frac{u(C)}{C} \right)^2 + \left(\frac{u(f_{PRF})}{f_{PRF}} \right)^2 + \left(\frac{u(f_0)}{f_0} \right)^2 + \left(\frac{u(v_{Ti})}{v_{Ti}} \right)^2 + \left(\left| -\frac{1}{\tan \theta} \right| u(\theta) \right)^2} \end{aligned} \quad (10)$$

The uncertainty of C and θ has already mentioned. The uncertainty of the repetition frequency and the basic frequency are based on the clock of a processor. As mentioned, these factors might be negligible.

In normal UVP, the velocity data is digitized to 256 steps. The uncertainty caused by resolution as shown in next equation should be included according to GUM.

$$u(v_{Tinsti}) = 0.5 / \sqrt{3} = 0.29 \quad (11)$$

2.2 Uncertainty estimation for actual device

Since the flowrate measurement by UVP has so many parameters to measure the velocity profile, the uncertainty might be different case by case. Here, the measurement condition is set as Tab.1.

As a result of the uncertainty analysis, the budget sheet for 20° of inclination angle is shown in Tab.2. As mentioned, the uncertainty of the split width and the radial position is consists of one of the delay time, the sound speed and the transducer inclination angle. The uncertainty of the delay time is depending on the clock of the device. In a comparison of the frequency between calibrated frequency counter and UVP-Duo, any difference was not observed. Then, the uncertainty of the calibrated frequency counter is only used in this estimation. The uncertainty of the sound speed is caused by one of the temperature and pressure

measurement and the resolution. The uncertainty of measurement of the temperature and the pressure is negligible small. In UVP-Duo, the sound speed is set manually with a step of 1 m/s. For the transducer angle, the standard uncertainty of the measurement of angle is estimated as 0.015° and the property of it estimated as 0.035° by considering as a linearity of an ultrasonic is 0.1%. The combined standard uncertainties of the split width and the radial position are estimated as 0.032%.

The uncertainty of the velocity is estimated as 0.247%. This uncertainty is relatively larger than other factors. Especially, a dominant factor of the uncertainty of the velocity is the raw velocity and the transducer angle. The dominant uncertainty source of the raw velocity is a resolution of it as shown in Eq.(11). When the ratio between the averaged velocity and the maximum one is set to 0.5, the standard uncertainty increases 0.224%.

Moreover, the contribution of the angle of transducer is very large in the uncertainty of the velocity. The standard uncertainty of it is estimated as 0.182% and this is the most dominant factor. The expanded uncertainty ($k=2$) of the transducer angle is estimate as 0.076° in this estimation. The contribution of the inclination angle increases with decreasing of it.

Expanded uncertainty for each inclination angle is shown in Tab.3. Since the uncertainty caused by inclination angle is dominant, expanded uncertainty is strongly influenced by it.

3 EXPERIMENT

3.1 Experimental facility and pipe layout

An experiment was carried out using the national standard of flowrate in Japan. The national standard of flowrate is supplied using static weighing tank system[7]. A schematic diagram of the experimental facility is shown in Fig.2. Since water is supplied to the test section from the constant level head tank, a fluctuation of flowrate is relatively smaller than using pumps. Also, this calibration rig has a long straight pipe to achieve a fully-developed flow profile. In this experiment, the 250 mm test line and the 50 t weighing tank system are used. The standard uncertainty of the facility is $u_c=0.027\%$ and the expanded uncertainty ($k=2$) of the calibration is 0.060%.

The detail of a test section is shown in Fig.3. From the upstream side, the test section is consists of a bubble generator, a flow conditioner, an over $50D$ straight pipe and a measurement device. As mentioned, the ultrasonic transducer is aligned as immersion to water.

In the following test result, the flow condition and the device condition including a setting parameter of UVP-Duo is according to Tab.1 and the inclination angle is 8° .

Table 1: Conditions for uncertainty estimation

Testing condition	
Water temperature	20 °C
Pressure	0.2 MPa
Flowrate	600,400,250, 170 m ³ /h
UVP condition	
Number of measuring point	134
Split width	0.74 mm
Basic frequency	2 MHz
Repetition frequency	256
Averaged velocity / Maximum velocity	0.7
Device condition	
Pipe diameter	198.85 mm
Inclination angle	8°,12°,20°,30°

Table 2: Uncertainty budget sheet for 20° of inclination angle of transducer

Uncertainty Factor		Relative standard uncertainty
Split width	Δr	0.032%
Delay time	$\Delta \tau$	0.004%
Sound speed	C	0.021%
Temperature		0.008%
Pressure		0.000%
Resolution		0.019%
TDX angle	θ	0.024%
Measurement		0.010%
TDX property		0.022%
Radial position	r_i	0.032%
Velocity	v_i	0.243%
Sound speed	C	0.021%
Repetition freq.	f_{prf}	0.004%
Basic freq.	f_0	0.004%
Raw velocity	v_{Ti}	0.160%
TDX angle	θ	0.182%
Measurement		0.073%
TDX property		0.166%
Combined uncertainty		0.25%
Expanded uncertainty ($k=2$)		0.49%

Table 3: Expanded uncertainty for each inclination angle of transducer

Transducer inclination angle	Expanded uncertainty ($k=2$)
8°	1.00%
12°	0.70%
20°	0.49%
30°	0.41%

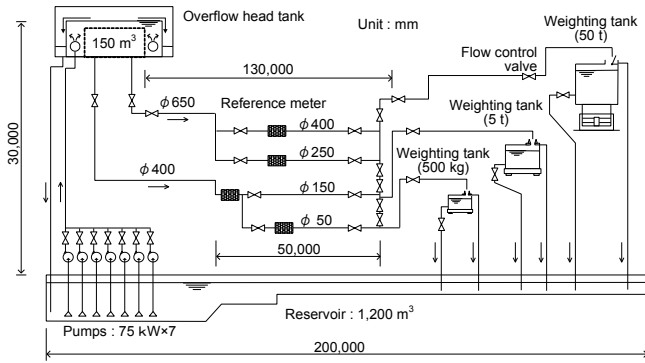


Figure 2: Flowrate calibration facility

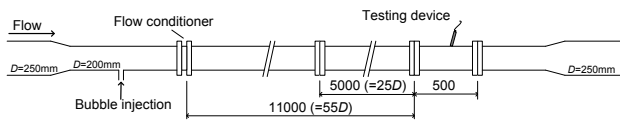


Figure 3: Test section

3.2 Velocity profile

In order to check the velocity profile, UVP measurement was carried out on 6 azimuthal angles. In order to eliminate the error caused by a transducer setting or an installation of pipe, the test device with upstream pipe (25D) is rotated.

Velocity profiles are shown in Fig.4. Velocity profile at each angle show good agreement. Also, these velocity profiles are in good agreement with the power law. It can be concluded that this flow field is completely axisymmetric fully developed flow.

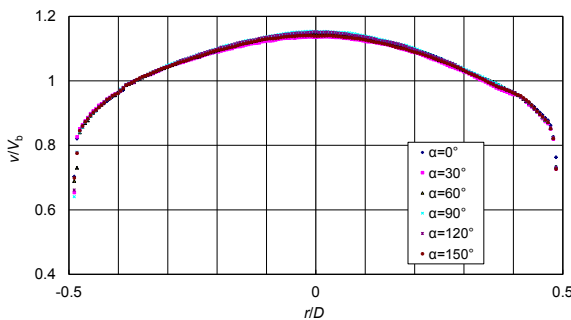


Figure 4: Velocity profile. Flowrate is 695 m³/s

3.3 Calibration result

Typical calibration results are shown in Fig.3. Vertical axis means a deviation from the standard value. Subscripts of UVP and ref. in figure mean a flowrate given by UVP and a reference flowrate obtained by the weighing tank. Error bars mean expanded uncertainty U calculated by the next equation.

$$U = k \sqrt{u_{CMC}^2 + \sigma^2 / n} \quad (12)$$

Here, σ is a standard deviation of the calibration result, n (=5, in this experiment) is a number for repetition, k (=2.4~2.7 in this experiment) is a coverage factor which is satisfied 95% confidential

level. In this examination, the expanded uncertainty is 0.14%~0.31% depending on the standard deviation of UVP measurement. Experiments were carried out at different three days to check reproducibility.

The deviation from the reference flowrate is result is less than 1% all over the measurement flowrate range. At flowrate 600 m³/h, it is 0.4% at most. This result is inside of uncertainty estimated in section 2. Reproducibility is 0.5% at most for all flowrate range and it is 0.32% at 600 m³/h. A combined uncertainty of the calibration, deviation and reproducibility is 0.51% at 600 m³/h. This uncertainty is inside of the analytical uncertainty.

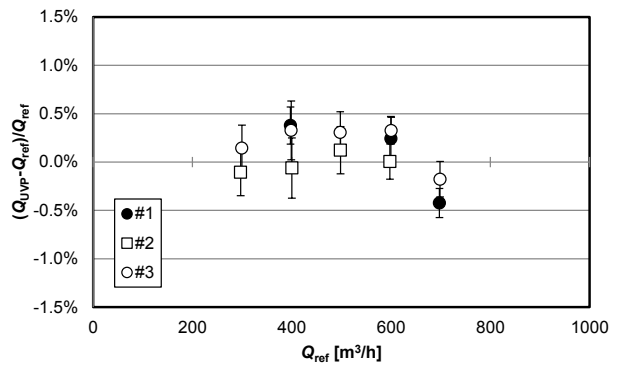


Figure 5: Calibration result

4 SUMMARY

The uncertainty of flowrate measurement using UVP-Duo is estimated as 0.4%~1.0% according to GUM uncertainty analysis. Dominant uncertainty factors are the resolution of velocity and the inclination angle of the transducer. The result of actual flowrate calibration using national standard is estimated as 0.51% for the analytical flowrate point. This value is inside of the analytical uncertainty.

REFERENCES

- [1] Mori et al, Development of a novel flow metering system using ultrasonic velocity profile measurement, *Exp in Fluids*, 32 (2002), 153-160
- [2] Tezuka et al, Calibration tests of pulse-Doppler flow meter at national standards loops, *Flow Meas. and Inst.* 19 (2008), 181-187
- [3] Wada et al, Development of pulse ultrasonic Doppler method for flow rate measurement in power plant, *J Nucl Sci and Tech* 41 (2004), 339-346
- [4] Ohkubo et al, Accuracy evaluation of high-accuracy flowmeter using UVP, *Transactions of the Japan Society of Mechanical Engineers, Series B* 72 (2006), 81-89 (in Japanese)
- [5] Kikura et al, Effect of measurement volume on turbulent flow measurement using ultrasonic Doppler method, *Exp. in Fluids*, 36 (2004), 187-196
- [6] Guide to the Expression of Uncertainty in Measurement (GUM) (1995) ISO
- [7] Furuichi et al, Calibration Facilities for Water Flowrate in NMIJ, *Proceedings of 7th International Symposium on Fluid Flow Measurement*, (2009), CD-ROM

Cavitation risk estimation at orifice spillway based on UVP and dynamic pressure measurements

Michael Pfister, Rafael Duarte, Michael Müller and Giovanni De Cesare
Laboratory of Hydraulic Constructions (LCH), Ecole Polytechnique Fédérale de Lausanne (EPFL), CH-1015 Lausanne, Switzerland. E-mail: michael.pfister@epfl.ch

Orifice spillways might be affected by cavitation if the profile of the inlet structure includes a relevant curvature. At one of the world's largest dams, such damages were observed on the profiled slab. To limit their progression, an adapted operation regime of the gates had to be defined using physical model tests. The risk estimation was based on dynamic pressure and velocity measurements, indicating that a maximum gate opening ratio of 0.8 should be respected until the damage is repaired and the profile re-shaped. Beside this, the data set allowed to compare the flow characteristics at the profile surface in terms of turbulence intensity and dominant frequencies. The Ultrasonic Velocity Profiler (UVP) provides comparable characteristic values as the dynamic pressure transmitter (DPS).

Keywords: Cavitation, pressure, spillway, turbulence, velocity

1 INTRODUCTION

Fast flows in contact with concrete structures are known to potentially generate cavitation damages, in particular if the related bottom pressure is low. Several spillways and chutes evacuating severe floods from reservoirs, thus avoiding dam overtopping and the related failure, suffered from these damages. However, cavitation erosion on such structures may be suppressed if applying chute aerators [1, 2], so that their safe operation under extreme conditions is possible.

A different spillway type may also be prone to cavitation, even if this is less obvious. Orifice spillways intend to remove the water from the concrete surface by generating free jets, thus avoiding cavitation and other unwanted phenomena. However, the inlet structure of these orifices might be a sensitive element, even if the flow velocities and pressures are a priori below a critical range. The cavitation potential of these inlets results from the curvature of the inlet profile inducing a curvature of the streamlines, increasing local velocity and decreasing pressure. Furthermore, the flow may separate from the surface and generate a local back flow zone.

2 CAVITATION ANALYSIS

2.1 Situation

Severe cavitation damages on an orifice spillway inlet profile were observed at one of the world largest dams. The dam owner paid particular attention to that damage, as a proper operation of the gates is necessary to guarantee a safe reservoir management. Physical model tests were therefore conducted to assess the cavitation potential for different gate opening ratios (equivalent to discharges), based on which the dam owner defined

an adequate operation regime as a first step. Rehabilitation and an adaption of the concrete profile will follow in a second step.

The cavitation potential depending on the operation mode was estimated in a physical model on the base of dynamic pressure measurements and on velocity sampling. The latter indicates a flow separation zone for maximum gate opening. Combined with the analysis of the dynamic pressure measurements, a comprehensive description of the flow processes was possible.

A model including all orifices was built (Fig. 1) with a geometrical scale factor of 65 and considering the hydraulic similitude according to the Froude number. The maximum spillway discharge of 9'000 m³/s in prototype corresponds to 264 l/s in the model. The model tests were conducted with a constant reservoir water level. The cavitation potential was estimated for various operational scenarios (Table 1).



Figure 1: Physical model of orifice spillway seen from reservoir, considered gate is second from right

Two sensors were installed (Fig. 2):

- A piezoresistive dynamic pressure transmitter DPS (Series 23, www.keller-druck.com) of pinhole type with an acquisition range between ± 0.1 bar, an acquisition frequency of 1 kHz and an acquisition time of 65 s. The pressures were

measured at a defined “measurement point” MP on the slab of a particular orifice, where severe cavitation damages occurred in prototype. The latter is located in the transverse center of the orifice. The tap hole connecting the transmitter with the surface was drilled 3 mm below the abrupt profile edge (model dimensions). The measurement cavity was de-aerated to avoid resonance phenomena.

- An UVP transducer (TX1-13-16, www.met-flow.com) with an emitting frequency of 1 MHz, an active diameter of 20 mm (instead of 13 mm) and an acquisition time of 10 s. The measurement beam was horizontal ($x=0$ m at MP) and pointing to the tap opening of the pressure transmitter. The transducer was located 0.24 m away from MP to avoid an effect of the UVP on the flow, corresponding to 15.6 m in prototype. Only the 7.0 m closest to MP were considered in the data analysis. The values were furthermore corrected with the angle of the profile, which is approximately 25° relative to the horizontal at MP. Positive velocities represent a flow direction from left to right in Fig. 2, and negative values indicate a flow from right to left.

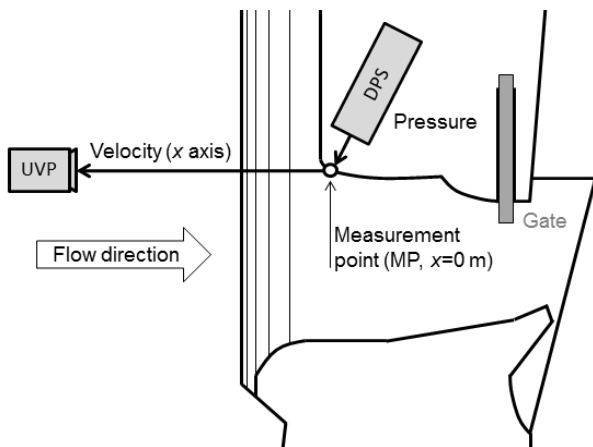


Figure 2: Section of dam with orifice spillway and measurement equipment

Table 1: Test scenarios

Scenario	Opening ratio of considered gate	Opening ratio of neighbor gates
A1	0.2 (20 %)	0.0
A2	0.4 (40 %)	0.0
A3	0.6 (60 %)	0.0
A4	0.8 (80 %)	0.0
A5	1.0 (100 %)	0.0
B1	0.2	1.0
B2	0.4	1.0
B3	0.6	1.0
B4	0.8	1.0
B5	1.0	1.0

2.2 Velocity measurements

Figure 3 shows the up-scaled horizontal velocity profiles, with $x=0$ m at MP and $x>0$ m at increasing distances from the latter (Fig. 2).

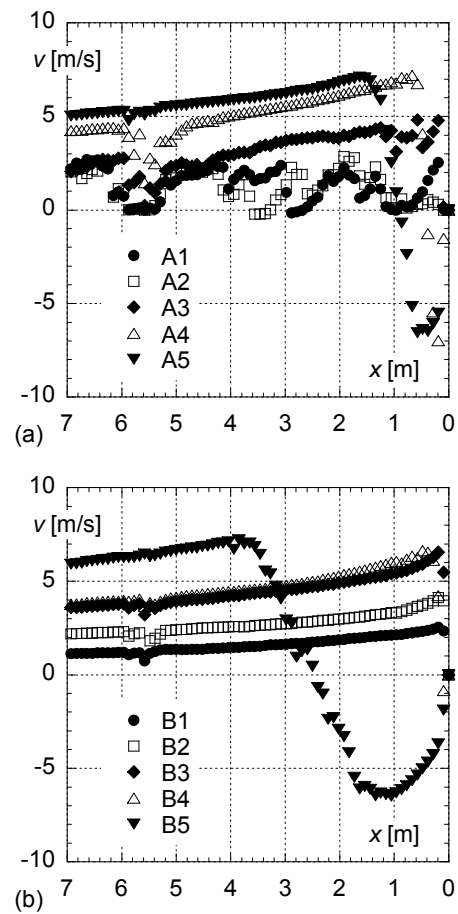


Figure 3: Average flow velocities v ($x=0$ m at MP of Fig. 2, prototype values) for scenarios (a) A and (b) B

The following observations were made:

- The velocities increase towards the profile if approaching MP. This is due to streamline curvature, induced by the rounded inlet profile. This increase of velocity is linked to a drop in pressure, both supporting the occurrence of cavitation.
- The profiles indicate a discontinuity between $x=5$ to 6 m. The latter is caused by an inlet vortex as observed in prototype. There, the horizontal velocity component decreases, whereas the rotational component (not detected by UVP) increases.
- The velocities generally increase with increasing opening ratio, as the related discharges also increase.
- Small discharges (small opening ratios) show an unstructured flow characteristics if the neighbor gates are closed (A1, A2), whereas larger gate openings generate higher velocities and more

homogenous flow fields.

- Negative velocities occur for maximum gate opening ratios, indicating a flow separation zone with back flow close to the profile. The main flow is thus unable to follow the profile shape, indicating a too pronounced curvature. The back flow zones are related to cavitation formation, as the shear zone between the two flow cells is highly turbulent with pronounced pressure peaks. The thickness of the separation zone increases with the discharge.

2.3 Pressure measurements

Figure 4 shows the up-scaled pressure heads at MP. For small gate opening ratios, the average values are close to the hydrostatic head of 17.8 m water column (WC). With increasing gate opening ratio, the pressure heads decrease. For maximum gate opening ratios of 1.0, distinctively negative pressures are detected. Cavitation onset is observed in prototypes for pressures around -7 to -10 m WC [3] (grey area in Fig. 4), i.e. at opening ratios of 1.0 for the present case. Note that pressures below these values will not occur in prototype, as the water changes its phase to vapor.

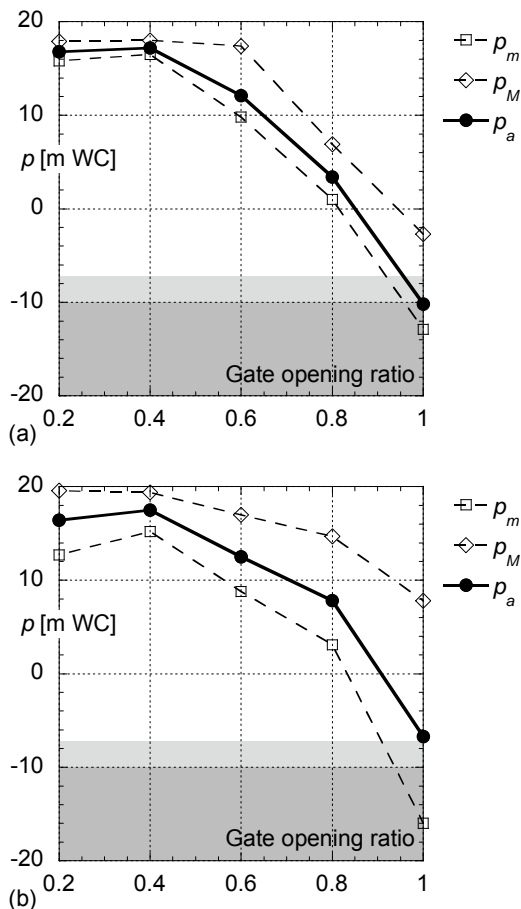


Figure 4: Pressure heads p (prototype values) vs. gate opening ratios for scenarios (a) A and (b) B, with m = minimum, M = maximum, a = average, in grey: cavitation zone below vapor pressure

2.4 Interpretation

Model tests clearly support observations on prototype: Under full operation, the investigated orifice represents a significant risk for cavitation damages. The results of the interpretation concerning the two scenarios A and B are similar for high discharges. The velocity measurements indicate that a separation zone with back flow emerges for gate opening ratios of 0.8 to 1.0. The pressure measurements show that the values drop below vapor pressure for the maximum gate opening ratio. The following applies:

- The herein derived results are only valid for a smooth inlet ceiling profile. Cavitation is more likely for a rough and already damaged surface than for a smooth one.
- The results were derived based on the analysis and interpretation of measurements at one single point MP in a scaled model. They have thus a qualitative character, but are nevertheless revealing a significant cavitation risk.

3. COMPARISON UVP WITH DPS

3.1 Turbulence intensity

Regarding cavitation, the flow turbulence is relevant because it also indicates the occurrence of minimum pressures. For measured time series, the turbulence intensity is defined as [4]

$$T_u = \frac{RMS}{\bar{x}} \quad (1)$$

with RMS as root mean square of a time series and \bar{x} as mean value. Figure 5 shows T_u for both acquisition systems (UVP and DPS) and for both scenarios. The T_u values of the DPS are located on the profile surface at $x=0$ mm (MP), and those of the UVP at $x>0$ mm.

The T_u values of the DPS measured on the profile surface are between 1.0 and 1.2 for all scenarios. Those from UVP are derived in the flow at different locations x near the profile. The UVP measurement closest to the surface at $x=0.61$ mm indicates a T_u which is one order higher than that from DPS, both located in the turbulent boundary layer (TBL). For large distances of around $x \geq 9.49$ mm the UVP values are around $T_u=0.1$ to 0.5, as probably located in potential flow. Between these extremes, the T_u of the UVP are close to those of the DPS. Removing the outlier at A2 ($T_u=62$ at $x=2.09$ mm) in the UVP data set and averaging all scenarios between $2.09 \text{ mm} \leq x \leq 3.57 \text{ mm}$ results in $T_u=1.14$, and averaging all scenarios in the UVP data set between $2.09 \text{ mm} \leq x \leq 5.05 \text{ mm}$ results in $T_u=0.90$. These averages are close to the mean of all DPS measurements with $T_u=1.03$. The flow turbulence near a surface is thus correctly represented by UVP if considering the DPS data as reference and if

taking into account the zone between 2 mm and some 4 to 5 mm away from the rigid surface. Besides that, the general trend with increasing T_u towards the surface, i.e. in the TBL, is confirmed.

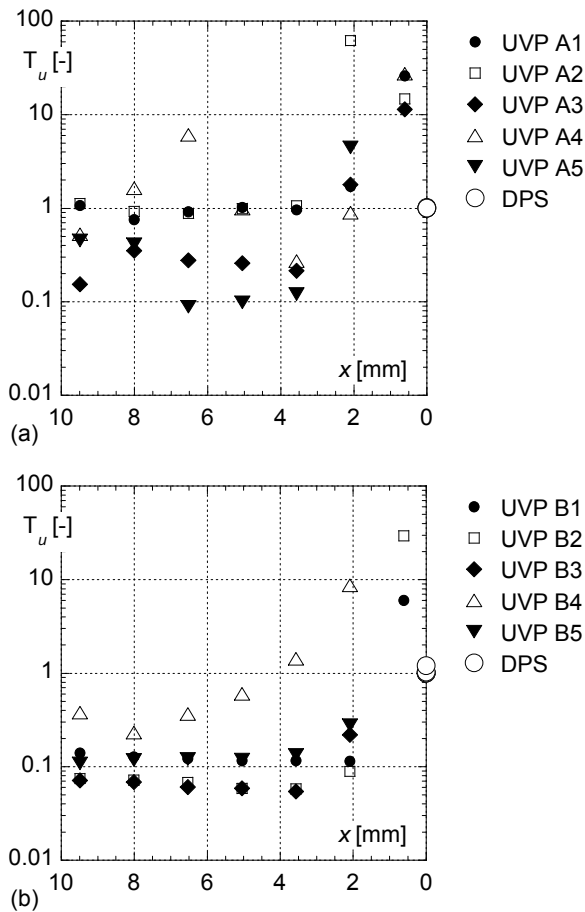


Figure 5: Comparison of T_u derived from UVP and DPS for scenarios (a) A and (b) B ($x=0$ mm at MP of Fig. 2, model values)

3.2 Power spectra

The power spectral densities based on the Welch periodogram are shown in Fig. 6, including A5 and B5 and comparing the DPS and the UVP data ($x=3.57$ mm for A5, at $x=2.09$ mm for B5). The unit of the ordinate is Bar^2/Hz for pressures, and $(\text{m/s})^2/\text{Hz}$ for velocities. The curves of the velocity were smoothed by a symmetrical moving average over five values.

For A5, no dominant frequency occurs for both sensors, whereas B5 indicates a peak at around 2 to 3 Hz in both curves. The general trend seems similar for both instrumentations.

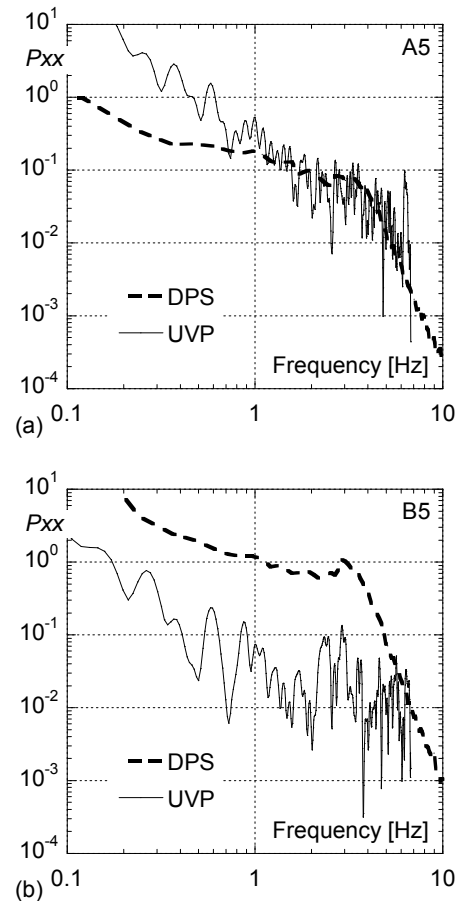


Figure 6: Power spectra derived from UVP and DPS for scenarios (a) A5 and (b) B5

4. CONCLUSIONS

Dynamic pressure measurements are essential for cavitation prediction. Velocity sampling supports the analysis of the flow field. Basically, DPS and UVP provide comparable turbulence characteristics and dominant frequencies. Beside a sufficient acquisition period, the distance to the rigid surface was found as essential parameter for UVP turbulence estimation.

REFERENCES

- [1] Pfister M, Hager WH: Chute aerators I: Air transport characteristics, J Hydraulic Eng, 136(6), 352-359 (2010).
- [2] Pfister M, Hager WH: Chute aerators II: Hydraulic design, J Hydraulic Eng, 136(6), 360-367 (2010).
- [3] Vischer D, Hager WH: Dam Hydraulics, John Wiley & Sons, Chichester (1998).
- [4] Ervine DA, Falvey HT, Withers W: Pressure fluctuations on plunge pool floors, J Hydraulic Res, 35(2), 257-279 (1997).

Peristaltic flow characterization of shear thinning fluid through elastic tube by UVP

S. Nahar, S. A. K. Jeelani, Y. Takeda and E. J. Windhab

Laboratory of Food Process Engineering, Institute of Food, Nutrition and Health, ETH Zurich, Schmelzbergstrasse 7, 8092 Zurich, Switzerland.

In-vitro small intestinal flow characteristics of a non-Newtonian fluid are investigated by transient '2-wave'-squeezing of an elastic tube under different speed of peristalsis. Such peristaltic flow is the essential physiological transport mechanism in the gastro-intestinal tract. The peristalsis involves both expansion and contraction type of flow (crest and trough of a wavelength). We met the challenge of implementing the UVP technique for monitoring the velocity fields during appropriate peristaltic propulsion of a shear thinning fluid through an elastic tube (*in vitro* modeled small intestine). The higher wave speed of peristalsis results in higher magnitude of back flow velocity (negative) both in the wave crest and trough regions with positive value being near the tube wall. The higher value of back flow is expected to be responsible for the improved mixing and convection leading to higher mass transport through the intestinal wall. The measured pressure difference between crest and trough of a peristaltic wave increased, as the wave speed got faster. However, the crest region showed a higher pressure compared to the trough region since the magnitude of back flow velocity in the wave trough is found to be much higher compared to that in the wave crest.

Keywords: Elastic tube, *in vitro*, peristaltic flow, shear thinning fluid

1 INTRODUCTION

The detail understanding of steady and unsteady flow characteristics of non-Newtonian fluids in collapsed elastic tube [1] followed the interest to investigate experimentally the flow behavior of a shear thinning fluid during peristaltic propulsion through an elastic tube (*in vitro* modeled small intestine). Peristaltic flow is a primary physiological transport mechanism encountered in the most tubular organs of the human body (e.g. transport of food through the esophagus, and carrying & mixing motion of chyme in the small intestine). Some experimental and theoretical features of peristaltic flow have been studied for Newtonian fluids as described in [2-3]. In addition, an *in-vivo* study has been carried out to characterize and visualize the flux over time in small bowel segments [4]. For more realistic non-Newtonian fluid systems, systematic work is still missing. Most of the physiological fluids and foods are known to be non-Newtonian and their rheological properties (shear and extensional viscoelasticities) play an important role in the peristaltic flow characteristics. The theoretical investigation of a power-law has been studied involving the influence of shear-thinning and shear-thickening properties under peristaltic motion [5].

Present study involves the measurements of axial velocity profiles using pulsed ultrasound Doppler based velocity profile (UVP) technique under various speeds of peristalsis. In addition, the pressure difference between crest and trough within a wavelength is also measured under peristaltic motion of a shear thinning fluid through an elastic tube.

2 EXPERIMENTAL

2.1 Set up for peristaltic flow experiment

A silicone elastic tube (Lindemann GmbH, Germany) with 20 mm inner diameter, 1 mm thickness and 1165 mm long is mounted between two aluminum pipes and immersed in a water filled open tank (width 250 mm and length 1300 mm). The schematic diagram of the experimental setup with the positions of pressure sensors (P_1 & P_2) is given in Figure 1a. In addition, three distinct UVP measuring lines (ML1L, ML1 and ML1R) both horizontal and vertical positioning of ultrasound transducer and wave troughs are also inserted as in Figure 1b and 1c respectively. Three pairs of rollers (outer diameter of 30 mm) are placed (both top and bottom surface of the tube) to induce the peristaltic motion on the elastic tube. The distance between two adjacent rollers along tube length as well as the gap (4 mm) between top and bottom rollers are so adjusted that generates the peristaltic wave with wavelength of 82 mm. The speed of the rollers is controlled by an electric motor (MCD EPOS 60W, maxon motor) for the variation in peristaltic motion while squeezing of the elastic tube. The elastic tube is filled with a non-Newtonian 1.5 % carboxymethyl-cellulose aqueous solution (with 0.3% polyamide) and two outlets are connected to an aqueous solution filled reservoir. Two optical fiber based pressure transducers with a control unit (Samba sensors, Sweden) are used for the measurement of local and total pressure difference in a wavelength at different speeds of peristalsis. The velocity profiles are monitored by UVP technique with an ultrasound transducer (5 mm outer diameter and 2 mm beam or active diameter) of 8 MHz emission

frequency. The measured sound velocity in the test fluid is 1499 m/s at 22 °C.

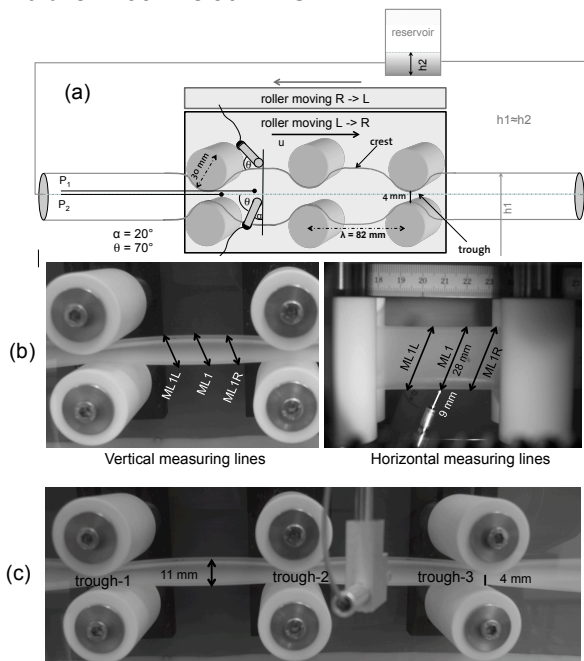


Figure 1: (a) Schematic representation of the experimental set up showing peristaltic squeezing of an elastic tube with the positions of pressure sensors (P_1 & P_2) and ultrasound transducer, (b) Three distinct vertically & horizontally adjusted measuring lines (ML1L, ML1, ML1R), (c) three wave troughs of the '2-wave'-squeezing of an elastic tube.

2.2 Shear thinning fluid

A carboxymethyl-cellulose (CMC; Blanose CMC 7MF, IMCD Switzerland AG) at 1.5 % w/w (with 0.1 M NaCl; $M_w = 2.5 \times 10^5 \text{ g/mol}$) aqueous solution is used in the peristaltic flow experiment. In addition, polyamide particles ($\rho = 1030 \text{ kg/m}^3$; and 20 μm diameter; Dantec Dynamics, Skovlunde, Denmark) at 0.3 % w/w are added to the CMC aqueous solution (velocity magnitude is relatively low under peristalsis) for better resolution of UVP measurement. CMC aqueous solution represents an inelastic shear thinning behavior as demonstrated in [6]. The viscosity flow curve is not altered after adding the polyamide particle in the CMC aqueous solution, since small mass fraction (0.3 %) of the added particles, which lead to negligible particle-particle interaction.

2.3 UVP in peristaltic flow

The main study challenge is to investigate the velocity fields under peristalsis (squeezing of an elastic tube), which are not measured previously due to lack of applicable methods. Consequently we successfully applied the UVP technique for monitoring the steady and unsteady flow fields through a collapsible elastic tube as demonstrated elsewhere [1]. We met the challenge of implementing the UVP method for investigating the velocity fields during appropriate peristaltic

propulsion of a shear thinning fluid through an elastic tube. The details of the UVP technique applied here can be followed as described in Nahar et al. [1].

The velocity profiles are monitored by UVP both in the crest and trough region (of the '2-wave'-squeezing of an elastic tube) while ultrasound transducer placed at three distinct measuring lines (ML1L, ML1, ML1R, positioning the ultrasound transducer both horizontally and vertically at the crest, and only horizontally at the trough as shown in Figure 1) with a Doppler angle of 70° in a moving frame. In the moving frame, the transducer is moving longitudinally at the same speed as the wave speed in both directions (left to right, L → R or right to left, R → L) depending on the study interest. The measured velocity profiles are found to be uniform and stable for the entire measurement (in both directions). All the measured velocity profiles shown later are transformed into the laboratory frame by adding or subtracting of the wave speed respect to the wave direction (as $V_{\text{real}} = V_{\text{meas}} + V_{\text{wave}}$ for L → R and $V_{\text{real}} = V_{\text{meas}} - V_{\text{wave}}$ for R → L, where V_{real} , V_{meas} and V_{wave} are the actual, measured and peristaltic wave velocities respectively).

3 RESULTS AND DISCUSSION

3.1 Velocity profiles in the wave crest

The measured velocity profiles in a wave crest at the measuring line ML1 (horizontal) are represented as a function of distance inside the tube in Figure 2 under different wave speeds (as 3 to 10 mm/s). The results show that higher wave speed of peristalsis develop in higher velocity being of specific interest for improved mixing and mass transfer conditions of nutrients. A positive velocity is detected near the tube wall while moving the peristaltic wave from L → R (Figure 2a) or R → L (Figure 2b), since the moving rollers to impose the peristalsis are in direct contact with the tube wall. In contrast, the velocity magnitudes are gradually becoming larger and negative (representing a back flow) towards the tube center due to forward movement of the peristaltic wave from L → R (Figure 2a) and correspondingly the fluid is moving backward. The reason is that the pressure rises inside the leading wave (fluid ahead the roller) than that in the lagging wave (fluid behind the roller) during peristalsis, which can lead to a mixing mechanism near the wave trough. The behavior is vice versa when the peristaltic wave is moving from R → L (Figure 2b), where the obtained positive velocity magnitudes are represented as negative values by correction with relative of roller-speed. In both cases, when the wave speed of peristalsis got faster that is velocity near the tube wall is more positive and correspondingly the velocity magnitude at the tube center becomes more negative (back flow) due to higher pressure drop depending on the wave speed.

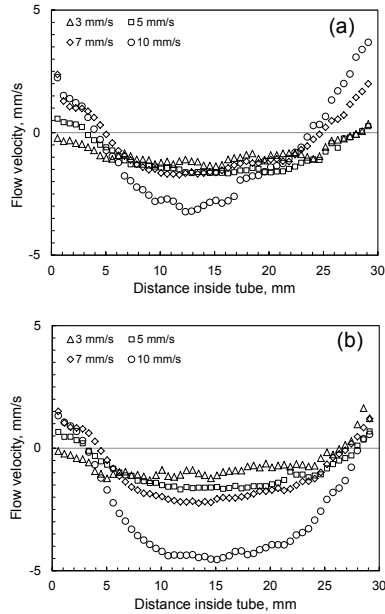


Figure 2: Experimentally measured velocity profiles in the wave crest under different speed of peristalsis, while the peristaltic wave moving left to right (a), or right to left (b).

The accuracy of the measurement is confirmed by symmetric and overlapping of the normalized (by velocity at crest center) velocity profiles at different peristaltic speeds as shown in Figures 3a and 3b. The measured velocity fields are found to be influenced by the memory of the traveling waves and wave speeds. It is seen that the normalized velocity profiles during peristaltic wave moving from L→R are having little deviation for variation in speeds of peristalsis (Figure 3a), where the measured velocity profiles are affected by lagging of a wave respect to the direction of wave speed. On the other hand, the wave moving from R→L is leading a wave that shows a more symmetric and overlapping normalized velocity profiles (Figure 3b) under various peristaltic speeds.

In addition, velocity profiles are also measured at two other measuring lines ML1L and ML1R in the crest, which are 20 mm back and forth from ML1 respectively, while the peristaltic wave moving from L→R at the wave speed of 10 mm/s.

The results (Figure 4a) depict that the maximum velocity magnitude (negative) inside the tube is much higher while measuring horizontally at ML1L compared to those measured at measuring lines ML1 and ML1R and a higher positive velocity value is observed at the tube wall. The reason is that the measuring line ML1L is close to and leading the wave crest which has much higher contraction (smaller cross sectional area) in the first half measuring region from the tube center resulting to a higher negative velocity values at that regime. On the other hand, the second half measuring region from the tube center is showing a less negative velocity values, which confirms a region of bigger

cross sectional area. In contrast, the measuring line ML1 is aligned at the center of the wave crest with a uniform cross sectional area along the measuring line showing more symmetric velocity profile.

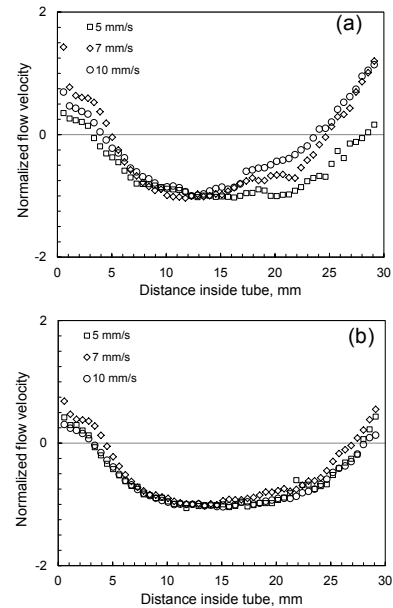


Figure 3: The normalized velocity profiles in the wave crest under different speed of peristalsis (as in Figure 2), while the peristaltic wave moving L→R (a), or R→L (b).

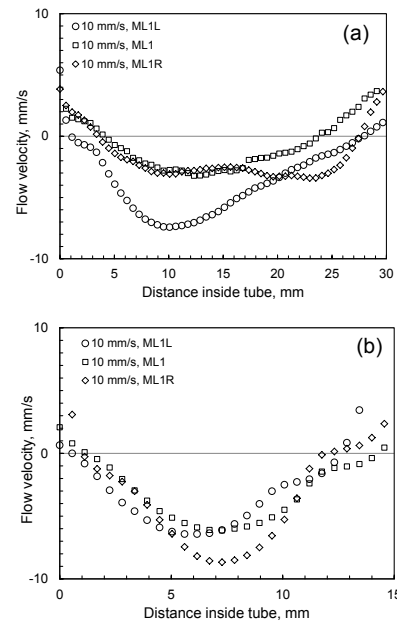


Figure 4: Experimentally measured velocity profiles in the wave crest as monitored by positioning of ultrasound transducer both horizontally (a) and vertically (b) at the wave speed of 10 mm/s.

Furthermore, the measuring line ML1R is fixed at the end of the wave crest with a small contraction in the second half of the measuring line, representing a more negative velocity magnitude than that obtained in the first half with more uniform tube shape. The velocity profiles measured at ML1R is showing slightly higher negative value at the end

part of the measuring line since it starts in leading to the wave crest with little contraction (small cross sectional area). Hence, the resultant velocity magnitude differs depending on the corresponding tube deformation (tube cross sectional area), so the target and actual measuring lines for UVP measurement do not remain identical. In contrast, the larger velocity magnitude (negative) inside the tube is observed at ML1R while measuring vertically compared to those measured at measuring lines ML1 and ML1 (Figure 4b). The reasons can be speculated as explained for the horizontal measurements.

3.3 Velocity profiles in the wave trough

The velocity profiles are also measured at the first and second wave trough (trough-1 & trough-2) with same history of wave propulsion moving from L→R as shown in Figure 5.

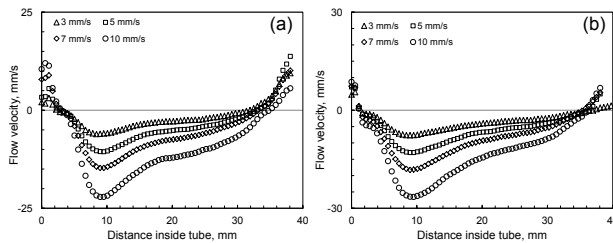


Figure 5: Measured velocity profiles in two wave troughs (of the '2-wave'-squeezing of an elastic tube), trough-1 (a) and trough-2 (b) under different speed of peristalsis.

The higher wave speed of peristalsis results in higher velocity magnitude (negative) inside the tube, which corresponds to higher back flow with a positive velocity value at the tube wall. The measured velocity profiles are representing a higher velocity magnitude in the first half of the investigated region along the adjusted measuring lines in the wave troughs (trough-1 & trough-2), indicating more contraction of the squeezed tube at that region (so the target and actual measuring lines are seen to be different by UVP). The velocity magnitude measured in the second trough is observed to be more negative than that of the first trough, as trough-2 is forwarded by the trough-1 along the wave direction.

3.4 Pressure difference under peristalsis

The local pressure in a wavelength is measured by placing pressure sensors (P_1 & P_2) in direct contact with the fluid as shown in Figure 1a. The speeds of peristalsis are varied as 2, 4, 6, 8 and 10 mm/s. The two pressure sensors are also connected with moving part of the peristalsis (the sensors are always seen to be at the same position as the peristaltic wave travels). The distance between two sensors are about 25 mm. The pressure difference between tube crest and its corresponding two troughs is measured. The crest region shows a higher pressure compared to the trough region, since the magnitude of back flow velocity in the wave trough is much higher (negative) compared to

that in the wave crest. Therefore, a higher velocity head corresponds to a lower pressure head as in the wave trough according to Bernoulli's law. The pressure difference between crest and trough of a peristaltic wave is found to be increased with increasing the wave speed as expected (Figure 6).

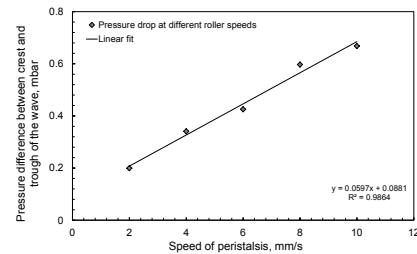


Figure 6: Variation in the pressure difference with different speeds of peristalsis.

However, the pressure difference between center of crest and trough is found to be low about 0.2 - 0.7 mbar due to low mean fluid velocity and relatively large gap in the trough (required to locate the pressure sensors).

4 CONCLUSIONS

The velocity profiles and pressure differences are investigated experimentally under peristaltic flow of a shear thinning CMC aqueous solution in an elastic tube. The higher wave speed of peristalsis results in higher magnitude of back flow velocity both in the wave crest and trough regions with positive value adjacent to the tube wall. The higher value of back flow is expected to be responsible for the improved mixing and convection leading to higher mass transport through the intestinal wall. The pressure in the tube crest is found to be higher than that at the trough. The detailed knowledge gained about non-Newtonian peristaltic flow is aimed to use in future for mass transport investigations across the elastic membrane tube wall.

REFERENCES

- [1] Nahar, S, Jeelani, SAK and Windhab, EJ: Influence of elastic tube deformation on flow behavior of a shear thinning fluid, Chem. Eng. Sci. 75 (2012), 445–455.
- [2] Lew, HS, Fung, YC and Lowenstein, CB: Peristaltic carrying and mixing of chyme in the small intestine (An analysis of a mathematical model of peristalsis of the small intestine), J. Biomech. 4 (1971), 297–315.
- [3] Yin, FCP and Fung, YC: Comparison of theory and experiment in peristaltic transport, J. Fluid Mech. 47 (1971), 93–112.
- [4] Gutzeit, A, Patak, MA, Weyarn, C, Graf, N, Doert, A, Willemse, E, Binkert, CA and Froehlich, JM: Feasibility of small bowel flow rate measurement with MRI, J. Magn. Reson. IM. 32 (2010), 345-351.
- [5] Rao, AR and Mishra, M: Peristaltic transport of a power-law fluid in a porous tube, J. Non-Newtonian Fluid Mech. 121 (2004), 163-174.
- [6] Nahar, S, Jeelani, SAK and Windhab, EJ: Steady and unsteady flow characteristics of a shear thinning fluid through a collapsed elastic tube, Proceedings of ISUD7. (2010), 61–64.

Fluid Flow Characterisation of Process Equipment using Ultrasonic Pulsed Doppler Technique

Krishna Mohanarangam, Kosta Simic, Andrew Brent and Philip Fawell*

CSIRO Process Science and Engineering, P.O. Box 312, Clayton South, VIC 3169, Australia.

*CSIRO Process Science and Engineering, P.O. Box 7229, Karawara, WA 6152, Australia.

The measurement of fluid flow patterns within pilot or large scale process vessels is an important step in understanding their base-line behaviour and optimising operating performance. Traditionally, velocity measurements within such vessels could not be readily carried out using laser based techniques due to their size and often, due to the non-transparent nature of the slurries encountered. This has changed with the advent of the UVP (Ultrasonic Velocity Profiling) system, with Doppler echoes used to quantify velocity measurements along the beam path. This paper deals with the application of UVP to obtain velocity flow patterns within a pilot-scale "feedwell", a key element of gravity thickeners, in which the incoming feed energy is dissipated and particle aggregation can be induced to enhance solid-liquid separation. Critically, UVP has highlighted the highly turbulent and unsteady nature of the flows, something that had not been previously considered with other measurement techniques. The results obtained not only provide a useful insight into feedwell flow behaviour but also enable the development and validation of new designs using CFD (Computational Fluid Dynamics) modelling.

Keywords: Process industry, pilot-scale, process equipment, feedwell, UVP, CFD modelling.

1 INTRODUCTION

Solid-liquid separation is a key stage in wastewater and mineral processing operations. For applications in mineral processing requiring high throughputs of fine particle feeds, this process is most commonly achieved through gravity thickeners. They will be found within most hydrometallurgical flowsheets, often performing multiple duties that can include pre-leach thickening, liquor clarification, residue washing (counter-current decantation), concentrate dewatering and paste tailings production.

While thickeners can take on a range of sizes and geometries, they typically comprise of a cylindrical feedwell to which the feed is delivered, surrounded concentrically by a much larger, deeper tank that forms the main body for sedimentation [1]. The primary function of thickener feedwell was originally to dissipate the feed stream momentum and achieve uniform discharge to the sedimentation zone. Feedwell use as a '*flocculation reactor*' is a relatively recent innovation, largely a consequence of the introduction of synthetic polymer flocculants in the 1960s to enhance throughputs [2]. High molecular weight flocculants (typically acrylamide and sodium acrylate copolymers) aid in fine particle aggregation and in turn greatly enhance settling. Due to the high molecular weight and viscoelastic nature of flocculant solutions, their mixing hydrodynamics (also studied by the current authors [3]) within the slurry feed is crucial in controlling flocculation kinetics [4]. The efficiency of this process may also potentially influence underflow density and overflow solids losses.

White et al. [5] showed previously that physical

investigations focussing on fluid flow within the main tank rather than the feedwell did not recognise (as discussed above) the importance of the feedwell. Where feedwells have been considered, the techniques used to measure velocities had an error band of 20% or higher and the feedwell designs were usually oversimplified. Velocity measurements in more realistic feedwell geometries using laser-based techniques were carried out by Sutalo et al. [6, 7] and White et al. [5], wherein the associated errors were about 3%. These detailed measurements were restricted to single-phase flow within laboratory scale feedwells. While this data was useful in its own right to validate a single-phase Computational Fluid Dynamics (CFD) model, detailed CFD studies show that single phase fluid structures bear no semblance to the multi-phase flows found in feedwells.

Until now, the opaque nature of multi-phase systems limited the choice of measurement techniques that could be used to quantify their flows. Advances over the past decade have made it possible to use UVP (Ultrasonic Velocity Profiling) system to measure such multi-phase flows. This paper presents detailed flow measurements performed inside a pilot-scale feedwell. UVP was able to highlight for the first time the unsteady and transient nature of the flows encountered within such feedwells.

2 EXPERIMENTAL SETUP

Earlier investigations revealed that flows within the pilot feedwell and its discharge could be strongly coupled to the outer surrounding tank. In order to capture a more realistic flow behaviour of the

feedwell independent of its surroundings, a platform was constructed to conduct pilot-scale studies within the clarification zone of an operating thickener. Figure 1 shows a schematic of the pilot scale facility, as well as a photograph of the installed platform.

The measurement grid used for flow mapping is shown in Figure 2a and the vertical plane of measurement (red centreline) in Figure 2b. The diameter of the feedwell used in the present study is 0.6 m with a depth of 0.85 m. A shelf (60 mm wide, 6 mm thick) was located within the feedwell at a depth of 250 mm from the free surface. The flow enters the feedwell through a tangential inlet pipe (48 mm ID) placed just above the shelf. For single phase flow measurement with no solids, the pressure from the mains water supply was sufficient to achieve the required flow rate, with a flow meter and flow control valve used to regulate the desired flow rate to the feedwell. For two-phase flow measurement, slurry was pumped to the feedwell to achieve the required flow rate.

All measurements were conducted with a UVP Monitor (Model UVP-Duo) Met-Flow unit [8]. A 1 MHz transducer was used to measure the axial (vertical) velocities, while a 2 MHz transducer was used for radial (horizontal) velocities. The intersection of these two transducer beams in a selected measurement plane enables the 2-D vector to be obtained by simple vector addition at that point of intersection. A time averaged velocity profile was obtained by averaging 100 s of data.

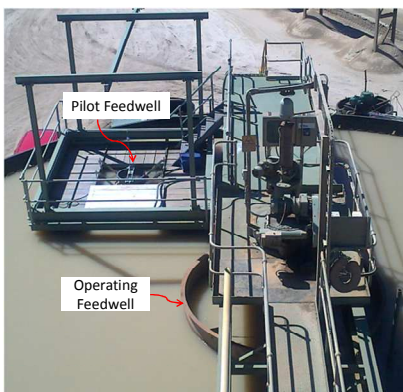
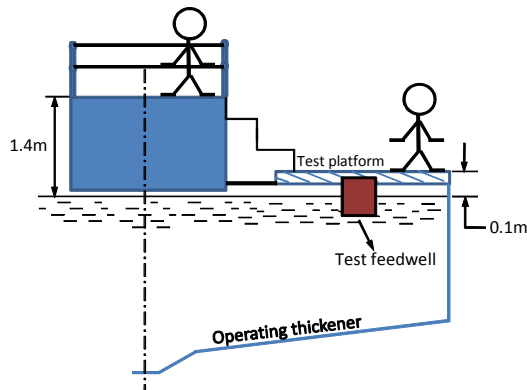


Figure 1 Schematic (a) and photograph (b) of the installed platform for UVP measurements

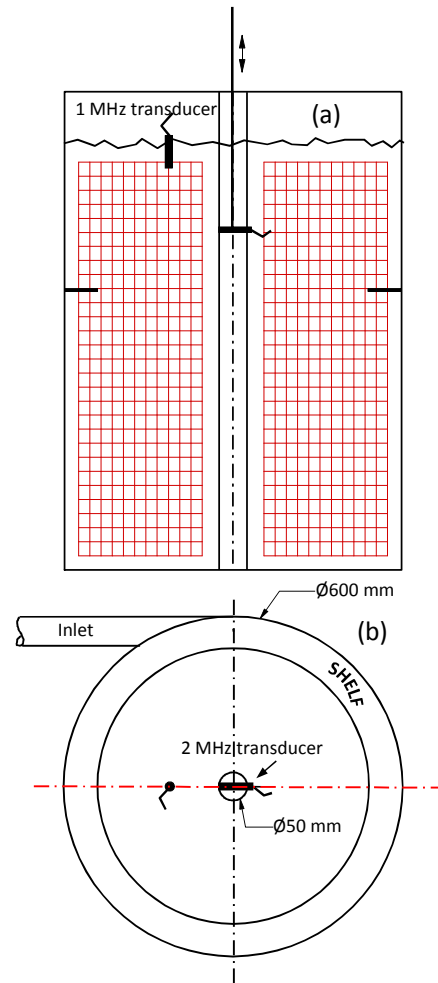


Figure 2 Measurement schematic

3 RESULTS AND DISCUSSION

3.1 Detailed Flow Map

The detailed flow map consisted of velocity measurements within the entire feedwell from the free surface right down to the discharge. The measurements were carried out at 20 mm intervals along the radial direction, while the measurement interval was 25 mm along the axial direction. A total of 80 measurement locations were considered for a flow map of the entire plane across the diameter of the feedwell.

The inlet feed velocity for the detailed flow map was maintained at 1 m s^{-1} for both the presence and absence of solids. Figure 3 shows the time averaged flow velocity vectors inside the feedwell for both water and 6%w/w solids. It can be seen that there is an up-flow along the entire central shaft of the feedwell with a down-flow close to the feedwell wall. This gives rise to recirculation regions both above and below the shelf. For the same inlet velocity, the flow in the presence of solids has a more pronounced effect with a larger downward momentum (near the feedwell wall).

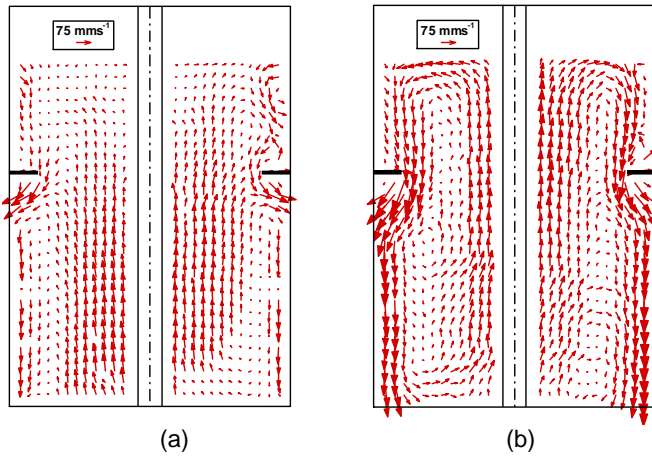


Figure 3 Detailed time averaged 2D flow map (a) Water (b) Solids at 6%w/w

Figure 4 shows contour plots of the axial velocity for both cases. The dark (red) colour signifies flow moving upwards, blue flow downwards. From these contour plots the degree and extent of natural dilution (i.e. flow into the feedwell) can be assessed. Natural or forced (through mechanical devices) dilution is an important aspect of feedwell performance; high solids dilution generally favours larger aggregate sizes, while dilution flows can also be utilised to promote adequate mixing between the slurry and the viscoelastic flocculant solution. For the water case, the “dilution” flow is confined mostly below the shelf, while the solids case shows dilution flow prevalent over the entire depth of the feedwell.

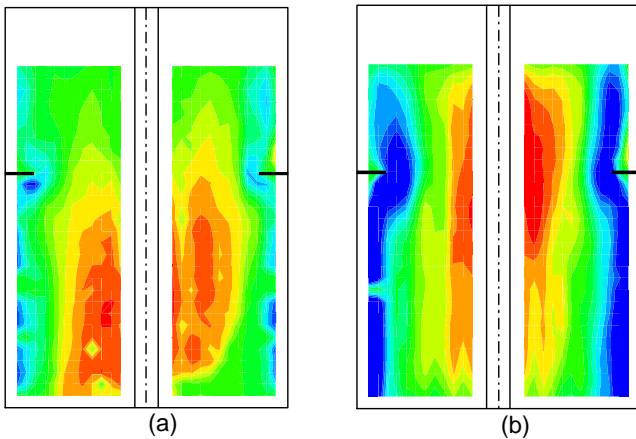
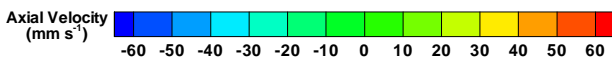


Figure 4 Time-averaged axial velocity contours (a) Water (b) Solids at 6%w/w

3.2 Targeted Flow Map

Based on the detailed flow mapping results, targeted measurements to study the effect of inlet flow rate and/or solids concentration were conducted 25 mm on either side of the shelf for the left plane shown in figure 3b. Table 1 shows the process conditions for the targeted flow measurements.

Figure 5 and Figure 6 shows the time averaged 2D velocity vector map for the low and high flow conditions, respectively. Near the feedwell wall, the flow moves downwards in proximity to the shelf, both above and below it. Halfway across the measurement plane towards the central shaft, the flow changes direction and starts to move upwards. The velocity vector pattern for all conditions remained the same while the magnitude of the vectors increased with the solids concentration and inlet velocities (high flow condition). This increase is mainly attributed to the density currents setup by the solids plunging close to the feedwell wall, causing an upwelling of liquid (or dilution) close to the central shaft.

Table 1 Process conditions for targeted flow map

Designation	Inlet velocity U_0 (m s ⁻¹)	Solids concentration (% w/w)
Low flow	0.5	0, 3 and 14%
High flow	1.0	0 and 14%

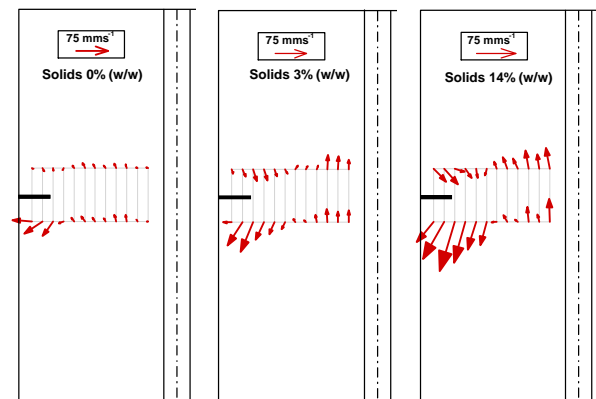


Figure 5 Time-averaged 2D velocity vectors for *low flow*

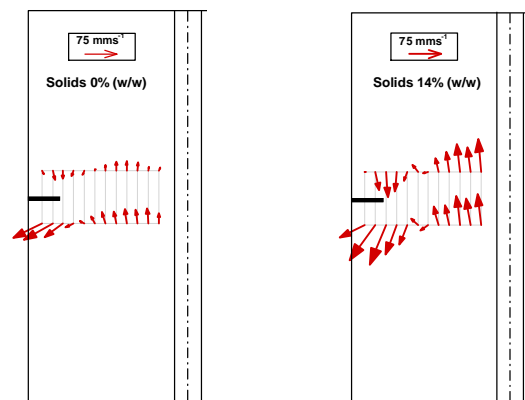


Figure 6 Averaged 2D velocity vectors for *high flow*

3.3 Axial Fluctuations

In order to better understand the turbulent and unsteady nature of flow inside the feedwell, axial velocity fluctuations, which indicate the deviation of

instantaneous velocities from its mean, were plotted across the feedwell width in the shelf region. Figure 7 plots the fluctuations of axial velocity for the measurement period above and below the shelf at high inlet flow velocities. The x-axis shows the radial distance in the feedwell, starting from the centre (0 mm) and moving towards the feedwell wall (-300 mm) in this measurement plane. The black dashed line represents the extent of the shelf away from the feedwell wall. The fluctuating velocities plotted along the Y-axis have been normalised relative to the inlet velocity.

There is a noticeable increase in fluctuations that corresponds with the increase in solids concentration; the presence of solids seems to create more unsteadiness within the feedwell. This was observed across all the process conditions tested. The axial fluctuations show a general increase from the feedwell wall to the edge of the shelf. Across all conditions tested for the no-solids (water) case, peak fluctuations were recorded at the shelf edge, which may be attributed to the flow separation. Past this location towards the central shaft, there was a decreasing trend before flattening out.

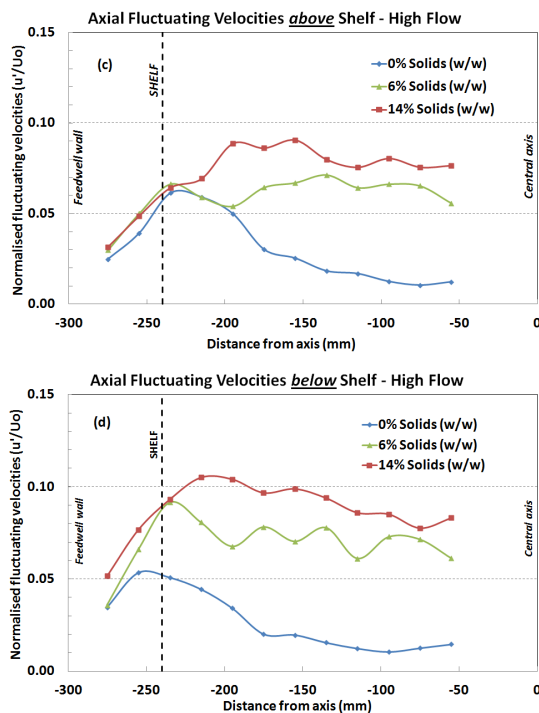


Figure 7 Axial fluctuating velocities above and below the feedwell shelf measured by UVP high flow

Flow velocity data of this nature could not previously be obtained in a pilot-scale feedwell using other available measurement techniques. The ability of UVP to quantify flow fluctuations has provided the first physical evidence to support CFD predictions of flow instabilities within single tangential inlet feedwells. The velocity data generated here will assist in the development and validation of two-

phase CFD models used for predicting flows in full-scale feedwells; such models are being used to identify design and operating strategies to enhance existing feedwell performance, as well as propose new feedwell designs.

4 CONCLUSION

The UVP system was used to measure and characterise flow patterns inside a pilot-scale feedwell fitted with a shelf. Two different inlet flow conditions and three different feed solids concentrations were considered for these studies. Detailed flow mapping inside the feedwell was carried out on one plane for two selected conditions with targeted flow mapping for the remainder of the operating conditions tested. It was found that upward dilution flows near the central shaft increase with the solids concentration due to the density gradients setup by the solids. This ultimately leads to a corresponding increase in velocity fluctuations and unsteady feedwell flow behaviour.

ACKNOWLEDGEMENT

The support of the Parker Centre for Integrated Hydrometallurgy Solutions (supported under the Australian Government's Cooperative Research Centres Program) and AMIRA P266F "Improving Thickeners Technology" sponsors are gratefully acknowledged.

REFERENCES

- [1] Fawell PD, Farrow JB, Heath AR, Nguyen TV, Owen AT, Paterson D, Rudman M, Scales PJ, Simic K, Stephens DW, Swift JD & Usher SP: 20 Years of AMIRA P266 "Improving Thickeners Technology"— How has it Changed the Understanding of Thickeners Performance? 12th International Seminar on Paste & Thickened Tailings, 21-24 April (2009), Viña del Mar, Chile, pp. 59-68.
- [2] Moody GM: Pre-treatment chemicals. *Filtration & Separation*. 32 (1995), 329-336.
- [3] Mohanaragam K, Yang W. & Simic K: Application of Ultrasonic Velocity Profiler (UVP) in Minerals Industry. Proceedings, 17th Australian Fluid Mechanics Conference (AFMC), 5-9 December (2010), Auckland, New Zealand.
- [4] Fawell PD, Owen AT, Grabsch AF, Benn FA, Labbett DM & Swift JD: Factors affecting flocculation within gravity thickeners. *Water in Mining 2009: Proceedings*, 15-17 September (2009), Perth, Western Australia, AusIMM. Publication Series No. 10/2009, AusIMM. Carlton, Australia, pp. 71-76.
- [5] White RB, Sutalo ID and Nguyen T: Fluid flow in thickener feedwell models. *Minerals Engineering*, 16, (2003), 145-150.
- [6] Sutalo ID, Nguyen T & Rudman M: Modelling studies of fluid flow in a thickener feedwell model, CHEMECA, Perth, Western Australia, 9-12 July (2000).
- [7] Sutalo ID, Nguyen T, White RB & Rudman M: Experimental and numerical investigations of the fluid flow in thickener feedwells, Sixth World Congress of Chemical Engineering, Melbourne, Australia, 23-27 September (2001), paper 941.
- [8] Met-Flow SA: UVP Monitor Model UVP-DUO users guide (2002), Metflow SA, Lausanne, Switzerland.

